Testing the Models of Cosmological Structure Formation

Stephen John McNally

Presented for the Degree of Doctor of Philosophy
at the University of Edinburgh
1996

This thesis is solely my own composition, except where specifically indicated in the text.

Stephen McNally,
September 1996.

Acknowledgments

Having trotted out 200 pages of scientific mumbo-jumbo I find myself nearly suffering writer's block in starting this section. So many people have contributed to my life here in Edinburgh through assistance with work, kindliness and friendliness that I can do them no justice in a couple of paragraphs here.

Several members of the Observatory staff deserve a mention. Firstly my supervisor John Peacock whose sharp eye for detail and blisteringly quick wits are the scourge of all sloppy arguments. A thoroughly nice bloke, I should add, whose consistent and heartening interest in my work and well-being kept me on the rails over the past four years. Eelco van Kampen who generously proof-read a big chunk of this thesis and is a good friend. Good luck in Denmark Eelco! Also Alan Heavens who has been instrumental in keeping my confidence afloat during the most ego-mangling parts of the last four years. A true son of the Fatherland (Yorkshire) and a Leeds Utd. fan to boot. I must also acknowledge Drs. Stephen Dodds, Andy Taylor and Mike Hawkins for providing some useful data and code for chapters 5 and 6, and all the other freaks of figure and form that make the ROE such an unusual and interesting place to work. Moving abroad, I would like to thank Mark Hindmarsh and Dick Hunstead for providing useful responses to my out-of-the-blue Emails.

I've been dead lucky in my office-mates during this PhD. In turn I would like to thank Harry for the demented/inspired zeal he brings to astronomy/football/life, Jonny for being so unflappably good-humoured (particularly over the last few months) and Thackers for being such a schmashing goy. Outside the murky recesses of R8 thanks to: Bill 'Haircut' Ballinger, Nice Guy Henry, Mike 'Macca' McCartney, Alison 'Sterling' Stirling, Rachel 'Scary' Johnson, Milagros, Han Ying, Mike Read, Nick and others too numinous to mention, for being such a jolly bunch. Wandering out into Edinburgh at large I'd like to say cheers to Bondy, Mad Dave, Tom, Jonno, Sophie and Amanda for being really good mates. Down in merrye England, the Beverley Mob (Dave P, Jim, Leppo, Tex, Isobel, Catherine, Bruvver Andy Mac) – see you soon. Kirsty, love you for putting up with my nonsense. Finally, biggest thanks and hugs to my parents for supporting me in all things.

I would like to acknowledge PPARC and Torphichen Street Dole Office for funding me during this thesis.

Abstract

The introduction describes promising theories which extend the Standard Model – *inflationary* and *topological defect* models. Although inflation solves some important problems the model is poorly motivated in terms of currently understood particle physics. Furthermore, conclusive tests of inflation are elusive. Topological defects, while less of a panacea for the problems of the field, are well motivated by theories of Grand Unification at $T \sim 10^{16}$ GeV and make plausible candidates for the source of primordial inhomogeneities. Crucially, cosmic strings, the best investigated class of topological defect models, have testable consequences for the microwave background and the lensing of galaxies. Chapters 2 – 4 adapt the second of these effects into a search method for strings. Chapter 2 draws heavily on simulations of string networks to set limits on the shape and distribution of horizon-spanning strings. Chapter 3 investigates the appearance of galaxies lensed by such strings. In chapter 4 this knowledge is then built into an algorithm which searches for strings on Schmidt plates. Ultimately only a weak density limit of $\lesssim 90$ long strings per horizon volume can be set with this survey medium. Finally, an extension of the work to deeper surveys is considered – running the search algorithm on the large area Sloan survey should test the cosmic string model conclusively.

The introduction in chapter 1 also exposes the most significant grey areas in the Standard Hot Big Bang model: (a) determining the form and density of the energy content of the Universe, and reconciling this to (b) the age of the Universe, and (c) the observed clustering of galaxies. This thesis makes two contributions to this area. Chapter 5 discusses a variant of the Cold Dark Matter model in which a dark matter component decays radiatively at early times. The model has the virtue that it can accommodate the *low* apparent value of Ωh inferred from observed large-scale galaxy clustering and the *high* measured values of Ω and h. Limits on the small-scale clustering predicted by such models constrains the mass and lifetime of the decaying component to $0.5 < m < 30$ keV, $0.2 < \tau < 500$ years. Chapter 6 contributes to the observational tests of large-scale galaxy clustering by constraining the clustering signal of a sample of high-redshift radio galaxies. The clustering measured here is consistent with that measured with other radio surveys. The high redshift data are important as they give clues to the evolution of the

density field with time. Forms of bias evolution which arise from continuity constraints on the equations of motion for galaxies and the mass (i.e. $b[z] = b[0] - \alpha + \alpha[1+z]$) are shown to be entirely consistent with the data, as are unbiased $b[z] = b[0]$ models. Schemes in which bias in galaxy numbers arises from the differential formation and motion of dark matter haloes (predicting $b[z] = b[0] - \alpha + \alpha[1+z]^2$) are shown to be only marginally consistent with the clustering measured at the highest redshifts, ($z \simeq 1.5$). Improvements to the dataset which would allow more conclusive limits are discussed.

Contents

Chapter 1

Introduction

In the last few years observations of structure on the very largest scales in the universe have advanced tremendously. They have reached a point where, at last, it is a serious proposition to test theories of the composition of the universe and the processes at very early times that generated present day structure. Many once fashionable theories of structure formation can now reliably be dismissed. There remains, however, a plethora of models which are as yet consistent with observations and, conversely, observations which, as yet, have no credible explanation in terms of well understood physics.

The purpose of the work described in this thesis is to develop and apply tests of the most promising theories. The current observational and theoretical status of the field will be reviewed in this chapter. Chapters 2 to 4 investigate a promising scenario for the generation of primordial fluctuations responsible for present structure – the cosmic string model. Chapter 2 discusses the model, with reference to simulated and observed data. Chapter 3 introduces an observational test for strings and Chapter 4 describes its application to the UK Schmidt survey plates. Chapter 5 attempts to reconcile galaxy formation and clustering data with dark matter models. It develops stringent new tests for a promising variant of CDM with a decaying particle species. Chapter 6 describes work on a very deep galaxy catalogue generated from stacked Schmidt plates, with particular reference to the clustering of high redshift galaxies. Chapter 7 advances suggestions for future work in these areas and focuses on some of the remaining important questions.

1.1 Background Cosmology

1.1.1 The Standard Model

The following is a summary of basic results for an expanding isotropic universe. The evidence for and against the Standard Model is not dealt with here – suffice to say that the model has passed stringent tests and made some telling predictions – relevant discussions can be found in Peebles (1993) and Sandage (1995).

The formulae are adopted from Padmanabhan (1993). Natural units in which $c = \hbar = k_B = 1$, and the Planck mass $m_p = G^{-1/2} \sim 10^{19}\,\mathrm{GeV}$ are used throughout this text. $\mathrm{M}_\odot$ denotes the solar mass $\simeq 2 \times 10^{30}$ kg.

The starting point for discussions of the global structure of the universe is embodied in the *cosmological principle*, i.e. the universe is homogeneous and isotropic. Hence it appears the same in every direction from every point in space. The most general line element consistent with this principle is the Friedmann-Robertson-Walker form

$$d\tau^2 = dt^2 - a^2(t)\left[\frac{dr^2}{1-kr^2} + r^2(d\theta^2 + \sin^2\theta d\psi^2)\right]. \tag{1.1}$$

Spatial hypersurfaces have positive, zero and negative curvatures for $k < 0$ (open) $k = 0$ (flat) and $k > 0$ (closed) cases respectively. k is determined by the spatial topology and global geometry of the universe. Closed universes are compact whereas flat and open universes are spatially infinite. $a(t)$ is the universal *scale factor*, with the present day value a_0. The time dependence of the scale factor implies a universal expansion or contraction with time. The observations indicate a present universal expansion such that a stationary observer finds distant galaxies to be receding. r, θ and ψ are analogous to 3D spherical polar coordinates and remain fixed for a particle smoothly following the Hubble expansion, i.e. they are *comoving coordinates*. Equation 1.1 can be recast as

$$d\tau^2 = dt^2 - a^2(t)\left[dr^2 + S_k^2(r)(d\theta^2 + \sin^2\theta d\psi^2)\right] \tag{1.2}$$

with $S_k(r) = \sin r$ for $k = 1$, $S_k(r) = r$ for $k = 0$ and $S_k(r) = \sinh r$ for $k = -1$, with all the comoving coordinates now dimensionless.

Hubble's constant $H(t)$ measures the rate of universal expansion at time t

$$H(t) = \frac{\dot{a}(t)}{a(t)} \tag{1.3}$$

with $H_0 = 100h\,\mathrm{km\,s^{-1}\,Mpc^{-1}}$ its present value. Current observations imply $h = 0.5-1.0$ and are discussed more fully in section 1.1.2. The physical distance of two comoving particles separated by l grows in proportion to $a(t)$ such that in the rest frame of one the other recedes at $v = H_0 l$. In this fashion light from distant objects is *redshifted.* The redshift z of a frequency emitted by a source expanding with the Hubble flow is given by

$$\frac{w_e}{w_0} = \frac{a(t_0)}{a(t_e)} \equiv 1 + z \tag{1.4}$$

with t_e and t_0 the age of the universe at emission and at the present day respectively. $z \simeq H_0 d$ is valid for sources expanding with the Hubble flow provided $z \ll 1$.

The dynamics of the universe as a whole are given by the Friedmann Equations

$$H^2 = \left(\frac{\dot{a}}{a}\right)^2 = \frac{8\pi G\rho}{3} - \frac{k}{a^2} \tag{1.5}$$

$$\frac{\ddot{a}}{a} = -\frac{4\pi G}{3}(\rho + 3p) \tag{1.6}$$

with p and ρ the pressure and density respectively, of the cosmological fluid and G the gravitational constant. Here ρ includes all contributions to the energy density – non-relativistic matter ρ_m, relativistic species ρ_r and a possible vacuum term ρ_v. In the standard model the relativistic contributions are radiation at density ρ_γ and three massless neutrino species at a combined density of $\rho_{3\nu} = 0.68\rho_\gamma$.

Given the energy density an equation of state, $p = p(\rho)$, completely specifies the expansion behaviour of the universe. In typical models the universe evolves through successive phases where one form of energy density dominates all the others. In such cases the equation of state has a simple form:-

non-relativistic matter	$p = 0$	$\rho_{\rm m}(z) = \rho_{\rm m,0}(1+z)^3$
radiation	$p = \rho_{\rm r}/3$	$\rho_{\rm r}(z) = \rho_{\rm r,0}(1+z)^4$
vacuum energy	$p = -\rho_{\rm v}$	$\rho_{\rm v}(z) = \rho_{\rm v,0}$

where the "0" subscripts denote present day ($z = 0$) values. The redshift dependencies are true so long as no process operates to convert energy from one form to another. The epoch at which the matter and radiation densities are equal at $z = z_{\rm eq} \simeq 24\,000\Omega h^2$ is a crucial one. It is at this point that the universe becomes matter dominated and small-scale structure can begin to grow. More will be said about this important phase of universal evolution in section 1.2.3.

1.1.2 Fundamental Parameters: Ω_0, Λ and H_0

A key question that cosmological theory must confront is that of the composition of the universe. The first thing to note is that the density of matter, radiation and vacuum energy governs the ultimate fate of the universe. The universe may be *closed, open* or *flat* depending on the relative magnitudes of the expansion rate, set by H_0, and the total energy density. Open universes expand indefinitely whereas closed universes ultimately enter a contraction phase and collapse in a "Big Crunch". The flat case describes a universe which is poised precisely between the open and closed states. The kind of universe we inhabit is parameterized by Ω_0, where

$$\Omega_0 = \frac{8\pi G\rho_0}{3H_0^2} \tag{1.7}$$

with $\Omega_0 > 1$, $\Omega_0 < 1$ and $\Omega_0 = 1$ characterizing the closed, open and flat cases respectively. These correspond to $k > 0, < 0$ and 0 in equation 1.1, and so affect the large scale geometry of the universe. Alternatively the density can be expressed as

$$\rho_0 = 2.78 \times 10^{11}\Omega_0 h^2\ {\rm M}_\odot\,{\rm Mpc}^{-3}. \tag{1.8}$$

A considerable amount of controversy surrounds recent attempts to establish the values of both Ω_0 and H_0 and we will examine each in turn.

Establishing the value of Ω_0 is at the forefront of cosmological research for numerous reasons. One reason is noted above, Ω_0 dictates the long-term behaviour of the universal expansion. A second reason is of particular importance for structure formation theory – the rate at which overdensities grow depends on the amount of gravity available. Structure grows more quickly in high-Ω universes. This is vital if we are to understand how fluctuations at the recombination epoch at $z \simeq 1100$ (probed by CMB studies) have grown into inhomogeneities of the sorts of amplitudes observed today at $z \simeq 0$. Furthermore, we wish to test inflationary models (see section 1.3.3) which generically predict $\Omega_0 = 1$ universes.

A fundamental problem in the direct evaluation of Ω_0 from observation is that we do not appear able to see directly the majority of the matter. The evidence for this is necessarily indirect, though compelling. The main component of *luminous* matter available is in the form of stars and gas in galaxies. This provides an Ω_0 of roughly 0.3%. The expected radiation background of CMB photons and relic neutrinos is insignificant by comparison ($\Omega_{r,0} = 4.2 \times 10^{-5} h^{-2}$). There would appear to be little extra mass available in the universe unless there is substantial ionized gas between the galaxies.

Numerous lines of enquiry, however, indicate that we are not seeing the major sources of mass in the universe. For example, spiral galaxy rotation curves seem to indicate gravitational fields far greater than can be accounted for by the luminous component. Allowance for this extra unseen halo mass suggest $\Omega_0 \simeq 2\%$. At larger scales, if we assume that clusters of galaxies are in virial equilibrium then the discrepancy becomes even more marked. The cluster galaxies move in a gravitational environment which seems to require $\Omega_0 \sim 20\%$. Finally on the largest scales, large scale flows due to supercluster infall suggest hidden mass on supercluster scales which is ~ 100 times in excess of the visible matter. In a sense, these are *lower* bounds on Ω_0, since the addition of homogeneously distributed matter on larger scales than these would leave the dynamics unaffected. A review of the data is given in White (1989).

Not only is the additional matter invisible, it is very likely to be *non-baryonic*. A sufficiently good understanding of the nucleosynthesis era of the Big Bang permits accurate simulation of the abundances of the light elements generated from primordial baryons.

It turns out that the ^{3}He and D abundances are highly sensitive to the baryon density Ω_B and the expansion rate h to the extent that observations yield the firm constraint of

$$\Omega_B h^2 = 0.0125 \pm 0.0025 \tag{1.9}$$

(Walker et al. 1991) which is far below what is needed to account for all the matter. What, then, is the nature of the extra matter? Since the baryons are the only stable, significantly massive particles within the standard model we are forced to look beyond established physics for a solution. Many viable dark matter candidates have been suggested in the literature. The candidate identifications of the dark matter span an enormous range of mass from axions of mass $\sim 10^{-5}$eV to black holes of mass $\sim 10^6 M_\odot$. The greatest attention has been focused on models in which a Weakly Interacting Massive Particle (WIMP) species forms an, as yet, undetected, cosmic background. The models fall into two main categories.

- *Hot Dark Matter* (HDM) – particles that were relativistic when they decoupled from the rest of the matter in the universe and retain high velocity thermal motions. The prototypical example is a massive μ or τ neutrino.
- *Cold Dark Matter* (CDM) – particles with insignificant thermal velocities – axions or high mass supersymmetric particles are a popular choice.

In addition to these categories we could have *Warm Dark Matter* (WDM) which has properties inbetween those of the above, or *Mixed Dark Matter* (MDM) which allows varying fractions of HDM *and* CDM. A review of the motivations and candidates for dark matter models is provided by Trimble (1987).

The detection and identification of dark matter particles in the laboratory may prove to be a difficult task. Despite our relative ignorance of the relevant particle physics we can, however, predict how varying types of dark matter would affect the origins and growth of structure. HDM and CDM make sufficiently distinct predictions about the important scales and order of events in structure formation for firm tests to be applied.

The comparison of rival dark matter theories will be discussed further in section 1.2 and chapter 5.

In addition to standard matter and radiation backgrounds we could also appeal to models with a significant gravitational contribution from *vacuum energy*, typically parameterized by

$$\Lambda = 8\pi G\rho_{\rm v}. \tag{1.10}$$

Such models are, however, not well motivated by existing theories of particle physics – Planck scale values of $\Lambda \sim m_p^4$ are a factor of 10^{120} in excess of observational limits (see, for example, Carroll, Press and Turner 1992). On the other hand values allowing $\Omega_{\rm v} = \Lambda/3H_0^2 = 0.2 - 0.8$, though seemingly *ad hoc* are not easily ruled out on direct observational grounds.

Obtaining the value of H_0 is also of great importance for cosmology. Firstly it sets the *length scale* associated with distant objects, where we have only the redshift to set the radial distance. This also directly affects the masses and densities which we infer, e.g. the critical density in equation 1.8 is proportional to h^2. Secondly H_0 relates to the *age* of the universe, it is simply $t_0 = \frac{2}{3}H_0^{-1} = 6.52h^{-1}$ Gyr in the Einstein-de Sitter case. For open models and models with significant vacuum energy contributions the age of the universe can be approximated by

$$t_0 \simeq 6.52h^{-1}[0.7\Omega_{\rm m} + 0.3 - 0.3\Omega_{\rm v}]^{-0.3} \tag{1.11}$$

with $\Omega_{\rm m}$ and $\Omega_{\rm v}$ the fraction of critical density contributed by the matter and vacuum energy respectively. The expression (from Carroll, Press & Turner 1992) gives answers correct to within a few % over plausible ranges for the parameters.

Perhaps unsurprisingly, measuring H_0 is far from straightforward. Relatively crude methods are used to infer cosmological distances independently of redshift and errors are often hard to estimate. Until recently the possible values of h covered a broad range of $0.5 - 1.0$ (Rowan-Robinson 1986). Greater accuracy was promised by the key project of the Hubble Space Telescope – observing Cepheid variables in distant galaxies.

From observing these well understood high-luminosity stars in a Virgo-cluster galaxy a measurement of $H_0 = 80 \pm 17\,\mathrm{km\,s^{-1}\,Mpc^{-1}}$ was published (Mould et al. 1995).

In an Einstein-de Sitter Universe ($\Omega = 1$, $\Lambda = 0$) this suggests the age of the universe to be $t_0 \simeq 8\,\mathrm{Gyr}$. This is in serious disagreement with independent estimates of the age of the galaxy from globular clusters of $14 \pm 1.5\,\mathrm{Gyr}$ (Bergbush & VandenBerg 1992). In fact *most* of the indirect arguments prefer a low value ($h \lesssim 0.5$), (e.g. equation 1.24 in the next section). The HST measurement, if correct, indicates that we occupy a universe of low density ($\Omega = 0.1 - 0.3$) or a significant component of the closure density is provided by vacuum energy ($\Lambda > 0$). At this stage, however, the new generation of Hubble constant measurements have yet to converge to a convincing value. For example, supernova methods with the HST still give $h \simeq 0.5 - 0.7$ (e.g. Saha et al. 1994, Riess et al. 1995). It will take some time before we will know how seriously discrepant the models are and which of the assumptions are wrong[1].

1.2 The Matter Distribution

This section briefly describes the standard formalism for evaluating and evolving cosmological density fields. It then proceeds to describe the current status of observations and the theories that seem best able to account for what is seen. Greater detail on each issue can be found in Peacock (1992) and Efstathiou (1989).

1.2.1 Mathematical Tools

Generally, in characterizing a density field we are interested in quantifying the deviations from homogeneity on a given scale or in assessing the density at a given point. The characteristic of prime importance is the density contrast δ defined by

$$\delta(\mathbf{x}) = \frac{\rho(\mathbf{x}) - \bar{\rho}}{\bar{\rho}}. \tag{1.12}$$

[1] $h = 0.75$ is assumed in this thesis except where explicitly stated otherwise.

We can characterize the inhomogeneities at a given scale with the *autocorrelation function* of the density field

$$\xi(\mathbf{r}) \equiv \langle \delta(\mathbf{x})\delta(\mathbf{x}+\mathbf{r}) \rangle. \tag{1.13}$$

We can readily transform the density field $\delta(\mathbf{x})$ into its Fourier modes δ_k with

$$\delta_k = \int \delta(\mathbf{x}) e^{i\mathbf{k}\cdot\mathbf{x}} d^3x. \tag{1.14}$$

Note this really assumes that our field occupies a flat space (i.e. $k = 0$ in equation 1.1) in which the plane waves $e^{i\mathbf{k}\cdot\mathbf{x}}$ are a complete set, otherwise the corresponding curved space results are needed. Such a transform is immensely useful when dealing with gravitational growth. For small density perturbations growth occurs *linearly* and the modes δ_k grow *independently* of each other, i.e

$$\delta_k(t) = D(t)\delta_k(0). \tag{1.15}$$

A form for $D(t)$ and an initial prescription for δ_k lets us easily evolve the density field from $t = 0$ all the way to the non-linear phase (where $\delta \simeq 1$ and the modes are no longer independent).

This recasting of the field in terms of Fourier components leads us naturally to the definition of the *Power Spectrum* of the fluctuations

$$P(k) \equiv \langle |\delta_k|^2 \rangle \tag{1.16}$$

which can easily be shown to be the Fourier transform of the autocorrelation function $\xi(\mathbf{r})$. A useful statistic – the *variance* of the field – can be readily derived

$$\sigma^2(k) = \int_0^k 4\pi k^2 P(k) dk \tag{1.17}$$

and leads to an alternative casting of the power spectrum which is dimensionless and independent of $\sqrt{2\pi}$ factors in differing Fourier conventions:

$$\Delta^2(k) \equiv \frac{d\sigma^2}{d\ln k} = 4\pi k^3 P(k) = \frac{2k^3}{\pi} \int_0^\infty \xi(r) \frac{\sin kr}{kr} r^2 dr. \tag{1.18}$$

1.2.2 The Measurement of Clustering

Of course we cannot directly measure the density field as a continuum; we are limited to observations of luminous objects i.e. galaxies. A seemingly reasonable assumption is that *light traces mass* so that galaxies are clustered where the underlying dark mass is clustered. If this were true, we could view galaxy clustering as a point process which samples the density field of *all* the matter. With a mean galaxy density n, the point probability δP of finding a galaxy in each of volume elements δV_1 and δV_2 separated by r would then be

$$\delta P = n^2(1 + \xi(\mathbf{r}))\delta V_1 \delta V_2. \tag{1.19}$$

In practice the assumption that light accurately traces mass appears too strong. We have to allow for a *bias* function b to relate the distribution of galaxies, measured as $\xi_g(r)$ or $\Delta_g(k)$, to the distribution of matter, specified as $\xi(r)$ or $\Delta(k)$. Although many physical mechanisms to generate bias have been suggested, none are particularly convincing and the issue is a major stumbling block in attempts to compare theory (which, in general, predicts a value for Δ) with galaxy-galaxy correlation measurements. The bias is defined such that

$$\left|\frac{\delta\rho}{\bar{\rho}}\right|_{galaxies} = b\left|\frac{\delta\rho}{\bar{\rho}}\right|_{mass}. \tag{1.20}$$

In some cases the form of the bias can be quite simple, in a model due to Kaiser (1984), galaxies form only in regions where the density contrast exceeds some threshold. If this threshold is greater than the rms fluctuation on the relevant scale then the galaxies are born *more* clustered than the mass and hence

$$\xi_g(r) = \langle \delta_g(\mathbf{x})\delta_g(\mathbf{x}+\mathbf{r})\rangle = b(r)^2\xi(r) \tag{1.21}$$

with $b(r)$ approaching a constant when $\xi(r) \ll 1$; one which may well vary depending on the type of galaxy used to probe the density field. Typical attempts to quantify bias pick out scales on which the linear growth of perturbations should still be a valid

approximation. A commonly encountered parameter is σ_8, the rms mass fluctuation in cubes of side $8h^{-1}$ Mpc. This is the scale on which the rms fluctuation in *galaxy number counts* is observed to be ~ 1. Studies with N-Body codes reveal that bias values of ~ 1.6 (CDM) and ~ 2.7 (HDM) can arise quite naturally once attempts are made to model the complicated role of baryonic hydrodynamics in galaxy formation (e.g. Cen & Ostriker, 1992). Non-linear effects may well cause the bias to become a scale-dependent function in regions below $8h^{-1}$ Mpc. As a further complication it is well-established that different classes of galaxy – (e.g. IRAS, optical, radio) are biased to different degrees (Peacock & Dodds 1994). We will have more to say about attempts to quantify the bias in later chapters.

1.2.3 The Evolution of Structure

With a model for the initial power-spectrum of density perturbations we can turn to the calculation of the present day spectrum. Later sections will argue that both cosmic strings and inflation yield a scale-invariant or *Harrison-Zel'dovich* power spectrum of fluctuations in the early universe (i.e. $P(k) \propto k^n$) with $n \simeq 1$ (e.g. Zel'dovich 1972). In inflation $\delta\rho/\rho$ is the same at each epoch on the horizon scale and the same amplitude is imprinted on each wavelength as it leaves the horizon. For strings the existence of a scaling solution means that scales are subject to the same perturbation whenever they enter the horizon.

The subsequent behaviour of perturbations depends on the universal expansion and the prevailing form of the dark matter. Once modes have entered the horizon the expansion rate will determine whether gravitational growth is possible. In general during the radiation dominated epoch the expansion is too fast and growth of sub-horizon scale fluctuations proceeds at best logarithmically. After $t = t_{\rm eq}$ the time of matter-radiation equality at $z \simeq 24\,000\Omega h^2$ the modes can grow in proportion to the scale factor $a(t)$. The changeover between the two eras imprints a characteristic scale on the power spectrum, that of the horizon size at matter-radiation equality,

$$r_{\rm H} = \frac{16.0}{\Omega h^2}\,{\rm Mpc}. \tag{1.22}$$

At large scales that have only entered the horizon since $t_{\rm eq}$ we expect to see evidence of the primordial power spectrum with $P(k) \propto k$. For smaller scales, i.e. $k > k_{\rm eq} \simeq 2\pi r_{\rm H}^{-1}$ the power spectrum should 'turn over' to the form $P(k) \propto k^{-3}$.

The dark matter can imprint a second characteristic wavelength in the fluctuation spectrum. If the thermal motions of the constituent particles are of relativistic size (as in Hot Dark Matter models) then free streaming diffusively erases small-scale structure at early times. This effect corresponds approximately to Gaussian filtering of the power at a scale $\lambda_{\rm FS}$ of order

$$\lambda_{\rm FS} \simeq 28\,{\rm Mpc}\left(\frac{m_\nu}{30\,{\rm eV}}\right)^{-1} \tag{1.23}$$

for a hot background of neutrinos with mass m_ν (Bardeen et al. 1986; hereafter BBKS). In such scenarios there are typically negligible fluctuations on galactic scales and so galaxies must form by the fragmentation of larger supercluster sized objects. However it turns out that numerical simulations of structure formation show this model to be inconsistent with observations of galaxy clustering. Furthermore HDM-type models matching the large-scale clustering data have insufficient small-scale power to form the observed abundances of high-redshift QSO's, radio galaxies and damped Lyman-α systems (e.g. Mo & Miralda-Escudé 1994). HDM models with scale-invariant primordial spectra are thus waning in popularity.

No such severe problems exist in the rival Cold Dark Matter (CDM) scenarios. Here the random thermal motions of the particles are insignificant on the scales of interest and any initial small scale power survives unmolested to late times. Structure can thus grow hierarchically – small objects first, larger objects later – which seems more in accord with what is observed. The assumption in HDM and CDM models is that the baryonic contribution to Ω is dynamically insignificant and the baryons simply follow the clustering of the dark matter after photon drag becomes unimportant at $t_{\rm rec}$ (the recombination epoch). Power spectra for representative CDM and HDM-type models are given in figure 1.1.

Despite a promising qualitative agreement between the properties of CDM type models and the observations a quantitative problem arises when direct comparisons are made.

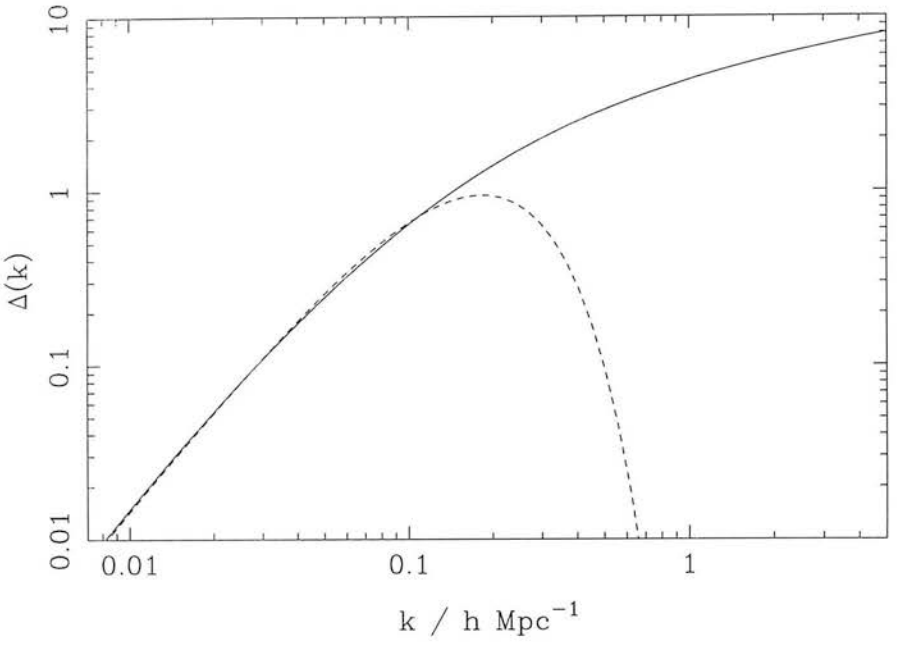

Figure 1.1: *COBE* normalized model power spectra from BBKS (1986). The solid line shows an adiabatic CDM model, the dashed line is an adiabatic HDM-type model with one massive and two massless neutrino species. In both models $\Omega = 1$ and $h = 0.5$. Note the severe damping of power above $k \simeq 0.2h\,\mathrm{Mpc}^{-1}$ in the HDM case due to free-streaming of the constituent particles.

CDM transfer functions can be reliably calculated (BBKS) and effectively have only two free parameters. Firstly, there is a shape parameter Ωh which determines the scale at which r_{H} features in the spectrum. Secondly we require a normalisation of the amplitude at some large scale i.e. by constraints on σ_8 or the *COBE* rms quadrupole measurement which constrains the power on scales of hundreds of Mpc. A baryonic contribution to Ω also modifies the predicted power though not significantly for fractions as low as (1.9). The problem arises when $\Omega = 1$ CDM spectra consistent with plausible values for Ωh (i.e. 0.5–1.0) are extrapolated well away from the chosen normalisation scale. Spectra normalised on the very large *COBE* scales ($k \simeq 0.002h\,\mathrm{Mpc}^{-1}$) generate too much small scale power yielding predicted galactic velocity dispersions up to twice the size of those observed. Normalisation by σ_8 (defined in section 1.2.2) underproduces large-scale clustering compared to that observed in galaxy catalogues. As both σ_8 and the *COBE* quadrupole are quite well pinned down it is apparent our guesses for the shape parameter are incorrect.

Attempting to allow for the modification of the observed power by bias, nonlinear

evolution for $\Delta^2(k) > 1$ and redshift-space distortions, Peacock & Dodds (1994) fit CDM transfer functions to various clustering datasets and conclude a best fit for

$$\Omega h = 0.255 \pm 0.017. \tag{1.24}$$

A spatially flat CDM universe looks like being ruled out by this analysis. The significance of this puzzling result and attempts to explain it are the basis of chapter 5.

1.3 Extending the Standard Model

1.3.1 The Main Issues

The standard model has several notable successes in accounting for global properties of the Universe, notably the Hubble expansion, the CMB radiation and the light element abundances. It would seem fair to believe that we have a good description of the important physical processes operating up to $T \sim 1\,\mathrm{GeV}$. However numerous enigmas persist which have no explanation within established physics. The most significant of these are

- *The horizon problem* The universe appears homogeneous and isotropic even between regions which have never been in causal contact. The range of causal contact a time t after the Big Bang is given by

$$r_{\mathrm{H}} = \int_0^t \frac{c\,dt}{a(t)} \tag{1.25}$$

  which is convergent as $a \propto t^{1/2}$ in the radiation dominated phase. The temperatures of the microwave sky in opposite directions agree to within $\sim 0.01\%$ and yet the horizon size at last scattering was $\sim 100\,\mathrm{Mpc}$ subtending about 2° on the sky. The standard model offers no mechanism by which we would expect such causally disconnected regions to be so similar.

- *the flatness problem* $\Omega = 1$ universes are in unstable equilibrium as

$$\Omega(t) - 1 = \frac{\dot{a}_0^2}{\dot{a}^2}(\Omega_0 - 1). \tag{1.26}$$

To have $\Omega \sim 1$ at the present epoch requires $\Omega = 1$ to better than one part in 10^{60} at the Planck epoch. Either $\Omega = 1$ exactly due to some unknown principle or an incredible fine tuning of the parameters is required to have a universe where Ω is even *close* to 1.

- *density fluctuations* The inhomogeneities in the Universe are often believed to have formed by the gravitational amplification of initially tiny density perturbations formed in the early universe. The source of these initial fluctuations is not provided in the standard model. The current understanding of the origin of large-scale universal structure is that small density fluctuations in the early universe form an initial spectrum of overdense and underdense regions. The overdense regions are unstable to gravitational collapse and grow at the expense of the underdensities. Over a substantial fraction of the age of the universe these small primordial fluctuations evolve into the large-scale inhomogeneities of the present day. This basic picture has much to recommend it. Over the scales of interest gravity is the only known force with the strength to form bound or collapsing structures. If we view galaxies as test particles in a cosmological force field then their peculiar velocities appear consistent with the action of gravity (the peculiar velocity of a galaxy is its deviation from the homogeneous Hubble flow). Furthermore, the observation of bound objects at high redshift, such as quasars, and the recent detection of fluctuations in the cosmic microwave background tell us that substantial deviations from homogeneity are not a recent development.

  We also want to understand how the present day amplitude of the density fluctuations has arisen. The degree of fluctuation on the horizon scale δ_h is fixed by the *COBE* measurement to be of order

$$\delta_h \sim \frac{\Delta\phi}{c^2} \sim \frac{\Delta T_{\rm CMB}}{T_{\rm CMB}} \sim 10^{-5} \tag{1.27}$$

  as discussed in Appendix C of Padmanabhan (1993).

It may be possible that all these problems will be solved by a theory of quantum gravity. Such a theory becomes essential when we try to understand the properties of the Universe at times earlier than the Planck time of $\sim 10^{-43}$s. Until the effects of

quantizing gravity are better understood it may seem reasonable to regard the solution to these problems to be in initial conditions laid down at the Planck epoch. An important recent advance in cosmology, however, is the realisation that many of these problems may have an explanation in processes occurring at energies of $\sim 10^{15}$ GeV at the later GUT epoch. This holds out the possibility that the crucial physics can be analysed in classical spacetime without recourse to quantum gravity. The most widely discussed model in which these issues are addressed is the *inflationary* paradigm of Guth (1981) which will be described after a brief description of the relevant high energy physics.

1.3.2 GUTs, Scalar Fields and Symmetry

The concept of symmetry is a crucial one in current theories of fundamental particle interactions. The key idea is that physical laws describing quantum fields should be invariant under groups of transformations – spacetime ones i.e. translations, rotations and Lorentz boosts and internal ones relating interacting fields to each other. Two general types of symmetry are distinguished. *Gauge* symmetries are "local" in the sense that the laws are invariant under symmetry transformations which differ at every spacetime point. *Global* symmetries are invariances only respected by transformations which are constant in space or time. An important goal of physics is to find a single underlying symmetry responsible for all the interactions of particles and fields. An attempt to do just this is embodied in supersymmetry theories which try to unite the behaviour of spin 1/2 particles and the spin 1 *gauge bosons* which exchange forces between them.

The apparent problem with this view is as follows – the existence of gauge symmetries implies the masslessness of all associated gauge bosons – whereas only one, the photon satisfies the condition. For example, gauge bosons mediating the weak force have masses of $\sim$ 100 GeV. The difficulty is resolved by invoking *phase transitions* to break the symmetry of the quantum fields concerned via the *Higgs* mechanism (e.g. see Zel'dovich 1986). The scheme works by introducing spin 0 scalar fields with equilibrium states at non-zero field values. That means that for a scalar field ϕ the initial symmetry can be broken by the field evolving from $\phi = 0$ to a $\phi = \phi_0$ ground state. The ground state is invariant only under a subgroup of the transformations of the original symmetry group.

The example will be made more explicit in the subsequent discussions of inflation and topological defects.

Such behaviour is well established in condensed matter physics. For example, above the Curie temperature a ferromagnet has a rotationally invariant Hamiltonian. As the temperature drops below the critical value the magnet spontaneously acquires a magnetic moment pointing in an arbitrary direction, breaking the symmetry of the original state.

It appears that two of the four fundamental forces of nature, namely the electromagnetic and weak, can be described by the unified gauge theory of Weinberg, Glashow and Salam. At low energies these two forces appear very different but above the energy scale of $\sim 100\,\mathrm{GeV}$ (roughly the mass of the W and Z bosons) an underlying symmetry emerges. It is expected therefore that there exists a phase transition at roughly this temperature and below that value the high energy symmetry is broken. Furthermore, strong interactions are well described by an SU(3) symmetry group – another phase transition occurs at $\sim 100\,\mathrm{MeV}$ when quarks and gluons become confined in hadrons. Particle interactions can be described by a theory comprising the contribution of three symmetry groups $\mathrm{SU}(3) \times \mathrm{SU}(2) \times \mathrm{U}(1)$. The associated couplings g_3, g_2 and g_1 are logarithmically energy dependent and become roughly comparable at $\sim 10^{15}\,\mathrm{GeV}$ (i.e. $10^{-4} - 10^{-3}$ of the Planck scale). It is possible that a *Grand Unification* of the weak, strong and electromagnetic interactions will appear above this energy scale, i.e. a GUT phase transition occurs at $T \sim 10^{15}\,\mathrm{GeV}$.

A picture now emerges of a sequence of phase transitions in the early universe which give rise to the present day behaviour of particles. Admittedly the extrapolation of physics applicable at 100 GeV scales to energies 13 orders of magnitude higher is a huge one and probes energies well beyond those attainable in terrestrial accelerators. However in addition to solving some deep problems in particle physics the existence of GUT scale phase transitions may provide answers to some of the cosmological enigmas posed above – we now turn to these considerations.

1.3.3 Phase Transitions & Inflationary Models

Comprehensive reviews of the inflationary model are given in Brandenberger (1993) and Liddle & Lyth (1993).

If we are to solve the horizon problem we need all regions within the present horizon to have been in causal contact at some early time during the universal evolution. In the standard model the universal expansion rate obeys $a \propto t^{\alpha}$ with $0 < \alpha < 1$ e.g. $\alpha = 1/2$ during radiation domination, $\alpha = 2/3$ when matter comes to dominate. The value of $r_{\rm H}$ in equation 1.25, which represents the range of causal contact, therefore converges to smaller values at earlier times.

If, however, we postulate an epoch of universal expansion where $\alpha > 1$ the comoving horizon size in equation 1.25 becomes divergent. We then have a mechanism whereby all locations within the present particle horizon can once have been in causal contact and then expanded beyond the horizon to subsequently re-enter at some later time with $\alpha < 1$. This would imply, for example, that apparently disconnected parts of the last scattering surface were once within the same horizon, prior to a $\alpha > 1$ "inflationary" phase.

To generate a $\alpha > 1$ expansion turns out to require an unusual equation of state, not satisfied by matter or radiation, of

$$\rho + 3p < 0. \tag{1.28}$$

Such a state of affairs could occur if the dominant gravitational component were to act as a *cosmological constant*. In this case $p = -\rho$ and the time evolution of the scale factor becomes exponential. The expansion (regardless of any initial curvature which rapidly becomes insignificant) obeys

$$a \propto e^{Ht} \tag{1.29}$$

with Hubble constant

$$H^2 = \frac{8\pi G \rho_v}{3}. \tag{1.30}$$

These solutions of the Friedmann equations are known as de Sitter space and satisfy the conditions of an inflationary phase. The exponential expansion rapidly redshifts away any matter and radiation contributions to the background density. Also the curvature in equation 1.1 which varies as k/a^2 soon becomes insignificant compared to the vacuum density. Substantial curvature prior to inflation can thus be redshifted away to near negligible levels – solving the flatness problem.

The duration of inflation is characterized by the number of e-foldings, i.e. the natural logarithm of the amount of expansion between the onset and end of inflation. We have two conditions

- The present horizon of $\sim 3000h^{-1}$ Mpc must have occupied the pre-inflationary horizon of ~ 10 m and
- a general initial curvature must have been sufficiently eradicated for its dynamical effects to be insignificant over most of the post-inflationary universe. so that $|\Omega - 1| < 10^{-52}$ after inflation at the GUT scale.

Both conditions require an inflationary expansion of at least $\sim e^{60}$ i.e. more than 60 e-foldings before inflation terminates.

To connect inflation with the standard model we clearly need inflation to end at some epoch and the standard evolution to ensue. As mentioned inflationary expansion would dilute all matter and radiation contributions to Ω to negligible levels. To have dynamically significant values of these fields today requires that we eventually dump the vacuum energy of inflation into these fields. The model therefore requires a *phase transition* during which the latent heat within the vacuum "reheats" the universe as $\rho_v \to 0$. A phase transition which is not instantaneous reheats the universe to some substantial fraction of the pre-inflationary temperature.

In the search for an entity whose energy density mimics that of a cosmological constant and ultimately changes phase attention has been focused on the high-temperature behaviour of quantum fields. Scalar quantum fields with the potential to undergo phase

transitions have been explored in the context of spontaneous symmetry breaking in particle physics. Such fields were described in the previous section in the context of Grand Unified Theories.

The properties of scalar fields are generally specified by constructing a Lagrangian density

$$\mathcal{L} = \partial_\mu \phi \partial^\mu \phi - V(\phi) \tag{1.31}$$

consisting of a kinetic term and a potential term. In this notation the pressure p and energy density ρ are given by

$$p = \frac{1}{2}\dot{\phi}^2 - V(\phi) - \frac{1}{6}(\nabla\phi)^2 \tag{1.32}$$

and

$$\rho = \frac{1}{2}\dot{\phi}^2 + V(\phi) + \frac{1}{2}(\nabla\phi)^2. \tag{1.33}$$

Symmetry breaking fields result when the zero-temperature potential has a minimum at non-zero field values. Many potentials can be constructed to satisfy this requirement – one example is the *Mexican Hat* form

$$V(\phi) = -\mu^2|\phi|^2 + \lambda|\phi|^4 \tag{1.34}$$

which has a minimum at $|\phi| = \mu/\sqrt{2\lambda}$ representing the stable equilibrium or ground state of the field. This description is incomplete if we allow ϕ to interact with an environment at temperature T as thermal fluctuations will also feature in the energy distribution. In the most natural extensions of the scheme an interaction term $\mathcal{L}_{int} \propto |\phi|^2 T^2$ is added to the Lagrangian and can be absorbed into $V(\phi)$ to yield an effective potential $V(\phi, T)$. The appearance of the potential at various temperatures is shown in figure 1.2.

The possibility of a temperature dependent phase transition now becomes apparent. At large T the potential is temperature dominated and is effectively a parabola with a minimum at $\phi = 0$. As T decreases the other potential terms become steadily more

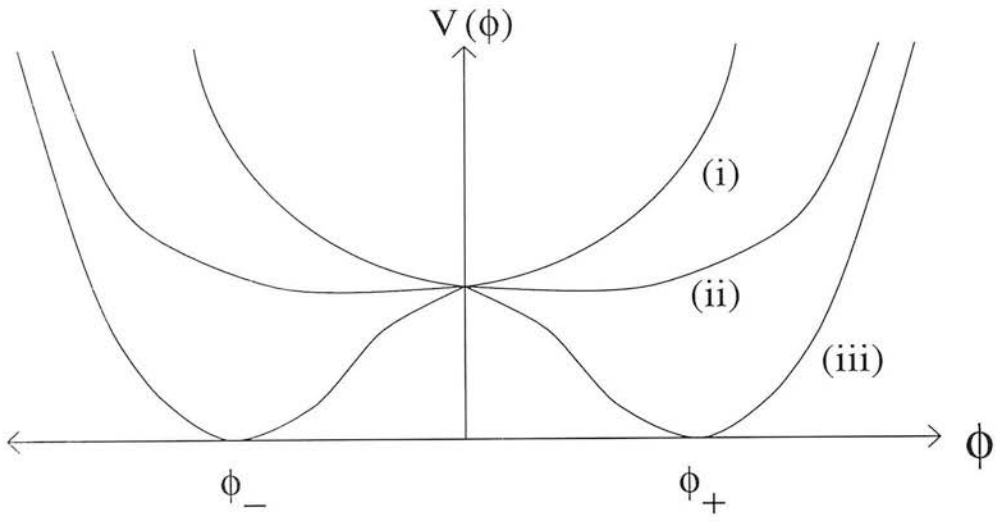

Figure 1.2: Symmetry breaking potential as a function of temperature. (i) $T \gg T_c$ and the true ground state lies at $\phi = 0$, (ii) $T \sim T_c$, the $\phi = 0$ state becomes degenerate with $\phi \neq 0$ states (iii) $T \ll T_c$ the true ground states of the field are now ϕ_+ and ϕ_-, the field can evolve from the $\phi = 0$ metastable state to stable equilibrium with $V = 0$.

significant until at a critical temperature T_c the $\phi = 0$ state becomes degenerate with one or more non-zero ϕ states of the same energy. As $T < T_c$ the equilibrium or "false vacuum" at $\phi = 0$ becomes unstable and a new "true vacuum" ground state is established at $\phi \simeq \mu/\sqrt{2\lambda}$. The expectation is thus that the field undergoes a phase transition at $T \sim T_c$, $\phi_{\text{false vac.}} \rightarrow \phi_{\text{true vac.}}$ and the latent heat of the transition $\sim V(0)$ is emitted through couplings to other fields. An energy difference of $\Delta V \sim \mu^4/2\lambda$ exists between the initial and final equilibrium states. If $V = 0$ in the final ground state the field can function as a cosmological constant with energy density $\sim \Delta V$ until it falls to the new equilibrium point. Such a transition occurring at the GUT scale has to reheat the Universe to a temperature of $\sim 10^{15}\,\text{GeV}$ and the corresponding energy density of the false vacuum is of order $\sim T_v^4$ so $\rho_v \sim 10^{80}\,\text{kg m}^{-3}$.

To ensure sufficient e-foldings during inflation we need ϕ to change slowly with time which implies $V \gg \dot{\phi}^2, (\nabla\phi)^2$. This ensures that $p + \rho = 0$ while inflation proceeds as it satisfies the requirement that equations 1.32 and 1.33 are dominated by the potential terms. Spatial derivatives of ϕ rapidly become negligible as the expansion damps them away.

These considerations result in a simple equation of motion for the field

$$3H\dot{\phi} = -\frac{dV}{d\phi} \tag{1.35}$$

which comes from applying the Euler-Lagrange equations to 1.31 in an expanding FRW spacetime and ignoring the spatial and temporal derivatives of ϕ. The Hubble value, $H = \dot{a}/a$ parameterizes the expansion rate as usual. The *slow rolling* criteria can be expressed in terms of two dimensionless parameters as

$$\epsilon = \frac{m_p^2}{16\pi}\left(\frac{V'}{V}\right)^2 \ll 1, \tag{1.36}$$

$$\eta = \frac{m_p^2}{8\pi}\left(\frac{V''}{V}\right) \ll 1. \tag{1.37}$$

The Planck mass $m_p = G^{-1/2}$. These conditions ensure the potential is flat enough for its time evolution to be slow.

De Sitter space contains an event horizon of size H^{-1}. In analogy with black holes, thermal fluctuations can appear as Hawking radiation, at temperature

$$T_{\rm dS} = \frac{H}{2\pi}. \tag{1.38}$$

These quantum fluctuations can be frozen in by the expansion to become classical curvature perturbations. The invariance of de Sitter space under time translations yields a scale invariant power spectrum of fluctuations ($P(k) \propto k$) which is gravitationally amplified after inflation and hence can provide the initial density perturbations. The scale invariance of the power spectrum can thus be counted as a prediction of inflation. Furthermore the fluctuations are expected to be Gaussian (the density field is a superposition of Fourier modes with independent random phases) and adiabatic, i.e. curvature fluctuations which do not discriminate between matter and radiation.

The picture is complicated by the fact that density perturbations within the present horizon were generated during the final 60 e-foldings of inflation when the inflationary expansion was coming to an end and may not be precisely exponential. If the derivatives

of $V(\phi)$ are no longer negligible at this stage the primordial power spectrum can exhibit *tilt* away from scale invariance ($P(k) \propto k^n$ with $n = 1$) such that

$$(1 - n) = 6\epsilon - 2\eta \tag{1.39}$$

in terms of the dimensionless derivatives of (1.36,37).

The amplitude of density fluctuations on the horizon scale can be shown to be (e.g. Peacock 1996)

$$\delta_h \sim \frac{H^2}{\dot{\phi}} = \frac{3H^3}{V'}. \tag{1.40}$$

Using equations 1.30, 1.35 and 1.36 we can rewrite this as $\delta_h \sim \sqrt{\rho_{\rm v}}/m_p^2\sqrt{\epsilon}$. Inflation must end with $\epsilon \sim 1$ and so with $\rho_{\rm v} \sim T_{\rm v}^4$ we get $\delta_h \sim T_{\rm v}^2/m_p^2$. A GUT scale $T_{\rm v}$ gives the observed value of $\delta_h \sim 10^{-5}$. Unfortunately this turns out to require a *very* weakly coupled ϕ-field to get the required number of expansion e-foldings. With regard to equation 1.34, $\lambda \lesssim 10^{-15}$. There is no known physical principle to explain why the coupling should be so small and the problem is regarded as a serious shortcoming for the inflationary model.

One further relic effect of inflation would be a background of gravitational waves generated by the coupling of the fluctuating ϕ-field to gravity. Probably the most stringent test of their presence would be in a measurement of scalar and tensor contributions to the CMB anisotropy (Starobinsky 1985). The ratio of these would furnish a measurement of ϵ. There exists, therefore, some hope of measuring the parameters characterizing inflation.

Although inflation solves many of the cosmological questions posed in section 1.3.1 it has many free parameters and is not a well-constrained theory. The search for the description of an inflaton field that behaves as required has proved discouraging and in some respects the problem of appealing to special initial conditions at the Planck epoch is not circumvented. We now turn to look at a rival theory, also based on phase transitions in the early universe.

1.3.4 Topological Defect Models

Not all symmetry breaking phase transitions taking place in the early universe necessarily lead to inflation. In fact, we have seen in the above section that certain rather specific conditions must be met for an inflationary phase to account for cosmological observations. There is, however, another property of phase transitions which is relevant to the issue – their capacity to generate *topological defects*. This class of theory is considered a serious rival for inflation in its explanation of primordial density fluctuations and has the general advantages of fewer free parameters and less ambiguous observational effects.

In terms of the previous discussion, topological defects arise when a phase transition drives a scalar field from a $\phi = 0$ initial state to one of the *degenerate* ground states of the potential $V(\phi)$. This means that more than one set of components of ϕ can satisfy $|\phi|^2 = |\phi_0|^2$ with $V(\phi_0) = 0$. As a prototype we hold ϕ to be a multiplet of scalar fields ϕ_i observing

$$|\phi|^2 = \sum \phi_i^2 \tag{1.41}$$

with potential

$$V(\phi) = \frac{1}{4}\lambda(|\phi|^2 - \sigma^2)^2 \tag{1.42}$$

in which λ and σ are constants for the field.

A phase transition during the cooling of the early universe drives ϕ to a fluctuating function of position. ϕ is then at the ground state nearly everywhere and subsequently attempts to relax to a coherent alignment (i.e. zero field derivatives) over larger and larger scales as the horizon expands. That is, initially causality limits the coherence range of the field to the horizon volume at the phase transition – later neighbouring volumes come into contact and alignment continues where they meet. This can continue unhindered except where field configurations cannot be erased by a local internal rotation of the field. The topological defects that such locations represent are trapped field configurations – the field derivatives around such points are non-zero and so an energy density is frozen in at defect sites. Given a theory which admits topological defects such regions are

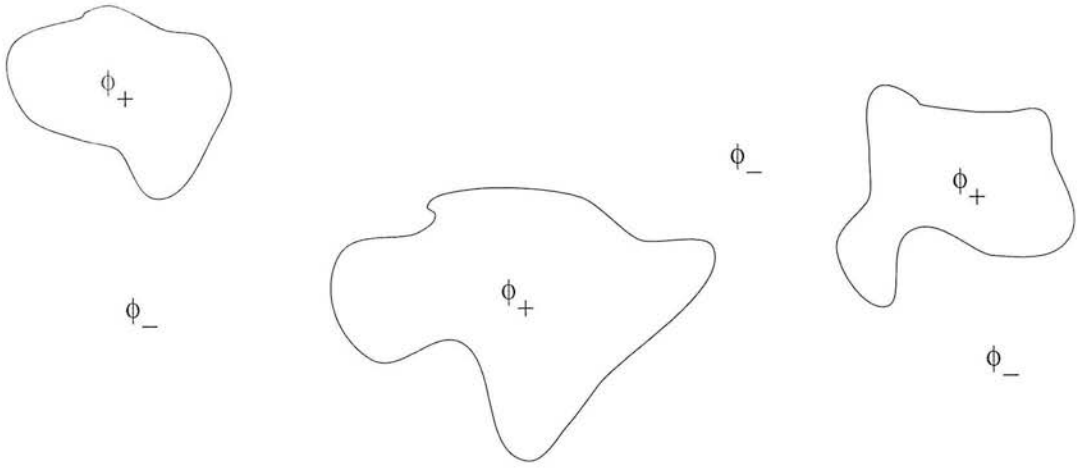

Figure 1.3: Domain walls as the boundaries between distinct but degenerate ground states of the ϕ-field in the $T \ll T_c$ regime.

guaranteed to form during a phase transition in the early universe (Kibble 1976). The gravitational effects of these seed perturbations then generate CMB anisotropies and structure (typically with *non-Gaussian* characteristics).

Various types of topological defect can arise depending on the internal dimensionality of the field ϕ and whether the broken symmetry is of the *global* or *gauge* kind. In the gauge case both scalar and gauge fields adjust to minimize the energy trapped by the defect and so the energy is quite well localized. Global defects do not have a corresponding mechanism to quash the long range field derivatives and generally have divergent total energy integrals and long range interdefect forces.

- *Domain Walls* arise if ϕ has one internal degree of freedom and the low temperature field exhibits spontaneously broken discrete symmetries, i.e. $V(\phi)$ has a discrete set of degenerate minima. Domain walls are planar defects separating regions of different phase (figure 1.3). The field passes through $\phi = 0$ as it changes value and so there is a trapped energy on this surface where ϕ steps from ϕ_- to ϕ_+. Adjoining walls with oppositely directed steps can join and annihilate. Walls will move at speeds $\lesssim c$ so we expect no more than a few per Hubble volume. It can be shown that cosmological domain walls would perturb radiation backgrounds to an unacceptable degree unless $\sigma < 1\,\mathrm{MeV}$ which is way below the energy associated with GUT phase transitions. GUT-scale domain walls would overclose the universe

by a factor of 10^{52}! (e.g. Brandenberger 1993). Straightforward implementations of domain wall generated perturbations are therefore ruled out.

- *Strings.* In this case ϕ is a complex scalar field with two degrees of freedom. The phase of ϕ changes continuously by integer multiples of 2π in a loop around each defect. This yields linear defects or *strings*. Such defects are observed to form in low temperature phase transitions in liquid ^{4}He as quantized vortex lines (Hendry 1994). This case has been the most intensively investigated and is discussed in more detail in the next section. Global strings have an energy per unit length which diverges logarithmically with distance from the string and have not been investigated in depth in cosmological contexts. We therefore confine subsequent comment to the gauge case.

- *Monopoles.* Here ϕ has three dimensions and the associated defects are particle-like. Gauge monopoles can behave as *magnetic monopoles* with a magnetic charge M and their existence would imply the quantization of charge. As briefly discussed below, gauge monopoles would be expected to dominate the mass of the universe at the present epoch and so the simplest models are inconsistent with the data. In the global case there are long range inter monopole forces which an allow annihilation at a rate comparable with the universal expansion yielding a scaling solution. Such scenarios are harder to rule out (Rhie & Bennett 1990).

- *Textures* arise in 4-component symmetry breaking fields. Ground state occupation leaves three free functions of position – the Higgs field can point in any direction in a 4D-space. Inhomogeneities in the field gradient energy density represent transient energy concentrations, the texture can subsequently unwind and allow the field to reconnect smoothly. For textures to cause scale invariant initial conditions for structure formation at the $\delta_h \sim 10^{-5}$ level requires $\sigma \sim 10^{17}$ GeV which is within a plausible GUT range. Implementations of the model are described in Cen et al. (1991).

In early versions of topological defect models the existence of monopoles was seen as a problem. Phase transitions at the GUT scale yield monopoles at a density of $\sim$ one per GUT horizon volume. They would dominate the mass density of the Universe

to an enormous extent at the present epoch unless some mechanism aligned the field over scales well beyond the current horizon. This concern was a motivating force behind inflationary theories. The huge stretching of the gradients during exponential expansion "inflates" the monopoles to a very low density. Thus topological defects occurring prior to any inflationary phase would probably not be of great significance once inflation had ceased.

1.3.5 The Formation of Strings

We now focus on the gauge string model. We consider the Lagrangian density in the Abelian Higgs string model (Nielsen & Olesen 1973) in which the complex scalar field ϕ interacts with a vector field A_μ (which is the gauge field required for the energy of the string to be localized) .

$$\mathcal{L} = \frac{1}{2} D_\mu \phi D^\mu \phi - V(\phi) + \frac{1}{4} F_{\mu\nu} F^{\mu\nu}. \tag{1.43}$$

The covariant derivative is given by $D_\mu = \partial_\mu - ieA_\mu$ with gauge coupling constant e. The potential $V(\phi)$ is the 2D version of equation 1.42, the "Mexican Hat" (figure 1.4a). $F_{\mu\nu}$ is the antisymmetric tensor $\partial_\mu A_\nu - \partial_\nu A_\mu$. The Lagrangian has $U(1)$ symmetry and describes the simplest model for gauge strings with a localized energy density.

Below the critical temperature the ground states form a circle with $\phi = \sigma e^{i\theta}$ where θ is the polar angle along C. Such a potential admits one-dimensional topological defects known as strings. The formation proceeds as follows.

At $T \gg T_c$, ϕ sits at the origin with zero expectation value. As the temperature in the early universe falls the equilibrium at the origin becomes unstable and ϕ falls to a stable equilibrium point somewhere in the circular trough of the potential *nearly* everywhere. The ground state expectation value for this complex scalar field will then be $\langle\phi\rangle = \sigma e^{i\theta}$ with arbitrary phase angle θ. But at some points $V(\phi)$ cannot fall to zero, e.g. at point P in figure 1.4b the local field points away from P at every neighbouring point. The field *at* P therefore cannot totally align itself with the local field whichever direction it points in the 2D ϕ field and so it is constrained to remain at the origin. The

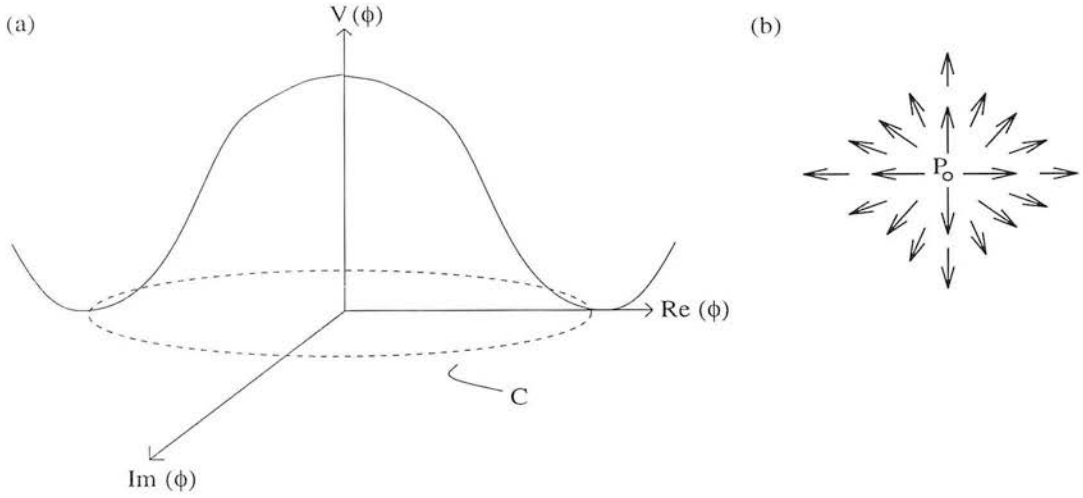

Figure 1.4: (a) The Mexican Hat potential at $T = 0$. The ϕ field is complex. A rotationally invariant potential $V(\phi)$ contains a circle C of ground states for which $|\phi| = \sigma$. (b) Trapped point within an otherwise relaxed field configuration. The field at P cannot align itself with the local field and so remains at $|\phi| = 0$ with a trapped energy of $\sim V(0)$. The field makes a rotation of 2π in any circuit around P. Thus P is the site of a *topological defect* in the field which cannot be removed without reheating to $T \sim T_c$.

non-zero field derivatives and the residual potential energy thus contrive to produce a trapped energy density at P. Mathematically speaking this corresponds to loops around P having a non-trivial winding number i.e. the phase angle θ changes by 2π as the loop is traversed. By translational symmetry there is a continuous line of points with $\langle\phi\rangle = 0$ which form the high mass core of the string. Thus a thin tube remains in the false vacuum state.

The mass per unit length of the string is $\mu \simeq \sigma^2$ for gauge strings. A string that lies along the z-axis has stress-energy tensor

$$T^{\alpha\beta} = \mu\delta(x)\delta(y)\mathrm{diag}(1, 0, 0, -1). \tag{1.44}$$

In cosmological contexts the scalar field arises from a grand unified theory of the fundamental forces, and in the case of most interest is the field breaking the symmetry between the strong and electroweak interactions. In this case $\sigma \sim 10^{15}$ GeV and $\lambda \sim 1$. Causality implies that the scalar field will not be coherent over scales greater than the horizon size, so as T falls below T_c a network of strings will form with correlation length $\xi < t$ (i.e. $\sim$

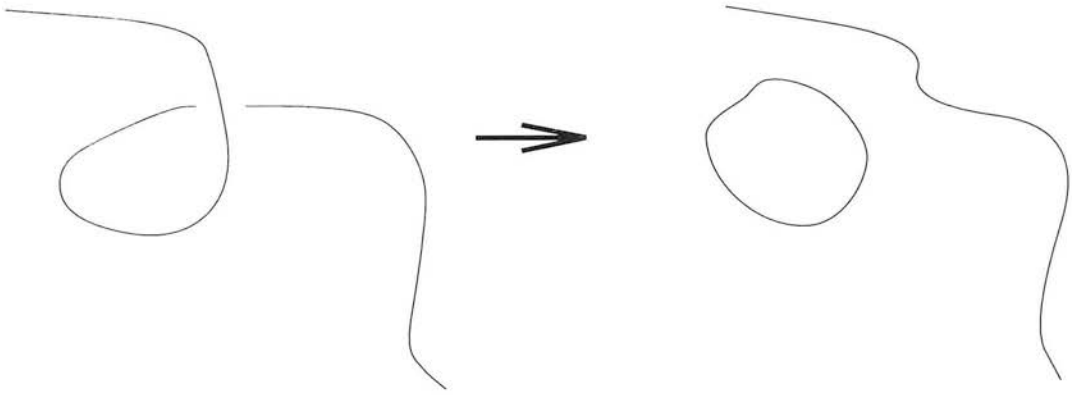

Figure 1.5: Loop formation by a self-intersecting long string.

one long string per horizon volume). Numerical simulations of the formation phase (also discussed in chapter 2) indicate that $\sim 80\%$ of the initial network energy is in "infinite" horizon crossing strings and $\sim 20\%$ in closed loops (Vachaspati & Vilenkin 1984).

After formation the network evolves principally via loop production by infinite strings (figure 1.5) and loop shrinkage due to gravitational radiation. The two processes yield a mechanism by which the string network can lose energy. If this loss of energy is such that the correlation length of the network always obeys $\xi(t) \sim t$ then a scaling solution results (e.g. Bennett 1990). If ρ_s is the energy density in long strings then

$$\rho_{\rm s} \sim \mu/\xi^2 \sim \mu t^{-2} \tag{1.45}$$

and so

$$\frac{\rho_{\rm s}}{\rho_0} \propto \mu \tag{1.46}$$

i.e. ρ_s is a fixed fraction of the background density and so "scales" in an epoch dependent way. If we calculate the resulting density fluctuations on the scale of the Hubble volume then

$$\delta_{\rm h} \sim \frac{\rho_{\rm s}}{\rho_0} \sim \frac{8\pi G\rho_{\rm s}}{3H_0^2} \sim 30G\mu \sim 30\frac{\sigma^2}{m_{\rm pl}^2}. \tag{1.47}$$

To generate the observed $\delta_{\rm h}$ requires $\sigma \sim 10^{16}$GeV which is in the range encountered in discussions of strong and electroweak unification.

1.3.6 Cosmological Effects of Strings

Having dealt with the motivation for the string model we now move to consider the cosmological implications of strings in more detail and examine constraints that can be placed on the theory.

General relativistic properties of strings have been investigated by Vilenkin (1981) and Gott (1985). It can be seen from the form of $T^{\alpha\beta}$ in equation 1.44 that the active or Newtonian gravitational potential of a straight string vanishes as

$$\nabla^2\phi = 4\pi G T^{\alpha}_{\alpha} = 0. \tag{1.48}$$

Locally an observer close to the string feels no acceleration in this *weak field* approximation. However the global solution to Einstein's equations for the metric around a z-axis string is

$$d\tau^2 = dt^2 - dz^2 - dr^2 - r^2(1 - 4G\mu)d\psi^2 \tag{1.49}$$

which is the same as for a flat spacetime except it has an *angle deficit* of $8\pi G\mu$. Although the metric is locally flat the global spacetime has the geometry of a cone.

Initially parallel light beams are, after passing the string, convergent with an angle of convergence of up to

$$\psi = 8\pi G\mu \tag{1.50}$$

effectively lensing the source. Observing an object which is behind a long string will generally yield two identical images separated by up to ψ. More detail will be given in chapter 2 which adapts this effect into a search method for strings.

The gravitational effects of strings should give rise to several observable effects. An example is the situation in which an observer views a point source of radiation with a string transversely crossing the line of sight. The radiation is Doppler shifted by the moving string and a discontinuous shift in the frequency of the radiation is observed as

the string passes. In the case of a uniform radiation background the observer detects a discontinuity across the locus of the string. For the CMB the temperature would vary by

$$\frac{\delta T}{T} = 8\pi G\mu\gamma \mathbf{n}\cdot(\mathbf{v}\times\mathbf{s}) \tag{1.51}$$

either side of the moving string. Here $\mathbf{s}$ is the vector direction of the string locus and $\mathbf{n}$ a unit vector along the line of sight. $\mathbf{v}$ is the velocity of the string and γ the Lorentz factor $(1-|\mathbf{v}|^2)^{-1/2}$

If the strings are sufficiently massive the observed fluctuations of the microwave background temperature could be generated by the superposed contributions of strings between $z=0$ and the last scattering surface (Kaiser & Stebbins 1984). The microwave sky would then be a mosaic of small patches of constant temperature radiation with discontinuous boundaries at string loci. The mean patch size would be set by the angular separation of strings at the highest intervening redshift, roughly the horizon size at $z_{\rm rec}$ of $\Theta_{\rm H}=2^\circ$. Additional sources of CMB anisotropy include the standard model ingredients of: the Rees-Sciama effect from potential fluctuations between $z=0$ and $z=z_{ls}$, temperature, potential and velocity perturbations on the last scattering surface and gravitational wave effects.

Numerical simulations of the CMB in the string model have been generated by Bennett, Stebbins & Bouchet (1992) and generate an rms temperature fluctuation of $\delta T/T \simeq 19G\mu$. If strings *alone* are responsible for the *COBE* rms measurement then the mass per unit length of strings is constrained to be

$$G\mu = (1.5\pm0.5)\times10^{-6} \Rightarrow \mu = 2.0\times10^{21}\,{\rm kg\,m^{-1}} = 3.1\times10^{7}{\rm M_\odot\,pc^{-1}}. \tag{1.52}$$

Coulson et al. (1994) have argued that this is an underestimate and calculate $G\mu=(2.0\pm 0.5)\times10^{-6}$. It appears that for CMB anisotropy experiments with angular resolution of order a few arcminutes that string generated perturbations would give a pattern clearly distinct from the Gaussian perturbations of inflation. Therefore there is hope that the new generation of CMB experiments will provide a means of discriminating between the models (e.g. see Hara et al. 1993, Moessner et al. 1994).

Matter moving past the string at relativistic speeds also converges and would form shock regions in wakes behind the string. Two particles initially at rest begin to move towards each other when a string passes between them. In the case where the string moves at velocity $\mathbf{v}$ perpendicular to the line connecting the particles, the particles acquire a relative velocity of $u = |\mathbf{v}|\gamma\psi$.

In addition to providing scalar gravitational effects we also expect gravitational radiation from long strings which may have measurable indirect effects. The existing gravitational wave background is constrained by nucleosynthesis arguments and by millisecond pulsar timing. The observed densities of primordial isotopes are affected by the expansion rate at nucleosynthesis which is increased by extra radiation backgrounds, e.g. gravitational waves, extra neutrino species and so forth. Unacceptable ^{3}He and D fractions would result from string generated gravitational waves unless $G\mu < 6 \times 10^{-6}$. The waves would also affect the observed rate of pulse emission from millisecond pulsars. In interpreting the measurements some estimate must be made of the spectrum of gravitational radiation from string loops – the most conservative arguments give limits on $G\mu$ comparable to the above. These additional constraints are discussed in Hindmarsh & Kibble (1995).

If we supplement a perturbation generating string network with a chosen form for the dark matter we have the ingredients needed to form structure. A moving string can generate velocity perturbations in the dark matter which streams past and thus form accretion wakes in a plane behind the string. Thus the global gravitational effects of strings naturally generate planar overdensities. Small scale structure on the strings reduces the string tension (T^{33} in equation 1.44) and yields an active gravitational potential. Thus cylindrical accretion is also possible and can give rise to filamentary overdensities. The relative proportions of the two effects depend on the degree to which string microstructure (i.e. wiggliness) is present and the velocity distributions of the strings and dark matter. Long-string mediated structure formation is addressed in Aguirre & Brandenberger (1995). Loops can act as pointlike gravitational sources and also seed structure (Bertschinger & Watts 1988). Numerical simulations show that strings with $G\mu =$ a few $\times 10^{-6}$ combined with HDM is compatible with observations for reasonable values of the $8h^{-1}$ Mpc bias and Hubble's constant (e.g. Mähönen 1996). The status with CDM is less

clear though the string model certainly does not alleviate any of the problems discussed in section 1.2.3.

We would expect to be able to distinguish a string-motivated scenario from, say, an inflationary version, by the non-Gaussian nature of the density perturbations. In the string model correlations exist between the phases of different power spectrum modes. On the other hand the present day density field contains contributions from many overlapping wakes and so the field may be fairly close to Gaussian. Whether present data really allow us to discriminate between strings and explicitly Gaussian models such as inflation is as yet unclear (though see Robinson & Albrecht 1995).

1.4 Summary

To conclude this chapter I will summarize the key conclusions and map out the areas to be addressed in subsequent chapters.

The Standard Hot Big Bang model has had some notable successes and still deserves to be taken seriously as a framework for interpreting cosmological observations. The first half of this chapter has exposed the most significant grey areas – (a) determining the form and density of the energy content of the Universe and reconciling this to (b) the age of the Universe, and (c) the observed clustering of galaxies. This thesis makes two contributions to this area. Chapter 5 discusses a variant of the CDM model in which a dark matter component decays radiatively at early times. The model has the virtue that it can accommodate (a) the low apparent value of the power spectrum break wavenumber ($\propto \Omega h$ for CDM models, equation 1.24) inferred from observed large-scale galaxy clustering *and* (b) the high measured values of Ω and h (section 1.1.2). Chapter 5 uses measures of the *small-scale* clustering predicted in such models to constrain the principal attributes of the decaying particle species, its mass and lifetime, producing tight bounds on the allowed parameter space which remains. Chapter 6 contributes to the observational tests of large-scale galaxy clustering by constraining the clustering signal of a sample of high-redshift radio galaxies. The high redshift data are important as they give clues to the evolution of the density field with time and yield constraints on the

Standard Model parameters of section 1.1 and the bias parameter described in section 1.2. Recent work with comparable datasets has measured clustering of a surprisingly high amplitude for such redshifts – chapter 6 addresses the question of whether these values are plausible in the light of our data.

The second half of this introduction has examined two promising theories which extend the Standard Model – *inflationary* and *topological defect* models. In conclusion, although inflation solves some important problems – the horizon and flatness problems of section 1.3.1 – the model is poorly motivated in terms of currently understood particle physics. Furthermore, conclusive tests of inflation are elusive and may have to await substantial advances in high-energy physics and gravity-wave detectors. Topological defects, while less of a panacea for the outstanding problems of the field, are well motivated by theories of Grand Unification at $T \sim 10^{16}$ GeV and make plausible candidates for the source of primordial inhomogeneities. Crucially, cosmic strings, the best investigated class of topological defect models, have testable consequences for the microwave background and the lensing of galaxies. Chapters 2 to 4 adapt the second of these effects into a search method for strings. Chapter 2 draws heavily on simulations of string networks to set limits on the shape and distribution of horizon-spanning strings. Chapter 3 investigates the appearance of galaxies lensed by such strings. In chapter 4, this knowledge is then built into an algorithm which searches for strings on Schmidt plates. Finally, an extension of the work to deeper surveys is considered – running the search algorithm on the large area Sloan survey should test the cosmic string model conclusively.

Chapter 2

The Properties of Cosmic Strings

As discussed in the introduction the detection of cosmic strings would be of huge significance for physics. The unambiguous observation of string lensing of galaxies with measurable redshifts would, at a single stroke allow us to

- demonstrate the occurrence of a phase transition in the very early universe, (probably one of crucial importance to particle physics) and allow us to measure the energy scale at which this occurred.
- provide a much-needed mechanism for seeding structure.
- allow us to directly measure Ω which is a function of the lensing angle per unit redshift.

The most attractive aspect of the string scenario is that an unambiguous detection *is* possible given a deep enough galaxy catalogue to search for potential lensing events. The next three chapters describe the way in which such a search could proceed. This chapter seeks to estimate the most important parameters influencing any search programme, drawing on analytical and simulated research on strings. Chapter 3 discusses the nature of individual lensing events which are the observational signature of strings. Chapter 4 describes the application of a search method to $\sim$ 100 high galactic latitude UKST plates and looks forward to extending the search with the next generation of deep galaxy surveys.

2.1 String Lensing

The spacetime in the environment of a cosmic string is locally but not globally flat – it is conical as if a wedge of angular size $\psi = 8\pi G\mu$ were removed and the faces identified. A prediction of this spacetime configuration is that strings will *gravitationally lens* background galaxies. If an observable galaxy lies beyond the string with its line of sight within an angle $\sim 8\pi G\mu$ to the line of sight to the string then lensing effects will give rise to a two images of the galaxy with separation

$$\psi = 8\pi G\mu \frac{D_{\rm SG}}{D_{\rm G}} \frac{\sin\theta}{\gamma(1-\mathbf{v}\cdot\mathbf{n})} \tag{2.1}$$

(Vilenkin 1986), with $D_{\rm G}$ and $D_{\rm SG}$ the angular-diameter distances of the background galaxy and between the string and galaxy respectively. $\gamma = (1-|\mathbf{v}|^2)^{-1/2}$, with $\mathbf{v}$ the velocity of the string, $\mathbf{n}$ a unit vector in the observer to object direction and θ the angle at which the string crosses the line of sight to the lensed object. The v dependent terms are relativistic effects in the general case of a moving string. The situation is illustrated in figure 2.1a. It will be useful later to have equation 2.1 in a redshift dependent form, thus

$$\psi = 8\pi G\mu \left(1 - \frac{1-(1+z_{\rm s})^{-1/2}}{1-(1+z_{\rm g})^{-1/2}}\right) \frac{\sin\theta}{\gamma(1-\mathbf{v}\cdot\mathbf{n})} \tag{2.2}$$

with $z_{\rm s}$ and $z_{\rm g}$ the string and galaxy redshifts. These equations are valid so long as $\Omega_0 = 1$ and $D_{\rm G} \ll H_0^{-1}$.

Given the range of mass per unit length μ quoted in equation 1.52 the angular separations of lensed objects should range up to $\simeq 10''$. A single long string lying in front of a number of galaxies would manifest itself as a line of double galaxy images across the sky, i.e. a lane $\sim 20''$ wide containing aligned image pairs separated by up to $10''$, see figure 2.1c. The lane would form a great circle on the sky in the case of a straight horizon-spanning string. Most image pairs due to long straight strings are expected to be identical in magnitude, size and colour in this simple picture – there is no significant

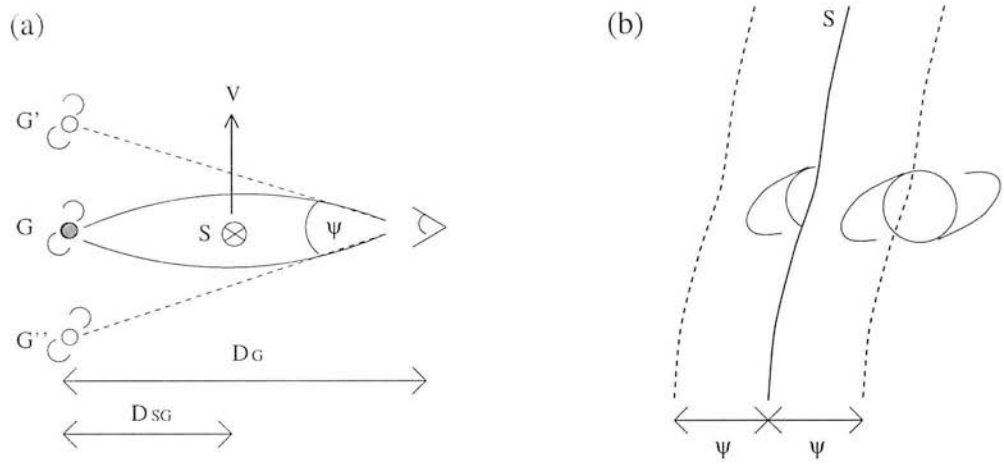

Figure 2.1: (a) Basic lensing arrangement as described in the text. The string **S** lies perpendicular to the plane of the page and moves at velocity **v**. G' and G" are identical images formed due to lensing of the background galaxy G. (b) Partial lensing which may occur with extended objects. Only part of the galaxy falls within the lensing region (dashed lines) and so a truncated secondary image is formed.

magnification or distortion (Gott 1985) and Doppler shifting between images in a pair is at the

$$\Delta\omega/\omega \sim 8\pi G\mu|\mathbf{v}| \tag{2.3}$$

level (Stebbins 1988). If the lensed object is sufficiently extended there is a possibility that only part of it will fall into the lensing region in which case one of the images will be truncated and have a sharp edge at the position of the string, figure 2.1b (Paczyński 1986). The Space Telescope would probably be needed to resolve such effects. Terrestrial telescopes would see such partial lensing events as *differences* in magnitude between the two images.

Examining the velocity dependent factors in the lensing equation (2.1) shows that the lensing angle ψ takes a value in the range

$$\kappa^{1/2}\psi_0 \sin\theta < \psi < \kappa^{-1/2}\psi_0 \sin\theta \tag{2.4}$$

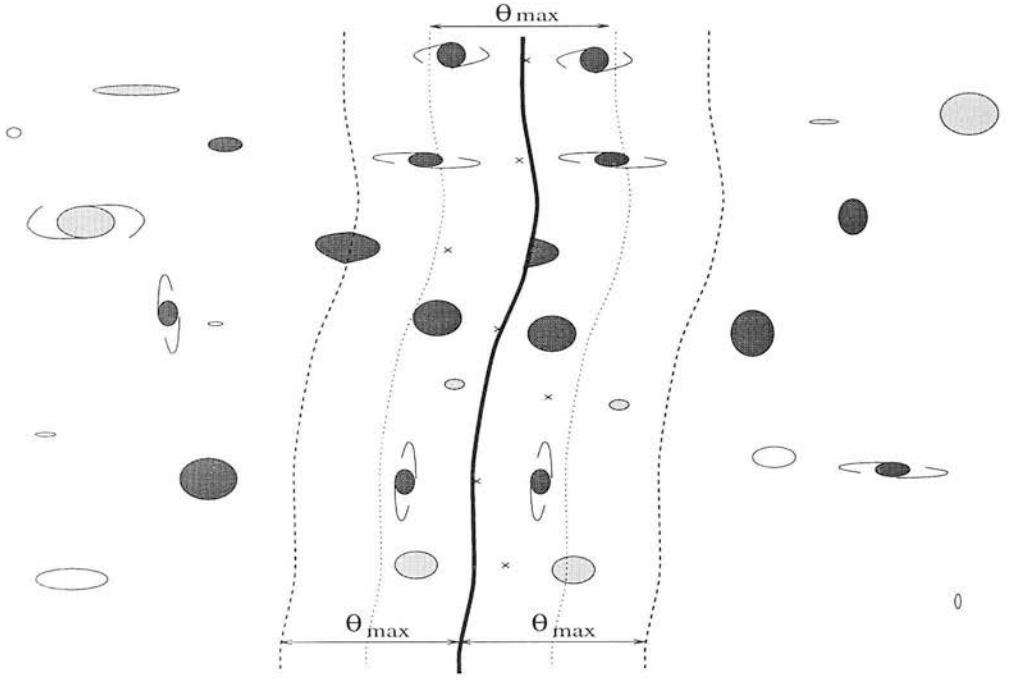

Figure 2.1: (c) Lane of double images produced by a cosmic string (solid line) with a background of galaxies. Galaxies or parts of galaxies that fall within the region $\theta_{\max}(z_s)$ from the string (dashed lines) are lensed into two identical images either side of the string. Images in each pair are separated by up to $\theta_{\max}$, the maximum value of expression 2.2 which is $\sim 10''$ with the mass-per-unit length of equation 1.52. The centroids of each image pair are shown by crosses – a lane $\theta_{\max}$ wide (dotted lines) contains all these centroids.

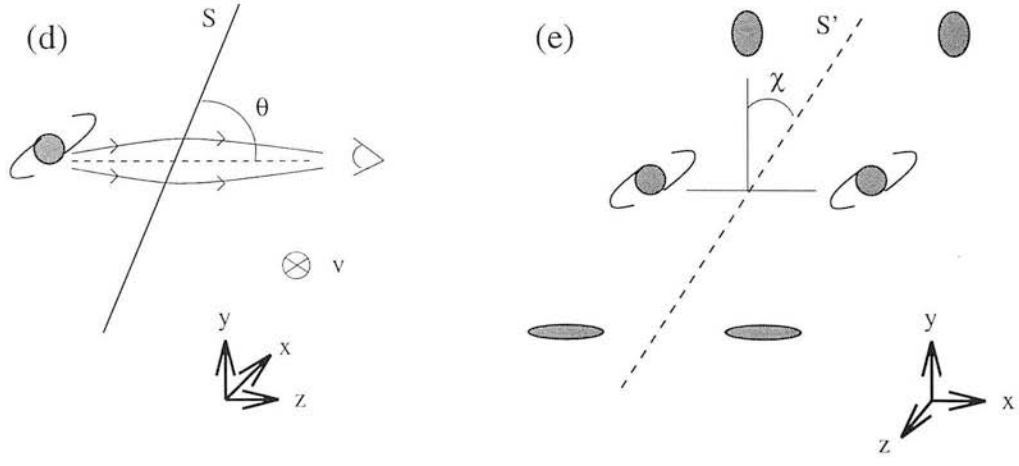

Figure 2.1: (d) Lensing in the case of a string with relativistic transverse motion. The string **S** is tilted at angle θ to the line of sight (in the yz-plane). It moves at speed **v** in the x-direction. (e) The appearance of galaxies lensed by such a string. Each pair is *sheared* by an angle χ from the apparent path of the string **S'** inferred from the distribution of lensed pairs.

where $\psi_0 = 8\pi G\mu D_{SG}/D_G$ and $\kappa = (1 - v)/(1 + v)$. Taking the mean value of the transverse string velocity to be $\overline{v} = 0.5$ and $\overline{\sin\theta} = 2/\pi$ gives

$$0.37\psi_0 < \psi < 1.10\psi_0. \tag{2.5}$$

From this it appears that moving, randomly oriented strings, on average, do not cause significantly greater lensing than do stationary strings, though a combination of orientation and motion effects can cause the lensing angle to be significantly reduced. However the mean value of ψ expected when all these effects are taken into account is still $\psi = \psi_0$ so we will continue to use ψ_0 as the best estimate of ψ when the orientation and velocity are unknown.

An additional complication to the basic model, first noted by Vilenkin (1986), arises when the string has rapid transverse motion $v \sim c$ and does not lie perpendicular to the line of sight to the distant galaxy (figure 2.1d). In this case the observer sees more distant parts of the string with a retardation and the apparent direction of the string differs from its true direction. This effectively shears the line of galaxy pairs as shown in figure 2.1e, with shear angle

$$\tan\chi = \frac{v}{c}\cot\theta \tag{2.6}$$

These are the crucial predictions of the cosmic string model as far as direct observational search programmes are concerned (e.g. Hindmarsh 1990). The presence of a lane of aligned, largely identical galaxy pairs on the sky could not be produced by any other plausible mechanism. Chapter 4 will develop this signature into a test for the presence of strings on existing galaxy catalogues as an extension to the methods of Hindmarsh. The rest of this chapter is concerned with the properties of strings that are relevant to such a search programme.

These arguments apply to long horizon-spanning strings. Closed loops of string can cause significant relative magnifications of the images (Hogan & Narayan 1984). If the loop is moving relativistically the magnified images can detectably change position and magnitude over a timescale as short as a few months. One possible loop detection was

reported in 1987 in which a small $\sim$ arcmin^2 field appeared to contain lensed galaxy pairs but after follow-up observations it is still unclear whether these are not just accidental close pairs of galaxies. This candidate is discussed in Cowie & Hu (1987) and Hu (1990). We do not expect to detect string loops with the methods described here. The search programme discussed in this work relies heavily on the similarity of objects in lensed pairs and their line-like distribution on the sky – as predicted for horizon-spanning strings. Neither signature applies particularly well in the case of loops.

2.2 String Microstructure

One further characteristic of horizon spanning strings is of importance here. Numerical simulations of strings indicate that the build up of large-scale features is accompanied by the survival of relatively microscopic structure (Bennett 1990, Bouchet 1990, Albrecht 1990, Shellard & Allen 1990; hereafter Be90, Bo90 A90 and SA90). The scales at which substructure exists may be smaller than that allowed for in string simulations – even as low as the correlation lengths during the original string formation process. Furthermore, string segments may intercommute and velocity and direction discontinuities result – also contributing to the microstructure.

An effect that gives concern for attempts to detect lensing would be wiggliness on the scales separating the background galaxies. A significant degree of string curvature here would wreck the hypothetical alignment of galaxy pairs in a strip. Since pair alignment is one of the key signatures for string lensing any search programme would be made substantially more difficult. In the search algorithm developed in chapter 4 we will be looking for lanes of galaxy pairs on the scales of several arcmin to a few degrees on the sky. At Schmidt plate depths of $z \sim 0.2$ this means we will be searching for string segments with lengths of order $10h^{-1}$ Mpc. Before any such programme is undertaken it is therefore crucial to have an estimate of the level of substructure on $1 - 50h^{-1}$ Mpc scales. We examine this issue in the following section.

2.2.1 The Basic Concerns

As with many fields in contemporary physics the input of numerical methods and computer simulation has been crucial to the understanding of cosmic strings. A string network in an expanding universe represents a non-equilibrium system with chaotic initial conditions. Although important progress towards modelling strings has been made with analytical methods many features have only come to the fore by examining the results of high-resolution simulations.

A typical issue is that of string loops – once central to models of string mediated structure formation. A high density of loops in the matter dominated era would have provided point-like gravitational seeds around which matter could collect in galaxy sized clumps. Indeed the correlation function expected of loops and that observed of galaxy clusters had a notably similar form (Turok 1985). The large gravitational wave output of these loops was, however, far in excess of limits provided by pulsar timing data (section 1.3.6). The cosmic string model remained on shaky ground until simulations (Be90, Bo90) showed that the newly-discovered phenomenon of string microstructure rendered all but the smallest loops unstable. Since then the model has been rethought with the structure formation around long strings playing a much more dominant role.

The analysis of string microstructure has revealed some interesting features which we will discuss in turn:

- Simulations of the formation and evolution of a string network show that on very large scales infinite strings have the form of a Brownian walk which can be characterized by a persistence length ζ – the scale above which neighbouring lengths of string make effectively random angles to each other. The network tends to incoherence on scales where the light travel time approaches the age of the universe. The infinite string is therefore not straight, over large enough scales we expect *curvature* parameterized by a radius $\sim \zeta$. The simulations imply ζ is, at each epoch, some substantial fraction of the horizon size, Hindmarsh (1990; hereafter H90) suggests

$$\zeta(z) \simeq \frac{20^\circ \beta}{z} \tag{2.7}$$

where ζ is given as the apparent angular persistence length of a string on the sky and β is the coherence length of the string network (i.e. the mean inter-string distance) in horizon units. β is estimated to be of order ~ 0.3 by Albrecht & Turok (1989). At late times the velocities of the string segments tend to be coherent over similar scales as the string locus itself is coherent (SA90).

- Strings exhibit *wiggliness* on small scales. Simulated strings in an interacting network develop kinks and curvature at scales well below the horizon size. Kinks arise as a by-product of the loop formation and intersection processes outlined in section 1.3.5. A newly formed kink is a sharp discontinuity in the direction of the string locus and typically propagates along the string at speeds of $\sim c$. Kinks from loop formation decay *very slowly* in the matter dominated era, their amplitude decreasing as $\sim t^{0.1}$ (Be90). Whether this is significant to lensing depends on the resolution of the experiment being performed – a wiggly string appears smooth if below the experimental resolution but the effective mass per unit length is increased to $\bar{\mu}$. Thus wiggly strings give greater lensing as $\psi = 8\pi G\bar{\mu}$. Again appealing to simulated data we find that $\bar{\mu}(\beta) \simeq 1.5\mu$ in the matter dominated epoch on the scale of the coherence length of the string network, β (SA90). We will show later that this effect is insignificant on the scale of individual galactic lensing events and so $\bar{\mu} = \mu$ can be assumed in what follows.

- The *fractal dimension* of the long strings changes as a function of scale. If L is the total length of string between two points and R the straight line distance between the same points then $(L/H) \propto (R/H)^d$ with H the horizon scale. The fractal dimension d increases from ~ 1 at $\sim 100h^{-1}$ Mpc scales to the Brownian walk value of 2 at $\sim 1000h^{-1}$ Mpc scales where the string tends towards incoherence (SA 1990).

- In the case of string *loops* a characteristic cut-off scale is generated by the gravitational back reaction. Strongly curved portions of string emit gravitational radiation at a rate of

$$\dot{E} = \gamma G\mu^2 \tag{2.8}$$

with γ dependent on the loop configuration but $\sim$50 from simulated data (Vachaspati & Vilenkin 1985). The energy of any loop is $E = l\mu$ so loops of length

$$l_{\rm G} < G\mu\gamma t_{\rm H} \tag{2.9}$$

with $t_{\rm H}$ the Hubble time, will have decayed away by the present epoch. It follows that we should not expect to see any loops of size $\lesssim 0.5h^{-1}$ Mpc by the present.

- For infinite strings the situation is slightly more complicated – curvature on a variety of scales gives a spectrum of gravitational radiation. The damping of substructure by radiation may be less efficient than a naive estimate would imply (Sakellariadou 1990). This is because the damping becomes less efficient as the amplitude of the wiggles decreases. In this case $l_{\rm G}$ is probably only an upper limit to the scale on which strings can be considered straight.

All these factors are of importance for a thorough understanding of microstructure. However the discussions offered in the literature are difficult to relate directly to quantities we want to understand from a *lensing* point of view. In practice, therefore, it will be invaluable to estimate the parameters of interest from simulated data. The only way we can estimate the power in the substructure of long strings is to analyse data for large ($\gtrsim 20h^{-1}$ Mpc) scales as no significantly higher resolution datasets were available. We work on the assumption that there are no characteristic scales between $\sim l_{\rm G}$ and the correlation length of the string network $\sim t_{\rm H}$. If we can establish a power-law dependence of power on large scales we may feel safe in extrapolating this down to $\sim 0.5h^{-1}$ Mpc.

2.2.2 Analysis of Flat Space Simulation

The data we choose to analyse are the results of simulations on a Cray supercomputer (Hindmarsh et al. 1996) and were kindly provided by Dr. Mark Hindmarsh. String networks are evolved on a 256^3 cubic lattice in a flat spacetime. The initial conditions correspond to those of Vachaspati & Vilenkin (1984) in that the strings are originally random walks with a correlation length of order the horizon size. From this initially chaotic configuration the network is evolved to a steady state by determining positions

and velocities on two interlocking but non-overlapping lattices. The calculations required between timesteps are described in Smith & Vilenkin (1987). Energy and momentum are conserved and when two strings intersect they are presumed to intercommute in accord with an analysis by Shellard (1988). Ultimately most of the energy resides in loops of the minimum size allowed by the simulation, but with a few long strings stretching across the horizon. As these are *flat space* simulations they take no account of universal expansion. Any expansion will serve to damp out string substructure and so we can consider the results of our analysis to be a worst case – it will at least serve to keep our resulting estimates conservative.

The simulation data are provided in a series of conformal time steps upto a final state in which the putative horizon size is half the lattice size, i.e. $l_{\rm H} \sim \frac{1}{2}L$. A record is made after each time step of an ordered set of pointers, the string locus lying between successive lattice points $(x_{\rm L}, y_{\rm L}, z_{\rm L})$ in the list. $l_{\rm sim} = L/256$ will denote the lattice point spacing in what follows. All the output strings are closed loops (i.e. they begin and end at the same lattice point) but an approximation to horizon crossing strings is made by loops much longer than the width of the simulation cube. Also provided are the crudely quantized velocities (in steps of $0.5c$) of string at the points it passes through - we have chosen not to use them in our analysis since here we are only interested in the instantaneous loci of strings on the sky. The assumption will be that the transverse string velocity is coherent over the same range that the string locus is coherent.

Slices through a typical simulation cube are shown in figure 2.2.

We wish to find long strings which most closely approximate those which we expect to observe. Thus we take the final configuration of one of the simulations and extract the longest strings within it. It turns out that the longest strings are contained in two loops of combined length $\sim 80L$ in lattice units. These two loops represent *all* the horizon-spanning string within the simulation – each horizon-length piece can be considered a separate long string. The fact that all these segments add up into closed loops is merely an artefact of the periodic boundaries. The other objects within the simulation all have lengths $< l_{\rm H}$ and can be considered to be true loops.

Initially we imagine projecting the string on an arbitrary plane in the sky i.e. we

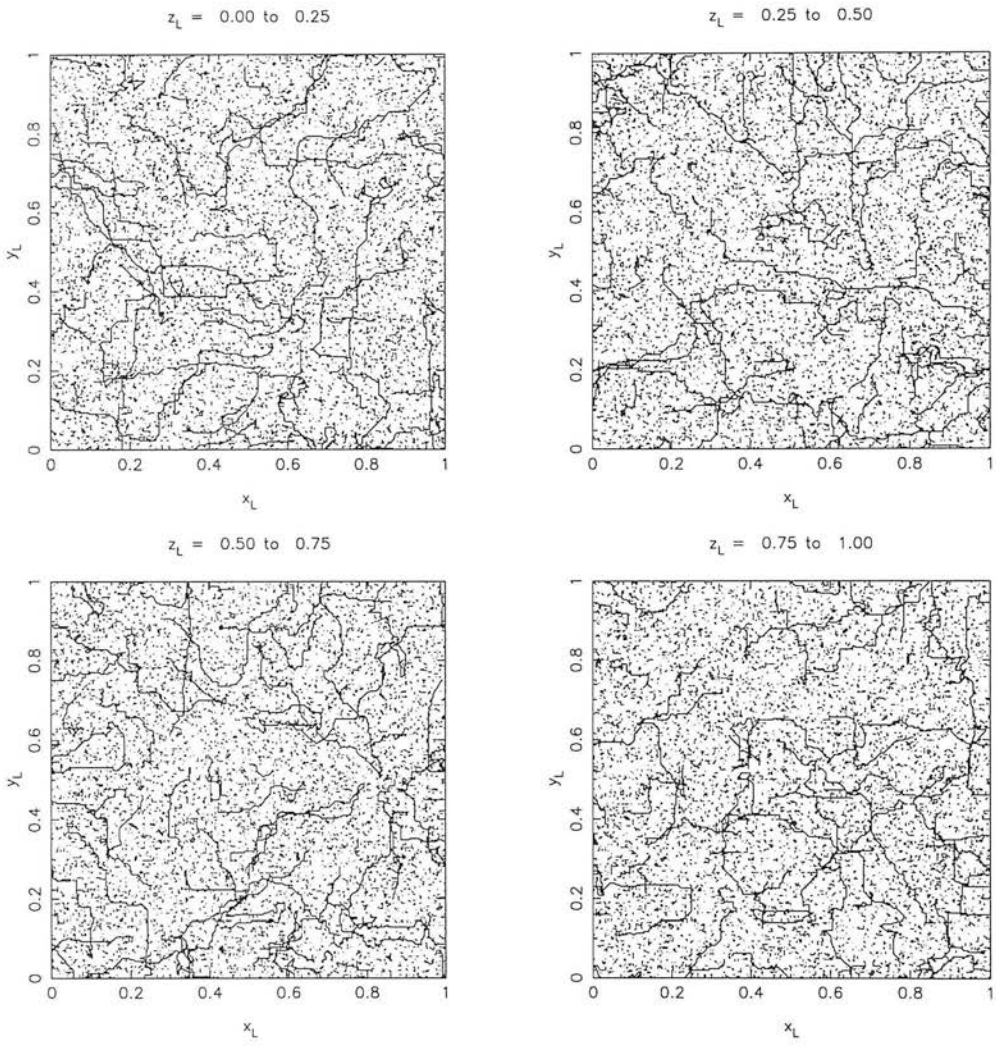

Figure 2.2: Four slices through the final state of the flat-space string simulations. The simulation volume is a cube of side L with periodic boundary conditions. The horizon scale in this figure is $l_{\rm H} = \frac{1}{2}L$ and the coordinates are in units of L. In addition to many small loops there are two long strings of combined length $\sim 80L$ which takes the form of two very large loops, each spanning a given horizon volume many times.

suppress one of the spatial dimensions in the simulation. Taking a long portion of the string we can envisage forming a vector $\mathbf{X}$ joining the two end points. $\mathbf{X}$ lies within our arbitrary plane – if we define another vector $\mathbf{Y}$ perpendicular to $\mathbf{X}$ but also in the plane we can now characterize deviations from string straightness as motion in the $\mathbf{Y}$ direction. That is we have reduced the string locus to a function $y(x)$ where x and y are displacements from the origin in the directions of $\mathbf{X}$ and $\mathbf{Y}$. Figure 2.3a shows this pictorially. This casts the string locus in the most useful form. We are interested in how

the wiggle of the string causes it to deviate from its average direction on the sky. Here y measures the deviations perpendicular to the mean direction x.

There are several ways we could analyze the wiggle from here on. For example we could use spline fitting to the discrete data to define a "smooth" string and find the average curvature of the string as a function of scale. Here we propose to Fourier analyse $y(x)$ using an FFT to attempt to characterize the typical amount of substructure on a given scale, i.e. we want to calculate

$$\tilde{y}(k) = \int_0^\infty y(x) e^{ikx} dx \tag{2.10}$$

and obtain the *power spectrum* of the transverse displacements

$$P_y(k) = \langle |\tilde{y}(k)|^2 \rangle. \tag{2.11}$$

Certain mathematical niceties must be observed before we can proceed down this route. Firstly we must ignore the periodic boundaries of the simulated data and allow the string to continue into neighbouring cells – i.e. if the string moves out of the cell we let it enter the next cell along rather than enter at the opposite face of the existing cell. This ensures that we have one coherent function for one long string. Secondly we require $y(x)$ to be *single-valued* for the Fourier transform to be meaningful. Therefore we need to suppress the progress of the string in the $-\mathbf{X}$ direction. In practice we amend a portion of string which "turns back on itself" by reflecting it about the $\mathbf{Y}$ axis (figure 2.3b). This obviously removes curvature information from the data to some extent – however we expect the analysis to hold on scales below the typical number of steps, $l_{\rm TB} \sim 25 l_{\rm sim}$, the string takes before it "turns back" in this way. This is rather unphysical but we are really not that interested in the string behaviour on scales $\gtrsim l_{\rm TB}$ (where Brownian walk behaviour is expected) as this is easily modelled, e.g. equation 2.7.

Finally we must bin the data for the FFT algorithm in such a way that each bin contains some information without smoothing out the small-scale behaviour in which we are most interested. A resolution scale is imposed on the simulation in the form of the mean separation between lattice points – the data merely interpolate between these

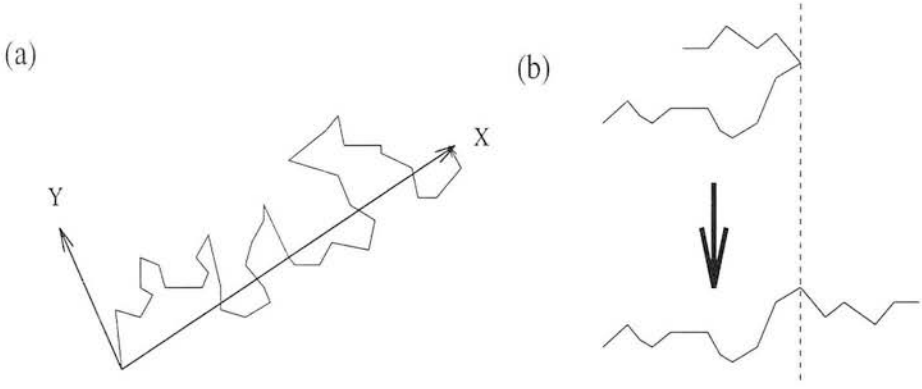

Figure 2.3: (a) Extraction of $y(x)$ from the string data described in section 2.2. (b) Amending strings that "turn-back" on themselves as described in the text.

points so there is no information on smaller scales. The optimum case is therefore to choose a bin size of order b where b is the largest single step a string can make between lattice points, i.e. $b \simeq \sqrt{3} l_{\rm sim}$.

The power spectrum of deviations from straightness is shown in figure 2.4 with the relevant simulation (and by extension astrophysical) scales indicated. Also shown is a two-parameter fit to $P_y(k)$ which is well modelled by

$$P_y(k) \simeq \alpha k^{-2.87} \tag{2.12}$$

with $\alpha = 0.34$ when k is in lattice units, $k = 2\pi L x^{-1}$. The fit would probably be shallower if more weight were given to low k values – reflecting the onset of decoherence at $k \lesssim k_{\rm H}$ – but it is the high $k \gg k_{\rm H}$ end that concerns us most and here the fit is extremely satisfactory. We expect no *physical* scales to be important for string evolution between the horizon size ($l_{\rm H} \sim t_{\rm H}$) and the gravitational back-reaction scale $l_{\rm G}$ (see page 42 for a discussion). We have no information on the power below $l_{\rm sim}$ ($\gg l_{\rm G}$) but if our expectations are correct then we can anticipate a scale-free spectrum in the range $l_{\rm H} - l_{\rm G}$ and therefore extrapolate the $k^{-2.87}$ behaviour beyond our simulation imposed cut-off.

We can see directly from the power law behaviour of $P_y(k)$ that the strings are not well modelled by a random walk $P \sim k^{-2}$ or a fractal or "flicker-noise" type spectrum with $P \sim k^{-1}$. We have tested the Fourier technique by putting in a random walk

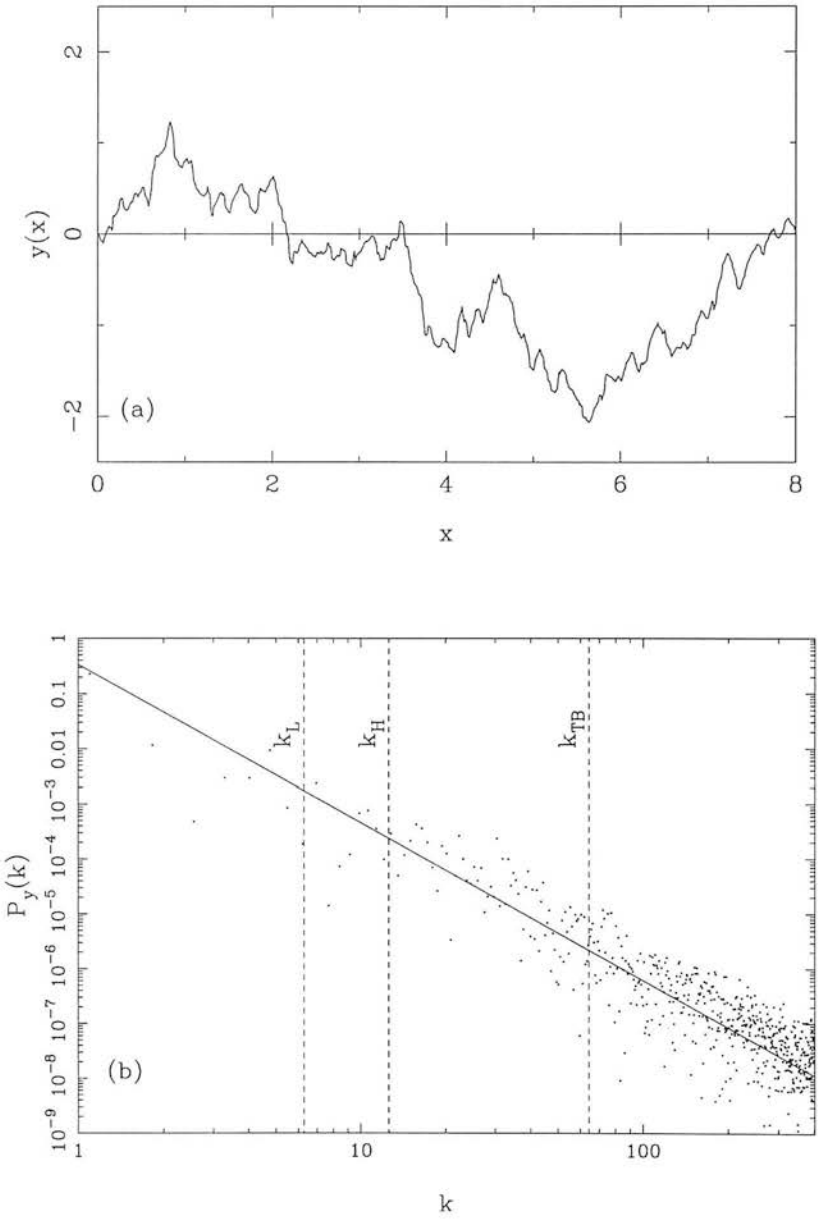

Figure 2.4: (a) The function $y(x)$ evaluated for the final string simulation in which $l_{\rm H} = 0.5L$. x and y are in units of L. (b) The power spectrum of the string 'wiggliness' function $y(x)$. k is measured in box size units i.e. $k = 2\pi L x^{-1}$. Shown are some of the key astrophysical scales, $k_{\rm L}$ the simulation scale, $k_{\rm H}$ the horizon scale and $k_{\rm TB}$ the 'turn-back' scale below which the string really *is* a single valued function of x. A two-parameter fit to the data yields $P_y(k) \simeq 0.34k^{-2.87}$ in the range of interest for lensing ($k \gg k_{\rm H}$).

string of step length b with the position angles varying randomly between each step. The process recovers the k^{-2} power expected.

Recall that we are interested in the coherence of lensed-pair position angles over a given scale. We can characterize the curvature as the variance in position angle between neighbouring image pairs on the sky, σ_θ^2. The local deviation from string straightness can be characterized by the gradient $y'(x) = dy/dx \simeq \tan\theta(x) \simeq \theta(x)$ [for $\theta \ll 1$] a distance x along the $\mathbf{X}$ vector. A relatively straightforward manipulation of the FTs gives us the relevant information as $\tilde{y'}(k) = ik\tilde{y}(k)$.

We have

$$\frac{d\sigma_y^2}{d\ln k} = \frac{P_y(k)}{\pi}k \simeq \frac{\alpha}{\pi k^2}. \tag{2.13}$$

and so

$$\frac{d\sigma_{y'}^2}{d\ln k} \simeq \frac{\alpha}{\pi} \simeq \text{const.} \tag{2.14}$$

i.e. the angular variance per $\ln k$ is approximately a constant. To integrate equation 2.14 over the range k_x to infinity (where k_x is the wavenumber corresponding to the inter-pair separation x) is impossible as the integral is divergent. However we expect gravitational radiation to damp down the microstructure for $k \lesssim k_{\rm G}$ (with $k_{\rm G}$ the wavenumber at the gravitational cut-off scale of equation 2.9) and so the best guess for average variance in the angle θ is given by

$$\sigma_\theta^2 = \sigma_{y'}^2 \simeq \int_{k_x}^{k_{\rm G}} \frac{\alpha}{\pi}\frac{dk}{k} \simeq \frac{\alpha}{\pi}\ln\left(\frac{k_{\rm G}}{k_x}\right). \tag{2.15}$$

Without a cut-off the upper limit $k_{\rm G}$ would be replaced by $k_\psi \simeq (2\pi/3000\ \psi\ z_{\rm s})h\,{\rm Mpc}^{-1}$ which is effectively the smallest scale on which a wiggly string could affect the position angle coherence – the scale of image separation for individual pairs. However for $10''$ lensing $k_\psi \gg k_{\rm G}$ for string redshifts of less than unity and as we anticipate no power for $k > k_{\rm G}$ the expression 2.15 gives the same result. This also explains why the wiggle does not give an amplified lensing angle as discussed on page 42. On the scales affecting individual lensing events the string can be considered straight.

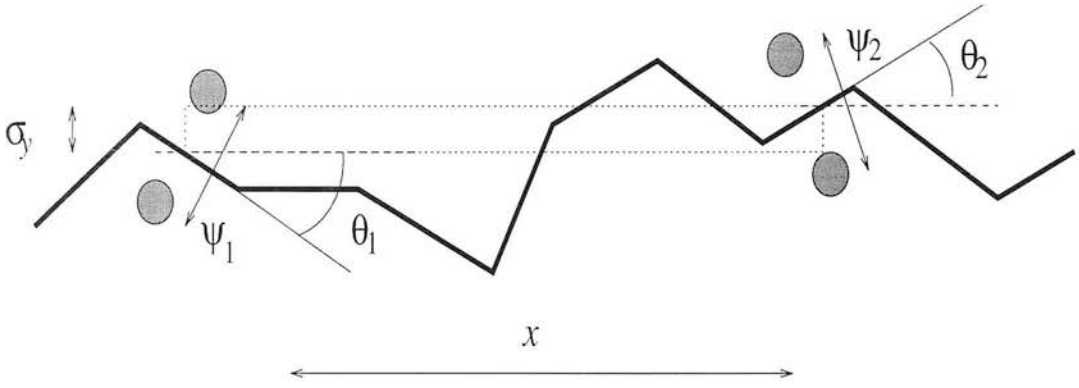

Figure 2.5: The parameters governing the scatter in position angle σ_θ of lensed pairs along a string. Here x is the separation between the pairs in the mean direction of the string locus. ψ_1 and ψ_2 are the angular separations of the galaxy images in lensed pair 1 and lensed pair 2 respectively. The symmetry axes of the pairs make angles θ_1 and θ_2 to the mean direction of the string locus. $\sigma_\theta(x)$ is then the mean value of $|\theta_1 - \theta_2|$ for pairs separated by x. The dotted box shows a strip in the direction of x, wide enough to contain the centroids of both image pairs. The mean thickness of such a strip will be given by $\sigma_y(x)$.

The behaviour of σ_θ^2 over the range of observational interest is shown in figure 2.6a. The simulation data are indeed well modelled by the form

$$\sigma_\theta^2(x)/\mathrm{rad}^2 = 0.11 \ln\left(\frac{x}{0.5h^{-1}\,\mathrm{Mpc}}\right). \tag{2.16}$$

This indicates a very slow increase in angular deviation as we look at larger and larger portions of string. It is clear that these simulations yield long strings with coherence lengths of order the horizon though an extrapolation upto $x \simeq l_\mathrm{H}$ is invalid as we have suppressed "turn-back" above about $500h^{-1}$ Mpc. It appears that the rms scatter in position angle along a $\sim 10h^{-1}$ Mpc length of string will be of the order of 30°. Previous arguments on the gravitational damping scale for long strings (page 43) have indicated that the k_G chosen here is probably a lower limit in which case the σ_θ^2 here is really a best case, though the function is fairly insensitive to small changes in k_G.

A plot of $\sigma_y^2(x)$ is germane to our discussion – it allows us to set the minimum width of strip that would contain all the lensed pairs due to a string segment of length $\sim x$.

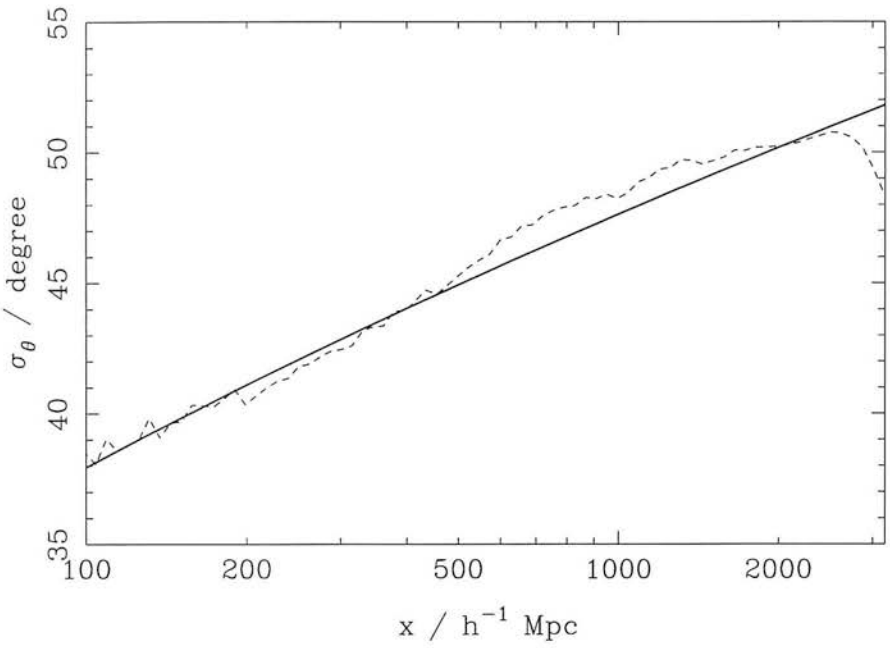

Figure 2.6: (a) The rms deviation of the string from straightness as a function of distance along the string x. σ_θ quantifies the mean angle of curvature of the string portion in degrees. The dashed line indicates rms values measured directly from the simulated data. The filled line shows the fit provided by $\sigma_\theta^2(x)/\mathrm{rad}^2 = 0.11 \ln\left(x/0.5h^{-1}\,\mathrm{Mpc}\right)$.

Such a plot is provided in figure 2.6b. The data are well matched by

$$\sigma_y^2 \simeq 0.028 x^{1.87} \tag{2.17}$$

Figure 2.5 shows how $\sigma_\theta(x)$ and $\sigma_y(x)$ bear on the discussion of lensing with string microstructure.

To review, we have analysed a specific string simulation to gain an estimate of string microstructure in ranges of importance to lensing based search programmes. We find the 2D projection of strings on the sky to be well modelled by a featureless power spectrum $P \sim k^{-3}$. Using this and the assumed absence of new physical effects between the gravitational back-reaction scale $\sim 0.1h^{-1}$ Mpc and the simulation resolution scale $\sim 20h^{-1}$ Mpc we have produced plots direct from the data and analytical formulae to model the sub-simulation scale behaviour. We will use these results in earnest to construct a string searching algorithm in chapter 4.

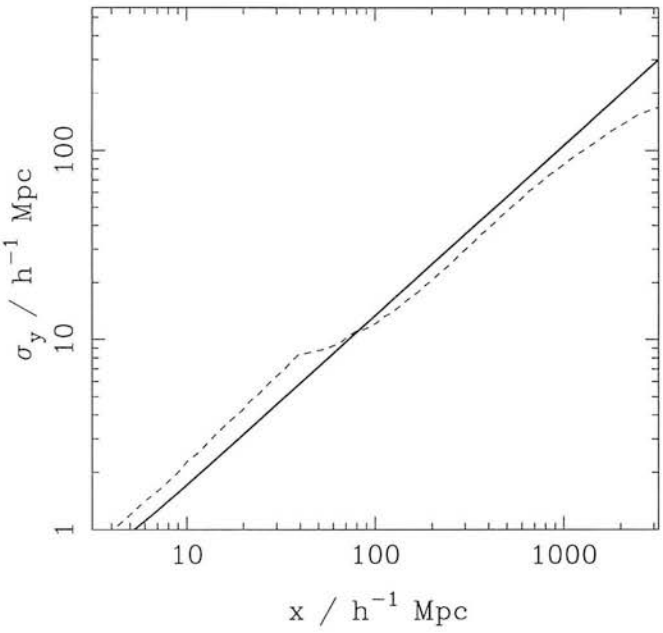

Figure 2.6: (b) The rms deviation of the string from straightness as a function of distance along the string x. σ_y is the average width a rectangle of length x must have to contain all the string portion. The dashed line shows the behaviour of the simulated data. $\sigma_y^2 \simeq 0.028x^{1.87}$ (solid line) is roughly observed in the $l_{\rm sim} \rightarrow l_{\rm H}$ region.

2.3 The Density and Detectability of Strings

In order to estimate the chances of success for any search for strings we need to have an idea of the volume density of long strings. From the final set of flat-space simulation data we note that the longest two strings in the simulation have a combined total length of $l_{\rm s} \sim 80L$. Most of the remaining segments of string lie in very small loops with radii the order of $l_{\rm sim}$ – a comoving scale of around $20h^{-1}$ Mpc. The area of sky in which lensing effects of a given loop are detectable is negligible compared to that of a single long string. We will therefore take $80L$ as an estimate of the total *detectable* string in the volume represented by the simulation ($\simeq 8l_{\rm H}^3$), at least where any lensing dependent search is employed.

For the final simulation cube we have $L \sim \frac{1}{2}l_{\rm H}$ and thus we have roughly $20l_{\rm H}$ of long string per horizon volume $l_{\rm H}^3$. This is in reasonable agreement with other simulation data. Bennett (1990) finds $\rho_{\rm s} = 31 \pm 7/l_{\rm H}^2$, Albrecht & Turok (1990) find $\rho_{\rm s} \simeq 18/l_{\rm H}^2$ and Shellard & Allen (1990) find $\rho_{\rm s} = 36 \pm 9/l_{\rm H}^2$ in the matter dominated era. These results

are collected in the monograph by Vilenkin & Shellard (1994). Our long string density is within a factor 2 of these amounts. Using our value for now, the volume density of string can be estimated as

$$\rho_{\rm s} = \frac{dl_{\rm s}}{dV} \simeq \frac{20}{l_{\rm H}^2}. \tag{2.18}$$

From this we can readily calculate the length of string (on average) out to a redshift z from an arbitrarily placed observer. For $\Omega = 1$

$$V(z) = \frac{32\pi l_{\rm H}^3}{3}\left[1-(1+z)^{-1/2}\right]^3 \simeq \frac{4\pi}{3} l_{\rm H}^3 z^3 \quad (z \ll 1) \tag{2.19}$$

and then

$$\frac{dl_{\rm s}}{dz} = \frac{dl_{\rm s}}{dV}\frac{dV}{dz} \simeq 80\pi l_{\rm H} z^2. \tag{2.20}$$

This can be converted into the angular length of string on the sky α as

$$\frac{d\alpha}{dz} = \frac{d\alpha}{dl_{\rm s}}\frac{dl_{\rm s}}{dz} \simeq 80\pi z \tag{2.21}$$

which can be integrated up to yield

$$\alpha = \int_0^z 80\pi z'\, dz' = 40\pi z^2 \,{\rm rad} \simeq 7.2\times 10^3 z^2 \,{\rm degree}. \tag{2.22}$$

In a similar calculation, Hindmarsh (H90, equation 16) finds $\alpha \simeq 4.1\times 10^3 z^2$ degree. This is within 50% of our value and reflects the scatter in the published values of $\rho_{\rm s}$. We will stick with the value in equation 2.22 for now, remembering that $\alpha \propto \rho_{\rm s} z^2$ if rescaling to a different density is required.

We are now in a position to estimate the chances of success of any string detection programme. The two crucial parameters will be the area of sky searched A, and the redshift limit $z_{\rm min}$ to which strings can be detected with a given survey. We will discuss this issue in successive layers of detail, firstly estimating the chances of *any* string at all crossing A. Then we will assume that only a small portion of that string needs to be within our area for a successful detection (borne out by simulations in chapter 4).

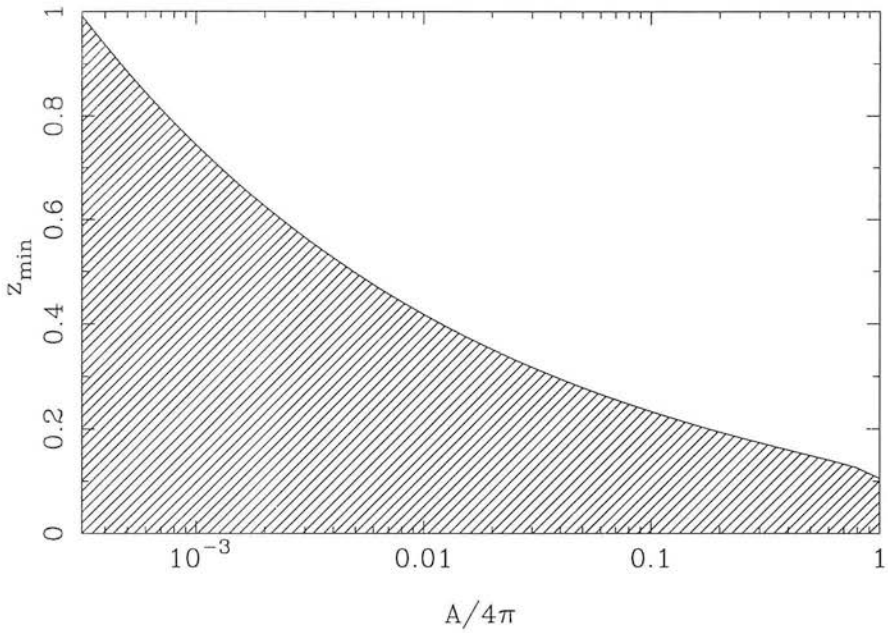

Figure 2.7: Estimate of the survey depth (in terms of a minimum redshift) required for a given area of A sterradian to contain a length of string. That is, given an area of sky A, what is the redshift of the nearest portion of string crossing that area? The survey depth must lie in the unshaded region for an above 50% probability that a string will be found in A.

Finally we will check these analytical arguments against the simulated data for the case where the search material is UKST plates of area 25 deg^2.

For a string to cross a circular patch of sky of radius β radians the patch centre must be within 2β of a string segment. Given the value of α above, we can calculate the area density of strings. In the case where none of these string segments overlap (a good assumption as long as $\alpha\psi \ll 4\pi$) the Poisson probability of our patch containing a length of string is

$$p = 1 - e^{-2\alpha\beta/4\pi}. \tag{2.23}$$

Strictly speaking a binomial distribution is more appropriate as we are interested in the chances of *one or more* strings crossing the area but the distributions coincide for α, $\beta \ll 1$. For p to exceed 50% requires that $\alpha\beta > 2\pi \ln 2$. We can convert this into some more useful units using equation 2.22 so that

$$\beta > \frac{\ln 2}{20 z_{\rm min}^2}. \tag{2.24}$$

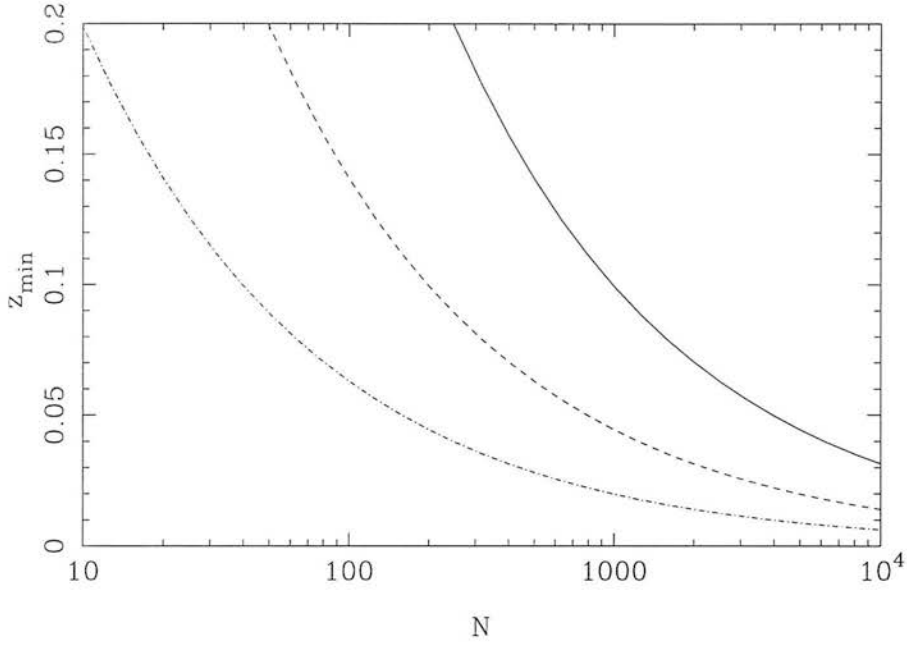

Figure 2.8: $z_{\rm min}$ as a function of the number of fields required for a string detection where the field size is $l_{\rm D} = 0.2°$, $1°$, $5°$ for the full, dashed and dot-dashed lines respectively. The parameters of the search dataset must fall above each line for a good (at least ~50%) chance of detection. Note that the $z_{\rm min}$ attainable be well below the *mean redshift* $\overline{z}$ of a given survey. The relevant effects will be discussed fully in section 3.2.

β can be at most π and so we have a rough limit for any all sky survey of $z_{\rm min} > 0.1$. As we shall see later this is really the upper limit of any detection programme based on UK Schmidt data. In terms of area we have $\beta = \cos^{-1}(1 - A/2\pi)$ and so our two survey parameters must satisfy

$$z_{\rm min}^2 \cos^{-1}(1 - \frac{A}{2\pi}) > 0.03 \tag{2.25}$$

for a search to have a good chance of success. The parameter space of A and $z_{\rm min}$ that a successful search must occupy is plotted in figure 2.7.

This analysis is, however, overly pessimistic as we do not necessarily need the string segment to be of the size of our search area in order to detect it. Imagine that for at least one successful detection we need only $l_{\rm D}$ of string to cross our search area and that

we therefore search N fields of radius l_Γ. Our detection probability is then

$$p = 1 - (e^{-2\alpha l_D/4\pi})^N. \tag{2.26}$$

50% success then requires

$$z_{\min}^2 > \frac{\ln 2}{20 N l_\Gamma} \tag{2.27}$$

which for a given $z_{\min}$ reduces the total area that needs to be searched by a factor of $\sqrt{N}$. Thus figure 2.7 can be recast in terms of the number of fields of size l_Γ one needs to search at a given $z_{\min}$ (see figure 2.8). This is, if anything, an overly *optimistic* argument as it assumes the string segments form a "gas" of l_Γ length units whereas in reality these segments are linked together and so fill the search area less evenly. The two equations 2.25 and 2.27 could reasonably be regarded respectively as upper and lower limits to the $z_{\min}$ required for searches over a given area.

These are simply estimates based on the expression 2.22. Using the string simulations we can randomly place observers within the simulation cube and see how much string lies on the sky out to a given redshift. All-sky projections for one such vantage point are given in figure 2.9. If we have a search area A and limiting redshift $z_{\min}$ in mind we can simply see if any string crosses the area, on average, when the observer's location and orientation are randomly selected within the simulation cube (assuming that we are not too near the edge). Anticipating the search method employed in chapter 4 we will use a search area of 5×20 Schmidt plates each of area $5^\circ \times 5^\circ$. We will then class the string as detectable if ~ 50 % of the areas contain a detectable length of string, i.e. more than 1° of string at $z \leq z_{\min}$ on at least one of the plate sub-areas. This is carried out for large numbers of random vantage points and lines of sight to obtain an ensemble average. This process should be reliable for $z \lesssim 1$ as then we are dealing with volumes which are significantly smaller than the simulation volume L^3 and can be considered as multiple independent realizations of the string network. The plot for the results (for this and other values of A) is provided in figure 2.10.

We will refer back to the results of this section later when assessing the usefulness of various datasets in searching for strings.

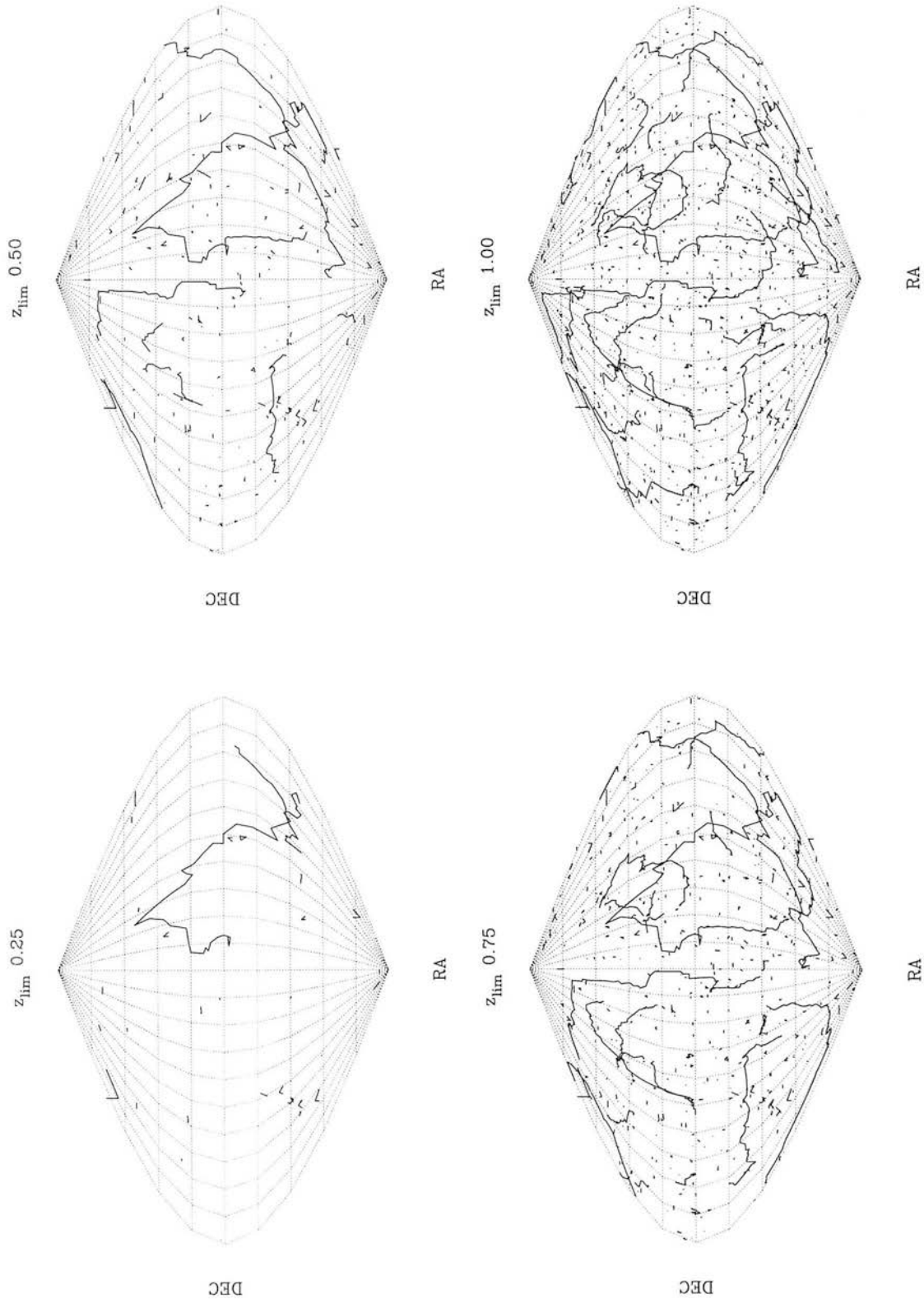

Figure 2.9: The simulation data as seen over the whole sky by an observer at the centre of the simulation cube of figure 2.2. Each successive plot increases the redshift out to which the observer can see string on the sky and hence the volume sampled.

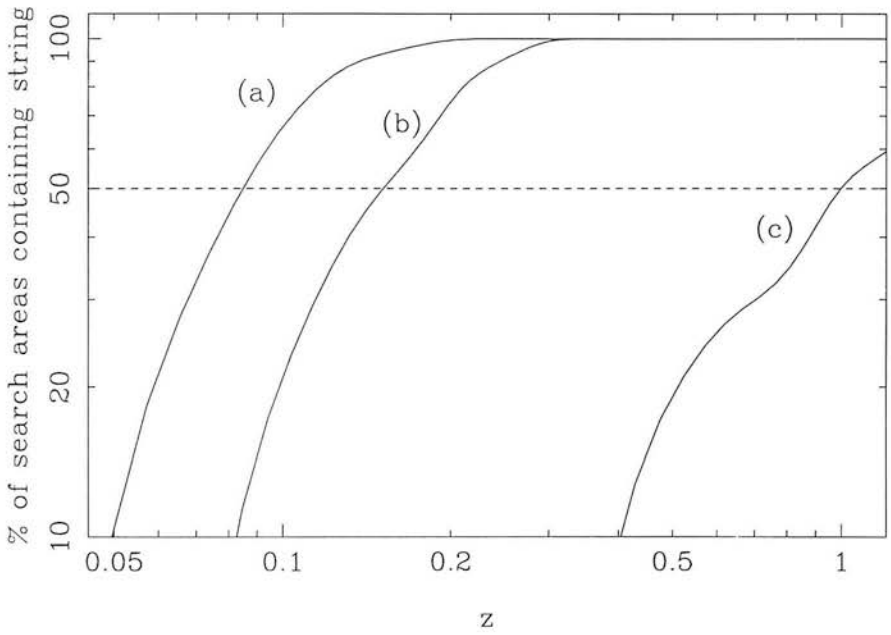

Figure 2.10: The proportion of search areas containing detectable string for the flat space simulation data. The areas employed are, (a) a π sterad area corresponding to the Sloan northern sky survey area. A 50 % chance of detection only arises for $z \gtrsim 0.09$, (b) a 5×20 sized zone of $5^\circ \times 5^\circ$ Schmidt plates with a > 50 % chance arising for $z \gtrsim 0.15$ and (c) the $3^\circ \times 100^\circ$ area of the Sloan deep survey which only contains significant lengths of string at $z \gtrsim 1$.

Chapter 3

The Characteristics of Lensed Galaxies

The previous chapter has investigated the characteristics of long strings that are important for any search method based on galaxy lensing. This chapter focuses on the appearance of those lensed galaxies dealing with issues of significance to search programmes made on *any* dataset. In each case, though, the arguments will be illustrated with reference to UKST/COSMOS data. It is on this dataset that a search is finally carried out (chapter 4), using ~ 100 high galactic latitude fields of the UKST B_J survey. The final part of chapter 4 will extend the discussion to search programmes based on deeper survey data and argues that with such data conclusive tests of the string model should be possible.

As this chapter principally illustrates its arguments using the specific example of Schmidt plates it will be helpful to discuss the general qualities of the plate data before beginning. The principle attribute of Schmidt telescopes is their wide field of view – they are very well suited for systematic photographic surveys over large areas of sky. The UK Schmidt Telescope in Australia has been operating since 1973. Its programme of obtaining wide-field B_J-band photographs of the whole of the southern sky is now complete. The survey comprises $\sim$ 900 Kodak IIIa-J plates, each roughly 6° across. The limiting magnitude is approximately $B_J \sim 22$ for plates exposed in the best seeing

conditions. Usually the seeing is of the order $3''$ - not great compared with that of 4m telescopes in the better sites – however this concern is offset by the sheer volume of data the plates can provide.

A typical plate, therefore, contains images of several hundred thousand stars and galaxies. The COSMOS plate scanning machine at the R.O.E. (MacGillivray & Stobie 1985) has digitised the best plates for each UK Schmidt field to produce pixel density maps suitable for computer analysis. Software can then extract the parameters of images on the plate by applying a threshold at a specified percentage above the local sky background intensity. Pixels above the threshold are connected up into discrete objects and parameters are determined for each using moments up to second order (Beard, MacGillivray & Thanisch 1990). The image characteristics of importance for a string lensing search, namely the $B_{\rm J}$ magnitude, orientation and ellipticity are recorded in *image analysis* files which are generally available to the astronomical community. There is therefore a database of the images in the southern sky, brighter than $B_{\rm J} \sim 22$, which can be interrogated to find the locations and characteristics of interesting objects. Our search for string-lensed objects will principally concentrate on high-declination ($0 > \delta > -30^{\circ}$) fields so that follow up work can be carried out on northern *or* southern hemisphere telescopes. We also stick to high galactic latitude plates (at $|b| > 30^{\circ}$) to reduce the prevalence of foreground stars.

The redshift distribution of galaxies on the plates can be estimated (Efstathiou 1995) using the formula

$$\frac{dN}{dz} \propto z^2 \exp\left(-\left[\frac{z}{z_{\rm c}(B_{\rm J})}\right]^{3/2}\right) \tag{3.1}$$

where

$$z_{\rm c}(B_{\rm J}) = 0.0113(B_{\rm J} - 17)^{1.5} + 0.0325 \tag{3.2}$$

is a good approximation for $B_{\rm J} \lesssim 22$. Plots of dN/dz for $B_{\rm J} \simeq 21.5$ and 22.5 (respectively average and good limiting magnitudes for Schmidt plates) are given in figure 3.1.

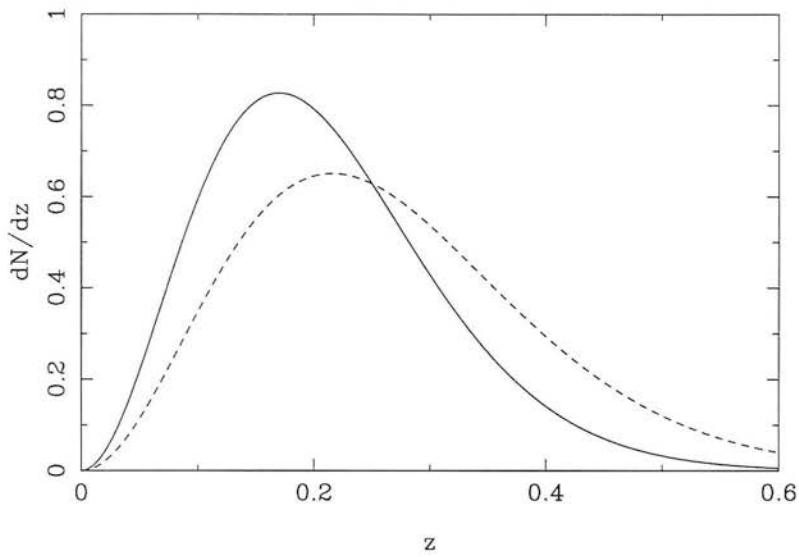

Figure 3.1: Redshift distributions for $B_J \leq 21.5$ (filled line – a typical limiting magnitude for B_J-band Schmidt plates) and $B_J \leq 22.5$ (dashed line – the limiting magnitude of the deepest Schmidt plates). The functional form is taken from Efstathiou (1995) and give median redshifts of $\overline{z} \simeq 0.20$, $(B_J \leq 21.5)$ and $\overline{z} \simeq 0.25$, $(B_J \leq 22.5)$.

3.1 The Appearance of Lensed Galaxies

3.1.1 Image Analysis of Lensed Galaxies

The types of objects we expect to see lensed on Schmidt plates have a range of characteristics. Generally these will be typical of galaxies in the range $z = 0.05 - 0.35$ where the bulk of the galaxies are found for $B_J \leq 21.5$ (see figure 3.1). B_J-band images of distinct lensing events can principally vary due to

- the magnitude and morphology of the individual galaxies in the lensed pair. These will be near identical for each *galaxy* in a given pair unless the lensed object is sufficiently extended that there is a possibility that only part of it will fall into the lensing region of the string (figure 2.1b). An attempt to model this effect is provided in section 3.1.2.

- the angular separation of the two component images in a pair. Whether or not the two images can be seen to be distinct depends on the lensing angle. This becomes a *deblending* problem as discussed below.

During the preliminary stages of our search programme it will be vital to utilize any information on what lensed pairs *can* look like. The more definitive criteria we can apply to close pairs in the data, the more effectively we can remove images that lie within $10''$ of each other by chance. This will reduce the noise due to chance alignments of otherwise unrelated close pairs and translates into a greater depth limit for the search technique.

At the $B_J \leq 21.5$ median redshift of $\overline{z} \simeq 0.20$ the angular size of an ~ 10 kpc diameter galaxy will be of order $3''$. This is comparable to the FWHM of the seeing disk on a Schmidt plate. This means that little morphological information will be available for the fainter galaxies on Schmidt plates – they will be approximately $3''$ FWHM Gaussian discs. As this is the bulk of any galaxies we can expect to be lensed at all (lensing probability goes as $\sim z^2$) we do not expect morphology differences between images in a pair to be a good discriminant. We will, however, use it when we reliably can. We need to remove pairs in which the component images are clearly of different magnitude. This depends on the accuracy of the magnitude estimates possible with COSMOS analysed Schmidt plates, which will be a function of B_J. We will attempt to estimate the function $\langle |\Delta B_J| \rangle$ below. Note this assumes that relatively few pairs are truncated in the manner of figure 2.1b. This issue will be dealt with in the next section.

The two criteria mentioned above are applicable when the two images in a pair are separated sufficiently for both to be seen as distinct. The COSMOS image analysis software features a deblending algorithm which attempts to distinguish overlapping images (Beard et al. 1990). Generally the effectiveness of the deblending is a function of the separation and magnitude of the underlying images. In cases where deblending fails the COSMOS analyser will interpret the two overlapping images as *one* image. We therefore need to investigate the likely appearance of such images and be sure not to exclude them when a final list of possible lensed objects is made.

In order to investigate these effects we must simulate the appearance of lensed pairs and subject them to the same image analysis process we apply to the real data. The steps involved are as follows

- Approximate each galaxy as a Gaussian disc with intensity profile $I_0 \exp(-r^2/2\sigma_s^2)$ with $\sigma_s \simeq 1.3''$ to simulate a seeing FWHM of $\simeq 3''$. As we are prepared for most

of the galaxies in the survey to be unresolved we neglect to model the $e^{-r/h}$ profile of spirals.

- Put pairs of such images down onto a pixel array with a range of separations ($s = 0 \rightarrow 10''$) allowing I_0 to vary between pairs. Allow $1''$ per pixel to simulate the COSMOS scanning scale.
- Add a Gaussian distributed noise component to each pixel to simulate the sky background
- Subject the pixel array to image analysis using parameters similar to those used in the original COSMOS/UKST plate analysis.
- Set the level at which $B_J = B_{Jlim} \simeq 21.5$ by the intensity I_0 at which only about *half* the individual images are detected by the image analyser.

In practice we did not have direct off-line access to the COSMOS image analyser and instead made use of the Starlink PISA software – this is the APM object finding software described in Irwin (1985). In basic function (detecting images as a series of contiguous pixels above some threshold intensity) the two programmes should behave in a very similar manner and produce comparable output for total intensities, image orientations and ellipticities. The one major difference which could be of relevance is in the efficiency of the deblending routines. We can use the COSMOS image analysis data themselves to estimate the separation at which COSMOS deblending starts to fail. Study of a typical image analysis file shows there are virtually *no* image pairs separated by less than $\simeq 4''$. If we then impose this limit on PISA by forbidding it to deblend lensed pair images with $s < 4''$ then we can simulate this effect. This implies that below $s = 4''$ close pairs will be treated as *single objects* as anticipated above.

Some examples of the pixel data and resulting image analysis are given in figure 3.2.

The PISA data are output in the form of an ASCII file containing for each image its ellipticity e, angle of orientation θ and integrated intensity I. By comparing these to the input parameters for the simulation, (s, B_J and θ_{true}) we find that

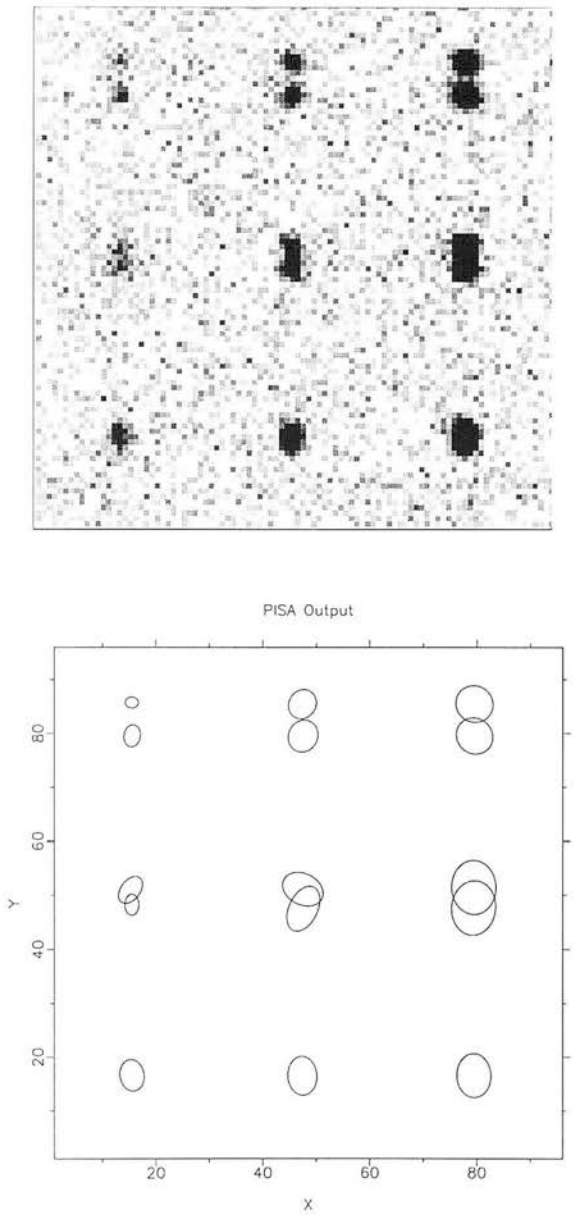

Figure 3.2: (a) A sample pixel file showing a range of simulated images of lensed galaxy pairs. Each galaxy is approximated as a Gaussian disc with FWHM $\simeq 3''$. Moving from left to right the galaxy magnitude in each column is $B_J \simeq 21, 20, 19$. Moving upwards from the bottom the lensing angles in each row are $s \simeq 2''$, $4''$ and $6''$. (b) The result of PISA image analysis on the simulated data. At $2''$ the images cannot be deblended and a single ellipse is output. At $4''$ the limit of the deblending range is reached - although this appears to be the limit of COSMOS deblending, the PISA algorithm fares quite well in apportioning the correct flux to each. At $6''$ the images are well separated and are of patently similar magnitude and shape.

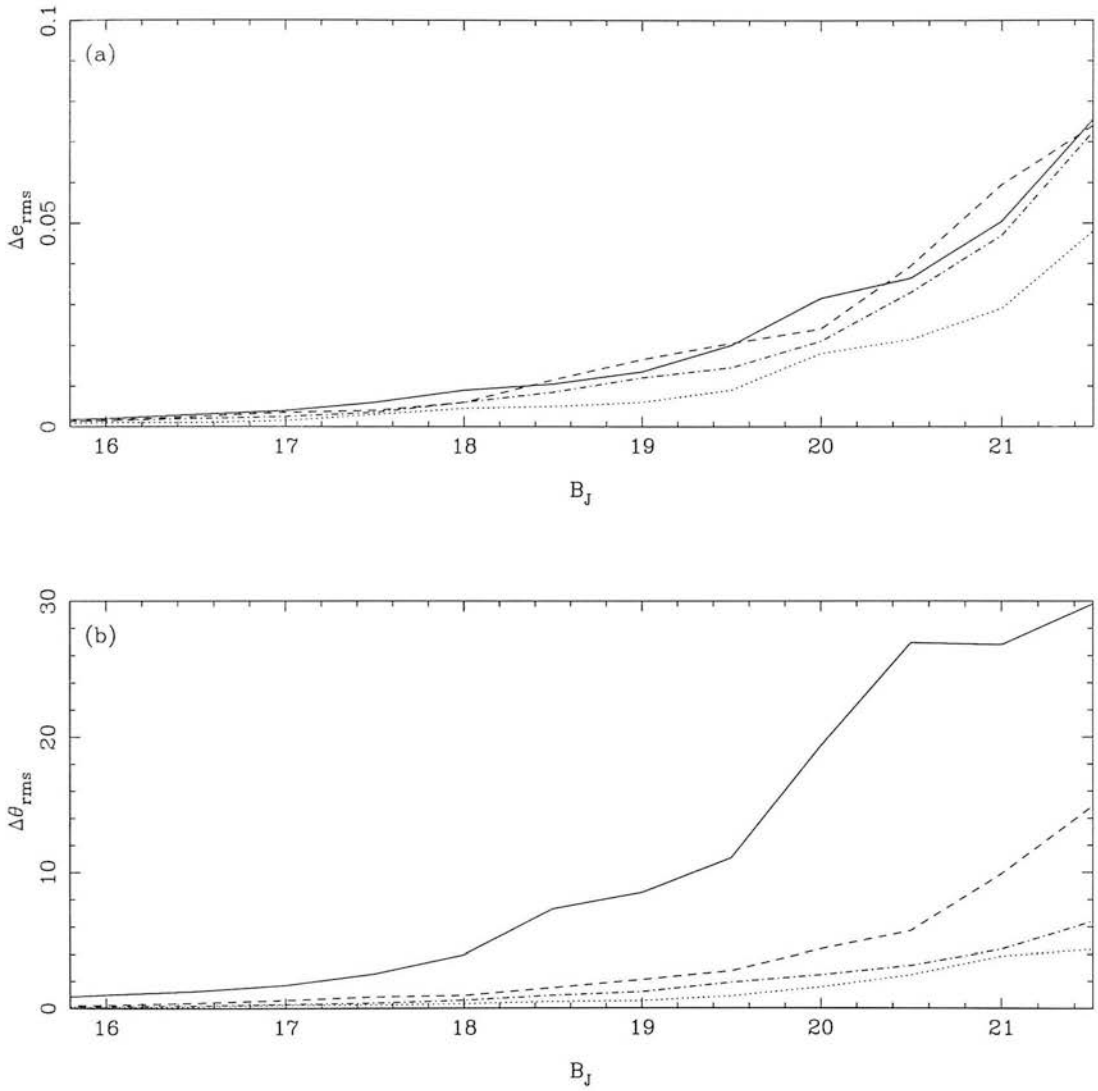

Figure 3.3: Plots of the rms values of (a) $\Delta e(B_J)$ and (b) $\Delta\theta(B_J)$ – the scatter in the PISA output parameters as a function of magnitude – for simulated lensing with separations 1″ (filled line), 2″ (dashed), 3″ (dot-dashed) and 4″ (dotted). The values are used to estimate tolerances (for the image analysis data) within which close pairs can be considered identical.

- below the deblending scale of 4″ the analysed image is in the form of an ellipse with its long axis directed along the line separating the images in the pair. The separation s can be recovered if the ellipticity e is known via

$$s(e) \simeq 4.1e + 8.2e^2 \tag{3.3}$$

where s is in ″ (this is an empirical fit to the PISA output).

- the errors in measuring the angle of orientation $\Delta\theta$ and ellipticity Δe are functions of the image magnitude *and* separation. Thus $\Delta\theta$ and Δe can be represented as 2D

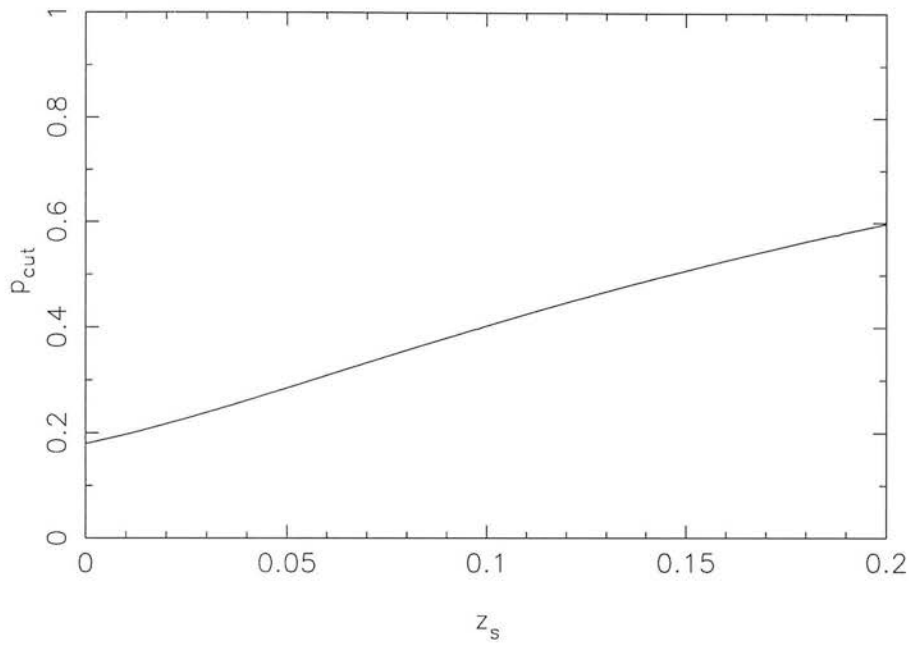

Figure 3.4: (a) Probability of partial lensing of background galaxies at $B_J \lesssim 21.5$ as a function of string redshift z_s. The function is sensitive to the galaxy radius r_g assumed. The value adopted here is $r_g = 5$ kpc.

arrays. Given B_J and s, the likely error for *real images* can be extracted from each array to estimate the reliability of COSMOS measurements. Plots for $\Delta\theta(B_J, s)$ and $\Delta e(B_J, s)$ are given in figure 3.3.

- the magnitude errors become significant above $B_J \sim 18.5$ and can be modelled by $\Delta B_J \simeq 0.1(B_J - 18.5)$. This agrees well with an analysis by MacGillivray & Stobie (1985).

3.1.2 Partial Lensing

With an established number count-redshift relation (equation 3.1) we can try to derive the probability of *partial* lensing (illustrated in figures 2.1b and 3.4b). If only half a galaxy were lensed in this fashion the magnitude difference with its partner would be $\Delta B_J \sim 2.5 \log_{10} 2 \simeq 0.75$. This is of the order of the matching tolerance we have allowed for calibration errors for the faintest objects (above). Since our method for extracting lensed pair candidates relies heavily on corresponding images having similar magnitudes the degree of partial lensing may be an important consideration.

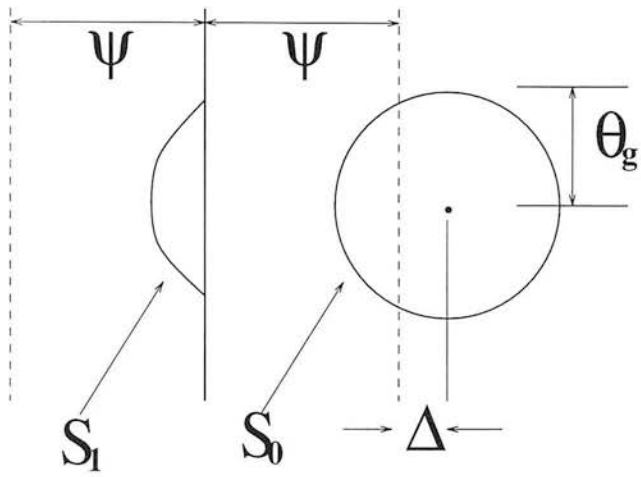

Figure 3.4: (b) Simulating the effects of partial lensing. The central bold line denotes the locus of the string, the vertical dashed lines are the limits of the lensing region. Δ is the offset of the centre of the background galaxy from the edge of the lensing region (with negative values denoting a centre within the region i.e. $\leq \psi$ from the string). The galaxy has an angular diameter of $\sim \theta_{\rm g}$ and a total flux of S_0. The partially lensed image formed to the left of the string has a flux $S_1 = S_1(S_0, \theta_{\rm g}, \Delta)$ with $S_1 \leq S_0$.

We can attempt a crude estimate of the frequency of such events by comparing the angular size $\theta_{\rm g}(z_{\rm g})$ of a galaxy at redshift $z_{\rm g}$ with the string lensing angle ($\psi(z_{\rm s}, z_{\rm g})$ of equation 2.2). We will assume to start with that the galaxies are uniformly bright discs of size $\sim \theta_{\rm g}$. The probability of such a galaxy being cut by the extreme edge of the lensing region, given that it is lensed at all, is then roughly

$$\begin{aligned} p_{\rm cut} &\simeq \theta_{\rm g}/\psi \quad (\theta_{\rm g} \leq \psi) \\ p_{\rm cut} &= 1 \quad (\theta_{\rm g} > \psi) \end{aligned}$$

and the chance of an average lensed galaxy being so affected is obtained by integration over the redshift distribution

$$\overline{p}_{\rm cut}(z_{\rm s}) \simeq \int_{z_s}^{\infty} p_{\rm cut}(z_{\rm s}, z_{\rm g}) \frac{dN}{dz_{\rm g}} dz_{\rm g}. \tag{3.4}$$

This function is dependent on the string redshift $z_{\rm s}$ and the assumed galaxy radius $r_{\rm g}$ as

$$\theta_{\rm g} = \frac{r_{\rm g}(1+z_{\rm g})}{R_0 S_k(r)} I_{\rm p}(z_{\rm g}). \tag{3.5}$$

Where $I_p(z)$ allows for the fact that we generally measure isophotal angular size rather than metric size. Surface brightness decreases as $(1+z)^{-4}$ so here $I_p(z) \simeq (1+z)^{-2}$. In figure 3.4(a) are plotted the $\overline{p}_{cut}$ values for $z_s = 0 - 0.2$ when $r_g = 5$ kpc. The redshift distribution is characteristic of a limiting magnitude $B_J = 21.5$.

Clearly, from figure 3.4a there are a significant portion of partially lensed pairs even for nearby strings with large lensing angles. A more refined treatment of the problem is required as real galaxies do *not* have uniform well-bounded brightness profiles. Figure 3.4a just gives the proportion of galaxies falling near enough to the lensing-region edge to be significantly affected. We will need to adapt our candidate selection criteria in two ways: (i) find an optimum ΔB_J that we allow between pairs so that we include as many partially lensed pairs as possible without arbitrarily increasing the background of accidental close pairs too much, and (ii) adapt the formula 3.3 converting ellipticity to inferred separation to allow for this effect.

The starting point for both issues is to simulate the effect numerically – a schematic diagram showing the important parameters is given in figure 3.4b. We will assume that the galaxy profile is given by $I(\theta)d\Omega = e^{-\theta/\theta_g}d\Omega$ where θ_g is given by 3.5, θ is the angle from the galaxy centre and $d\Omega$ is an element of solid angle on the sky. If the total flux from the galaxy is S_0 and the flux from the partially lensed image is S_1 then S_1/S_0 is a function of θ_g and the offset of the galaxy centre from the edge of the lensing region (an angle ψ away from the string) denoted by Δ. Δ can be negative or positive depending on whether the galaxy centre is within or without the lensing region.

The function S_1/S_0 can be found easily by numerical integration on a 2D grid. Figure 3.4c shows S_1/S_0 as a function of Δ for a range of galactic angular sizes. As $\Delta \to \infty$ the ratio goes to zero as progressively less and less of the galaxy is lensed at all, whereas for $\Delta \to -\infty$ virtually all of the galaxy is lensed and $S_1/S_0 \to 1$ – this is slightly artificial as Δ cannot fall below $-\psi$. All curves pass through $S_1/S_0 = 0.5$ at $\Delta = 0$ as this is the point where exactly half the galaxy is lensed, irrespective of its size. Empirically the shape of each curve is well fit by

$$\frac{S_1}{S_0} \simeq \frac{1}{2}\left[1 - \tanh\left(\frac{\Delta}{f(\theta_g)}\right)\right] \tag{3.6}$$

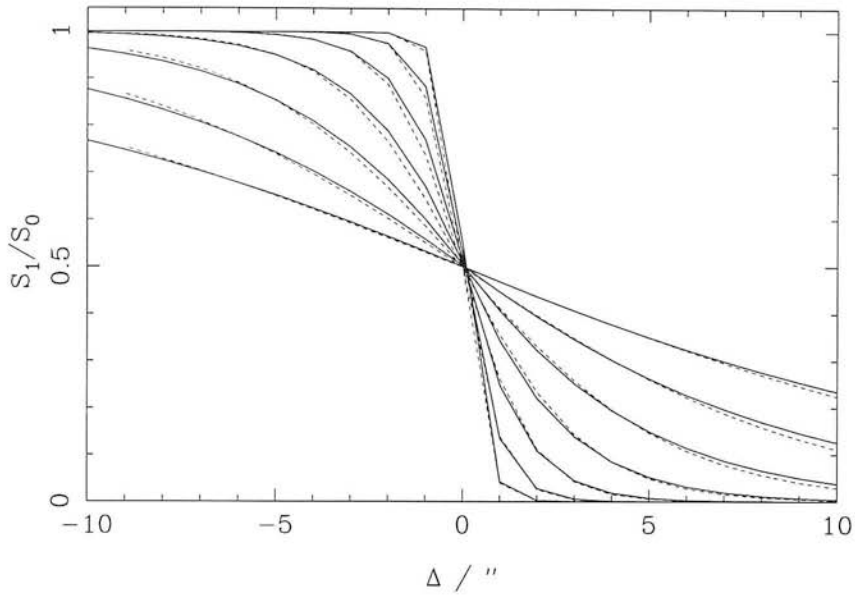

Figure 3.4: (c) The function $S_1/S_0\,(\Delta)$ for a range of galactic angular sizes. Shown are the curves for $\theta_g = 0.3''$ (the shallowest curve), $0.6''$, $1.0''$, $1.8''$, $3.2''$, $5.6''$ and $10.0''$ (solid lines). The dashed lines show the fit provided by equations 3.6 and 3.7.

with

$$f(\theta_g) \simeq 0.1 + 1.8\theta_g - 0.0023\theta_g^2. \tag{3.7}$$

The magnitude difference between the two images is $\Delta B_J = 2.5\log_{10}(S_0/S_1)$. Given a threshold for the allowed magnitude difference between images in a pair ΔB_{Jmax}, equation 3.6 can be inverted to find the maximum value of Δ that would give images within this tolerance, i.e.

$$\Delta_{max} = f(\theta_g)\,\mathrm{arctanh}(1 - 2\times 10^{-0.4\Delta B_{Jmax}}) \tag{3.8}$$

The effective size of the lensing region for this maximum ΔB_J is therefore $\propto \psi + \Delta_{max}$. Values of ΔB_{Jmax} which give $\Delta_{max} > 0$ allow the inclusion of galaxies with centres outside the lensing zone and hence includes more lensed pairs for a given background density. Clearly the converse applies for $\Delta_{max} < 0$. Increasing ΔB_{Jmax} yields to competing effects – the lensing zone is effectively widened allowing more genuinely lensed pairs to be detected – however this widening also allows more chance pairs from the background to be included. What is needed is an estimate of the ΔB_{Jmax} value which optimizes the

pair selection and gives the highest ratio of string lensed pairs to background or "noise" pairs.

The first stage is to find the overall effect of varying $\Delta B_{\rm Jmax}$ on a string at $z_{\rm s}$ lying in front of galaxies with area density per unit redshift $d^2N_{\rm g}/dz_{\rm g}dA$. The effective width of the lensing zone, $\psi + \Delta_{\rm max}$ is a function of $z_{\rm s}$, $z_{\rm g}$ and $\Delta B_{\rm Jmax}$. The number of detectable lensed pairs generated by the string, $N_{\rm s}$, over a length on the sky L will then be given by

$$N_{\rm s}(z_{\rm s}, \Delta B_{\rm Jmax}) = \int_{z_s}^{\infty} W_{\rm eff}\, L\, \frac{d^2N_{\rm g}}{dz_{\rm g}dA}\, dz_{\rm g} \tag{3.9}$$

where the effective width function $W_{\rm eff}$ is defined as

$$\begin{aligned} W_{\rm eff} = \quad & 2[\,\psi(z_{\rm s}, z_{\rm g}) + \Delta_{\rm max}(z_{\rm g}, \Delta B_{\rm Jmax})\,] \quad && (\psi + \Delta_{\rm max} > 4'') \\ W_{\rm eff} = \quad & 0 && (\psi + \Delta_{\rm max} \leq 4'') \end{aligned}$$

and serves to remove the contribution of galaxies which are lensed by less than $4''$ and are consequently not deblended into pairs (see page 63). The factor of 2 arises because a lensing region of $\psi + \Delta_{\rm max}$ is present on either side of the string.

The strings will be *found* by placing a strip on the sky and looking for the pairs within it (see figure 2.1c for the appearance of a strip containing all the lensed pair centroids). We can set the length of strip by requiring at least some number $N_{\rm min}$ of lensed objects to fall within it. Later on we will set this number to be $N_{\rm min} = 6$, hence using that value here gives $L = 6/N_{\rm s}(1\,{\rm deg})$. The width of the strip is $\sim \sigma_y(L) + \theta_{\rm max}$ where $\sigma_y \simeq 0.2L$ is the strip widening factor allowing for string microstructure (equation 2.17) illustrated in figure 2.5.

The number of background chance pairs which act as "noise" within such a strip is given by

$$N_{\rm b} \simeq \frac{dN_{\rm p}}{dA}\,(\sigma_y(L) + \theta_{\rm max})\,L. \tag{3.10}$$

$dN_{\rm p}/dA\,(\Delta B_{\rm Jmax}, \theta_{\rm max})$ is the observed area density of pairs closer than $\theta_{\rm max}$, i.e. $\sim 10''$ (equations 1.50 and 1.52), and with magnitude differences less than $\Delta B_{\rm Jmax}$ on a

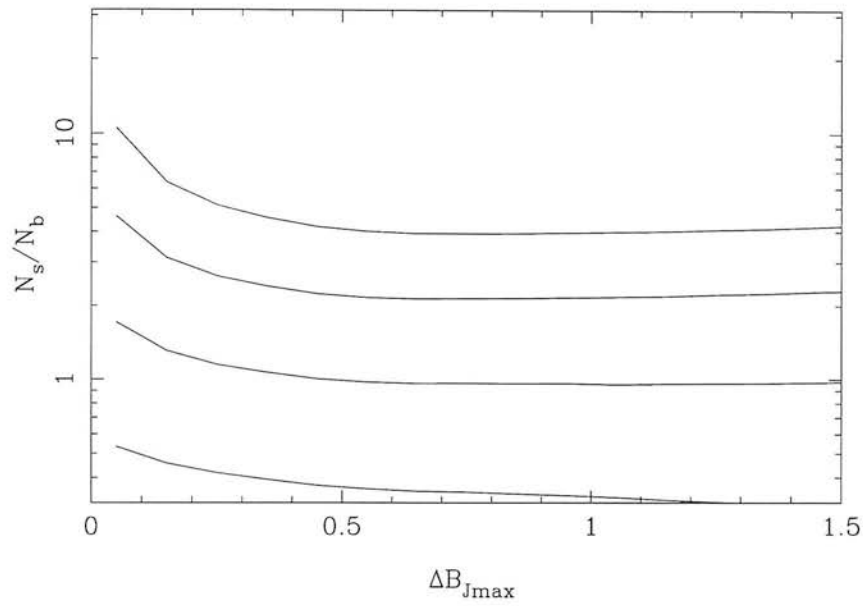

Figure 3.4: (d) Signal-to-noise as the ratio N_s/N_b for Schmidt plate pairs as a function of the magnitude-difference threshold $\Delta B_{\rm Jmax}$. The separate curves correspond to strings at different redshifts, moving downwards $z_s = 0.025, 0.050, 0.075, 0.100$.

stringless sky. Given that we define the length in terms of N_s and $N_{\rm min}$ we can write the expression for the signal-to-noise as

$$\frac{N_s}{N_b} \simeq \frac{N_s^2(1\,\deg)}{0.2N_b(1\,\deg)N_{\rm min}} \tag{3.11}$$

for $\sigma_y \gg 10''$. This formula will be useful later for comparing the signal-to-noise obtainable with deeper catalogues.

Choosing the optimum value of $\Delta B_{\rm Jmax}$ is therefore a matter of obtaining the maximum possible value of the ratio $N_s/N_b\,(z_s, \Delta B_{\rm Jmax})$ (in effect the signal-to-noise) consistent with allowing the magnitude scatter discussed on page 66. Figure 3.4d shows this using $r_g = 5\,{\rm kpc}$, $\theta_{\rm max} = 10''$, $L = 1^\circ$ and typical Schmidt plate forms for $d^2N_g/dz_g dA$ and dN_p/dA.

It is apparent from the figure that the signal-to-noise (i.e. true lensed pairs to chance close pairs) is a weak function of $\Delta B_{\rm Jmax}$ with a maximum at $\Delta B_{\rm Jmax} = 0$ and an almost constant value beyond $\Delta B_{\rm Jmax} = 0.5$. The best approach therefore will be to adopt the minimum magnitude-difference threshold consistent with the maximum scatter expected in estimating faint magnitudes i.e. $\Delta B_{\rm Jmax} = 0.6$ for a limiting magnitude of 21.5. It is

interesting that this analytical approach gives a signal-to-noise value which falls below unity when $z_s \gtrsim 0.075$ – this is roughly the maximum depth to which the search method proves effective when tested on simulated data (chapter 4).

Choosing a low value for $\Delta B_{\rm Jmax}$ also implies that the intensities of each object in a candidate pair will be quite similar. In fact, simulations with *PISA* suggest that in the range $S_1/S_0 = 0.5 - 1.0$ the mean measured ellipticity for a given separation varies by $\lesssim 10\%$. Choosing $\Delta B_{\rm Jmax} = 0.6$ means that $\overline{\Delta B_{\rm J}} \simeq 0.15$ for pairs lensed by a string at $z_s = 0.05$. Thus we will be justified in continuing to use equation 3.3.

3.1.3 Extracting Candidate Pairs from the Data

Having established the likely image analysis response to string lensed galaxies we now turn to the issue of extracting real close pairs from COSMOS data. Standard COSMOS image analysis files contain all the information we need, the X and Y coordinates of each image on a given plate, its magnitude, its RA and DEC, its ellipticity and orientation. Star/Galaxy discrimination methods are reliable for $B_{\rm J} \lesssim 20$ (MacGillivray & Stobie 1985).

The first step in our search programme is to reduce such files by cataloguing all the images that *could* be string lensing events, i.e. close pairs of galaxies or single high ellipticity objects. However care needs to be taken as diffraction spikes and haloes around bright stars, satellite trails and bright, nearby galaxies appear on nearly all the plates. The COSMOS image analyser often treats these features as if they were rows or clusters of objects (figure 3.5). We have to remove such objects lest they contaminate our subsequent analysis. Fortunately this is relatively straightforward. Bright stars only appear to have significant diffraction spikes when their images occupy $N_{\rm pix} \geq 250$ pixels. Each time such an image is found a sufficiently large square area of width $\sim 5\sqrt{N_{\rm pix}}$ pixels is completely removed from the dataset. This is found to be the minimum size consistent with removing all the spurious diffraction spike data. Satellite trails are found to contain very high ellipticity ($e > 0.7$) images which do not appear elsewhere in the dataset. The exclusion of small areas ($\simeq 50$ pixels square) around such images generally removes most of the contamination due to trails. In the case of bright galaxies COSMOS

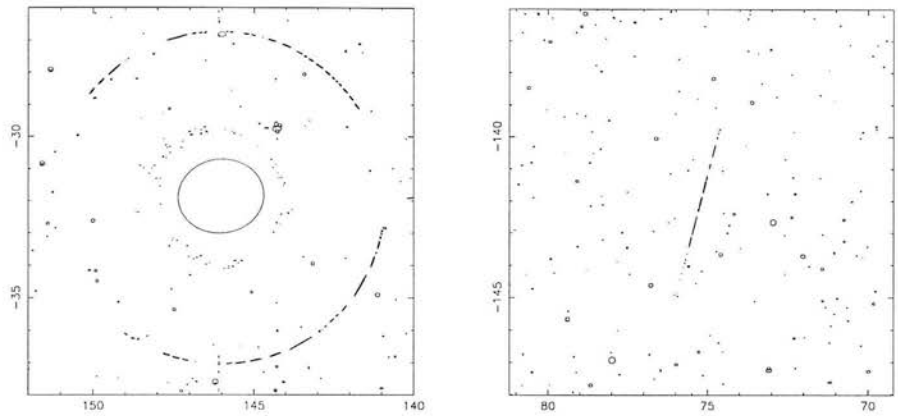

Figure 3.5: Cosmos image-analysis output for (a) a bright star (b) a satellite trail. In both cases the image analyser artificially breaks up the halo or trail into a curve of highly elliptical images. Such spurious objects need to be removed from the catalogue in case they interfere with image selection when searching for strings.

is quite effective at labelling fragmented objects at the edge as spurious. Typically this pre-processing removes about $\sim 2\%$ of the data from each file and so does not impair our area coverage significantly.

Having cleared the data of contamination we can perform a straightforward search for close pairs, recording the parameters of galaxies which lie within $10''$ of each other and any objects of significant ellipticity. Nearly all the objects in the catalogue are elliptical to some degree. We need a means of discriminating further to reduce the data to a manageable size. This is dealt with in the next section.

Because COSMOS star/galaxy discrimination becomes unreliable at faint magnitudes (i.e. $B_J \geq 20$) we also need to include all the *unclassified* images which form close pairs or are elliptical. However, we can use some of the information from section 3.3 to reject some of these pairs/ellipses:-

- We roughly know the separation at which deblending becomes unreliable to be $\simeq 4''$ therefore we will not trust images separated by $\leq 3''$ or so. By the same token objects separated by $\geq 6''$ should be very effectively deblended so images with $e \geq 0.6$ are almost certainly single objects and not merged pairs.

- Close pairs should have magnitudes differing by less than 0.6.
- Well separated elliptical objects that form pairs should have similar ellipticities and orientations within the allowable errors of section 3.3.

3.2 Likelihood Analysis

Although we can remove some of the more spurious images we are still left with a large quantity of data. Typically $\sim 10^2$ pairs and $\sim 10^4$ elliptical images per field remain by this stage. Clearly it would be useful to have a weighting scheme to assess the significance of these remaining data – i.e. a means of concentrating the search on the objects that are most likely to be string-lensed galaxies. We know how galaxies are distributed in space and have modelled how they would appear when lensed so it is possible to tackle the problem via probability arguments.

To this end we construct an expression for the *likelihood* $\mathcal{L}$ of a given image to be the result of string lensing. This will be influenced by our expectations for the redshift distributions of the galaxies and the strings. Our likelihood function will be chosen to represent the probability of lensing of a galaxy of apparent magnitude m by an angle θ as these are the parameters available for the image pairs in the data. That is we wish to estimate

$$\mathcal{L} = \frac{d^2N}{dm\,d\theta} \tag{3.12}$$

which, restated in terms of known functions, is

$$\mathcal{L} = \frac{d^2N}{dm\,dV}\frac{dV}{dz}\frac{dz}{d\theta} = \Phi(m)\frac{dV}{dz}\frac{dz}{d\theta} \tag{3.13}$$

Now, $\Phi(m)$ relates to the luminosity function for the galaxies on the Schmidt plates, i.e. the number density of galaxies with luminosities between L and $L + dL$. The function Φ is usually cast in luminosity dependent terms as a *Schechter function* such that

$$\Phi(L)dL = \Phi_* \left(\frac{L}{L_*}\right)^{-\alpha} \exp\left(\frac{L}{L_*}\right)\frac{dL}{L_*} \tag{3.14}$$

with parameters $\alpha \simeq 1$ and $\Phi_* \simeq 0.014h^3\,\mathrm{Mpc}^{-3}$ from Loveday et al. (1992). We convert this into a magnitude dependent form as

$$\Phi(M)dM \simeq 0.013e^{-x}dM\,h^3\,\mathrm{Mpc}^{-3} \tag{3.15}$$

with $x = (L/L_*) = 10^{-0.4(M-M_*)}$ and M_* is found to be $-19.68 - 5\log_{10}h$ in the B_J band. We can convert between apparent and absolute magnitudes using

$$M = m - 5\log_{10}\left(\frac{(1+z)R_0S_k(r)}{10\mathrm{pc}}\right) - K(z) \tag{3.16}$$

with a K-correction factor which we will take to be $K(z) \simeq 3z$ (after Shanks 1990). Finally by calculating dV/dz we can obtain the galaxy distribution in terms of z and m as

$$\frac{d^2N}{dm\,dz} = \phi(m)\frac{dV}{dz} = \phi(m)\frac{3000h^{-1}[R_0S_k(r)]^2}{(1+z)\sqrt{1+\Omega z}} \tag{3.17}$$

It ought to be stressed that this is a simple no-evolution model, Φ_* and M_* have no z-dependence, but it agrees well with observed counts and Schmidt-plate galaxy redshift distributions (e.g. equation 3.1).

From equation 2.2 we find the redshift z of any galaxy lensed by an angle θ by a string at redshift z_s.

$$1 + z = \left(\frac{8\pi G\mu - \theta}{\theta_\mathrm{max} - \theta}\right)^2 \tag{3.18}$$

and derive the factor $dz/d\theta$ that we need to convert equation 3.17 into our likelihood of equation 3.12,

$$\frac{dz}{d\theta} = 2\frac{8\pi G\mu - \theta}{(\theta_\mathrm{max} - \theta)^3}(8\pi G\mu - \theta_\mathrm{max}) \tag{3.19}$$

with $\theta_\mathrm{max} = 8\pi G\mu/\sqrt{1+z_\mathrm{s}}$. Note this ignores the velocity dependent factors in (2.1) in accord with the discussion on page 39.

Given a string redshift z_s we then calculate the probability of a galaxy of magnitude m being lensed by an angle θ. This is our likelihood as a function of string redshift

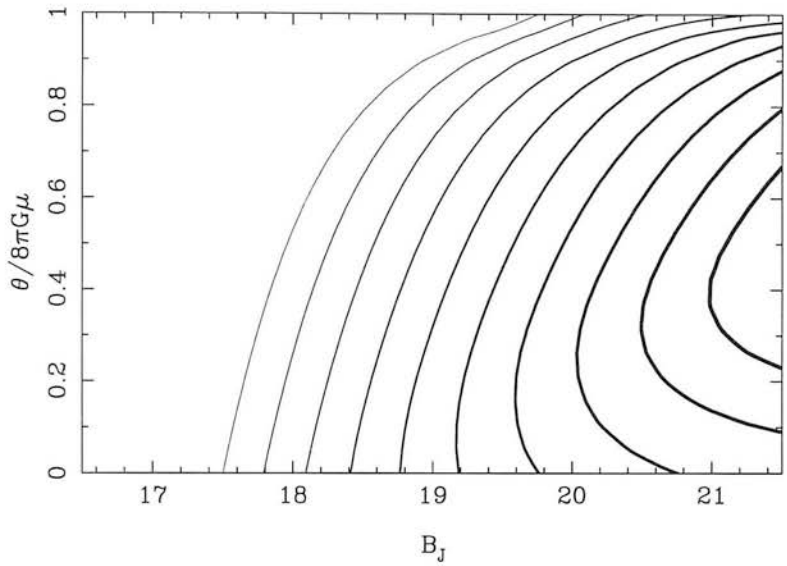

Figure 3.6: Contours of likelihood over the (θ, m) plane for pairs resulting from string lensing. Thicker lines denote higher contours and intervals are at $\Delta \ln \mathcal{L} = 0.5$. The highest contour is at $\sim 100 N_{\rm s}$ per magnitude per arcsecond per steradian where $N_{\rm s}$ is the number of strings per horizon volume. These values can be viewed as the number of string generated pairs expected in a given magnitude and separation range for surveys of limiting magnitude $B_{\rm J} \sim 21.5$.

$\mathcal{L}(m, \theta, z_{\rm s})$. We know from equation 2.21 that the angular length of string on the sky varies as $d\alpha/dz_{\rm s} \propto z_{\rm s}$ so we can integrate $\mathcal{L}$ over all possible string redshifts ($0 \rightarrow \infty$, remembering there is no lensing where $z_{\rm s} > z_{\rm g}$) to obtain a probability that any given pair is due to lensing, $\mathcal{L}(m, \theta)$ to compare with our data. A contour plot of this function is given in figure 3.6.

We will need to compare this with the distribution for all the close pairs and ellipses in the data. Even if strings are present we only expect a small fraction of the images present to truly be lensing events. The rest just *appear* to be lensed due to intrinsic ellipticity or the chance pairing of similar though distinct galaxies. It therefore makes sense to downweight $\mathcal{L}$ by a factor which takes into account the number density of all the objects used in the search as a function of m and inferred θ. We will denote this function by $\mathcal{L}_B$ as the "background" equivalent of equation 3.12. We will weight each object by a *likelihood ratio* defined as $p(m, \theta) = \mathcal{L}(m, \theta)/\mathcal{L}_{\rm B}(m, \theta)$ which then gives the relative probability that a given image is due to lensing. $\mathcal{L}_{\rm B}(m, \theta)$ is simply estimated from COSMOS data for 10 Schmidt plates. Plots of $\mathcal{L}_{\rm B}$ for ellipses and pairs, and the likelihood ratio in each case are given in figures 3.7 and 3.8.

With this function calculated we can reject some objects that have a very low likelihood of being due to lensing. This can be achieved by setting a threshold $p_{\rm lim}$ and rejecting objects with $p < p_{\rm lim}$. The optimum value will be set by subjecting simulated data to the technique, and picking the $p_{\rm lim}$ which gives our search the greatest depth.

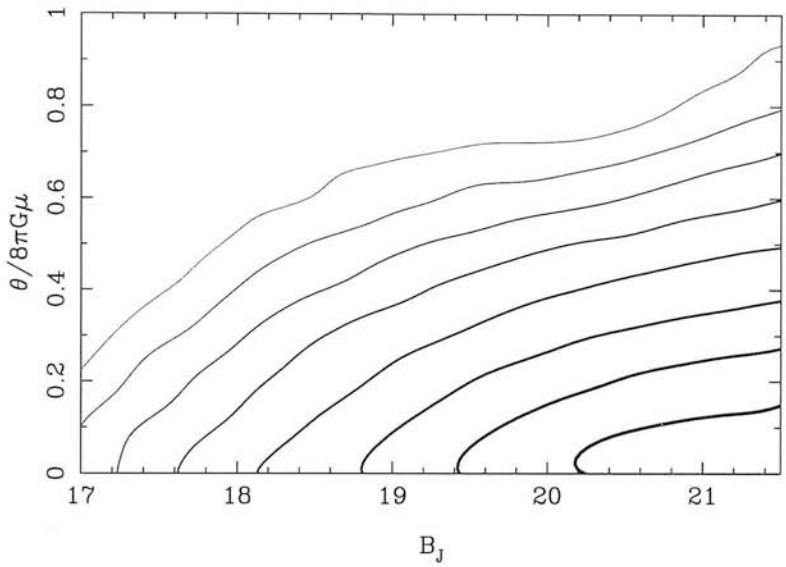

Figure 3.7: (a) Contours of likelihood over the (θ, m) plane for ellipses in the dataset. Thicker lines denote higher contours and intervals are at $\Delta\mathcal{L}_{\rm B} = 0.5$. The highest contour is at $\sim 400,000$ per magnitude per arcsecond per steradian. The plot represents the area density of elliptical images found per magnitude per inferred arcsecond separation for surveys of limiting magnitude $B_{\rm J} \sim 21.5$.

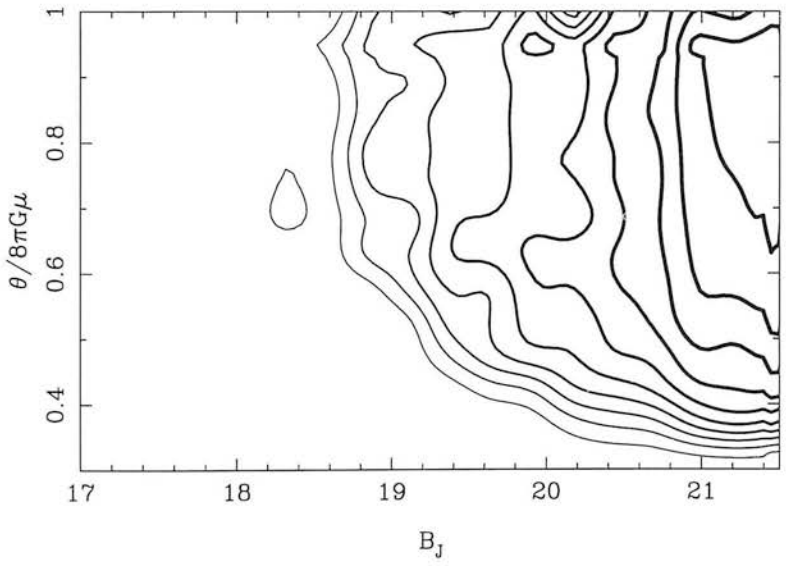

Figure 3.7: (b) Contours of likelihood over the (θ, m) plane for pairs in the dataset. Thicker lines denote higher contours and intervals are at $\Delta \ln \mathcal{L}_{\rm B} = 0.5$. The highest contour is at ~ 6000 per magnitude per arcsecond per steradian. The plot represents the area density of pairs found per magnitude per arcsecond separation for surveys of limiting magnitude $B_{\rm J} \sim 21.5$.

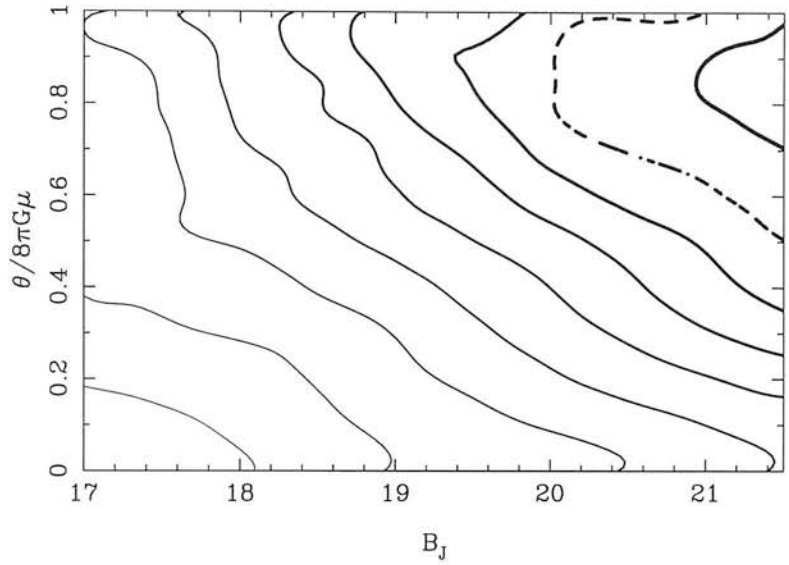

Figure 3.8: (a) Likelihood ratio contours $p = \mathcal{L}/\mathcal{L}_{\rm B}$ used in the weighting of *ellipsoidal* candidates. Intervals are at $\Delta p = 0.5$ with the thicker lines denoting higher regions. As can be seen, faint high ellipticity objects are most favoured by this scheme. The highest contour (thickest line) is at $p \sim 3 \times 10^{-3}$.

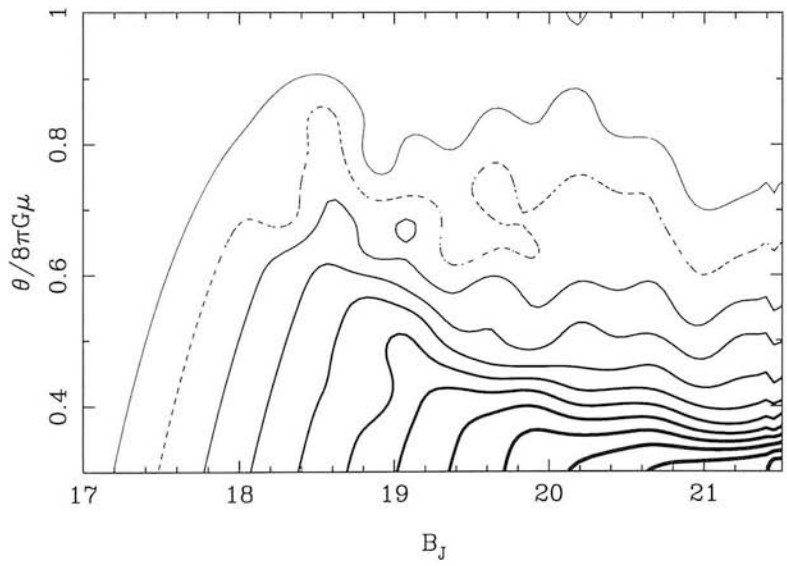

Figure 3.8: (b) Likelihood ratio contours $p = \mathcal{L}/\mathcal{L}_{\rm B}$ used in the weighting of *deblended pair* candidates. Intervals are at $\Delta p = 0.5$ with the thicker lines denoting higher regions. As can be seen, faint low separation images are most favoured here. The highest contour (thickest line) is at $p \sim 0.6$. Note the contour lines cannot be directly compared between (a) and (b) as pairs are, on average, ~ 100 times rarer than ellipses. The dashed lines are equivalent likelihood ratio contours. Close pairs of separations $\lesssim 4''$ do not feature in the dataset, the contours below $\theta \simeq 0.4 \times 8\pi G\mu$ are an artefact of the contouring process.

Chapter 4

Searching for Cosmic Strings

4.1 Searching for Strings

4.1.1 The Search Algorithm

Now that we have produced a catalogue of all the possible lensed objects over our search area we can turn to investigating their spatial distribution on the sky. Recall that the key signature of lensing due to a horizon-spanning string is a *line* of lensed pairs. The analysis presented in chapter 2 shows that the orientation of the pairs is non-random for short enough string segments, i.e. to some extent we should also expect the pairs to be *aligned*. This section will discuss the operation of a string search algorithm which takes the 'reduced' file of candidate pairs and attempts to extract those regions with the most stringlike properties.

Firstly, as we are going to consider aligned objects, it makes sense to bin the data according to orientation. We will consider the objects in one bin at a time when we look for non-random correlations between the object positions. The bin size $\theta_{\rm B}$ depends on the length x of string we expect to detect through the predicted scatter $\sigma_\theta(x)$ in equation 2.16. As noted in section 3.1.1 the estimate of the orientation of a given object also has an error $\Delta\theta(B_{\rm J}, s)$. As a result we may need to place the same object in several neighbouring bins if $\Delta\theta$ is $\geq \theta_{\rm B}$ – that is if the error is too big to determine exactly

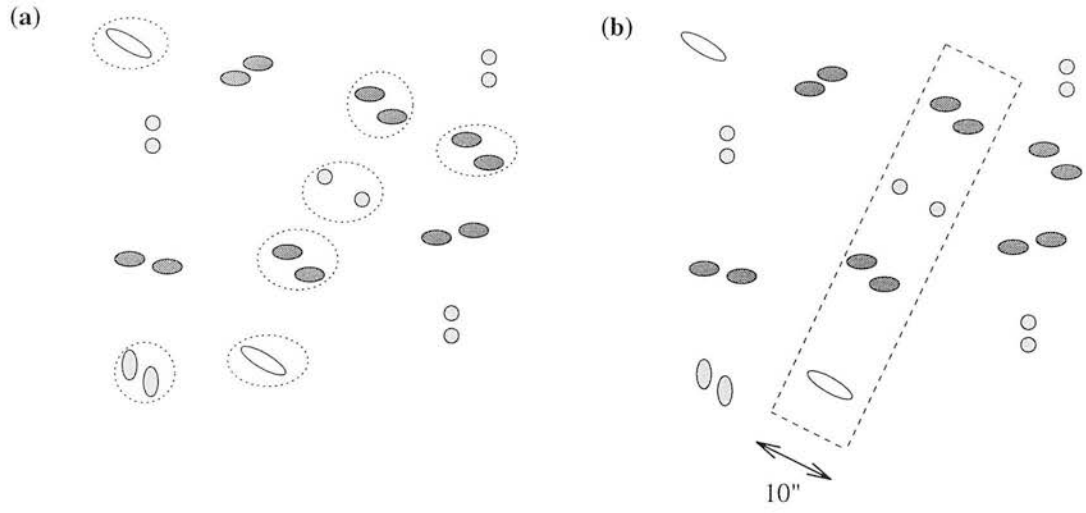

Figure 4.1: The basic search method once all close pairs and ellipses have been catalogued. In (a) the pairs/ellipses of similar orientation are identified. (b) Those objects in the same orientational bin which occupy strips of width $10''$ at a density greater than average are extracted as string candidates. The diagram takes no account of the widening of strips due to string curvature. Also ignored here is the fact that the strip and pairs/ellipses need not be co-directional in the case of shear (equation 2.6).

which bin it should occupy. In the resulting file of binned data, close pairs and elliptical images are treated on an equal footing.

We have now reached the crucial phase of analysing our potential lensing events for a stringlike distribution. The basic philosophy will be to extract pairs/ellipses of the same orientational bin which lie within a $10''$ strip on the sky. String candidates will be identified when objects occupy a given strip at a significantly greater density than average. The strip will not be assumed to be co-directional with the orientation of the pairs within it, to allow for velocity-shear (equation 2.6). We can also allow the strip to be widened beyond $10''$ to allow for string curvature (section 2.2), though with a corresponding increase in the "noise" due to random pairings. Figure 4.1 illustrates the basic method of grouping objects into strips.

In computational terms the strips of aligned images are obtained as follows

1. Select an object o_1 from the current observational bin.

2. Search through the rest of the data until an object o_2 is found, of like orientation

and less than $L_{\max}$ away.

3. Define a $W = 10''$ wide, $2L_{\max}$ long strip centred on o_1 and in the direction of $o_2 \rightarrow o_1$.

4. Find all the objects in this bin lying within the strip. If the number of objects exceeds $N_{\min}$ then record the $N_{\min}$ closest images within it and the length $L_{\text{cand}} < L_{\max}$ enclosing them. This means $L_{\text{cand}} = L_{\text{cand}}(N_{\min})$.

5. Return to step (2) until the given bin is exhausted.

6. Return to step (1) until the given bin is exhausted.

7. Work through all the orientational bins – then sort the total output for that field by L_{cand} to obtain the shortest strips.

This process thus yields the strips with the highest density of candidate lensed objects. In this we are assuming that the string will produce a notably higher density of co-directional images than are present in the background data. As the number of string lensed pairs on the plate decreases as a function of string redshift z_s there comes a point at which this assumption is no longer reliable. This criterion defines the depth limit z_{lim} of the search technique. The value of this limit will be set by running the programme on simulated data, described in the next section.

As described above the programme has some unfixed parameters, namely $L_{\max}$ (the maximum strip length to which the algorithm is sensitive) and $N_{\min}$ (the least number of candidate lensed objects allowed per strip). $L_{\max}$ can be set by demanding at least a *few* candidate strips to be output for each field. Initially $L_{\max}$ can be set to a small value which is then increased should *no* candidates be output. This is preferable to starting with $L_{\max} \rightarrow \infty$ which although guaranteed to yield the correct answer after sorting requires too much in terms of CPU time and pre-sort storage. $L_{\max}$ therefore becomes a function of $N_{\min}$.

Setting $N_{\min}$ is tricky. As our problem is essentially one of extracting the string-signal from a background of noise it would seem natural to require $N_{\min}$ to be as large as possible. In any orientational bin, a background of randomly positioned phoney

lensing events of density ρ_b, would contribute $\rho_b WL \pm (\rho_b WL)^{1/2}$ objects to a strip of dimensions W and L. Thus Poisson noise in the background will allow *some* regions to occupy strips at the required density and so be catalogued. Clearly the significance of this is minimized by making $\rho_b WL$ as great as possible, which given the previous considerations would suggest choosing the largest $N_{\min}$ possible – of order the largest number of true lensed objects there could be on the plate. The problems here are that at high string redshift the number of lensed objects on the plate is not very large (of order 10 for $z_s = 0.1$). Secondly the expected lack of straightness for strings (section 2.2) means that we must *widen* the strip as we move away from the centre (the position of object o_1) to allow for the uncertainty in the string locus caused by string microstructure (chapter 2). We model the width required via expression (2.17) such that

$$\sigma_y \simeq 0.2x \tag{4.1}$$

we must allow the strip to widen *perpendicular* to $o_2 \rightarrow o_1$ such that

$$W(x) = 10'' + 0.2x. \tag{4.2}$$

where x is the distance in arcseconds *parallel* to $o_2 \rightarrow o_1$. Therefore increasing the length L soon causes the area covered by the strip to behave as $\sim L^2$. Eventually the noise will become *more* significant than the string signal for very long strips. Optimizing $N_{\min}$ is not straightforward therefore. The best guess will be selected by simulation in the next section, picking a value that gives the largest $z_{\lim}$.

4.1.2 Testing the Search Algorithm

Before we undertake in earnest to search for strings it is vital to test our algorithm on simulated data. This will allow us to estimate the string redshift z_s out to which detection is viable with the Schmidt data. We also have some adjustable parameters in the search algorithm (described in the previous section) which we must optimize.

We have already dealt with much of the analysis relating to the appearance of string lensed galaxies on a plate. To summarize briefly we have looked into

- the curvature and small-scale wiggle of strings
- the appearance of lensed galaxies on a plate following COSMOS digitisation and image analysis
- the distribution of magnitudes and image separations of string lensed galaxies

Given this knowledge it is relatively straightforward to add data for simulated string lensed pairs to an image analysis file. Firstly we choose our string redshift z_s and a string locus, crossing one of our 5° Schmidt fields. We require the locus to represent the wiggly strings discussed in chapter 2 and so the string is allowed to deviate by upto $\sigma_y(5^\circ) \simeq 1^\circ$ (equation 2.17) as it crosses the plate, perpendicular to the line joining its start and end points. This is equivalent to choosing the string to be an arc with a radius of curvature in the range 15° (maximum deviation) to ∞ (no deviation).

Now, each time we find a galaxy of magnitude m in the dataset which lies within $\theta_s < 10''$ of our string locus, we sample a redshift z from the distribution in expression 3.1 and calculate a lensing angle ψ via equation 2.2. Now if $z > z_s$ and $\psi < \theta_s$ we have a lensed galaxy and will add a second, companion image to the data.

In deciding how to add the data for the second image in our newly simulated pair we need to refer to the results of section 2.2 and 3.2. If $\psi > 4''$ then the deblender would have been able to separate the pair. Therefore we can simply add an image identical to our original galaxy a distance ψ away and on the opposite side of the string. We want the pair to make an angle θ_o chosen randomly in the range $0 \leq |\theta_o| \leq \sigma_\theta$ to the local tangent to the string locus, thus simulating the wiggle effects studied in section 2.2. If $\psi \leq 4''$ the deblender would have *failed* to separate the paired images and we need to form an ellipse at the midpoint of the two original images. The ellipticity will be given by the inverse of equation 3.3, with a new magnitude of $m' \simeq m - 2.5\log_{10} 2$

Image cutting due to incomplete lensing of a galaxy was discussed in section 3.1.2. The effect can give rise to significant magnitude differences between the images in a pair and needs to be allowed for in the simulation. The offset Δ of any galaxy from the edge of the lensing region can be used to calculate the magnitude difference expected, $\Delta B_J(z_s, z_g, \Delta)$. In the deblended case a lensed image of magnitude $m + \Delta B_J$ is placed

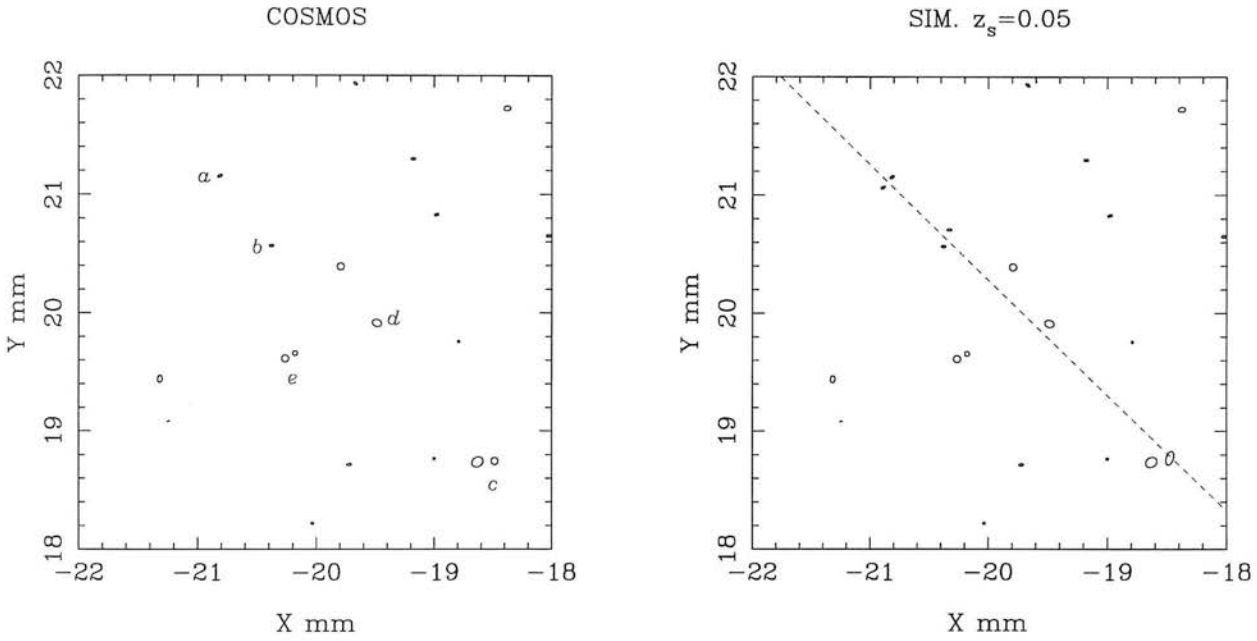

Figure 4.2: The simulation of galaxy lensing by a cosmic string crossing a Schmidt field. Shown on the left is an image analysis plot of a small 4mm × 4mm ($4.5' \times 4.5'$) part of UKST J-field no. 757. To the right is the same area with the data altered to simulate the effect of a cosmic string passing through the field (dashed line). The labelled objects illustrate some of the key considerations of chapters 2 & 3. Object *a* is a faint galaxy behind the string and so is lensed into two identical images either side of the string. *b* is a similar case but here the lensing plane is not exactly parallel to the string locus – this reflects the microstructure or wiggle – analyzed in chapter 2. Object *c* is lensed by only a small angle $\lesssim 4''$ and so the resulting pair is not resolved. The result is an ellipse with its long axis approximately perpendicular to the string locus. Object *d* is either a star or a galaxy with an inferred redshift $z \leq z_s$ and so is not lensed despite its apparent proximity to the string. *e* is a close pair of similar magnitude objects present in the data before the string was added and hence a source of noise in the subsequent analysis. Despite the straight appearance of the string here it in fact is an arc of radius $\sim 15°$ reflecting the anticipated large scale curvature of strings on the sky.

on the opposite side of the string locus, a distance $\psi + \Delta$ from the parent image. In the undeblended case the magnitude of the resulting ellipse is simply changed to $m' \simeq m - 2.5\log_{10} 2 + \Delta B_{\rm J}$. Note that this results in the partial lensing of some objects with centroids outside the lensing region, though typically these will be pairs with $\Delta B_{\rm J} \geq 0.75$ and will not ultimately be included in the list of candidates for the string-searching algorithm.

Proceeding along the length of the string in this fashion we can produce a new image analysis file containing a hidden string which we may then feed into our search algorithm. The fact that we simply add our lensed pairs to existing Schmidt data means that awkward effects such as chance alignments of pairs, plate defects, and so forth, are present in the simulated data and must be dealt with effectively before the algorithm will succeed. Figure 4.2 illustrates some aspects of the simulation process.

We use the simulated data to tune our free parameters $N_{\rm min}$ and $p_{\rm lim}$. To do this we construct a series of plates containing simulated string data. On each plate we hide a long string of with redshift $z_{\rm s}$ in the range $0 - 0.20$. We then allow the search programme to look through the plates using particular values of $p_{\rm lim}$ and $N_{\rm min}$. We define the string as *included* when an output strip of objects contains simulated string data. Clearly any string that manifests itself as a line of $\geq N_{\rm min}$ images with $p > p_{\rm lim}$ will eventually be catalogued by such a method, the issue is to extract it from the large number of other candidate strips generated by background pairs and ellipses. Here we will proceed by *ranking* the candidate strips according to image density, i.e. according to $\rho_{\rm c} = N_{\rm min}/L_{\rm cand}$ where $L_{\rm cand}$ is the length of the strip containing $N_{\rm min}$ images. The best candidates are the densest ones which, with $N_{\rm min}$ fixed, means those with the shortest $L_{\rm cand}$. This scheme works because the image density generated by a string monotonically decreases with $z_{\rm s}$, so the highest members of the ranked list are candidates relating to the nearest strings. The assumption will be that a given strip can be conclusively proved to be string-generated or not by some method (e.g. deep telescope imaging) once it is included in the ranked output list. In reality it will only be possible to test a finite number of candidates in this way. The number of list members which can be tested effectively determines the depth $z_{\rm lim}$ the survey can attain.

The position in the ranked output list which the string candidate occupies gives us a convenient way to compare the effects of varying the search parameters. Clearly the best case is where the simulated string that we added appears at the top of the list. If the string data only appears low down in the list (or is not included) then it will not be followed up by a conclusive test and we are beyond the depth the survey technique can attain. In this way it is possible to estimate $z_{\rm lim}(p_{\rm lim}, N_{\rm min})$ and hence optimize the likelihood ratio threshold defined in the previous section. The definitive test we propose here is to follow up the candidates by deep CCD imaging (see next section) and we estimate that ~ 200 candidates can be followed up in this way in a week of observing time. Thus a string crossing one of ~ 100 fields must be *at worst* the second ranked candidate for the field (on average).

The highest average rank attained by a simulated string crossing a plate is a function of the string redshift $z_{\rm s}$ and the parameters which affect the signal-to-noise, $N_{\rm min}$ and $p_{\rm lim}$. Plots pertaining to this function are given in figures 4.3a & b. Given the follow-up criteria discussed above, we define the string as *found* when the average rank of the true string on a plate is ≤ 2. Two sets of plots are given, the first set uses an angular bin size of $\theta_{\rm B} = 30^\circ$, the second $\theta_{\rm B} = 10^\circ$. 30° is the value required by the microstructure analysis of string simulations in chapter 2. If this is a worst case then a lower $\theta_{\rm B}$ may be allowed, but that can probably not be reduced below about 10° owing to random errors in the COSMOS measurements of position angles for faint objects. It can be seen from the plots that low $N_{\rm min}$ performs almost as well as the higher values and that an maximum detection redshift of $z_{\rm lim} \sim 0.07$ is attainable with $N_{\rm min} = 6$, $\ln p_{\rm lim} \simeq -6.6$ and $\theta_{\rm B} = 30^\circ$ so these values are adopted in what follows. Note that the lower value of $\theta_{\rm B} = 10^\circ$ allows detection at depths of $z_{\rm lim} \simeq 0.10$, i.e. the signal to noise for distant strings is significantly improved as the microstructure or wiggliness is reduced.

4.1.3 Output for UKST Fields

We have examined 100 UK Schmidt fields which represent the area we need to search to have a good chance of finding string out to our maximum detectable redshift of ~ 0.07 (sections 2.3 and 4.1.2). The plates have been chosen in an equatorial band, at $|b| \gtrsim 30^\circ$

thus optimising the chance of detecting a long string, which would roughly approximate a great circle on the sky. The range of sky covered is roughly RA $= 21^h \rightarrow 3^h$ and $\delta = -30^\circ \rightarrow 0$. Parameters for the search algorithm are taken from the optimum detectability case found by simulation (see previous section), i.e. $\ln p_{\rm lim} = -6.6$ and $N_{\rm min} = 6$. The idea is to output ~ 200 candidates from these fields which can then be followed up by deep CCD integration at a > 2m telescope, either (a) detecting a cosmic string or (b) establishing that $z_{\rm s} \gtrsim 0.07$ for the nearest string crossing the search area.

The plates were analysed as for the simulation data and a final list of candidates produced – i.e. the densest 200 strips of $N_{\rm min}$ candidates on the plates. On a DEC workstation this process requires about a day for each 50 plates analysed. It would therefore not be prohibitively expensive (in CPU terms) to analyse the whole southern sky (~ 900 plates) in this fashion.

Despite our careful pruning of the data before analysis the search procedure is found to produce some candidates which can be rejected by eye, typically plate defects and other misclassified objects from image analysis. Until recently the inspection of large numbers of candidates in this way would have been highly time consuming. However, publication of the STScI PDS scans of the UKST plates on CD-ROM has made it feasible to extract small $\sim$arcmin^2 images of large numbers of diverse regions of sky. We have made greyscale images of all our candidates and trimmed the list to those that appear plausible, rejecting all the candidates from a given strip if a single component is found spurious. The candidate strips which survive this stage constitute our final list.

Following up these candidates requires CCD images of the cosmic string candidates down to magnitudes $B_{\rm J} \simeq 24$ & $R \simeq 23$. With such data, it will be quite unambiguous whether a candidate is a true result of lensing or (as must be true in most cases), random noise. String lensing causes no distortion or amplification, so any pairs must be exact replicas, unless the string cuts the edge of a given image. Apart from checking the existing image pairs, a true string will generate extra pairs. At these CCD depths, we should detect $100-200$ galaxies per field with a median redshift $z \sim 0.5$. A cosmic string crossing the CCD field would produce ~ 5 additional lensed galaxy pairs. A comparable $B - R$ for each galaxy in a pair would add further weight to the lensing hypothesis.

A detection of additional "colour-verified" lensing events would give an unambiguous detection of a cosmic string.

Our candidate strips are far longer than could be encompassed by the field of view of a typical CCD chip ($\sim$ 5 arcmin^2). We can only follow up one candidate image per strip per CCD exposure and it makes sense that the highest likelihood candidate should be taken for this purpose. In this way we can form a list of image coordinates for the most promising object in each strip. Such a list is provided below (with coordinates in the J2000 form). The distribution of the candidate strips on the sky is shown in figures 4.4a & b. Figures 4.5a-d show 1 arcmin^2 CD-ROM images of the highest likelihood ratio object in each strip.

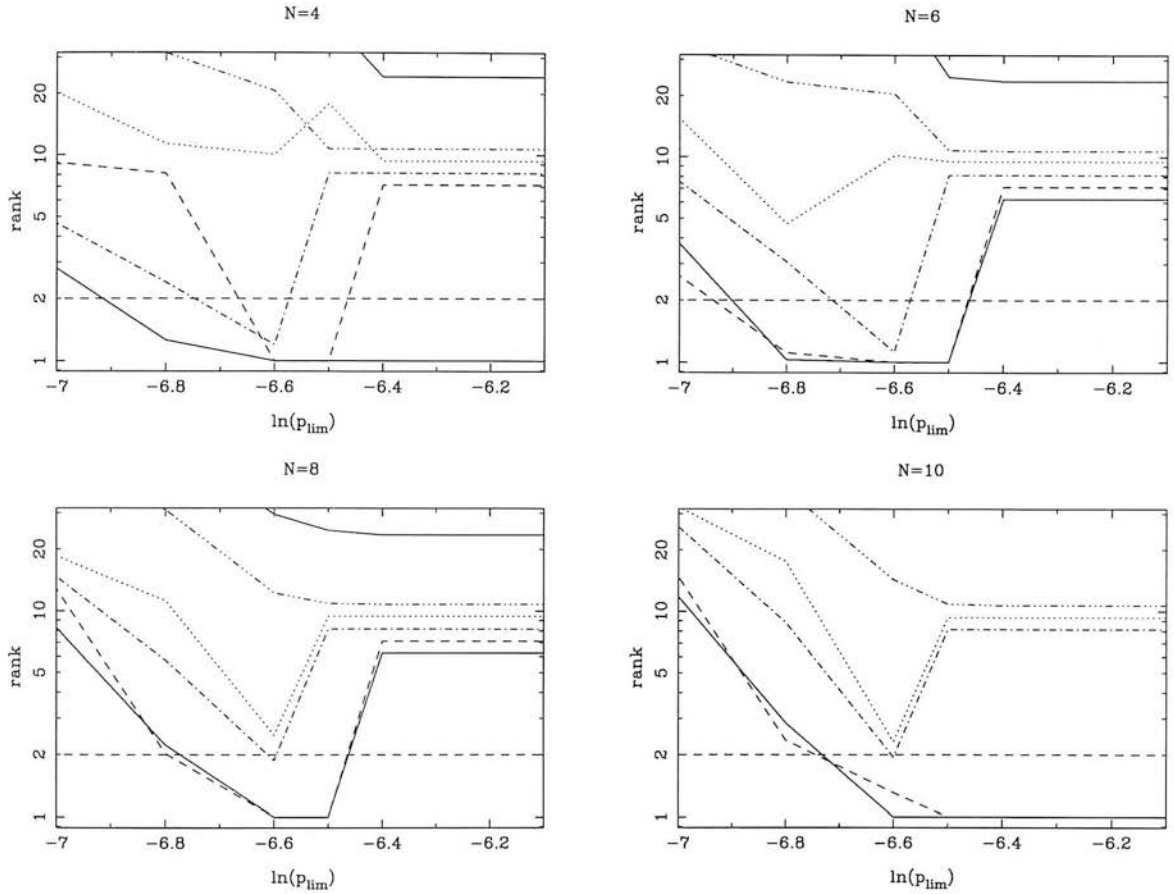

Figure 4.3: (a) The mean ranking for a simulated string candidate as a function of the likelihood ratio threshold $\ln p_{\rm lim}$ applied to the data and the number of candidates required per strip, $N_{\rm min}$. The objects were binned with $\theta_{\rm B} = 30°$ as required by the analysis of section 2.2.2. The string counts as detected if the rank ≤ 2 as the candidate can then be followed up by deep imaging. The various lines are for string redshifts, from the bottom $z_{\rm s} = 0.05, 0.06, 0.07, 0.08, 0.10, 0.12$. The detectability is insensitive to $p_{\rm lim}$ at redshifts $z_{\rm s} \lesssim 0.05$ as the string pairs/ellipses form the densest strips on the sky. Above $z \simeq 0.05$ a low threshold $p_{\rm lim}$ removes a lot of background pairs/ellipses allowing the string to stand out. Note that this can backfire as $\ln p_{\rm lim} \rightarrow 0$ as real lensed pairs are excluded from the data. Above $z \simeq 0.07$ the low thresholds start to exclude string data. Here therefore there is an optimum $p_{\rm lim}$ for detection at around -6.6, i.e. when images having a less than $\sim 0.1\%$ chance of being due to lensing are rejected. Above $z \simeq 0.08$ no value of $p_{\rm lim}$ ranks the true string highly enough for ultimate detection.

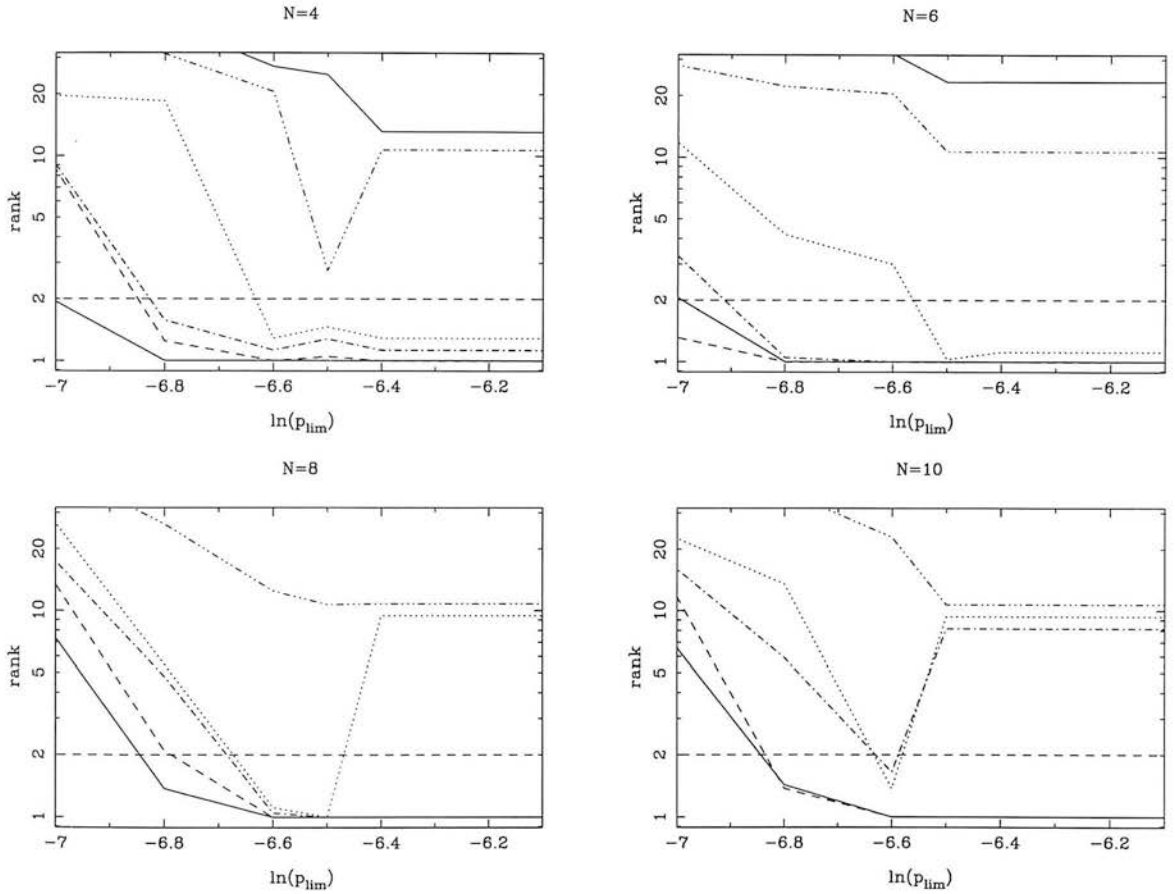

Figure 4.3: (b) The same plot but as for binning with $\theta_B = 10°$. This is a reasonable lower limit to the bin size applicable for Schmidt plates as figure 3.3 shows the error in ascribing orientations to low separation faint pairs to be of this order. If the analysis of section 2.2.2 predicts too much small-scale structure for strings compared with the more applicable case of expanding space simulations then this figure may be more relevant in defining the limiting depth of a search program.

ID No.	R.A. (J2000)			δ (J2000)		
0041	2	42	14.112	-22	3	59.56
0051	0	59	43.696	-14	42	21.04
0061	22	42	3.175	-14	50	33.53
0074	2	21	52.506	-23	28	13.45
0083	21	44	42.547	-24	2	40.25
0093	21	24	41.659	-8	28	39.72
0104	21	41	2.944	-21	34	33.79
0113	2	4	52.180	-25	12	58.16
0121	21	56	26.812	-13	49	39.56
0131	21	44	21.754	-25	26	46.37
0144	21	18	19.339	-9	18	45.70
0154	22	0	22.079	-10	47	34.32
0161	22	16	20.140	-25	23	44.49
0171	21	51	39.100	-21	14	25.30
0182	2	15	22.788	-26	50	38.20
0193	21	26	59.399	-20	7	59.43
0201	21	53	13.628	-26	49	55.44
0211	21	32	46.345	-10	11	46.68
0222	21	18	19.339	-9	18	45.70
0233	21	41	0.114	-20	55	9.29
0241	23	30	6.077	-16	47	30.01
0251	2	4	15.146	-27	24	45.15
0263	22	48	28.573	-23	29	34.25
0271	21	18	52.556	-12	3	36.99
0282	21	42	24.062	-25	21	6.13
0294	21	57	6.386	-20	5	3.50
0302	21	49	32.081	-26	44	52.68
0313	0	49	4.523	-10	41	51.80
0322	22	12	17.759	-26	53	27.49
0333	21	23	50.240	-20	1	21.19
0342	22	37	5.088	-23	31	40.32
0351	23	0	10.019	-16	14	45.64
0363	21	27	23.875	-20	32	5.36
0373	22	46	49.256	-19	4	10.32
0381	22	22	35.566	-8	35	34.70

ID No.	R.A. (J2000)			δ (J2000)		
0394	21	18	50.026	-17	39	52.02
0402	1	48	4.424	-24	7	28.03
0412	22	16	48.022	-23	42	13.78
0421	0	54	10.836	-22	0	40.15
0433	21	52	7.374	-8	12	37.88
0441	22	58	35.389	-14	54	52.66
0452	22	13	56.856	-25	22	27.67
0464	22	43	36.970	-23	4	33.95
0472	22	37	0.718	-15	22	41.13
0484	21	50	9.128	-21	27	45.39
0494	21	58	55.690	-10	16	14.73
0503	1	33	53.924	-23	51	40.90
0511	21	58	23.772	-3	51	4.40
0523	23	46	7.730	-15	57	33.53
0532	21	46	33.136	-3	34	49.50
0541	21	50	40.700	-9	10	54.99
0551	22	43	47.590	-22	45	29.94
0563	0	23	37.198	-11	44	45.58
0573	23	9	40.633	-15	22	29.96
0583	22	21	3.046	-8	20	2.20
0591	23	7	0.314	-15	20	2.00
0601	22	48	11.455	-21	48	20.31
0614	22	23	39.203	-26	57	12.44
0621	2	4	14.167	-20	48	57.65
0633	21	59	3.336	-26	33	56.07
0644	21	58	41.718	-13	48	48.66
0652	1	34	9.073	-14	14	28.78
0661	0	32	2.011	-12	9	57.90
0673	21	54	25.538	-4	4	43.92
0682	1	47	48.462	-15	50	40.38
0693	23	40	6.247	-15	6	2.36
0701	2	29	43.408	-21	54	26.54
0713	21	58	28.575	-13	51	44.43
0723	1	32	2.220	-24	23	34.98
0733	22	0	15.271	-24	10	21.88

ID No.	R.A. (J2000)			δ (J2000)		
0742	22	1	31.796	-19	38	40.35
0754	2	40	37.808	-6	4	22.54
0763	21	58	37.636	-3	58	20.35
0774	22	13	56.575	-8	59	16.98
0782	23	57	28.181	-22	18	0.05
0793	22	48	44.165	-19	49	50.28
0804	1	40	39.004	-11	54	48.46
0812	21	28	25.241	-12	16	59.78
0821	23	45	18.497	-23	30	10.02
0831	2	0	10.364	-22	34	45.51
0843	23	44	57.793	-5	25	8.00
0852	22	41	51.223	-18	11	57.45
0864	1	39	39.269	-14	23	28.47
0873	0	48	55.051	-5	48	40.55
0884	2	48	37.786	-3	44	0.16
0894	1	20	17.020	-26	27	58.41
0901	22	32	1.190	-8	35	19.71
0912	23	59	9.067	-21	7	3.86
0921	21	32	7.094	-10	26	21.04
0932	23	46	30.212	-13	41	43.76
0943	23	29	30.235	-21	9	20.28
0952	2	33	53.654	-19	32	28.06
0961	21	50	32.946	-2	36	22.57
0971	23	7	49.332	-11	24	24.14
0983	21	14	51.770	-14	32	24.03
0993	21	17	56.605	-14	42	28.38
1002	23	14	25.850	-26	33	18.30
1011	23	47	18.578	-25	39	34.14
1022	22	3	19.944	-18	29	58.42
1031	23	6	51.944	-5	28	56.34
1043	23	23	47.141	-16	9	59.75
1051	0	22	7.381	-26	2	3.69
1064	1	21	22.090	-23	21	25.08
1072	1	50	31.772	-15	38	17.87
1082	23	0	34.477	-7	54	40.62

ID No.	R.A. (J2000)			δ (J2000)		
1091	22	4	46.340	-17	44	14.66
1101	1	52	58.346	-4	11	44.96
1114	0	44	6.194	-26	9	32.35
1124	21	50	28.327	-15	41	34.74
1131	23	8	53.448	-22	56	38.80
1143	21	46	11.690	-14	31	50.62
1151	21	39	39.794	-8	1	34.40
1162	21	37	30.011	-11	52	45.13
1174	22	16	30.256	-9	26	54.95
1182	0	48	21.920	-12	20	9.19
1192	1	57	17.914	-2	44	37.31
1202	2	23	49.654	-9	0	27.20
1213	23	14	9.258	-14	4	47.30
1221	23	31	49.642	-13	53	40.34
1231	0	48	6.689	-10	11	36.17
1242	1	34	1.603	-20	22	46.89
1254	23	8	6.158	-22	52	24.81
1263	1	44	40.891	-5	49	11.99
1274	23	20	28.730	-21	54	57.71
1283	1	39	47.214	-11	20	30.77
1292	0	51	16.261	-17	47	30.13
1303	1	38	3.829	-11	1	55.24
1313	21	44	21.642	-3	50	7.20
1324	0	25	58.728	-22	45	15.31
1334	23	5	25.778	-24	1	43.28
1343	21	18	20.106	-14	42	41.28
1353	21	40	24.197	-14	56	26.94
1362	1	10	23.405	-15	57	40.80
1373	21	49	15.848	-2	56	17.90
1383	22	18	33.293	-15	9	32.16
1403	2	5	25.246	-5	43	53.92
1412	0	13	37.286	-10	51	42.13
1423	0	58	36.178	-19	14	22.07
1432	23	11	23.665	-14	6	6.48
1444	2	5	24.364	-5	44	6.82

ID No.	R.A. (J2000)			δ (J2000)		
1452	2	40	37.808	-6	4	22.54
1461	0	13	40.825	-9	22	18.28
1471	1	13	18.959	-18	2	47.10
1483	22	27	38.419	-19	54	8.44
1492	1	5	7.123	-17	12	53.29
1501	2	44	50.950	-27	18	9.80
1512	23	51	59.850	-7	55	35.04
1522	23	0	22.043	-5	52	2.13
1534	21	37	52.615	-5	49	56.25
1543	23	51	22.806	-19	49	24.37
1554	1	46	49.768	-22	49	4.46
1564	1	52	55.337	-27	7	50.97
1574	22	23	50.125	-19	52	50.77
1583	23	22	21.994	-10	4	57.69
1593	22	40	3.533	-4	31	29.36
1603	0	35	6.083	-24	56	31.64
1612	0	17	45.370	-25	42	8.09
1622	22	20	6.025	-20	8	20.14
1633	23	9	55.368	-19	37	28.82
1641	2	38	16.066	-18	52	33.42
1653	23	49	42.424	-20	20	30.33
1661	22	47	47.810	-4	3	42.94
1671	2	48	37.786	-3	44	0.16
1681	23	42	25.866	-21	25	48.51
1691	22	50	34.757	-8	45	40.44
1702	0	21	34.913	-16	2	21.56
1711	22	45	51.354	-3	8	32.33
1724	2	18	23.339	-9	45	16.88
1733	1	12	4.979	-15	5	1.52
1742	2	34	5.466	-21	22	0.40
1751	0	25	13.883	-8	45	52.29
1762	23	5	49.196	-12	27	35.07
1771	23	12	22.820	-19	30	20.06
1781	1	14	8.081	-25	47	30.91
1791	2	27	24.638	-16	24	45.16

ID No.	R.A. (J2000)			δ (J2000)		
1801	23	30	36.364	-26	8	21.27
1812	1	10	53.180	-2	15	45.57
1824	23	22	21.994	-10	4	57.69
1833	2	25	35.216	-20	14	0.88
1844	1	0	29.185	-25	59	58.93
1851	23	48	56.567	-3	52	21.11
1864	23	38	52.116	-10	36	57.87
1872	2	40	38.896	-19	18	12.81
1883	23	39	57.380	-9	45	58.95
1891	23	32	2.015	-7	17	53.42
1903	0	50	16.958	-23	44	51.53
1913	23	22	15.870	-21	4	30.68
1921	0	11	14.539	-16	43	0.57
1933	0	59	13.438	-15	0	46.45
1943	0	55	25.338	-26	24	37.22
1952	0	13	6.067	-16	21	49.58
1964	23	21	56.030	-22	56	8.86
1972	23	39	54.961	-17	36	5.72
1981	22	11	18.100	-7	11	53.56
1991	22	33	54.428	-21	29	46.86
2004	0	2	39.113	-26	55	17.18
2012	0	0	4.226	-27	25	49.42
2023	23	48	8.989	-26	10	4.52
2034	0	3	2.930	-24	59	16.21
2041	23	51	25.942	-26	25	49.33

4.2 Placing Limits on the String Model

4.2.1 The UKST Output

The ultimate aim of the work presented in the last three chapters is to place limits on the cosmic string model. We have seen that the model has numerous parameters despite its initial motivation (discussed in the introduction) as a better specified model than inflation. Of these parameters the most crucial in our analysis have been σ_θ and σ_y which quantify the string microstructure in a way which bears directly on the search method chosen. The other crucial parameter is the density of long strings in the Universe, ρ_s. Surveys which fail to find strings should be able to place an upper limit on this parameter. As indicated before it is not possible to place a very strong constraint by searching for strings on Schmidt plates – but these are early days in the search for strings. Future deep galaxy surveys will continue to push the limit on ρ_s downwards to a point where it contests the values (a) thought likely by simulators of string networks, and (b) thought necessary for strings to be a source of structure formation.

The overriding philosophy of the search method for strings espoused in chapters 2 and 3 can be summarized as follows:

- Select a survey medium which provides the largest available area coverage and depth.
- From a knowledge of (i) galactic image structure in the survey and (ii) the properties of simulated strings, find criteria which give the greatest signal-to-noise for strips of string-lensed images.
- Examine the strips, the densest first, to conclusively demonstrate whether or not they are due to strings. If a string is found then the search is, of course, successful and the work is complete.
- In the case where no true strings are found, the least dense string followed up in this way, i.e. the last strip examined, provides an estimated lower limit $z_{\rm lim}$ to the redshift of the nearest string crossing the survey area A.

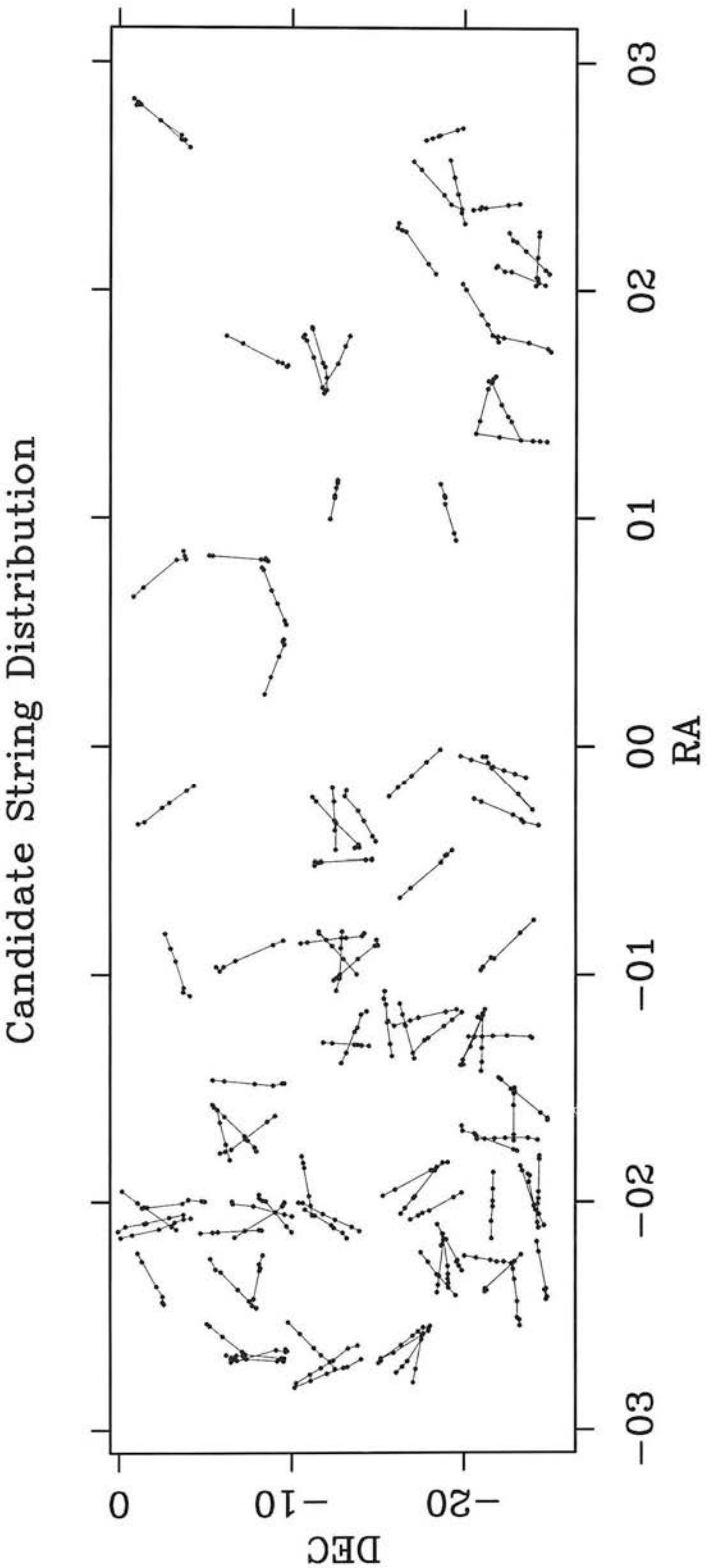

Figure 4.4: (a) Distribution of string candidates from the UKST plates searched. The 100 densest strips of candidate lensing events are shown. There are 6 pairs/ellipses per strip.

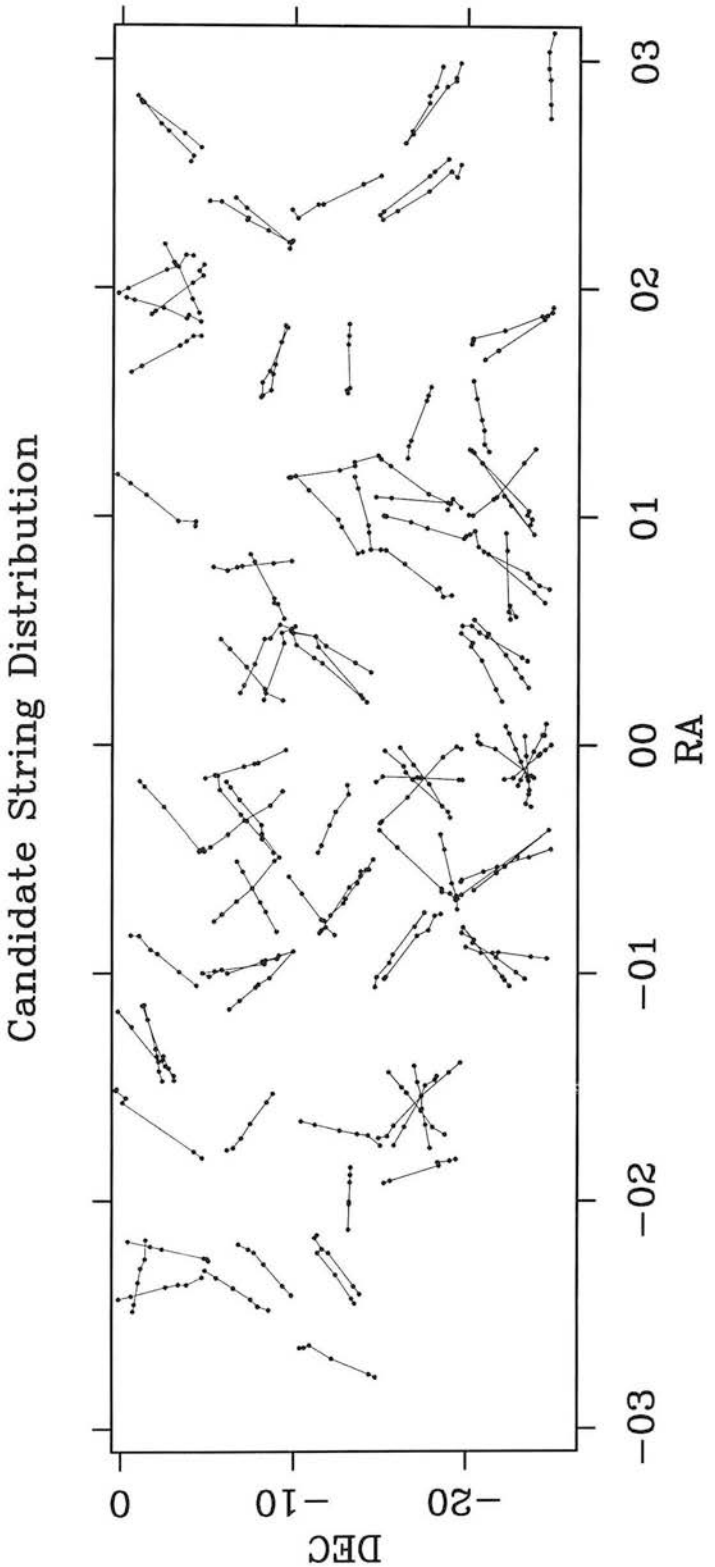

Figure 4.4: (b) As for (a) but with candidates ranked in the range 100 — 200.

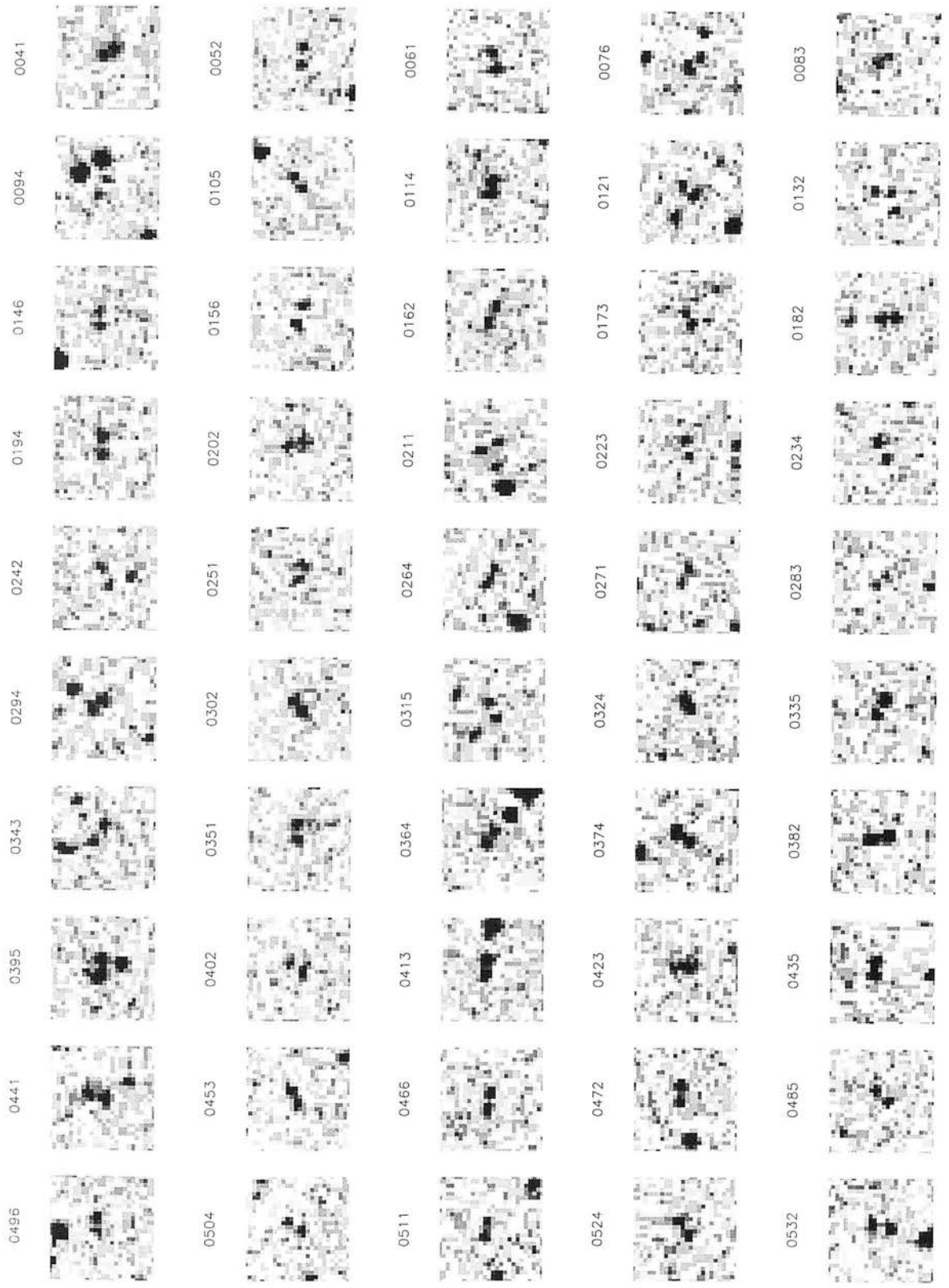

Figure 4.5: (a) Images of the best string-lensing candidates from the 100 plate survey. Each image is 45″ on a side.

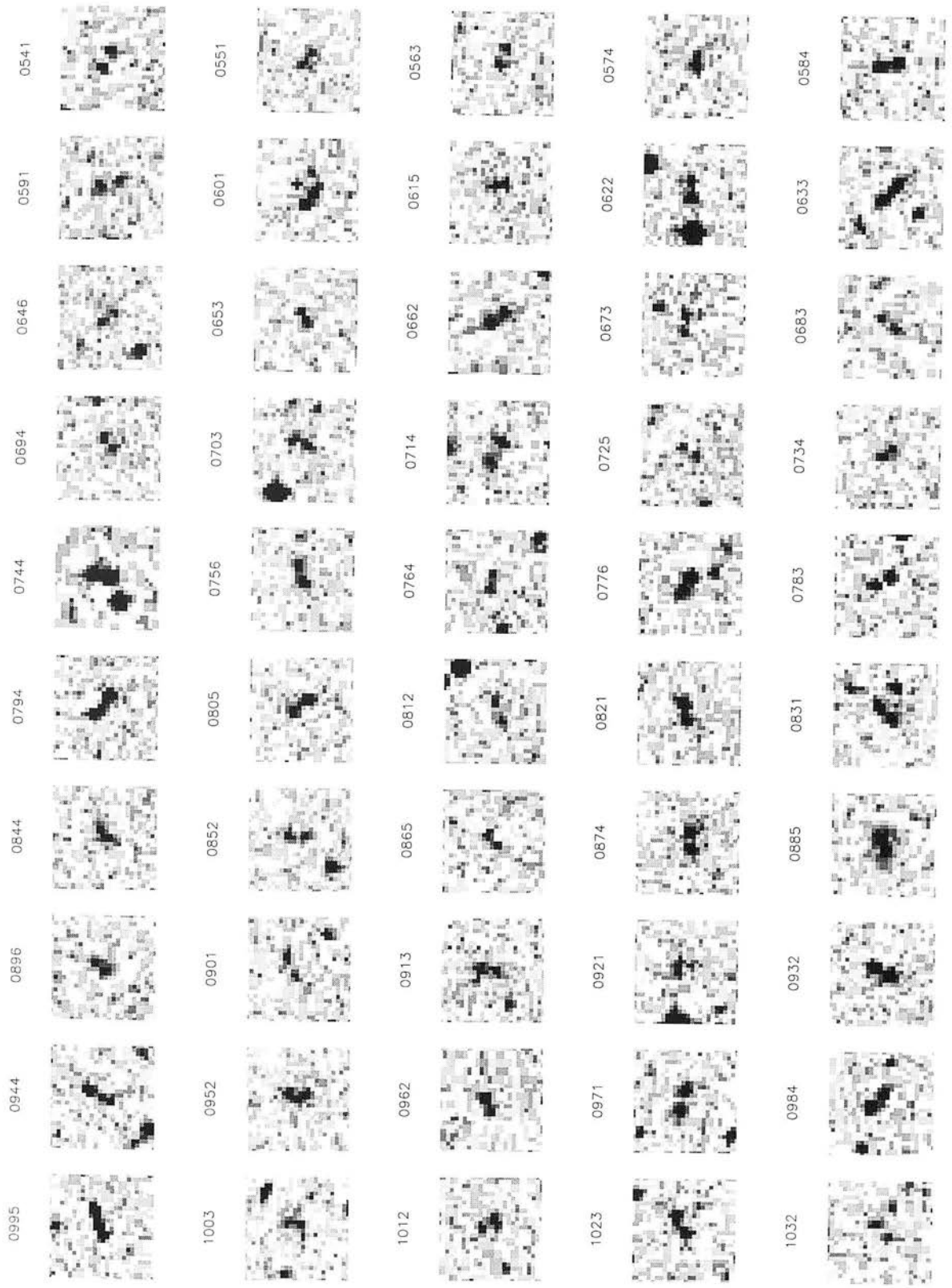

Figure 4.5: (b) Images of the best string-lensing candidates from the 100 plate survey. Each image is 45″ on a side.

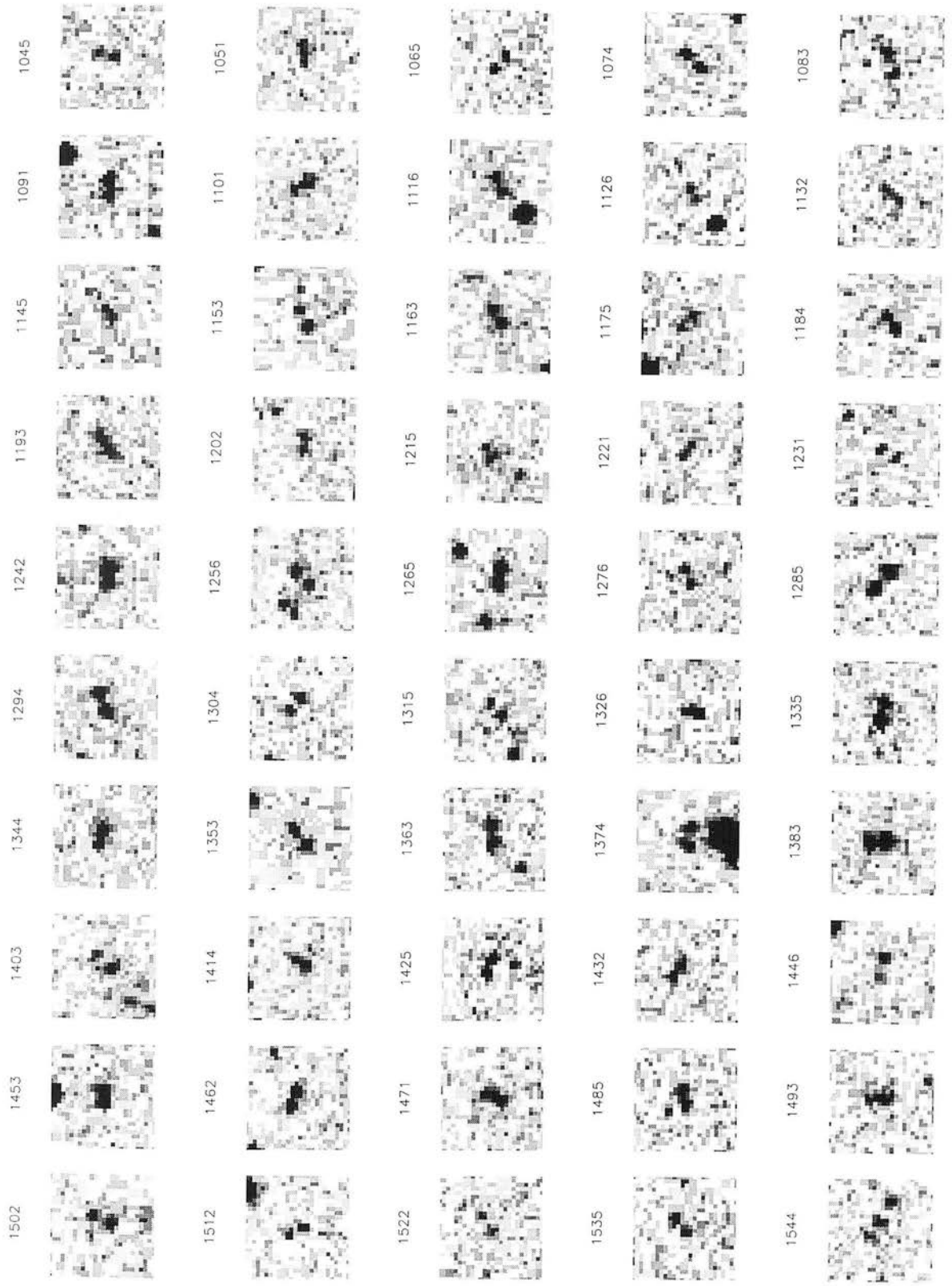

Figure 4.5: (c) Images of the best string-lensing candidates from the 100 plate survey. Each image is 45″ on a side.

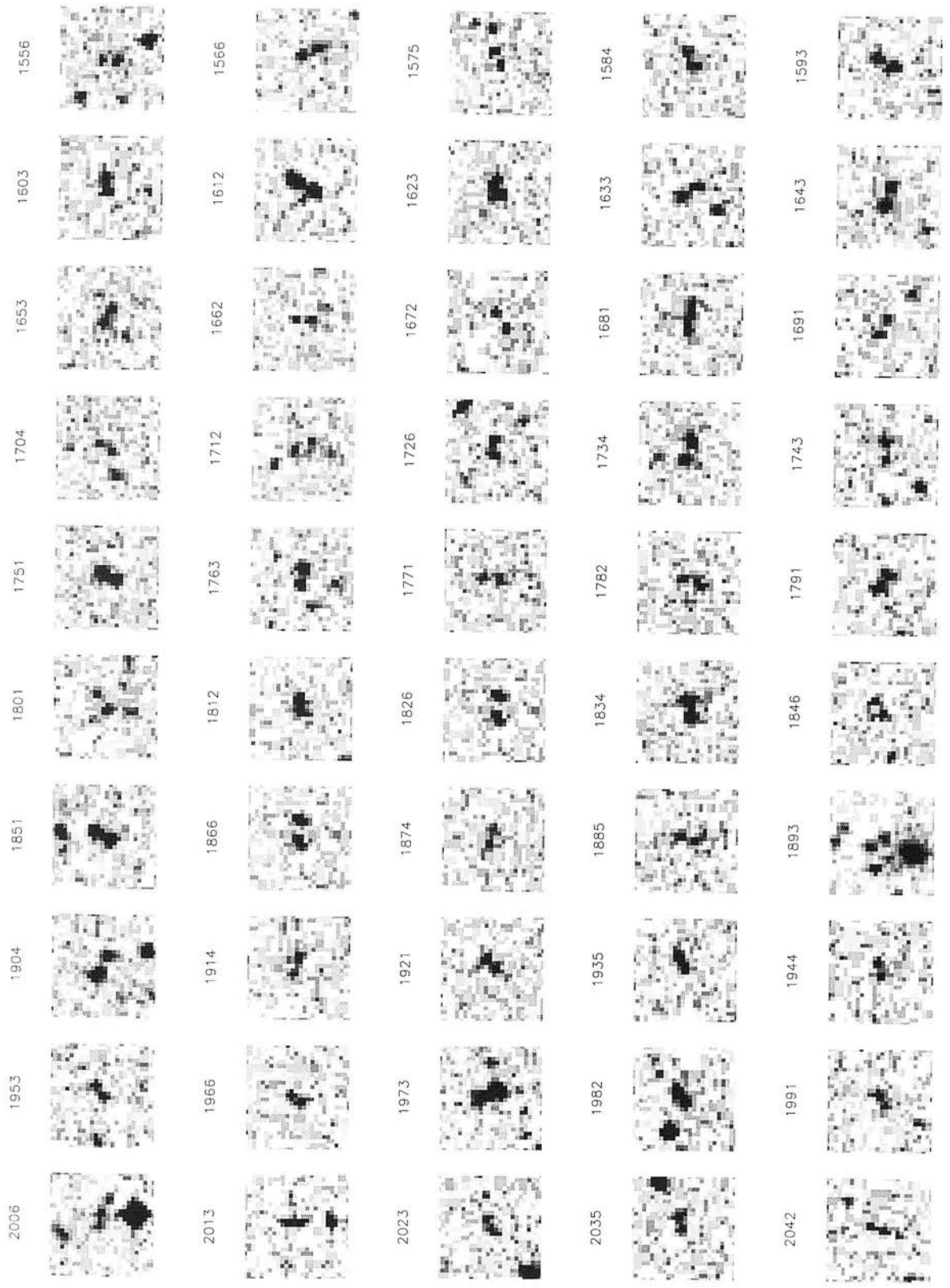

Figure 4.5: (d) Images of the best string-lensing candidates from the 100 plate survey. Each image is 45″ on a side.

- Using the formulae of section 2.3 these parameters can be converted into an upper limit on the string density ρ_s.

The remaining section of this chapter will establish the (weak) limits that can be placed with the UK Schmidt data and then discuss how these limits can be greatly improved by forthcoming large-area deep surveys.

In section 2.2 we established that for a 50% detection chance, the search procedure must reach strings at a redshift of

$$z \simeq \sqrt{\frac{\ln 2}{\rho_s \beta}} \tag{4.3}$$

as an upper limit to the redshift required and

$$z \simeq \sqrt{\frac{\ln 2}{\rho_s N l_D}} \tag{4.4}$$

as a reasonable lower limit. Here β was the radius of the search area in radians, N the number of plates of side l_D radians. We can invert these formulae to produce limits on ρ_s that follow from unsuccessful attempts to find strings. For example our search programme with Schmidt plates (when followed up by deep imaging) has a redshift limit of $\simeq 0.07$ and covers an area of $100 \times 25\text{deg}^2$ which means $\beta \simeq 0.8$ rad. By the first formula we can establish a hard upper limit of

$$\rho_s < \frac{\ln 2}{z_{\rm lim}^2 \beta} \simeq 170\, l_H^{-2} \tag{4.5}$$

The second argument gives a much tighter limit of

$$\rho_s < \frac{\ln 2}{z_{\rm lim}^2 N l_D} \simeq 16\, l_H^{-2} \tag{4.6}$$

These "back-of-an-envelope" calculations take second place to the estimate made using the string simulations (figure 2.10). Here we established that a 50 % chance of detection on 100 Schmidt plates would require $z_{\rm lim} \gtrsim 0.15$ when $\rho_s \simeq 20 l_H^{-2}$. We cannot reach this

limiting redshift but we know that in general $z_{\rm lim}^2 \propto \rho_{\rm s}^{-1} A^{-1}$, so a failure to find string in the range $z = 0 - 0.07$ gives us the constraint

$$\rho_{\rm s} \lesssim 90\, l_{\rm H}^{-2} \tag{4.7}$$

As we noted above this is almost an order of magnitude higher than the values of order $\rho_{\rm s} \simeq 20\, l_{\rm H}^{-2}$ that arise in matter-dominated expanding-universe simulations and so is a long way off from seriously contesting the model. Increasing our area coverage would help. Using the whole Schmidt plate survey (northern Palomar Schmidt plates and southern UKST plates) would give us ~ 1000 plates and lower the limit to $\rho_{\rm s} \lesssim 9\, l_{\rm H}^{-2}$. The problem with this is that we would need to obtain deep CCD images of ~ 2000 fields (i.e. 10 times as many as before) in order to successfully push $z_{\rm lim}$ to $\simeq 0.07$ over such an area. This is almost certainly prohibitive in terms of telescope time. It therefore must be concluded that Schmidt plates are inadequate as a means for searching for strings. However, having established the method, we can look forward to the deeper galaxy catalogues where conclusive tests should be possible.

4.2.2 The Sloan Survey

The Sloan Digital Sky Survey (Gunn & Knapp 1993) aims to provide a complete photometric and spectroscopic survey of π sterradians of the northern sky. Imaging data will be obtained in five bands (u,g,r,i,z) using an array of thirty 2048^2 pixel CCDs. Of order 10^8 galaxies will be imaged to $g \sim 23\,(B_{\rm J} \sim 23.5)$ mag – redshifts will be obtained for those brighter than $g \sim 19\,(B_{\rm J} \sim 20)$. In the southern sky repeated imaging of a $3^\circ \times 100^\circ$ patch of sky is expected to yield much fainter data – complete down to $g \sim 25\,(B_{\rm J} \sim 25.5)$ mag.

The Sloan survey will thus provide unprecedented depth and area coverage with median galaxy redshifts of order $\overline{z} \simeq 0.4$ for the large area northern-sky survey and $\overline{z} \simeq 0.6$ for the deeper southern sky project. The forthcoming data thus appear ideal for extending the search for cosmic strings. This section will offer a brief consideration of whether a search programme based on Sloan data would offer a definitive test of the existence of strings.

The amounts of string at the relevant survey depths and areas can be assessed by reference to figure 2.10. From this can be seen that at a search area of π sterad has a $\sim$100% chance of a degree long section of string lying within the median galaxy redshift of $\overline{z} \simeq 0.4$. The $3^\circ \times 100^\circ$ deep survey does not have a good chance of containing string at less than $z \sim 1$, here all the detectable string lies well beyond the median galaxy redshift of $\overline{z} \simeq 0.6$. Thus the chances of seeing large numbers of string lensed objects is quite low, something like $20 - 30\%$ (the value of curve (c) at $z = \overline{z}$). Given these considerations, the rest of the discussion will focus on the larger area survey.

In addition to the greatly superior volume coverage provided by the survey there are numerous other advantages over the largely photographic data available at present. Firstly the presence of multi-colour data for each object allows a very straightforward test of lensing in the case of close pairs. Equation 2.3 tells us that there is negligible relative redshifting or blueshifting of images when lensed by GUT-scale strings. Therefore in addition to requiring the magnitudes of close pairs to be very similar, we also expect similar colours. The existence of CCD quality photometry on each object will allow both magnitude and colour discrimination tests to be much more reliable. The much improved sampling of images permitted by the 0.5 arcsec pixels will also allow morphology a role in discriminating between otherwise comparable lensed image candidates. In addition the sampling will make deblending of images separated by a few arcsec simpler and less prone to error.

In essence therefore we expect that the Sloan survey, while observing a much larger region of the universe than has hitherto been possible, will also provide the means to greatly cut down the "noise" associated with cataloguing chance close pairs as lensing candidates. As a test of the improvements possible we estimate the signal-to-noise $N_{\rm s}/N_{\rm b}$ in analogy with section 3.1.1. It will be recalled that this gives the ratio of true string-lensed pairs to chance background pairs when a strip lies on top of a string, and must be $\gtrsim 1$ for a good chance of detection. The calculation is basically the same except that

- the limiting magnitude is $\simeq 2.5$ deeper than for Schmidt plates and so the galaxy density per deg^2 is roughly $10^{0.6\times 2.5} \simeq 30$ higher.
- the number of close pairs increases as, at least, the square of the image density

and so the background pair density is $\simeq 900$ higher. This assumes the objects have random positions, in fact the galaxies are clustered and hence the number of close pairs will increase more steeply than this – but this estimate will suffice for our purposes.

- The images will be much better sampled than on the Schmidt plates and with better signal-to-noise per pixel. Deblending should be possible above $\simeq 2''$. This means that a calculation of N_s/N_b for pairs alone should give a good estimate of the redshift limit for detectable strings. In the Schmidt calculation (section 3.1.2) no account was made of the elliptical images which ultimately had to be included in the search algorithm. Thus the good agreement between the calculated z_{lim} and that found from simulation is rather fortuitous.

- The magnitudes and morphologies of the image will be much better determined than is possible with Schmidt plates. Consequently the rejection of ill-matched chance pairs is much more effective. Since data will be provided in multiple bands we can also use colour as a discriminant – lensing is achromatic so the colours of each object in a pair should be the same.

Some of these aspects are illustrated in figures 4.6a-f. Figures (a) and (b) show a simulated string crossing a $2.5'$ square portion of the sky in the B($\simeq g$)-band (figure (a) with limiting magnitude $\simeq 24$) and the R($\simeq r$)-band (figure (b) with limiting magnitude $\simeq 23$). The string is placed at $z_s \simeq 0.075$ (the detection limit for Schmidt plates) and galaxy redshifts are selected according to magnitude using expressions 3.1 and 3.2. As it stands the path of the string is difficult to discern, owing to the high background density of images. Things are only slightly improved by image analysis and selection of close, similar pairs, i.e. (closer than $10''$, Δmag ≤ 0.6, as for Schmidt plates). The result of this pair selection is given in figure 4.6c for the B-band and 4.6d for the R-band data. The string locus is faintly discernible as an excess of pairs, running in the X direction, at $Y \simeq 350$. A huge improvement is made by enforcing a requirement that each of the lensed images in a pair has the same magnitude and *colour* (equation 2.3). Figures 4.6e and f show the B and R-band pairs that satisfy $|(B_1 - B_2)| \leq 0.2$, $|(R_1 - R_2)| \leq 0.2$, $|(B_1 - R_1) - (B_2 - R_2)| \leq 0.2$ (i.e. conservatively estimating an improvement factor of

~ 3 in the accuracy of magnitude measurement when the Sloan data is compared to the Schmidt). All seven of the string-lensed pairs which appear in *both* passbands are retained by this condition, but the background is reduced to two non-string pairs. The locus of the string is clearly marked out by the pairs along its length.

The simulated string in figure 4.6a-f was placed at a redshift $z_s \simeq 0.075$, the distance at which search methods using Schmidt plates are found to fail. It seems reasonable to suppose that this string would be quite easily found with the Sloan data and in fact much greater depths could be obtainable. This chapter ends with an estimate of the improvement in depth obtainable with such data, and whether this is adequate to set interesting constraints on the model. We calculate N_s/N_b as in equation 3.11, as a function of string redshift z_s for the two datasets – Schmidt and Sloan. The two functions are shown in figure 4.7.

The Schmidt result (a) is calculated as before, assuming that $\Delta B_J \geq 0.6$ and using a background galaxy density of ~ 1000 per deg^2. The background pair density is found from the plates and for $\Delta B_J \leq 0.6$ is ~ 10 per deg^2. The redshift distribution is of the form 3.1 with $B_J = 21.5$. Pairs are resolved if $\psi \geq 4''$.

The Sloan result (b) assumes that the background galaxy density is $\sim 3 \times 10^4$ per deg^2 and that magnitudes will be accurate to $\Delta B_J \simeq 0.2$. The background pair density can be (crudely) estimated from figures 4.6e and f (as real data were used as the basis for these simulations) to be $\sim 10^3$ per deg^2. This makes sense though, it was argued above that the pair density (at the same ΔB_J threshold) should be ~ 900 times higher for the Sloan data. There is a roughly threefold improvement in discrimination by requiring $\Delta B_J \leq 0.2$ instead of 0.6. The spread in colours between all image pairs is ~ 0.6 and so requiring the colours to be the same within ~ 0.2 of a magnitude gives another approximately threefold factor in pair rejection. Increasing the discrimination between images in a pair by a factor $\sim 3^2$ we expect to keep only $\sim 900/3^2 = 100$ times as many images, and this is found to be the case. The redshift distribution is again of the form 3.1 with $B_J = 24$. Pairs are resolved if $\psi \geq 2''$.

As demonstrated in chapter 3, the Schmidt result falls below unity at $z_s \geq 0.07$. The Sloan result, on the other hand, gives $N_s/N_b > 1$ out to $z_s \simeq 0.3$. In figure 2.10, the

50% chance-of-detection threshold is already satisfied for $z_s \simeq 0.15$ for the large area Sloan survey with $\rho_s \simeq 20\, l_H^{-2}$ but we can apparently go much deeper than this. Failure to detect string out to $z = 0.3$ with the Sloan survey would set the interesting limit of

$$\rho_s \leq 5\, l_H^{-2}. \tag{4.8}$$

Such a result would encroach very significantly on the range of ρ_s thought likely by simulators of string (cf. the much higher densities predicted by Bennet (1990) and Shellard & Allen (1990) quoted in section 2.3).

To conclude, therefore, searching for cosmic strings has proved difficult on Schmidt plates. The relatively sparse background density of galaxies fails to delineate strings on scales where they are significantly straight and the low mean redshift of galaxies $\overline{z_g} \sim 0.2$ means that only low-redshift strings have a good chance of lensing detectable objects. Furthermore the image discrimination is rather inefficient, deblending limitations become significant on the same scales as lensing is most likely to occur. This forces the inclusion of elliptical images which are already very abundant as background noise. Useful limits on the string model cannot be set using the Schmidt data without an unfeasible quantity of follow-up work on large telescopes. However the final part of this chapter has put forth arguments as to why an equivalent test on the large-area Sloan survey data should definitively test the model. A thorough search programme with the Sloan data will find cosmic string or force a substantial rethinking of the overall model.

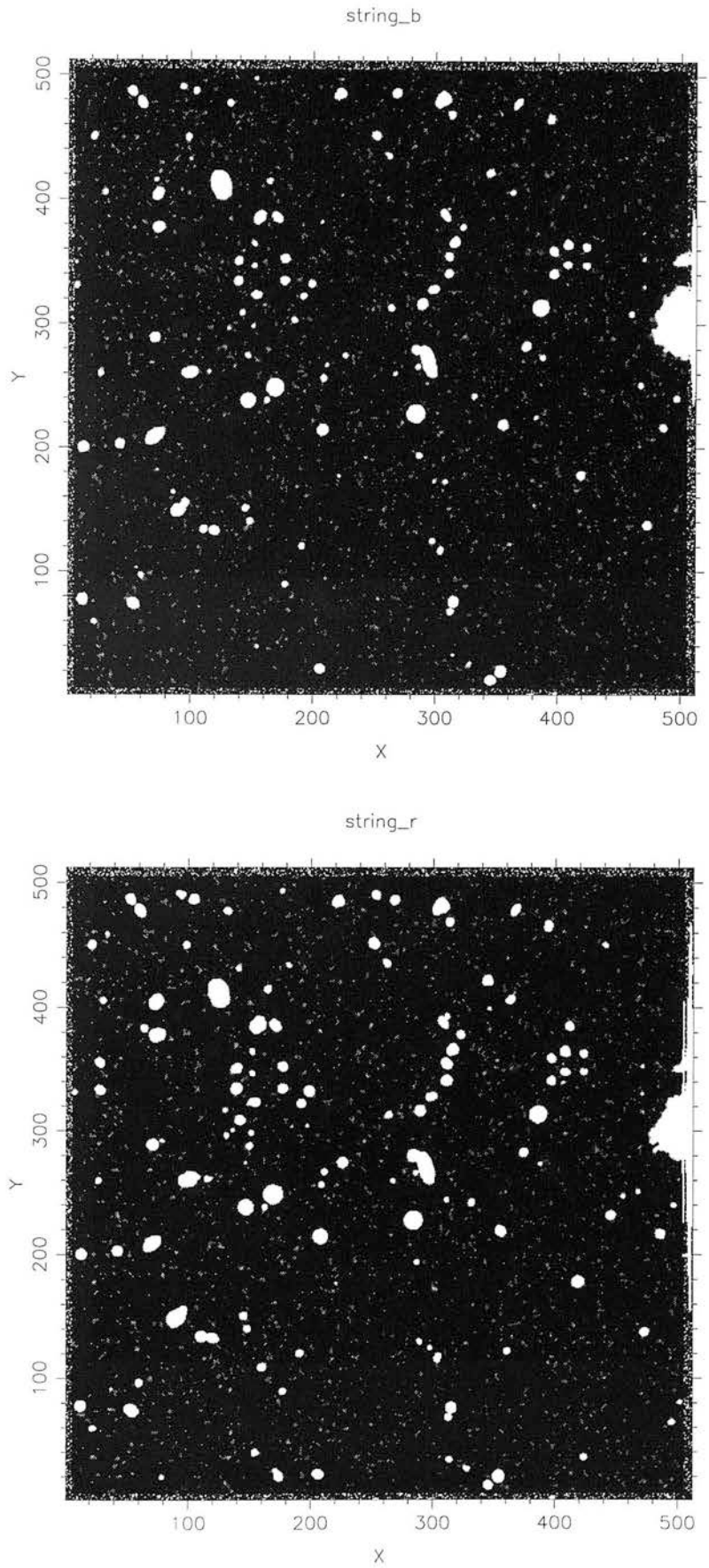

Figure 4.6: (a) and (b) see text for details.

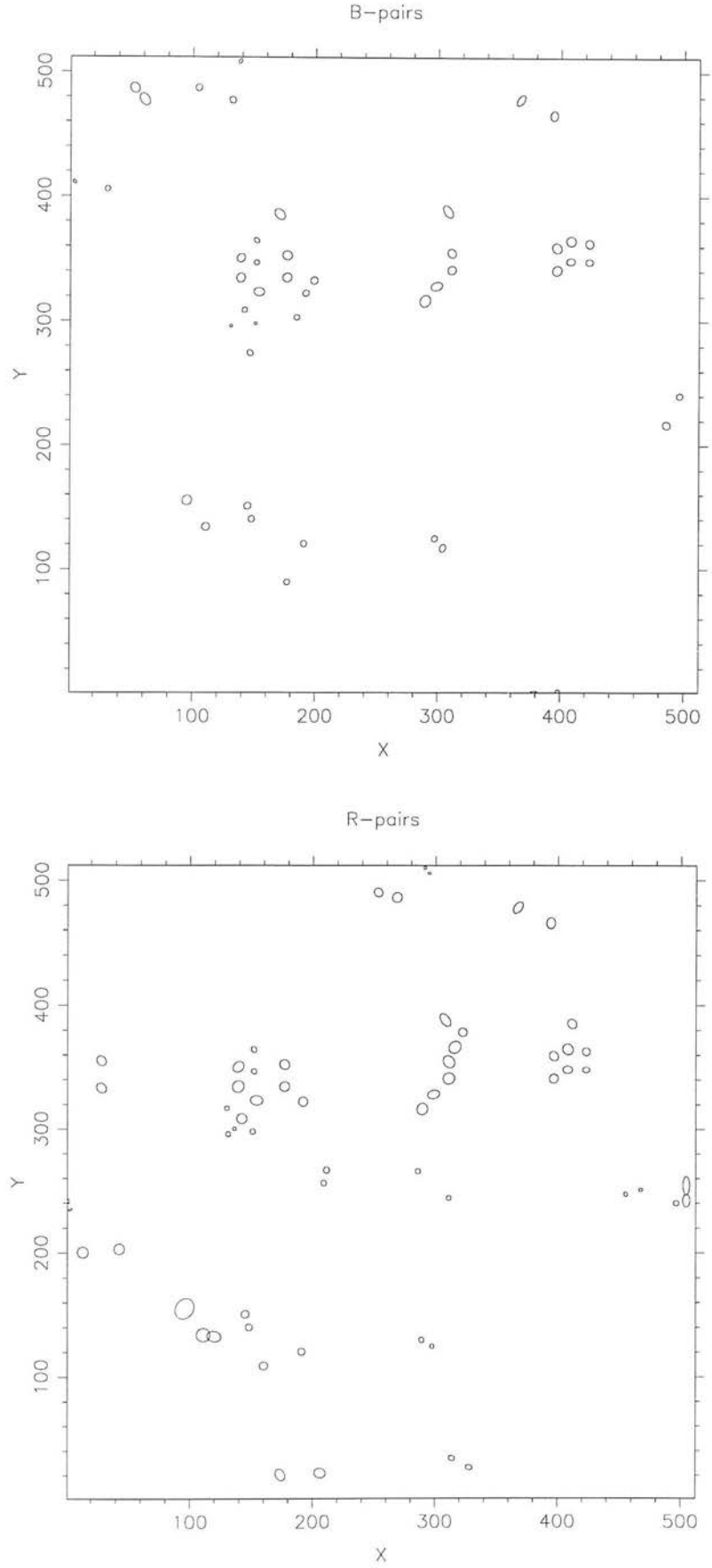

Figure 4.6: (c) and (d) see text for details.

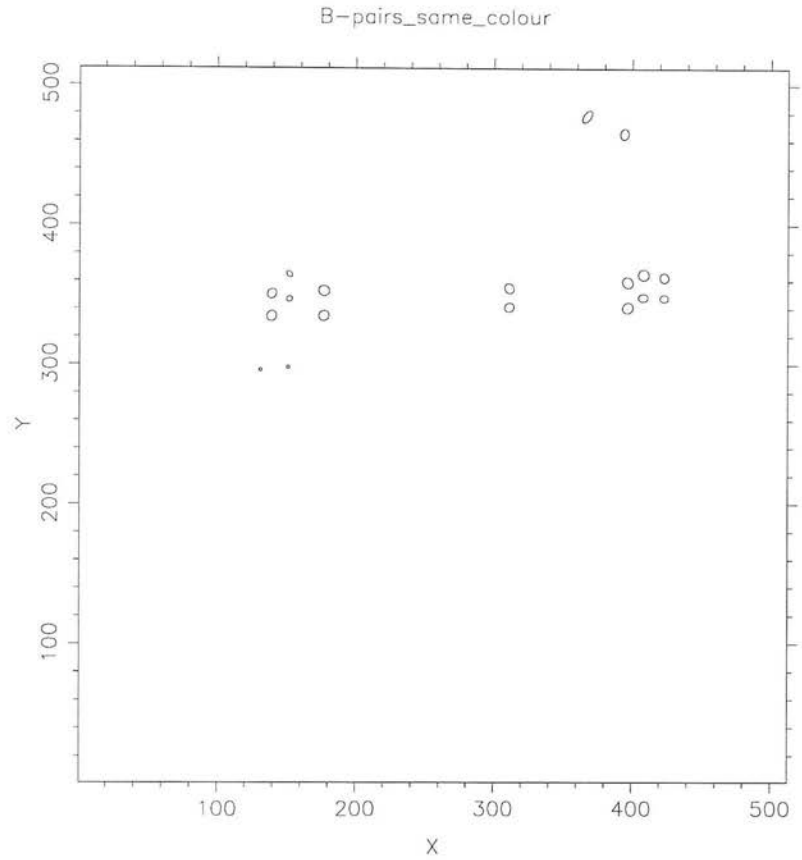

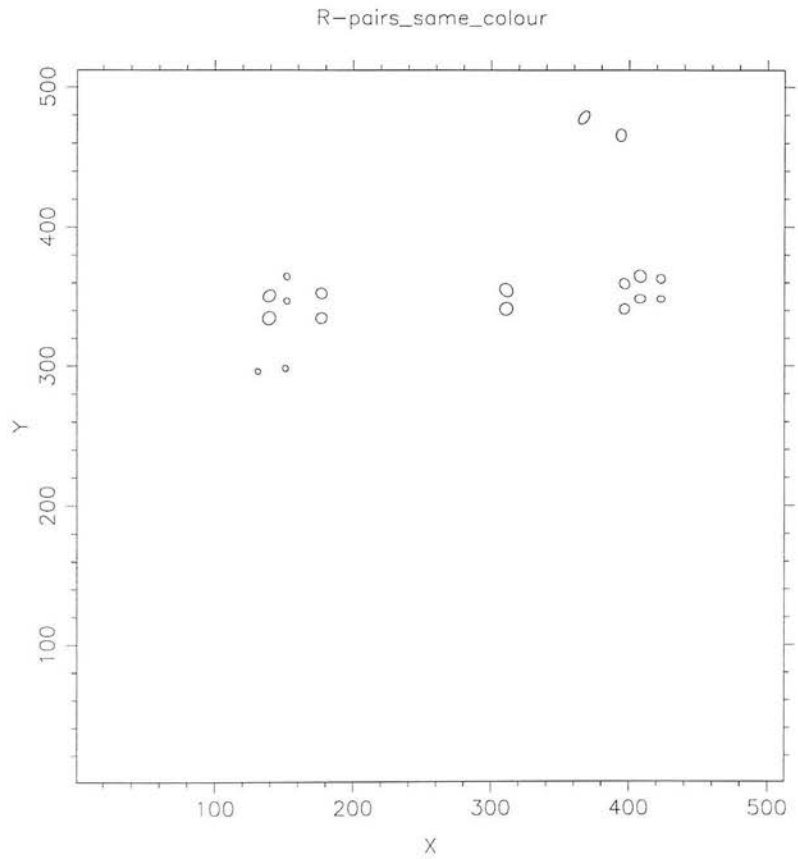

Figure 4.6: (e) and (f) see text for details.

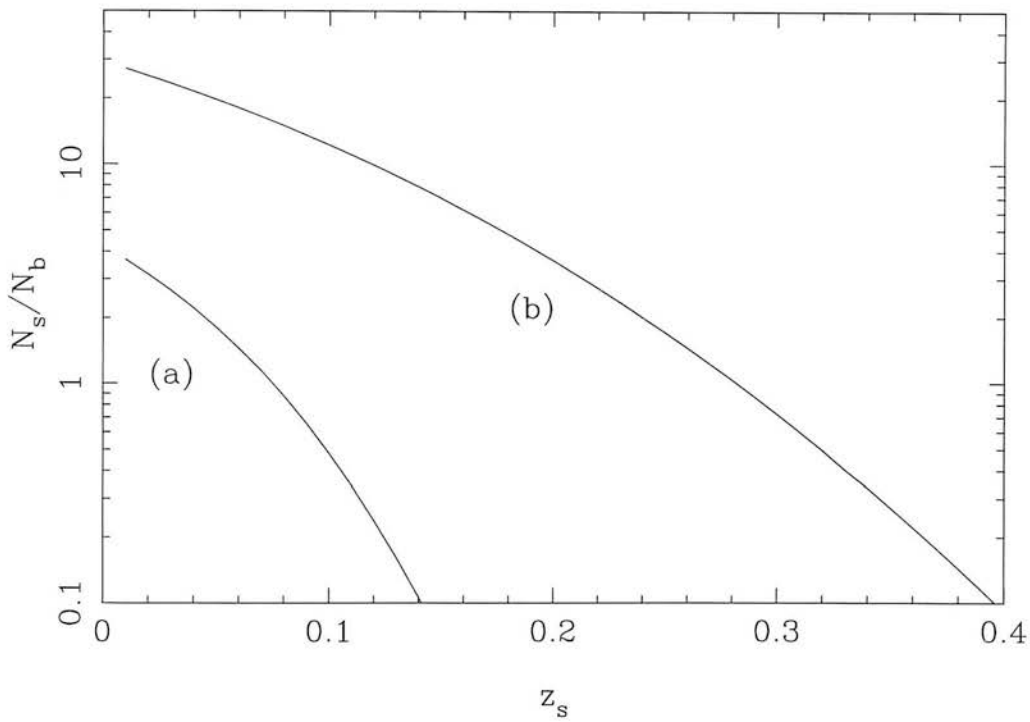

Figure 4.7: Signal-to-noise as the ratio N_s/N_b for string-lensed pairs as a function of string redshift z_s. Curve (a) shows the prediction for Schmidt plates for $\Delta B \leq 0.6$, a deblending limit of $\psi \geq 4''$ and image density appropriate to $B = 21.5$. N_s/N_b stays above unity until $z_s \simeq 0.07$. Curve (b) shows the corresponding prediction for the Sloan data with $\Delta B \leq 0.2$, $\Delta R \leq 0.2$, $|\Delta B - \Delta R| \leq 0.2$, a deblending limit of $\psi \geq 2''$ and image density appropriate to $B = 24$. The signal-to-noise is then greater than unity out to $z_s \simeq 0.3$.

Chapter 5

$\Omega_0 = 1$ CDM with Relativistic Decays

5.1 Introduction

As discussed in chapter 1, observations of large-scale galaxy clustering have produced something of a crisis for theories of structure formation. The paradigm for the past decade has been a model where scale-invariant adiabatic primordial fluctuations cause clustering to grow in collisionless cold dark matter. In many ways, observations have supported the basic elements of this picture. The clustering power spectrum is smooth and featureless, with no sign of the oscillatory features that would be expected if normal baryonic material were dynamically dominant (e.g. Peacock & Dodds 1994; hereafter PD). The detection of cosmic microwave-background (CMB) anisotropies on a variety of angular scales favours a fluctuation spectrum which seems close to adiabatic and scale-invariant for wavelengths above about 100 Mpc (e.g. White, Scott & Silk 1994).

Despite these encouraging features, there has emerged a consensus that there is a problem with the shape of the fluctuation spectrum. The density of the universe should be written on the sky in the form of a break in the spectrum at around the comoving

horizon scale at matter–radiation equality

$$r_{\rm H} = 16.0\,[\Omega h^2]^{-1}\ {\rm Mpc}. \tag{5.1}$$

This number, and all others in this chapter, assumes $T = 2.726$ K for the CMB temperature (Mather et al. 1994). Since observed wavenumbers come in units of h Mpc^{-1}, the combination Ωh is measurable, and in practice is estimated by fitting a model of a scale-invariant spectrum modified by the Cold Dark Matter (CDM) transfer function. According to PD, an approximate 95 per cent confidence range for the apparent value of the density is

$$0.22 < \Omega h|_{\rm apparent} < 0.29 \tag{5.2}$$

(allowing for effects of non-linearity and redshift-space distortions). The problem is that this number appears to be inconsistent with current estimates of h and an $\Omega = 1$ Einstein–de Sitter universe, and a variety of possible solutions have been suggested.

(1) Maybe $\Omega \simeq 0.3$. This is perhaps the most obvious solution observationally, but brings in philosophically worrying fine tunings, either if the universe is open or if vacuum energy provides the remaining fraction of the critical density.

(2) Perhaps h really is around 0.25 (Shanks 1985; Bartlett et al. 1995). This explanation has the merit of simplicity, but would fly in the face of all the experimental evidence.

(3) A primordial spectrum tilted away from scale-invariance alters the fitted apparent density. However, a large degree of tilt is required and this is difficult to reconcile with the CMB studies (Cen et al. 1992; PD).

(4) The fit assumes pure CDM. If the baryonic density parameter $\Omega_{\rm B}$ is non-zero, what is measured for $\Omega = 1$ is roughly $\Omega h \exp[-2\Omega_{\rm B}]$ (PD). If $h \simeq 0.7$, $\Omega_{\rm B} \gtrsim 0.5$ would be required; it is very hard to see how such a high value can be consistent with primordial nucleosynthesis (e.g. Walker et al. 1991).

(5) One can tinker with the dark matter content to improve things, and the Mixed Dark Matter model with roughly 20–30 per cent of the dark matter being light neutrinos has received considerable recent attention (e.g. Klypin et al. 1993).

(6) Lastly, the apparent low density can be regarded as informing us that matter–radiation equality must be later than the standard figure. This can be achieved with an enhanced density of relativistic species, probably associated with the decay of a massive particle.

With the exception of (1), all of these are measures designed to save the Einstein–de Sitter universe without abandoning the basic picture of gravitational instability. In this sense, all are tainted with something of an air of desperation. Nevertheless, because of the profound consequences of any disproof of the Einstein–de Sitter model, it is important to explore all avenues thoroughly. The least contrived escape routes seem to be those involving modifications either of the dark matter or of the relativistic content, and it is on this latter possibility that this chapter[1] concentrates. It turns out that the characteristic prediction of such a model is of an enhanced amplitude of fluctuations on small scales, and this feature can be used to place limits on the decaying particle involved in the model. In section 5.2, the model is reviewed and a fitting formula to describe the resulting power spectrum is established. Section 5.3 assembles the relevant observational constraints in terms of small-scale clustering and the abundances of high-redshift objects.

5.2 CDM with a Decaying Particle

5.2.1 The Basic Model

Structure formation scenarios incorporating decaying particles have a long history (e.g. Davis et al. 1981; Bardeen, Bond & Efstathiou 1987). However, this model was given a strong boost by experimental work suggesting the possibility of neutrino eigenstates with $m \simeq 17$ keV (e.g. Simpson 1985). Although it is now believed that these results were spurious, the possibility of a mass of this order for e.g. the τ neutrino is far from

[1]The work presented in this chapter was published as McNally & Peacock (1995)

being ruled out. Such a neutrino cannot be stable, otherwise it would close the universe many times over. An acceptable present density can be achieved if the massive neutrino decays to products that are relativistic today – either to other massless neutrinos or possibly to some exotic new species. Decays to photons are not allowed for two reasons. First, the *COBE* results on the lack of CMB spectral distortions severely limit the allowed energy injection prior to recombination (Mather et al. 1994). Secondly, the relativistic density in photons is observed, and a total relativistic density is conventionally obtained by multiplying by a factor 1.68 to allow for three species of massless neutrinos. The possibility considered here, however, is that the true relativistic density is higher. If the decays producing this enhanced background occurred at redshifts greater than conventional matter–radiation equality ($z \simeq 24\,000\,\Omega h^2$), the onset of matter domination would be delayed, and we would have an explanation of the large-scale structure problem. The other constraint on the model is that decay should happen after nucleosynthesis at $z \sim 10^9$, to ensure that the light element abundances are not affected; this leaves a wide range of possible lifetimes and hence masses for the model. Dodelson, Gyuk & Turner (1994) have discussed specifically more complicated nucleosynthesis effects which occur when the decay is contemporaneous with nucleosynthesis (decay lifetime ~ 10 s), but we will see below that lifetimes this short do not have such interesting consequences for the Mpc-scale fluctuation spectrum.

The analysis presented in this chapter follows on from work by Bond & Efstathiou (1991; hereafter BE). They calculated density fluctuations in $\Omega = 1$ models dominated by CDM, in which 17-keV neutrinos having lifetimes between 1 and 10^4 yr decayed to relativistic products. BE derived power spectra which differ from standard CDM in two key ways.

(1) The decay increases the density of relativistic degrees of freedom ('radiation' for short) and so delays the onset of matter–radiation equality. The length scale associated with the Hubble radius at this epoch is correspondingly modified. This modification is parametrized by θ (Bardeen et al. 1987) which is the ratio of energy density in relativistic species with a decaying particle to that without. Equation 5.1 now reads

$$r_{\rm H} = 16.0\,[\Omega h^2]^{-1}\,\theta^{1/2}\ {\rm Mpc} \tag{5.3}$$

and as a result the apparent value of Ωh (the effective shape parameter for CDM transfer functions) is dependent on the mass and lifetime of the decaying particle. An appropriate choice of these parameters can reconcile the $\Omega h \simeq 0.25$ value which best fits the observed large-scale structure with the theoretically favoured $\Omega = 1$ and the observationally implied $h = 0.5 - 1.0$.

(2) If the decay time exceeds $\sim 10 m_{\rm keV}^{-2}$ yr the universe can pass through *two* periods of matter domination, the first occurring when the density of undecayed particles exceeds that of relativistic species. This is followed by a phase dominated by the relativistic decay products. The second phase of matter domination arrives when the density of the cold dark matter exceeds that of the decay products. As a result of these processes the power spectrum is characterized by two length scales. Fluctuation growth can occur in the first matter-dominated epoch – providing greater small-scale power than is generated in the standard CDM scenario, and pushing the formation of sub-cluster-size objects to higher redshift.

This chapter extends the model of BE, allowing both the lifetime and mass of the hypothetical particle to vary. These parameters are then constrained by consideration of structure formation on large and small scales.

5.2.2 Power-Spectrum Scalings

It is useful to begin with a sketch of the dependence of θ on the mass and lifetime of the decaying particle. The units adopted will be

$$m \equiv \text{mass / keV} \tag{5.4}$$

$$\tau \equiv \text{decay time / yr.} \tag{5.5}$$

We will treat the decaying particle as a heavy neutrino, in the sense that the initial number density of the particle will be set equal to that for a massless neutrino. The energy density in decaying particles therefore becomes dominant over the radiation at time $t_{\rm eq1}$ when mc^2 is of the order of the radiation energy kT. Until this point $\rho \propto T^4$ and the age of the universe is $t \sim (G\rho)^{-1/2} \propto T^{-2} \propto m^{-2}$. Once they are non-relativistic, the density of heavy neutrinos scales as $\rho \propto a^{-3}$, whereas the density of radiation in the

standard massless neutrino model scales as $\rho \propto a^{-4}$. By the time of decay, the massive neutrinos therefore dominate the conventional relativistic density by a factor

$$\frac{\rho_{\rm decay}}{\rho_{\gamma+3\nu}} \simeq \frac{a_{\rm decay}}{a_{\rm eq1}} \simeq \left(\frac{\tau}{t_{\rm eq1}}\right)^{2/3} \propto m^{4/3}\tau^{2/3}. \tag{5.6}$$

Here $a_{\rm eq1}$ and $a_{\rm decay}$ are the scale factors at the first matter–radiation equality and at decay respectively; $\rho_{\rm decay}$ is the energy density in the relativistic decay products from the massive neutrinos; and $\rho_{\gamma+3\nu}$ is the standard energy density for radiation and three light neutrinos. This assumes an effectively instantaneous decay for the particles at time τ and a negligible mass for the two other neutrino species. We can now write

$$\theta = \frac{\rho_{\gamma+2\nu} + \rho_{\rm decay}}{\rho_{\gamma+3\nu}} \simeq \frac{1.45}{1.68}\left[1 + x(m^2\tau)^{2/3}\right], \tag{5.7}$$

with x a dimensionless constant. By a numerical solution of the full equations describing the problem, BE obtained $x \simeq 0.15$.

We now turn to the parameter dependences of the horizon sizes at the various epochs of matter–radiation equality. The horizon scale at the the time at which the non-relativistic density of the massive neutrinos first becomes dominant is given by equation 5.3. Now, a massive neutrino has $\Omega h^2 = m/0.095$ in our units (e.g. Kolb & Turner 1990, but scaling to the *COBE* $T = 2.726$ K); $\theta_{\rm eq1} = 1.45/1.68$; and $\theta_{\rm eq2}$ is as given above. We can therefore deduce the sizes of the comoving horizons at the two equality scales:

$$r_{\rm H}^{\rm eq1} = 1.41\, m^{-1}\ {\rm Mpc} \tag{5.8}$$

$$r_{\rm H}^{\rm eq2} = 14.9\, h^{-2}\left[1 + x(m^2\tau)^{2/3}\right]^{1/2}\ {\rm Mpc}. \tag{5.9}$$

The effect of this is to yield a power spectrum with two characteristic break wavenumbers, of order the reciprocal of the appropriate $r_{\rm H}$. The result can be modelled as the sum of two CDM spectra with differing power-law break lengths and different amplitudes, i.e.

$$\Delta^2(k) = \Delta^2_{\rm LSS}(k) + \alpha^2\Delta^2_{\rm LSS}(k/\beta). \tag{5.10}$$

Throughout, we shall express power spectra in dimensionless form:

$$\Delta^2(k) \equiv \mathrm{d}\sigma^2/\mathrm{d}\ln k = k^3 P(k)/2\pi^2. \tag{5.11}$$

The expression 5.10 says that the small-scale power spectrum looks like the CDM model which fits large-scale structure, but with a 'bump' superimposed which is a copy of the large-scale spectrum that has been shifted to smaller scales by a factor β and boosted by a factor α^2. The large-scale spectrum, $\Delta^2_{\rm LSS}$, would be just the standard BBKS CDM spectrum (Bardeen et al. 1987) with an apparent density

$$\Omega h|_{\rm apparent} = \Omega h \left(\frac{1.45}{1.68}\left[1 + x(m^2\tau)^{2/3}\right]\right)^{-1/2}. \tag{5.12}$$

The shift β is just the ratio of the horizon sizes deduced above:

$$\beta = 10.6 m h^{-2}\left[1 + x(m^2\tau)^{2/3}\right]^{1/2}. \tag{5.13}$$

The 'boost factor' α is more subtle. Until the decay epoch, the spectrum has only the small-scale break, and there can be no growth on these scales during the second period of radiation domination between $a_{\rm decay}$ and $a_{\rm eq2}$. The spectrum on larger scales can grow, which imprints the second break. If the spectrum has a primordial power-law index n, then $\Delta^2 \propto k^{3+n}$ on large scales; the difference in power at the two breaks (k_1 & k_2, say) is then given by a translational factor $(k_1/k_2)^{3+n}$ and the growth which occurs on large scales during the second period of radiation domination (a factor $[r_{\rm H}^{\rm eq2}/r_{\rm H}^{\rm decay}]^2$ in $\delta\rho/\rho$):

$$\alpha^2 = \frac{[r_{\rm H}^{\rm eq2}/r_{\rm H}^{\rm eq1}]^{3+n}}{[r_{\rm H}^{\rm eq2}/r_{\rm H}^{\rm decay}]^4}. \tag{5.14}$$

In the scale-invariant $n = 1$ case (assumed hereafter), this is just $\alpha = [r_{\rm H}^{\rm decay}/r_{\rm H}^{\rm eq1}]^2$. To obtain this ratio, note that $r_{\rm H} \propto t^{1/3}$ during the relevant (matter-dominated) phase; since we start at a time $\propto m^{-2}$ and end at τ, we finally obtain

$$\alpha = y\,[m^2\tau]^{2/3}, \tag{5.15}$$

where y is a further dimensionless constant which must be determined by fitting an exact integration. To obtain the value of this constant, the power spectrum 5.10 is compared

with the BE results for 17-keV neutrinos decaying at 0, 1, 10, 10^2, 10^3 and 10^4 yr. These spectra are reproduced in figure 5.1a. It was found useful to adopt a softening parameter γ such that that

$$\Delta^2(k) = \left([\Delta^2_{\rm LSS}(k)]^\gamma + [\alpha^2 \Delta^2_{\rm LSS}(k/\beta)]^\gamma \right)^{1/\gamma}. \tag{5.16}$$

This smooths the transition region at which the small-scale power of the second term becomes dominant over that of the first. The best fit obtained requires the prefactor for α to be $y = 1.29$, with $\gamma = 0.30$.

The above analysis has constructed the power spectra for a universe containing $\Omega = 1$ in CDM plus a decaying massive neutrino, including both the correct large-scale shape and the size plus location of the small-scale bump. The requirement for an apparent $\Omega h = 0.25$ fixes $m^2\tau$ if the true Hubble constant is known:

$$m^2\tau \simeq (125h^2 - 7)^{3/2}, \tag{5.17}$$

and this also fixes the boost parameter α. The only freedom in the model is then the location of the small-scale feature, which depends only on the mass. To illustrate this procedure, figure 5.1c shows three models with $m^2\tau = 120$, and fixing the apparent Ωh at 0.25. There is clearly a large range of possibilities for the power at $k \gtrsim 1$, which is what makes this model of interest.

To complete the picture we must allow for the damping of power that occurs due to free streaming of the massive neutrinos whilst they are still relativistic. An analysis of this effect by Bardeen et al. (1986) shows that damping corresponds to approximately Gaussian filtering of the linear power spectrum with $R_{\rm f} = 2.6(\Omega h^2)^{-1}{\rm Mpc} = 0.247 m^{-1}$ Mpc. In practice, the scales and masses of interest are such that this damping has a negligible effect. Finally, we have seen that there are a number of assumptions which lead to the restriction on α (assumed abundance of decaying particles; scale-invariant spectrum), there will be some advantages to abandoning physical preconceptions on occasion and treating α and β as completely free parameters which describe empirically any small-scale features in the power spectrum.

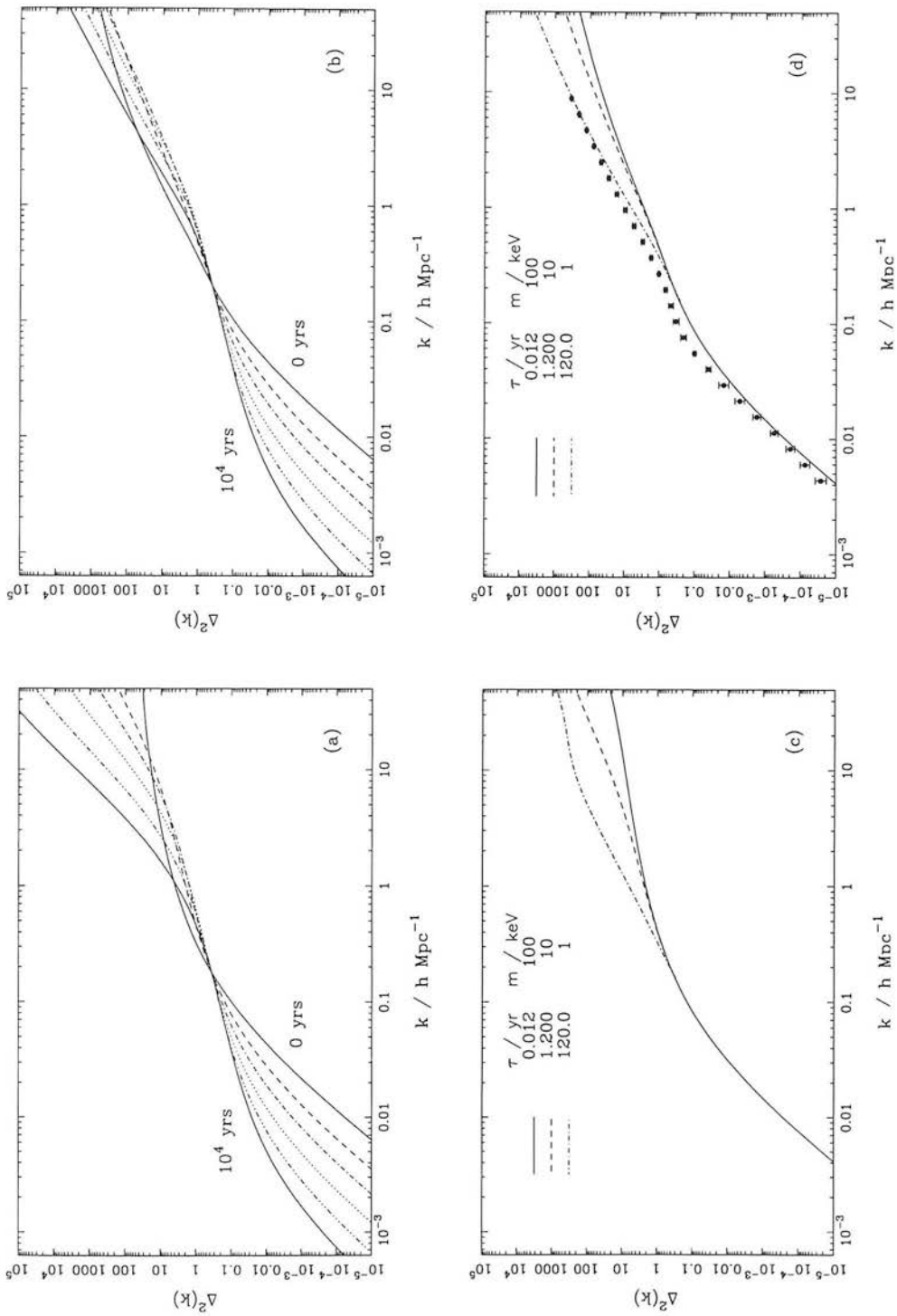

Figure 5.1: (a) Best fits to the Bond & Efstathiou (1991) power spectra obtained via the scalings of section 5.2. The mass is set at 17 keV and the lifetime varied from 0 to 10^4 yr. The 0-yrs curve is equivalent to standard CDM (BBKS). There is progressively more large-scale power as the lifetime is increased. $h = 0.5$ throughout. (b) The power spectra of (a) subjected to the non-linear correction of Peacock & Dodds (1994; PD). (c) Three power spectra with parameters satisfying $m^2\tau = 120$ and hence fulfilling the large-scale structure requirement (equation 5.2) for $\Omega h_{\rm true} = 0.5$. A range of small-scale behaviour is still possible. (d) The power spectra of (b) subjected to the non-linear correction of PD. The points with error bars are the power spectrum obtained by angular deprojection of the APM galaxy survey (Baugh & Efstathiou 1993).

5.3 Constraints

5.3.1 Normalization

We now need to place limits on the model by comparing its predictions with observations of structure in the universe. For this, we require normalization for the theoretical power spectra. This can be expressed as the linear theory rms density contrast when averaged over spheres of radius $8\,h^{-1}\,\mathrm{Mpc}$, i.e. σ_8. White, Efstathiou & Frenk (1993) use the observed abundance of rich clusters to deduce a hard allowed range of $\sigma_8 = 0.52 - 0.62$. Direct measurements of σ_8 from clustering require a knowledge of the bias parameter, and Feldman, Kaiser & Peacock (1994) give $\sigma_8 = 0.91/b - 0.18/b^{1.8}$ from the study of *IRAS* galaxies. Studies of peculiar velocities and comparison to density fields can yield estimates of b; such estimates are summarized in table 1 of Dekel (1994), and yield $1/b$ from this technique in the range $0.6 - 1.3$, corresponding to $\sigma_8 = 0.47 - 0.89$. The higher values can probably be eliminated by the pairwise random motions of galaxies. This issue was studied thoroughly by Gelb & Bertschinger (1994), who concluded that $\sigma_8 > 0.7$ was untenable, and that even $\sigma_8 = 0.5$ yielded uncomfortably high velocities. We shall adopt $\sigma_8 = 0.6$, which is perhaps at the higher end of the allowed range; since we are looking to see if extra small-scale power is required, it makes sense to be conservative and adopt the highest reasonable normalization for the large-scale mass spectrum. PD give a discussion of the relation between $\Delta^2(k)$ and σ_8, and argue that σ_8 largely measures the power at $k \simeq 0.2\,h\,\mathrm{Mpc}^{-1}$. For BBKS scale-invariant spectra, an accurate numerical fit for the effective wavenumber is

$$k_{\mathrm{eff}}/h\,\mathrm{Mpc}^{-1} = 0.172 + 0.011[\ln(\Omega h/0.34)]^2. \tag{5.18}$$

Finally, therefore $\Delta^2(0.18\,h\,\mathrm{Mpc}^{-1}) = 0.6^2$ is adopted as the normalization.

To evolve these linear power spectra to the present day ($z = 0$) involves non-linearities which can alter the power spectrum significantly at small scales. In evolving the $\Delta^2(k) \gtrsim 1$ portion of the power spectrum we use the formulae of PD (derived from the work of Hamilton et al. 1991, which was based on N-body simulations on the relevant scales) to incorporate the effects of non-linear evolution. Whilst this correction increases the

small-scale power for shallow power-law regions it actually removes power in regions with a strong k-dependence. Figures 5.1b & d show the non-linear correction applied to the spectra of 5.1a & c respectively.

5.3.2 High-Redshift Objects

One way of constraining the small-scale ($k \gtrsim 0.2\,h\,\mathrm{Mpc}^{-1}$) power is to require that it is sufficient to form the observed abundances of high-redshift objects, in particular quasars, radio galaxies and damped Lyman α systems. Radio galaxies have a well-defined mass, but this is rather large; they are also a rare population, so that current data do not set a very strong constraint on fluctuation spectra (Peacock 1994). Quasars are a more numerous population, but the ease with which observed quasar abundances can be attained is very much dependent on the (uncertain) mass assumed (e.g. Efstathiou & Rees 1988; Haehnelt 1993) and their use is avoided here.

More stringent constraints can be derived from recent deep measurements of damped Lyα systems with H I column densities greater than $\sim 2 \times 10^{20}$ cm^{-2} (Lanzetta et al. 1991). These have been used by several authors to investigate rival dark matter models. If the fraction of baryons in the virialized dark matter haloes equals the global value Ω_{B}, then these data can be used to infer the total fraction of matter that has collapsed into bound structures at high redshifts (Ma & Bertschinger 1994; Mo & Miralda-Escudé 1994). The highest measurement at $\langle z \rangle \simeq 3.2$ implies $\Omega_{\mathrm{HI}} \simeq 0.005$, and hence a collapsed fraction of $\simeq 10$ per cent if $\Omega_{\mathrm{B}} = 0.05$. The Walker et al. (1991) constraint to the baryon density is applied here, namely $\Omega_{\mathrm{B}} h^2 = 0.0125 \pm 0.0025$.

The assumption will be that the damped Lyα systems are the progenitors of present day spiral galaxies. Evidence for this view has been provided by absorption in lensed quasar systems, showing the systems to be of galactic dimensions (Wolfe et al. 1992). Furthermore the baryon mass inferred in present day galaxies is comparable to that of the damped Lyα systems at $z \simeq 3$. The photoionizing background prevents systems with circular velocities of less than about 50 km s^{-1} cooling sufficiently to form bound systems (e.g. Efstathiou 1992). We follow Mo & Miralda-Escudé (1994) and use this conservative velocity limit to estimate the minimum mass of object that the Lyα measurements detect.

Virial equilibrium for a halo of mass M and radius r_v demands

$$v_c^2 = \frac{GM}{r_v}. \tag{5.19}$$

For a spherically collapsed object this velocity can be converted directly into a Lagrangian comoving radius containing this mass (White et al. 1993):

$$r_0 = \frac{2^{1/2} v_c}{H_0 \Omega^{1/2}(1+z)^{1/2}(1+178\Omega^{-0.6})^{1/6}}. \tag{5.20}$$

The values introduced above require $r_0 > 0.15\,h^{-1}\,\mathrm{Mpc}$.

To use the measurement to constrain the candidate power spectra the well-known formalism of Press & Schechter (1974) is employed, which gives a collapsed fraction Ω_c above some mass scale M_{coll}, given a redshift z and a means of computing the $z = 0$ rms density contrast as a function of mass $\sigma(M, z = 0)$:

$$\Omega_c(> M_{\mathrm{coll}}, z) = 1 - \mathrm{erf}\,[\delta_c(1+z)/\sqrt{2}\sigma(M_{\mathrm{coll}}, z = 0)]. \tag{5.21}$$

$\sigma(M)$ can be evaluated by filtering the power spectrum on the required scale. Here we use a spherical 'top hat' filter of radius R_T (for which $f(k) = 3(\sin y - y\cos y)/y^3$ with $y = kR_T$) with a corresponding mass of $4\pi\rho R_T^3/3$. Our lower mass limit corresponding to $r_0 = 0.15\,h^{-1}\,\mathrm{Mpc}$ is therefore $M_{\mathrm{coll}} = 10^{9.6} h^{-1}\mathrm{M}_\odot$. δ_c is the critical overdensity required for collapse, which for a 'top hat' overdensity undergoing spherical collapse is 1.686. This canonical value has recently received support from N-body simulations on relevant scales by Ma & Bertschinger (1994).

Our power spectra are therefore required to produce an Ω_c which *exceeds* the Lyα collapsed fraction at all z, for $M > 10^{9.6} h^{-1}\mathrm{M}_\odot$. The true collapsed fraction could be higher than the observed one because some large fraction of the baryonic material in collapsed haloes could be ionized or in stars. Figure 5.2 shows how various models fare in meeting this demand. The points with errors are the H I fraction in damped Lyα systems from Lanzetta (1993) and Storrie-Lombardi et al. (1995). Standard $\Omega h = 0.5$ CDM, curve (c), successfully attains a sufficient collapsed fraction at the high- redshift

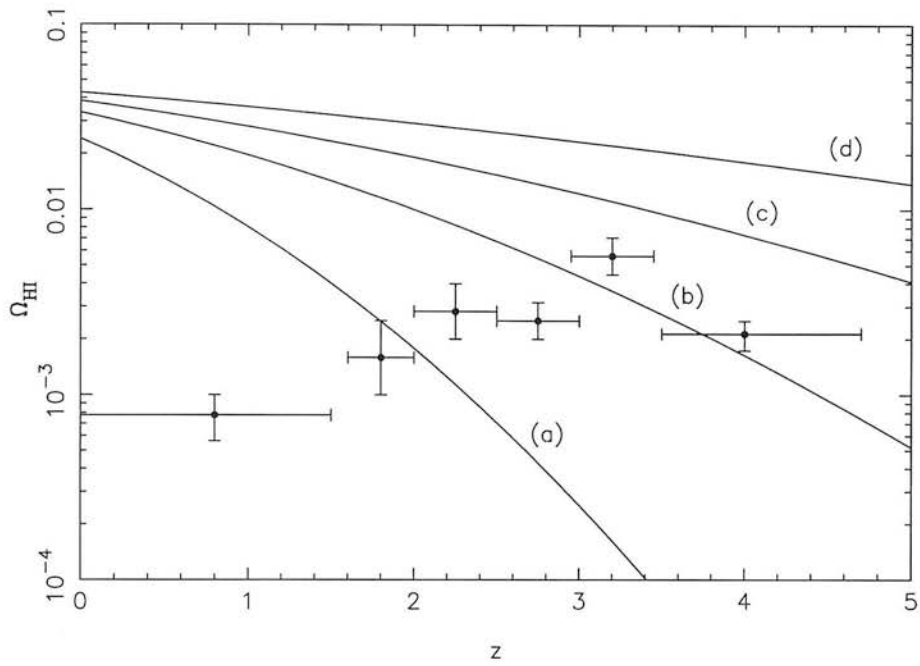

Figure 5.2: Collapsed baryon fractions (in terms of critical density) for four dark matter models. (a) Mixed Dark Matter with $\Omega_{\rm HDM}$=25 per cent, and $h = 0.5$, (b) CDM with $\Omega h = 0.25$, (c) CDM with $\Omega h = 0.5$, (d) CDM + relativistic decay model with $\Omega h = 0.5$, $\tau = 10$ yr and $m = 3.5$ keV. The points with 1σ error bars are damped Lyα system densities adopted from Lanzetta (1993) apart from the $z = 4$ point, taken from Storrie-Lombardi et al. (1995). Only models (c) and (d) have enough small-scale power to account for the collapsed fraction at $z \simeq 3.2$, though model (c) is ruled out by large-scale observations. We have assumed $\Omega_{\rm B} = 0.05$ throughout, each model being normalized to $\sigma_8 = 0.6$ at $z = 0$. All these comparisons assume $h = 0.5$; since $\Omega_{\rm HI}$ scales as h^{-1}, a higher true Hubble constant would lower the data points and make it easier for some models to satisfy the constraints.

end. Models that agree with the APM at large scales do less well. (b) $\Omega h = 0.25$ CDM and (a) MDM with $\Omega_{\rm HDM} = 0.25$ both fall short of having enough small-scale power. The $\Omega h = 0.5$ CDM + relativistic decay model (d) for $\tau = 10$ yr and $m = 3.5$ keV has ample small-scale power thanks to the extra bump from the first epoch of matter domination.

How seriously should these constraints be taken? A pure $\Omega h = 0.25$ spectrum does not fail to fit the data by a very large amount, and it is not implausible that such a model could be rescued by tweaking the assumptions in the calculations – perhaps most readily by assuming a larger $\Omega_{\rm B}$. Furthermore, the data themselves may not be definitive.

The inferred column density of a damped Lyα system is exponentially sensitive to its velocity width, and this can easily be artificially enhanced by superposition of Lyα forest systems in the wings. Storrie-Lombardi et al. (1995) also suggest that the $\langle z \rangle = 3.2$ Lanzetta point may be slightly too high. It cannot be claimed, therefore, that the need for extra small-scale power is rigorously established. Nevertheless, because it is unlikely that all collapsed H I can escape ionization, it is valuable to explore models that allow a significant increase of the collapsed fraction at high z.

5.3.3 Galaxy Clustering

The above constraints require only some minimum level of power; however, we are not at liberty to exceed this minimum by too large a factor. One limitation is provided by modelling the infrared Tully–Fisher relation between galaxy luminosity and circular velocity in the scenario of interest. A number of authors (e.g. Cole et al. 1994) have shown that standard $\Omega h = 0.5$, $\sigma_8 \simeq 0.7$ CDM has too much power on small scales, yielding, for a given luminosity, circular velocities which are 60 per cent larger than is observed. Without a relatively complicated modelling of galaxy formation the candidate spectra cannot be subjected to the same test.

A more straightforward upper limit to the power can be provided by comparison of the candidate power spectra with the observed small-scale power spectrum, best determined by angular deprojection of the APM galaxy survey (Baugh & Efstathiou 1993, who give data down to $k \simeq 8\,h\,\mathrm{Mpc}^{-1}$). The degree of small-scale bias relating the power spectrum of mass to that of the observed light is not known with any great accuracy, but the mass-to-light ratios of clusters strongly encourage us to believe that the small-scale clustering of light must exceed that of mass, if $\Omega = 1$. Although some models have been advocated in which this would not be true (e.g. the paper by Couchman & Carlberg 1992 on $b = 1$ standard CDM), it is reasonable to regard such a situation as observationally unacceptable. A conservative upper limit to the allowed degree of small-scale power can be set by demanding that the theoretical non-linear power spectrum of the mass at no point exceeds that of the light, as measured by the deprojection of the APM angular clustering. As with the Tully–Fisher relation, $\Omega h = 0.5$ CDM with our

chosen normalization fails this test.

5.4 Allowed Models

5.4.1 Limits on Parameters

The limits on the decaying neutrino models derived by the above methods are summarized in figures 5.3 and 5.4.

Figures 5.3a and b are more 'empirical' representations of the results in that they show the values of α and β that give a permissible power spectrum in light of the Lyman α and APM constraints. 5.3a and b differ in the assumed value of the Hubble constant, $h = 0.5$ and 0.75 respectively. The baryon fraction depends on h and is correspondingly modified. The large-scale portion of the theoretical power is fixed at $\Omega h = 0.25$ CDM and the small-scale high-k portion alone is varied. A band of acceptable values results, which narrows as h is increased, through the change in Ω_B. As β and α are dependent on the combination $(m^2\tau)^{2/3}$, selecting a particular value of h effectively fixes the 'growth' parameter α. The dot-dashed lines on the figure indicate the growth allowed when $m^2\tau$ is such that $\Omega h = 0.5$ and $\Omega h = 0.75$ are matched on to the large-scale observations. Within the usual range discussed for h ,therefore, the model is constrained to have a shift parameter $\beta \simeq 80 - 2500$ and a growth factor $\alpha \simeq 30 - 80$.

Figures 5.4a and b translate the results of figures 5.3a and b from general form, to apply specifically to the decaying neutrino model, identifying regions in the mass–lifetime plane ruled out by the constraints discussed above. Figure 5.4a refers to an $\Omega h = 0.50$ model with $\Omega_B = 0.050$, figure 5.4b to $\Omega h = 0.75$, $\Omega_B = 0.022$. The region disallowed by the Lyα structure formation requirement at $z = 3.2$ is indicated by the darker shaded areas. In order not to exceed the small-scale APM curve, the parameters must lie somewhere in the plane away from the lighter shaded region. The dashed line from top-left to bottom-right of each plot represents $m^2\tau \simeq 120$ and 500, the values required to reconcile $\Omega h_{\rm apparent} = 0.25$ with $\Omega h_{\rm true} = 0.50$ and 0.75. We can summarize

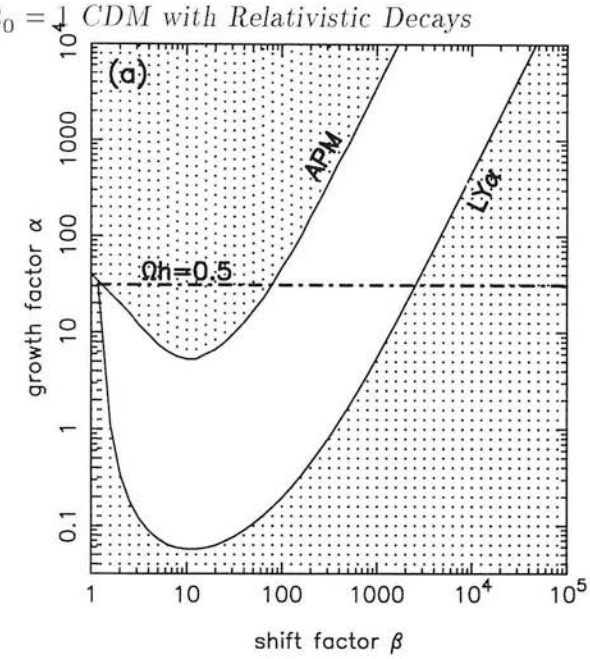

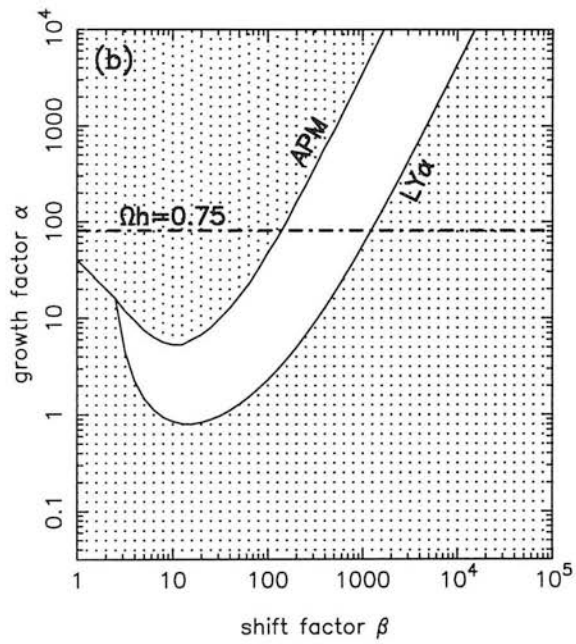

Figure 5.3: Constraints on the α and β parameters introduced in section 5.2.2. For a given value of β, α must lie *above* the Lyα line for a sufficient collapsed fraction to form at $z = 3.2$. α must however lie *below* the APM curve to avoid exceeding the APM power spectrum for $k > 1h$ Mpc^{-1}. A band of permitted α and β values results (unshaded region). Furthermore if $m^2\tau$ is fixed to match the large-scale structure then $\alpha =$ const. This is shown as the dashed-dotted line in each case: (a) $\Omega_{\rm B} = 0.050$, $\Omega h = 0.50$, (b), $\Omega_{\rm B} = 0.022$, $\Omega h = 0.75$.

the conclusions from these figures as follows:

$$\Omega h = 0.50 \;\Rightarrow\; 0.5 < m < 30 \text{ keV},\ 0.2 < \tau < 500 \text{ yr} \tag{5.22}$$

$$\Omega h = 0.75 \;\Rightarrow\; 2.0 < m < 30 \text{ keV},\ 0.5 < \tau < 100 \text{ yr}. \tag{5.23}$$

Are these parameter values physically plausible? The dot-dashed line in figures 5.4a and b shows the equation

$$m^5 \tau = 3 \times 10^4 \text{ keV}^5 \text{ yr}, \tag{5.24}$$

which is the form of a naive prediction for the relation between mass and lifetime for a particle that decays via the weak interaction. This takes the usual E^5 scaling of weak-interaction cross-sections and scales to the decay of the μ lepton. In neither case does this 'muon-decay' line cross the large-scale structure line in a permitted region; if the model is to be considered plausible, the decay physics involved must be more exotic.

5.4.2 Early Reionization

The existence of significant small-scale power in decaying-particle CDM can allow structures of mass $10^5 - 10^8 h^{-1} \mathrm{M}_\odot$ to form earlier than in the standard model and so may permit early reionization of the intergalactic medium. We have performed a brief analysis based on the method of Tegmark, Silk & Blanchard (1994). They estimate a parameter $f_{\rm net}$, the net efficiency of ionization processes from stars, and calculate $f_{\rm s}(M)$ the collapsed fraction of the universe (which gives rise to the star formation). These they relate to an ionization fraction χ such that

$$\chi \simeq 3.8 \times 10^5 f_{\rm net} f_{\rm s}. \tag{5.25}$$

Tegmark et al. give a range of $f_{\rm net}$ values they believe permissible, dubbing the top of the range 'optimistic' (in the sense of promoting early reionization), the bottom of the range 'pessimistic' and the median value 'middle-of-the-road'. Once $f_{\rm net}$ is set in this manner the requirement of 100 per cent reionization ($\chi > 1$) becomes a condition on $f_{\rm s}$ which can be calculated by the same Press–Schechter method as was used to analyse the Lyman

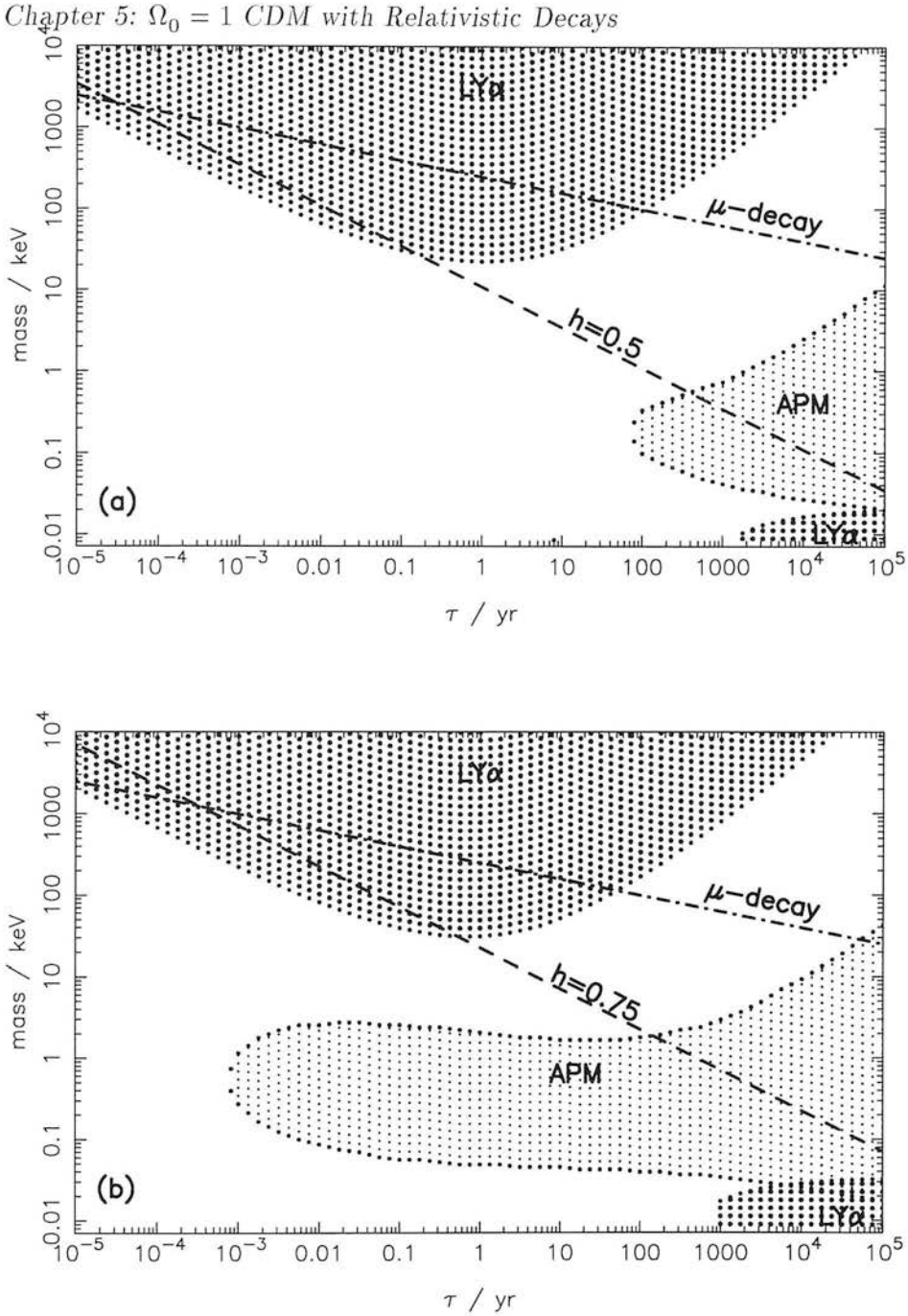

Figure 5.4: Constraints on mass and lifetime of hypothetical decaying neutrino. Limits are based on the damped Lyα fraction at redshift $z = 3.2$ (darker shaded region forbidden). Values that would exceed the APM power spectrum for $k > 1h$ Mpc^{-1} occupy the lighter shaded region. (a) Model constraints for $\Omega h = 0.5$, $\Omega_B = 0.050$. The dashed line shows the large-scale structure constraint for $\Omega h = 0.5$, the dot-dashed line the $m^5\tau \simeq$ const law for decaying heavy leptons. (b) Model constraints for $\Omega h = 0.75$, $\Omega_B = 0.022$. The dashed line shows the large-scale structure constraint for $\Omega h = 0.75$, the dot-dashed line the $m^5\tau \simeq$ const law for decaying heavy leptons.

α constraint. In order to get a feel for the sort of redshifts at which reionization could occur in our model we set $m^2\tau \simeq 500$, the value needed to give an apparent $\Omega h = 0.25$ in the case where $\Omega = 1$ and $h = 0.75$. We then vary the mass within the range 0.01 to 100 keV, τ being set at $500/m^2$. f_s is calculated for the resulting power spectra and used to derive the redshift at which reionization is complete.

Figure 5.5 shows the expected reionization redshifts for each of the $f_{\rm net}$ values suggested. The mass scale for the Press–Schechter integration (cf. equation 5.21) relates to the masses of the first galaxies to form, and there is a considerable range of possibilities from $10^5 h^{-1}{\rm M}_\odot$ (Couchman & Rees 1986) to $10^7 - 10^8 h^{-1}{\rm M}_\odot$ (Blanchard, Valls-Gabaud & Mamon 1992). Fortunately the power spectra are relatively flat in this range and the collapsed fraction is relatively insensitive to $M_{\rm coll}$. These results relate to the mass scale $10^7 h^{-1}{\rm M}_\odot$. In rough agreement with the Tegmark et al. results, typical reionization redshifts are in the range $\sim 10 - 200$ for an optimistic or middle-of-the-road $f_{\rm net}$. A pessimistic $f_{\rm net}$ permits early reionization only around $m \sim 1$ keV. CMB photons will be significantly scattered by the reionized plasma if the optical depth between $z_{\rm ion}$ and $z = 0$ is $\simeq 1$. To obtain this requires $z_{\rm ion} \simeq 50$ (e.g. Padmanabhan 1993) which can occur in the relativistic decay model for $m \sim 2 - 10$ keV – within our allowed range. Such a result may well be of importance in wiping out details of the last scattering surface on angular scales around $\sim 1^\circ$ (e.g. White, Scott & Silk 1994). White, Gelmini & Silk (1994) predict a sensitive dependence of degree-scale CMB anisotropies on the parameters of the decaying particle model. They suggest that $m^2\tau$ may, in principle, be determined from the CMB, with a large 1° bump for models with large $m^2\tau$. Such a feature is excluded observationally, but this work has shown that the small-scale power in this model may well cause sufficiently early reionization to complicate the measurements in this range.

5.5 Summary

This chapter has demonstrated that the parameters of the $\Omega = 1$ decaying-particle + CDM model can be constrained by small-scale power-spectrum requirements. Whilst we must generate sufficient power at $\sim 0.1 h^{-1}$Mpc scales to affect significantly the

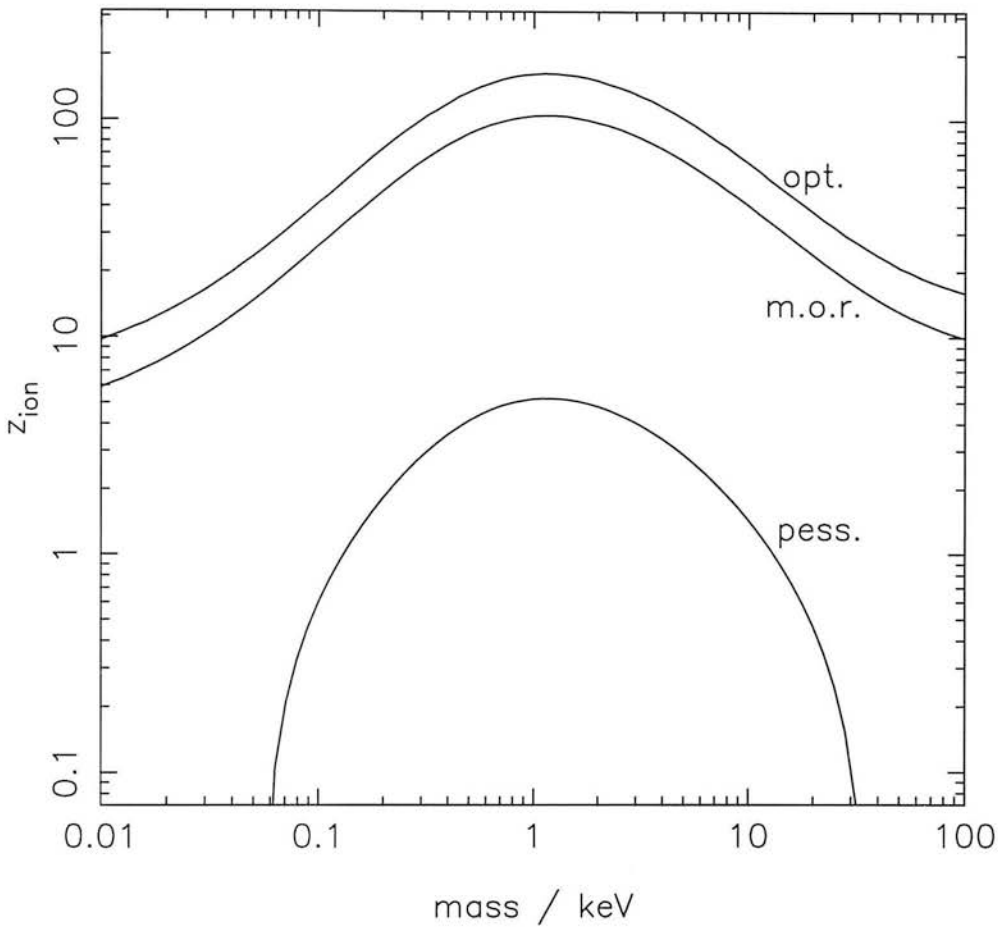

Figure 5.5: Reionization redshifts as a function of decaying-particle mass for the case $\Omega h = 0.75$, i.e. $m^2\tau \simeq 500$. We take the mass of the earliest galaxies to form to be $10^7 h^{-1}\mathrm{M}_\odot$ though the results are similar for the range $10^5 - 10^8 h^{-1}\mathrm{M}_\odot$. The labels 'optimistic', 'middle-of-the-road' and 'pessimistic' (abbreviated to opt., m.o.r., and pess.) refer to the efficiency of reionization by stars and are discussed in the text. Reionization occurs in the range $z \simeq 10 - 200$ for most of the parameter space investigated.

observed number of high-z damped Lyα systems, the existence of APM clustering data on comparable scales limits how much power can be added. Successful models of this general kind are therefore quite tightly constrained. Although present data cannot be claimed to provide definitive proof for a small-scale feature in the power spectrum, interesting consequences are predicted for future data on high-redshift objects.

Within an acceptable range for h, the mass of any decaying neutrino is constrained to lie between 0.5 and 30 keV and the lifetime to lie between 0.2 and 500 yr. Structure formation can commence sufficiently early in this scenario to permit early reionization

of the IGM. For a range of allowed parameters the reionization will inevitably occur sufficiently early to modify CMB fluctuations on scales of $\sim 1^\circ$ and below.

Although it thus has some attractive features, the model is not without its difficulties. Since we retain the Einstein–de Sitter universe, the problem of short Hubble times is not evaded, and may ultimately prove fatal. Furthermore, as with all high-density models, a convincing mechanism for biased galaxy formation needs to be supplied. However, the merit of the picture studied here is that it is reasonably well constrained and so testable directly in terms of particle physics. If the Einstein–de Sitter model is to be saved, this is arguably the least contrived way to do it.

Chapter 6

The Clustering of High Redshift Radio Galaxies

As chapter 1 has explained, the distribution of matter in the universe provides important tests for theories of the origin and evolution of large-scale structure in the universe. The distribution in space and the formation times of galaxies depend on the values of Ω_0, Ω_B and H_0, on the type of dark matter which is thought to be the dominant source of gravity on large-scales, and the nature of the initial perturbation spectrum (due to strings, inflation and so forth). Models in which these initial ingredients are specified make predictions about the shape and amplitude of the power spectrum of the initial fluctuations in the matter. This has a direct bearing on the observed clustering of galaxies and the formation epochs of massive high redshift objects (e.g. damped Lyα systems, radio galaxies and quasars).

There are, of course, significant difficulties in inverting cosmological observations to test these theories. Galaxy formation is a complex process involving forces other than gravity. The power spectrum on the scale of object formation has in general become *non-linear* such that simple extrapolations from the primordial power spectrum at early times are not trivial. Galaxy *clustering* studies can probe scales in which the perturbation spectrum is still evolving linearly though there are other difficulties, probably the most controversial example of which is that of *bias*. The biasing concept has arisen from

the realisation that the luminous objects in the universe, which we observe may not trace the mass, which we wish to infer. The issue was discussed in section 1.2.2 where the linear bias parameter b was introduced (equation 1.20). By this definition, b_i^2 is the factor by which the two-point correlation function of objects of class i exceeds the autocorrelation function of the mass fluctuations. Indeed Peacock & Dodds (1994) found a strong dependence of bias on object type, the relative bias factors for Abell clusters, radio galaxies, optical galaxies and IRAS galaxies being $b_{\rm A} : b_{\rm R} : b_{\rm O} : b_{\rm I} = 4.5 : 1.9 : 1.3 : 1$ for low redshifts $z \lesssim 0.2$. The content of this result is equivalent to the discovery that the scale length of clustering, r_i if $\xi(r) = (r/r_i)^{-\gamma}$, is such that $r_{\rm A} > r_{\rm R} > r_{\rm O} > r_{\rm I}$. These results however say nothing about the *evolution* of bias for a given class of objects, i.e. whether $b_i = b_i(z)$ where $b_i(z)$ may be an increasing or decreasing function of redshift. Indeed there are good theoretical reasons to expect the bias to have been greater in the past. These arguments will be dealt with at the end of this chapter. The main aim of this chapter is to establish limits on the high-redshift form of the bias for *radio galaxies*. Some recent controversial results have suggested that the bias may have a very strong dependence on redshift, i.e. $b(z) \gg b(0)$ for this class of objects. An understanding of these effects for a given class of objects will have important implications for the clustering of all galaxies at high redshift, since biasing mechanisms are presumed to operate in similar ways regardless of the object type used to trace the mass fluctuations.

6.1 A Brief History of Radio-Galaxy Clustering

In recent years, substantial work has gone into establishing the clustering of *optical* & IRAS galaxies, of which the majority are normal spiral galaxies at low redshift $z \gtrsim 0.2$. Probably the foremost example of such work was the APM galaxy survey (Maddox et al. 1990) which analyzed the clustering of Schmidt telescope $B_{\rm J} \lesssim 21$ galaxies. Here the angular correlation function $w(\theta)$ was found to obey a power law at small scales, $w(\theta) \propto \theta^{1-\gamma}$ with $\gamma \simeq 1.7$, and with a break at larger scales.

In contrast, radio galaxies form a rare and interesting subpopulation of extragalactic objects. Generally their hosts are giant elliptical galaxies of mass $\gtrsim 10^{12}\,M_{\odot}$. Radio galaxies provide a significantly different sample for clustering studies, radio surveys typ-

ically cover very large areas and sample very large volumes (crucially they can probe to $z \gtrsim 2$) but with sparser coverage owing to the intrinsic rarity of sources. On $\sim 10-100h^{-1}$ Mpc scales radio galaxies are useful in quantifying the large-scale structure of the universe – uniform source selection is relatively straightforward and the typical redshift of sources is $z \sim 1$. Radio surveys thus sample cosmologically representative volumes whereas optical surveys lack the necessary depth to investigate the large scale regime.

Establishing the degree of large-scale radio-clustering has been attempted by many authors with mixed success.

- The general isotropy of the radio sky is a long established result, e.g. Webster (1977) showed the radio galaxy count fluctuations in randomly placed Gpc sized cubes was $\lesssim 3\%$.

- Peacock & Nicholson (1991; hereafter PN) obtained redshifts for ~ 300 sources with $S \gtrsim 0.5$ Jy at 1.4GHz for which $z \lesssim 0.1$ and concluded that the $\xi(r) = (r/r_0)^{-\gamma}$ behaviour is observed for the sample, with $r_0 = 11.0 \pm 1.2\, h^{-1}$Mpc and $\gamma = 1.8 \pm 0.3$. This is greater clustering than for optical galaxies ($r_0 \simeq 5h^{-1}$ Mpc) and reflects the preference of the giant elliptical host galaxies for richer environments – clusters also have enhanced correlations with $r_0 \simeq 14h^{-1}$ Mpc (Sutherland 1988).

- More controversially, Kooiman et al. (1995; hereafter KBK) examine the angular correlations of 55,000 Green Bank catalogue sources (ν=4.85 GHz, $S > 25$mJy) and find a $w(\theta)$ amplitude 70 times in excess of that predicted by the PN parameters. One factor in the mismatch between the KBK and PN results is that they sample different redshift ranges – KBK obtain *angular* clustering data and use an uncertain redshift distribution $\phi(z)$ to compare their results with theory. There is, though, the possibility of very strong evolution of the observed clustering amplitude with redshift (i.e. $r_0 = r_0[z]$) due to biasing. To see if their proposed high-amplitude clustering is real is one goal of this chapter.

- Drinkwater & Schmidt 1996 analyse 263 Parkes sources (ν=2.7 GHz, $S > 0.5$Jy) and find they can rule out $r_0 \geq 50h^{-1}$ Mpc with 99.9% confidence. This would

formerly have been thought an uninteresting range, but the KBK analysis was thought to require r_0 in *excess* of this.

6.2 The Optical Stack Data

A current project at the Royal Observatory Edinburgh is the co-addition or "stacking" of Schmidt plates to generate star & galaxy catalogues with very faint limiting magnitudes. Over a period of 20 years a large set of exposures of a single UKST field (ESO/SRC 287) have been obtained in each of five colour bands. The field is centred on 21h 28m, $-45°$ (1950) and lies well outside the galactic plane with $b \sim -45°$. Hence it is ideal for extragalactic work. In the bands that we will be concerned with for our radio source investigation, J $(= B_J)$ and R, there exist 64 plates for each. An I-band stack of 30 plates is also available. Hawkins (1994) gives a detailed account of how the stacked datasets are constructed. Here we will give a brief overview of the stacking method and the properties of the resulting data. We will then describe how the data are used in our radio galaxy work.

Each plate to be stacked is digitized by the COSMOS machine producing an array of 16μm ($\sim 1''$) pixels, storing the value of the photographic transmission for each pixel. The array is then subjected to image analysis by the COSMOS software to obtain parameterized data for each image present. One plate is selected as the master plate and subdivided into $15'$ squares. A master coordinate system is then defined by requiring that stellar images in each $15'$ square on each plate have the same coordinates as on the master plate. In this way a position dependant coordinate transformation can be derived to rotate, translate and rescale each plate into the master coordinate frame. This is essential as differential refraction between plates taken at different hour angles means that the pixel data cannot be directly superimposed. Before addition the contribution of each plate is weighted by a factor $(\sigma_s\sigma_i)^{-2}$ where σ_s is the mean width at half maximum of stellar images on the plate and σ_i the sky noise in several standard regions. This optimizes the addition as the seeing and background noise vary from plate to plate. Each plate can then be added to the master pixel by pixel, using linear interpolation between the nearest four pixels to the transformed position. The pixels are added as the

logarithm of their photographic transmission, known as the photographic density. This is done because transmission is a highly nonlinear representation of the images on the plate. Taking the logarithm corrects for this somewhat and also has the advantage that the noise is roughly independent of density level – allowing a single weighting factor for each plate.

After stacking the co-added pixel data are analysed by COSMOS to produce parameterized data for each of the images. Calibration is carried out by comparison with deep CCD frames from the 3.6m ESO telescope at La Silla. Hawkins suggests that the limiting magnitudes for the J and R stacks are 25.5 and 24 respectively – close to the maximum improvement theoretically possible with 64 plates. Completeness limits are ~ 24 for J and ~ 22.5 for R. The 30 plate I-stack is only complete to $I \sim 20.5$ and is not of comparable depth. Here complete signifies the faintest magnitude at which *all* objects can be detected and limiting the faintest magnitude at which *any* object is found. There are reasons to expect traditional methods of star/galaxy discrimination to fail at these faint magnitudes. Principally it is because image profiles of faint galaxies *and* stars are dominated by the seeing of the Schmidt data (of order $3''$) confounding traditional methods of discrimination which rely on surface brightness differences between the two object types (e.g. MacGillivray & Stobie 1985).

A different method of calibration was attempted by me in the early days of my PhD. Here the stack was calibrated in intensity by reference to a CCD sequence of a $\sim 3'^2$ section of the field. After convolution with an appropriate Gaussian function to render the CCD seeing equivalent to the average for the stack, the two fields were aligned by least squares fit to a transformation allowing scaling, translation and rotation for ~ 20 star centroids. Following subtraction of the respective mean sky levels, corresponding pixels in the CCD and stack were compared and fitted to the functional form $I_{\rm CCD} = f(I_{\rm COS}) = A\, I_{\rm COS}\, e^{(I_{\rm COS}/B)^C}$, where A, B and C were chosen to give the best fit to $I_{\rm COS}$ (COSMOS pixel density) and $I_{\rm CCD}$ (linear CCD intensity). The form chosen gave a good agreement over a wide range of intensities. The function would then be used to generate a look-up table via which the COSMOS pixel data is linearised. Such a technique will be useful for future stack projects requiring accurate magnitudes for all the objects detected. This is most important for projects needing a large dynamic range in the

intensity measurements. For projects relying on faint galaxies, such as that described in this chapter the objects are near to the sky level intensity and nonlinearities in the plate response are not a problem. For this project, errors in a crude magnitude estimation are swamped by subsequent uncertainties in the redshifts derived from them (section 6.4) – so we use a simple magnitude estimator based on stellar CCD magnitudes.

The J & R stacks represent the deepest data available over a large contiguous area of $\sim 25\,\mathrm{degree}^2$. In the section 6.4 we describe how the data are used to detect the faint optical counterparts to $S \gtrsim 3$ mJy Molonglo radio sources. The radio search area is slightly greater than is covered by the optical stacks $\simeq 0.0083$ sr and so the number of $S \geq 6$ mJy sources which we could *hope* to optically identify is only 912 sources.

6.3 The Molonglo Survey Radio Data

Drs Dick Hunstead and Taisheng Ye of the University of Sydney, Australia have kindly provided us with a list of 1680 radio source positions (ν=843 MHz, $S > 3$mJy) in the ~25 deg^2 area of Schmidt field 287. The final radio map was constructed from a mosaic of 120 individual overlapping radio maps in the field, generated by the Molonglo Observatory Synthesis Telescope (MOST) described in Hunstead (1991). The rms of the individual maps is 1.5 mJy, though when several overlapping maps are combined – which is possible over most of the field – this is substantially lower and typically reaches $\sim$ 0.5 mJy (Ye – private communication). A simple point source fitting algorithm was used to generate the source list, with all sources of flux > 3 mJy catalogued. This effectively includes all objects with 6-sigma detections or better. The point-source fitting algorithm may cause the flux densities of extended objects to be underestimated but there should not be many such cases and we will not allow for the effect in this work. Number counts versus flux are shown in differential form in figure 6.1. The data are clearly incomplete for $S \lesssim 6$ mJy. The probable cause of this is that the mosaic technique provides incomplete coverage of faint sources in patches in the field where there are a below average number of radio map overlaps. If this is the case then the area coverage below ~6 mJy is not uniform and the fainter sources are not suitable for clustering analysis as they stand. Without direct access to the original radio data it is difficult to model the position dependency

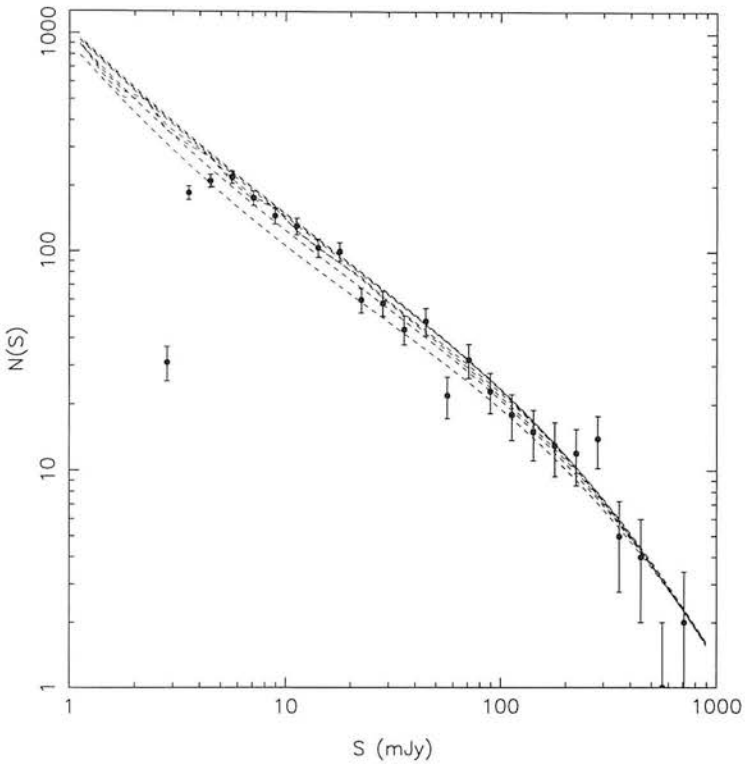

Figure 6.1: Differential number counts $N(S)$ vs. flux S for the Molonglo field 287 survey with $N^{1/2}$ error bars for each bin. The data are well described by a power law of index ~ 0.9 between ~ 6 and ~ 1000 mJy. The dashed lines are the predictions of the seven model radio luminosity functions from Dunlop & Peacock 1990. Below about 6 mJy the data clearly become incomplete.

of this incompleteness hence we take the simplest course of rejecting objects with $S < 6$ mJy in the clustering analysis – leaving 1071 sources in the list.

Ye has attempted to match the $S > 3$ mJy radio positions with optical objects on the COSMOS database of single J-plate data and has found ~ 200 matches within an offset of $\lesssim 5''$ (we will show his data when we perform our own matching). This is comfortably ahead of chance the association rate and shows that at least some of the radio sources have optical counterparts at $J \lesssim 21$ and $z \lesssim 0.5$. Here we attempt optical matching with deep 64 plate J and R-band stacks which should allow identification of most objects with $z \lesssim 1.5$. Crude redshift estimates can be made on the basis of the magnitudes of matching optical objects. It is our hope that the approximate radial distance information we can obtain in this way will help us overcome projection effects when we come to analyze the angular clustering of these objects.

6.4 Constructing the Radio Galaxy Catalogue

6.4.1 Radio/Optical Match-up and Calibration

The first step in matching optical images with our radio data is to extract small stack areas corresponding to the source locations. Software to convert RAs and DECs to the stack x, y coordinate system is employed but as this is part of the standard COSMOS repertoire it will not be described here. Armed with the Molonglo positions in stack coordinates we can proceed to the question of how large an area to extract around each. This is a question of how much offset we can expect between a radio source and its optical counterpart. Even without extended sources, the radio centroid positions are expected to be in error by $\sim 3''$ (Hunstead 1991 quotes this as a Gaussian r.m.s. of the offset) and the centroids of stack images by $\sim 1''$ at most, so we should allow at least $3''$ around each source even if the sources are perfectly coincident in real life. A further problem is that perfect coincidence may not be the norm when the radio and optical images are resolved and hence present an extended profile. The exact centroid position will then, to some extent, depend on the morphology and size of image. Clearly this is most significant for the optically bright galaxies and large radio sources.

We have no information on the angular size of our individual radio sources but we can estimate the relevant order of magnitude by comparison with other radio data. Oort (1988) has measured the median angular size of radio sources as a function of flux at 1412 MHz. He presents results for the median angular size $\theta_{\rm med}$ which can be approximately modelled as

$$\theta_{\rm med}/'' \simeq \sqrt{S/{\rm mJy}}. \tag{6.1}$$

A further issue we have considered is the presence of double-lobed Fanaroff-Riley II objects where the optical part of the galaxy lies in a radio-quiet region between the lobes. It has been found by Laing et al. (1983) that in 96% of FRIIs the optical centre lies within 0.2θ of the midpoint between the two radio hotspots - θ being the angular separation of hotspots.

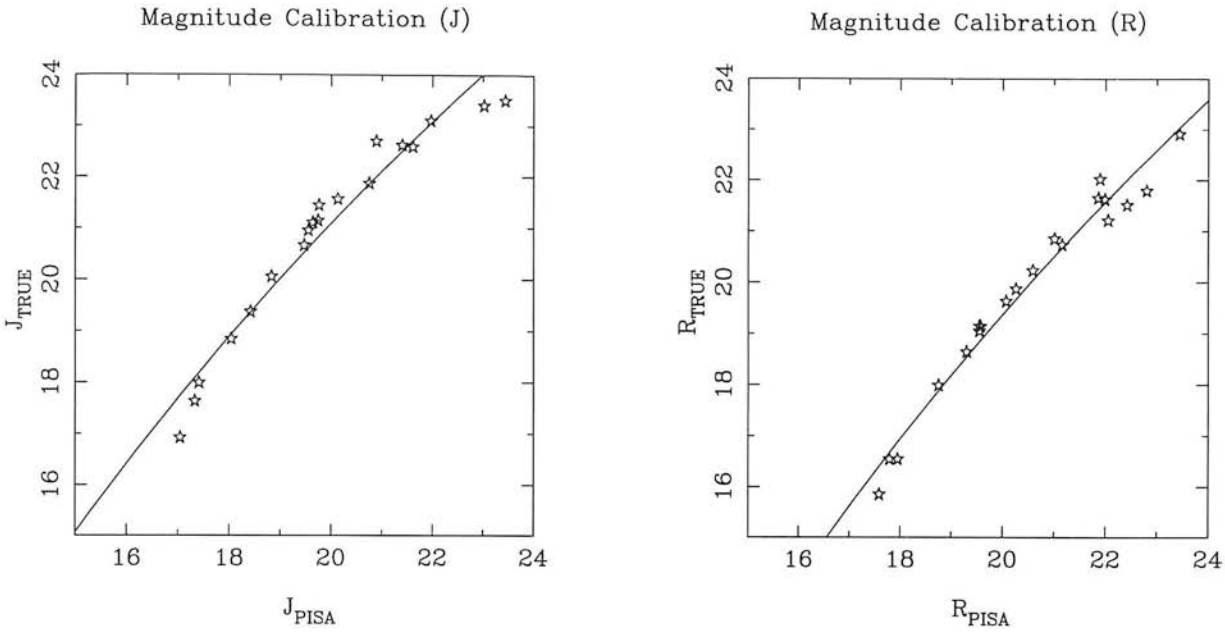

Figure 6.2: Two parameter fits to convert *PISA* magnitudes to observed CCD magnitudes. Measured star magnitudes for sequence stars on the J and R stacks are here fitted to CCD data from Hawkins (1986). The best fit formulae and standard deviations are $J_{\rm TRUE} = 48.20 \log_{10} J_{\rm PISA} - 41.61$, $\sigma_J = 0.45$ and $R_{\rm TRUE} = 53.18 \log_{10} R_{\rm PISA} - 49.81$, $\sigma_R = 0.34$

With all these considerations brought to bear it was thought safest to extract large areas to ensure that all optical counterparts, if any, were somewhere in the frame. We chose to take 64×64 pixel arrays (~ 1 arcmin^2) at each of the 1680 radio positions in each of J, R and I. To allow for the presence of FRIIs we also took 64×64 regions around the midpoint of any two sources separated by less than $1.5'$. There were 58 such locations. For each stack a 256×256 calibration field was also extracted corresponding to a region for which accurate CCD photometry was available. In order to obtain parameterized data for the objects in the extracted region, each 64^2 frame was subjected to image analysis using the Starlink PISA software. Beforehand each image was smoothed with a $3''$ FWHM Gaussian kernel to improve the signal-to-noise of the fainter objects in each field (by smoothing out uncorrelated pixel noise). The threshold for image analysis was set to be $2.5\sigma_{\rm sky}$ above the sky where $\sigma_{\rm sky}$ was the noise at the sky-level. We allowed any image of more than 3 contiguous pixels to be catalogued. The two 256^2 calibration regions were analysed in an identical fashion. PISA magnitudes (integrated pixel densities) were fitted to CCD magnitudes for the stars identified in Hawkins (1986) to allow a rough calibration of our data. The two parameter fits in J and R are shown in figure 6.2.

The effectiveness of the image analysis can be assessed by plotting the differential number-magnitude relation for the J and R data. Such plots are given in figure 6.3. They show that Hawkins' estimates of completeness are essentially correct with the number densities at $J \sim 24$ and $R \sim 22.5$ falling away from the $dN/dm \propto 10^{0.45m}$ power law found for galaxies in the magnitude range $20 - 25$ (e.g. Koo & Kron 1992). In this project the assumption is made that the magnitude limits are the same over regions within $\sim 2.5^\circ$ of the plate centre. Systematic effects such as vignetting are small ($\Delta m[\lesssim 4^\circ] \lesssim 0.1$ from Dawe & Metcalfe 1982) and random effects such as variations in plate sensitivities should be averaged out by the stacking process. The scatter in the redshift-magnitude relation is so large (section 6.4.2) that magnitude errors of ~ 0.5 would be needed before the results of this chapter were significantly affected. In addition the imposition of conservative completeness levels $J \leq 24$, $R \leq 22.5$ should prevent any position-dependent incompleteness in the image catalogue.

With all objects in each of the 64^2 J & R stack fields catalogued and calibrated we can turn to the problem of matching an optical image to each radio-source. This is not trivial since the expected radio positions may be in error by up to several arcsec and at these faint magnitudes fields crowded enough for confusion between different optical candidates to arise. The issue of assigning optical counterparts to radio sources in crowded fields has been considered by Downes et al. (1986) and we follow their straightforward "frequentist" method here. Given an optical candidate of magnitude m a distance r from the radio position one simply calculates the Poisson probability of such an object appearing by chance, that is the probability of something appearing in the parameter space ($\leq r$, $\leq m$). The candidate least likely to be there by chance is then selected as the candidate.

Given a surface density $\rho(< m)$ of objects brighter than m the expected number of objects within a radius r of the radio position is

$$\mu = \pi \rho(< m) r^2 \tag{6.2}$$

and the Poisson probability of at least one object appearing by chance is $P_m \simeq 1 - e^{-\mu} \simeq \mu$ for $\mu \ll 1$. If a probability threshold $P^\star$ is set the expected number of events for which

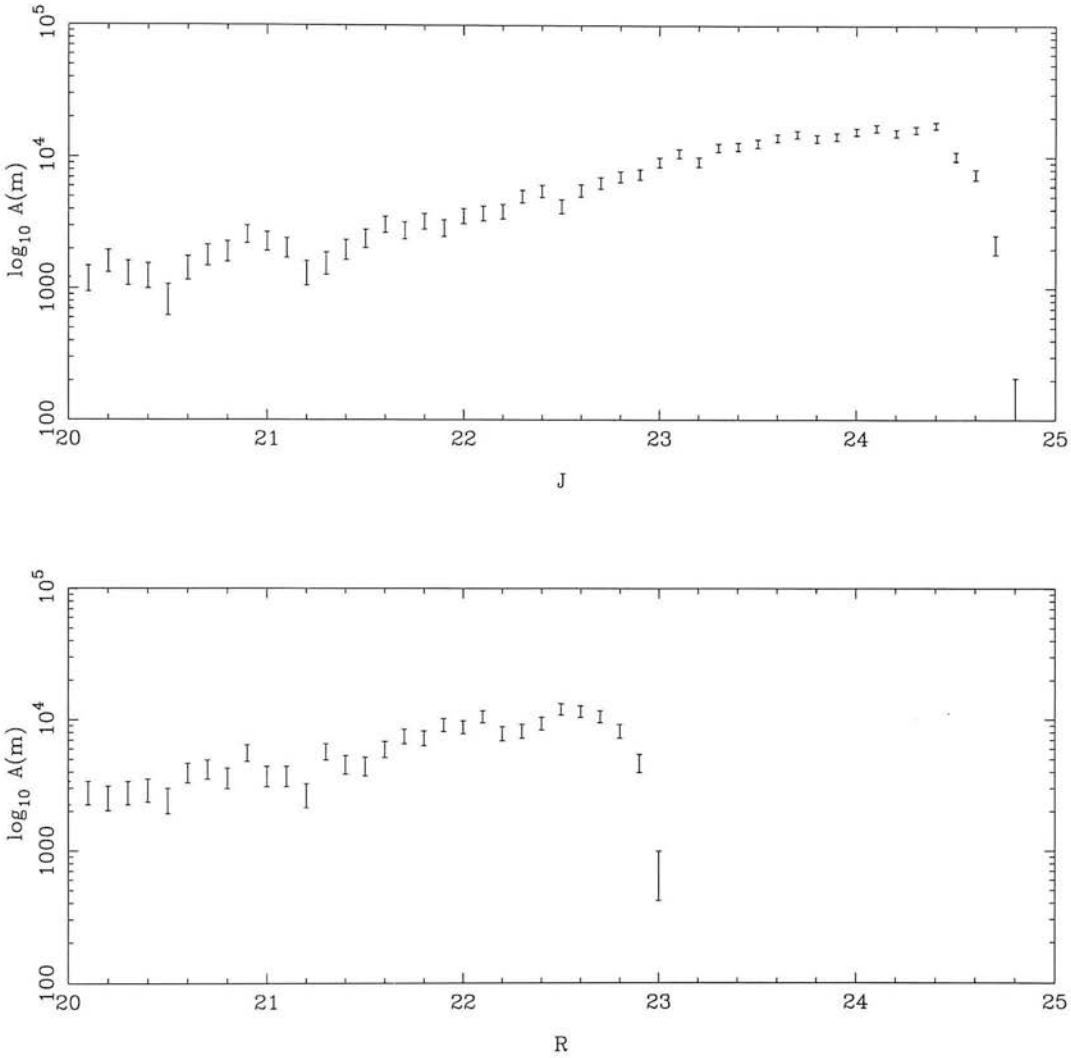

Figure 6.3: Differential galaxy counts $A(m)$ in number per square degree per magnitude for the J and R band stack data. The expected $A(m) \propto 10^{0.45m}$ relation is roughly observed in each case until incompleteness set in at $J \simeq 24$ and $R \simeq 22.5$. Note that the contribution of stellar images begins to dominate brighter than J, $R \sim 21$ changing the power law index.

$P_m \leq P^\star$ is

$$E = \quad P_c \quad P^\star \geq P_c \tag{6.3}$$

$$E = \quad P^\star\,[1 + \ln(P_c/P^\star)] \quad P^\star \leq P_c \tag{6.4}$$

where $P_c = \pi\rho(m_{\rm lim})r_s^2$ with $\rho(m_{\rm lim})$ the area density of *all* objects brighter than the limiting magnitude $m_{\rm lim}$ and there is an upper limit to the search radius such that $r \leq r_s$. Given $P^\star$ the Poisson probability of chance matchings occurring is $1 - e^{-E}$. Setting the value of $P^\star$ thus allows control of the number of spurious matches in the final sample.

Where multiple candidates appear within r_s the object least likely to be there by

chance (i.e. the lowest value of P_m) is picked. $\rho(< m)$ is estimated from the 64^2 cosmos fields using regions at least $10''$ away from the field centres and so avoiding contamination by most of the detectable radio sources. Each field contains ~ 20 objects and so a sizeable sample can be constructed with $\rho(< m)$ established in 0.2 mag intervals in J and R. The image density at the respective plate limits is $\rho(J_{\rm lim}) \simeq 2.5 \times 10^{-3}$ per square arcsec and $\rho(R_{\rm lim}) \sim 1.7 \times 10^{-3}$ per square arcsec.

For each field J and R images within $2''$ are matched to one another where possible – this is close enough for any confusion to be very rare while allowing for small centroiding offsets in each band. Thus there are effectively three datasets, the unmatched J-data, the unmatched R-data and a catalogue of images detected in *both* J and R.

Before we apply the machinery of the above ranking system it is important to check that there are no *systematic* offsets between the optical and radio positions. This is most simply achieved by stacking the combined optical data for the 1071 $S \geq 6$ mJy fields such that the central pixel, corresponding to the inferred radio position, is coincident for each of the co-added frames. Even given significant *random* offsets in the positions of radio sources and their optical counterparts we should expect to see a significant peak in the centre of the stack, due to an enhanced density of objects (the true optical counterparts) over the assumed random background. The results of this test are shown in figures 6.4 (a)–(d). Figures (a) and (b) show contour plots of the stacked fields for two subsets of the data, (a) is the half of the fields with the lowest RAs (b) the half with the highest RAs. It is clear that some sort of systematic effect is present: in figure (a) the peak object count is offset down and to the left, $\sim 2''$ away from the central position whereas in figure (b) the peak is central. Neither plot is very circularly symmetric. To attempt to correct for this offset a transformation allowing rescaling, rotation and translation was applied to the data such that

$$x' = x + a_1 \mathrm{RA} + a_2 \mathrm{DEC} + a_3 \tag{6.5}$$

$$y' = y + a_4 \mathrm{RA} + a_5 \mathrm{DEC} + a_6 \tag{6.6}$$

where the a_n are fitted by finding the values which minimize the sum of the squares of the offsets of *all* objects within $4''$ of the original radio position $(0, 0)$. The assumption is that in this range the number of *true* radio galaxy images will exceed the random background

so that the radio-optical offsets dominate the data given to the fitting routine. The best fit is provided by $a_1 = 5.353$, $a_2 = 0.261$, $a_3 = -103.048$, $a_4 = 0.010$, $a_5 = -0.292$, $a_6 = -13.410$. These values cause offsets in the range $x' - x \simeq -1.5 \rightarrow 1.5$ and $y' - y \simeq -0.5 \rightarrow 0.5$ over the range of RA and DEC covered by UKST field 287. The origin of this mismatch is unclear, it could be due to transformation errors in either the COSMOS or the radio data. Problems with single plate COSMOS parameters are discussed by Unewisse et al. (1993) and may be relevant, though having largely sorted the issue out with the transformation above, it is not investigated further here. Figure 6.4 (c) shows the combined optical data for *all* the radio sources before this correction is applied and figure (d), the same data with the correction. The peak in figure (d) is slightly more compact and symmetrical than that in (c) and is well fit by a Gaussian point spread function with $\sigma \simeq 2.7''$, which is close to the expected random error in the radio positions.

The following table gives the cumulative numbers of matches versus radio-optical offset for (i) Ye's match of all > 3 mJy sources with images from the COSMOS database (Hunstead – private communication), (ii) matches between the > 6 mJy radio sources and combined J and R data before the transformation and (iii) the match-up after the transformation. There is a clear gain in detection when the transformed positions are used with $\sim 20\%$ more objects within $1''$ of the radio position. The data also reproduce Ye's (1994) optical matching tolerably well when $J, R < 21$ images are matched to the whole > 3 mJy radio source list, which is a useful consistency check on the procedure so far.

offset	Ye (1994)	No trans.	Trans.
$< 1''$	23	49	61
$< 2''$	62	141	183
$< 3''$	118	269	301
$< 4''$	181	367	396
$< 5''$	224	465	486
$< 6''$	260	573	569

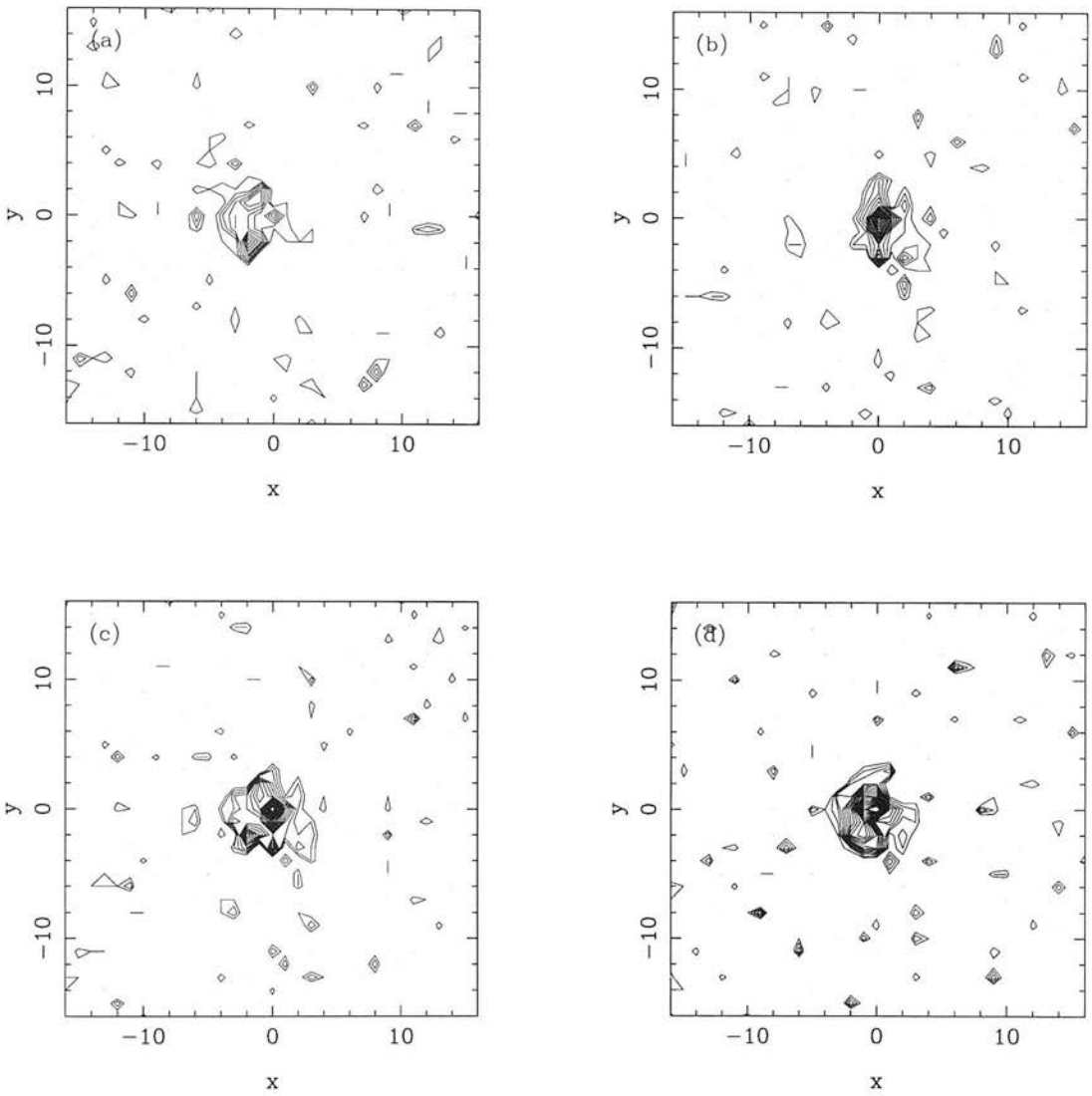

Figure 6.4: Contour plots of image density for superpositions of the optical data around each radio position. $(0,0)$ is the radio position when transformed to the COSMOS x, y coordinates for each field.

Having corrected for systematic effects we can return to the ranking procedure which tells us how to proceed when the *random* offsets in radio-optical position are comparable to the distance between optical objects, as here. The search radius r_s is set at

$$r_s = [(2\sigma_R)^2 + S(\mathrm{mJy})/6]^{1/2} \tag{6.7}$$

where $\sigma_R \simeq 2.7''$ is the radio positioning error established above and then allowed to vary by 2 standard deviations which should enclose $\sim 86\%$ of the sources. The S-term allows for significantly extended radio sources. From equation 6.1 we know that the angular extent of sources is roughly $S^{1/2}\ ''\,\mathrm{mJy}^{-1/2}$. Assuming the optical counterpart

can be anywhere in a circular region of radius $0.5S^{1/2}$ and calculating the r.m.s. offset gives $\langle \Delta r^2 \rangle^{1/2} = S(\mathrm{mJy})^{1/2}/\sqrt{24}$. Twice this r.m.s is allowed for, as with the Gaussian positional offset. The two terms are then added in quadrature to yield r_s. A maximum r_s of $18''$ is set to avoid going too near the edge of the pixel data for each field. $r_s = 18''$ is enforced for the 58 fields containing the putative lobe centres of FRII objects, consistent with being within 0.2θ of the midpoint of lobes separated by $\theta \leq 1.5'$.

Within r_s the optical images are then weighted according to $(P_J P_R)^{1/2}$, P_J or P_R depending on whether the object in question is matched or unmatched, and the best candidate (lowest P) picked. If no image lies within r_s in either band then a null output is recorded. Matchings in the 58 inter-lobe fields are accepted if a candidate there has a lower P value than any object at the lobe positions. In this case matchings in the two fields centred on the assumed lobes are rejected. This occurred in 10 cases.

A final catalogue of matchings is made when a threshold is applied to the data such that all objects with a probability of being due to chance coincidence with the radio position $P > P^*$ are rejected. Setting the threshold P^* is a matter of balancing the total number of objects detected, N_D say, against the number of objects appearing by chance, which can be estimated as $N_\mathrm{C} \simeq \sum_i E(P^*)$ where E is found using the expression 6.4 and summed over all the fields searched. Here P_c is calculated as $P_\mathrm{c} \simeq 0.5\overline{\pi r_s^2}[\rho(J_\mathrm{lim}) + \rho(R_\mathrm{lim})] \simeq 0.26$ with the stack parameters and a mean search area $\overline{\pi r_s^2} \simeq 127$ arcsec^2 when r_s is calculated as above for each field. The detection fraction is roughly $(N_\mathrm{D} - N_\mathrm{C})/N_\mathrm{D}$.

Applying these estimates to the optical matches for the 912 $S \geq 6$ mJy sources and 58 inter-lobe regions which lie on the stack gives the following results.

$P^\star$	$E(P^\star)$	N_D	true matches	det. frac.
0.001	0.0064	96	~ 91	95%
0.006	0.0294	278	~ 250	90%
0.018	0.0636	410	~ 349	85%
0.040	0.1086	530	~ 424	80%
0.066	0.1466	594	~ 446	75%
0.107	0.1831	634	~ 444	70%

It is apparent from this table that the number of estimated true matches $N_{\rm D} - N_{\rm C}$ steadily increases with $P^\star$ upto around $P^\star = 0.066$ and thereafter no improvement is made. At higher thresholds the number of coincidental matchings steadily increases and just reduces the fraction of true matchings. Choosing the threshold $P^\star$ depends on what the catalogue will be used for as there is a tradeoff between detection numbers and the signal to noise. For clustering studies the presence of a "rogue" fraction $N_{\rm C}/N_{\rm D}$ reduces the amplitude of correlations by a factor $\simeq (1-N_{\rm C}/N_{\rm D})^2$ assuming the chance matchings to be randomly distributed. On the other hand, error bars on $w(\theta)$ scale as $N_{\rm D}^{-1/2}$. The *significance* of a clustering signal in any one bin (i.e. the size of the error compared to the amplitude of the measurement) will therefore scale as

$$\frac{w(\theta)}{\sigma_w} \propto \sqrt{N_{\rm D}} \left(1 - \frac{N_{\rm C}}{N_{\rm D}}\right)^2 . \tag{6.8}$$

This has a maximum at $P^\star = 0.036$ which will be adopted for the rest of this chapter. At this value there are optical matchings for 506 objects of which roughly 20% will be spurious.

6.4.2 Redshift Estimation

Given estimates for the J and R magnitudes of the optical counterparts to the radio sources, an attempt to infer the redshift of each object can be made. This proceeds by trying to establish a relation between the optical magnitudes and the redshifts of radio galaxies. The optical Hubble diagrams for radio galaxies have relatively low scatter

about a well-defined magnitude-z relation (e.g. Spinrad & Djorgovski 1987) owing to the low spread in absolute magnitude of radio sources.

Here we establish the J and R band Hubble diagrams using a sample of ~ 60 radio galaxies from the Leiden-Berkeley Deep Survey (LBDS), described in Peacock, Dunlop & Windhorst, 1996. We assume that the relations will be the same for the LBDS data as for our Molonglo sources which is reasonable given the selection criteria of the LBDS sample, $S \geq 1$ mJy at $\nu = 1.4$ GHz. Optical data for these galaxies is provided in the photographic R and J bands (as used here) and the Gunn-Thuan g and r bands. Where only g and r data is available we use the rough conversions $R \simeq r - 0.3$ (Dunlop & Peacock 1993) and $0.7J \simeq g - 0.3r - 0.2$ adapted from Jorgensen (1994).

Plots of z versus R and z versus J are given in figure 6.5. Three parameter fits for $z(R)$ and $z(J)$ give us

$$\log_{10} z_R = -7.90 + 0.544R - 0.00822R^2 \tag{6.9}$$

and

$$\log_{10} z_J = -6.63 + 0.386J - 0.00426J^2 \tag{6.10}$$

The respective scatters in $\log_{10} z$ are 0.16 and 0.27 respectively, in terms of z these are $\Delta z_R = 0.37 z_R$ and $\Delta z_J = 0.62 z_J$. These relations are the optical analogues of the infrared $K(z)$ relation for radio galaxies (Lilly, Longair & Allington-Smith 1985) which for $z \lesssim 1$, $K \lesssim 18$ yields

$$\log_{10} z \simeq -5.368 + 0.384K - 0.00385K^2. \tag{6.11}$$

The scatters on the $z(R)$ and $z(J)$ relations are quite large, this can be improved slightly by using both relations in combination where both magnitudes are measured such that

$$z_{RJ} = \frac{z_R/\Delta z_R^2 + z_J/\Delta z_J^2}{1/\Delta z_R^2 + 1/\Delta z_J^2} \tag{6.12}$$

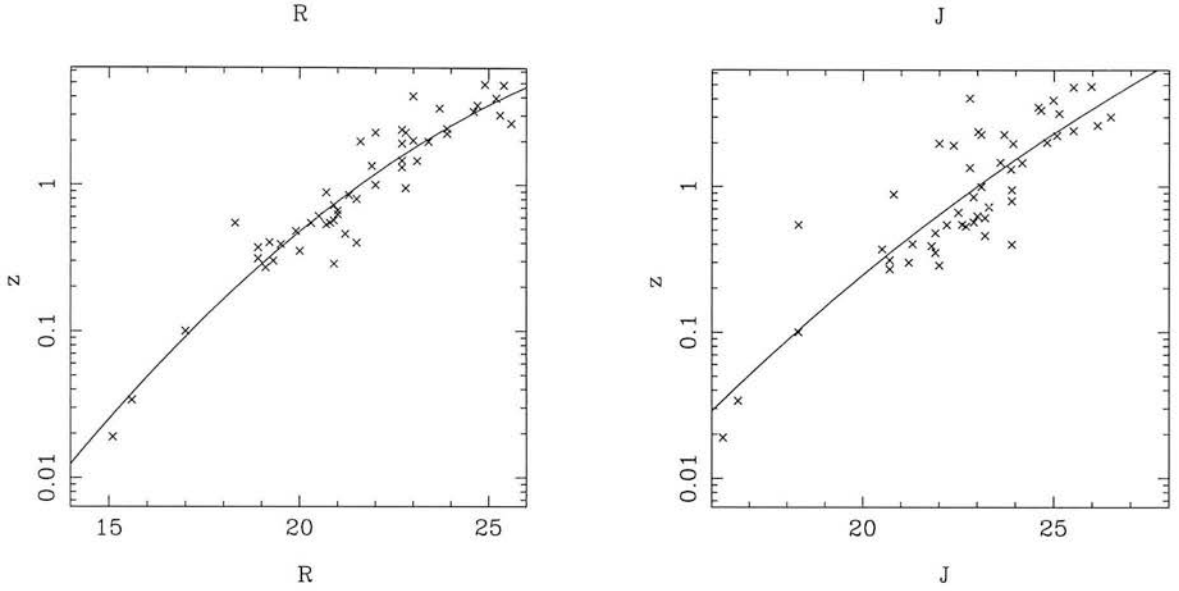

Figure 6.5: Three parameter fits for (a) $z = z(R)$ (b) $z = z(J)$ for the LBDS survey (Peacock, Dunlop & Windhorst, 1996). The scatter for $z(R)$ is substantially lower than for $z(J)$.

with a scatter of roughly $\Delta z_{RJ} = 0.31 z_{RJ}$. This is still quite a large scatter but this should not affect our clustering analysis too greatly. For the clustering studies undertaken here, it is more important that the galaxies are *ordered* correctly in redshift distance, as this will be the parameter used to divide the data up into subsets before the clustering analysis. The clustering amplitude in each subset will be parameterized by the median redshift of the galaxies which, with large numbers of objects, should be a reliable estimate, even if the errors in individual redshifts are quite large. At the completeness limits of the stack data, $J \leq 24$, $R \leq 22.5$ relations 6.9 and 6.10 imply a limiting redshift of $z = 1.5$ for the sample.

Our final catalogue is now complete and we can compare the observed numbers of identified sources and their redshift distribution with those expected. One estimate of the required quantities can be obtained by integrating the local radio luminosity function. This has been derived at 1.4 GHz by Windhorst (1984) and fits well to the parametric form

$$\frac{d^2N}{dV\, d\log_{10} P} = \phi^* \left(1 + \frac{P}{P^*}\right)^{-1} \tag{6.13}$$

with $\phi^* = 10^{5.2} h^3\,\mathrm{Gpc}^{-3}$ and $P^* = 10^{22.1} h^{-2}\,\mathrm{WHz}^{-1}\mathrm{sr}^{-1}$. The redshift distribution is

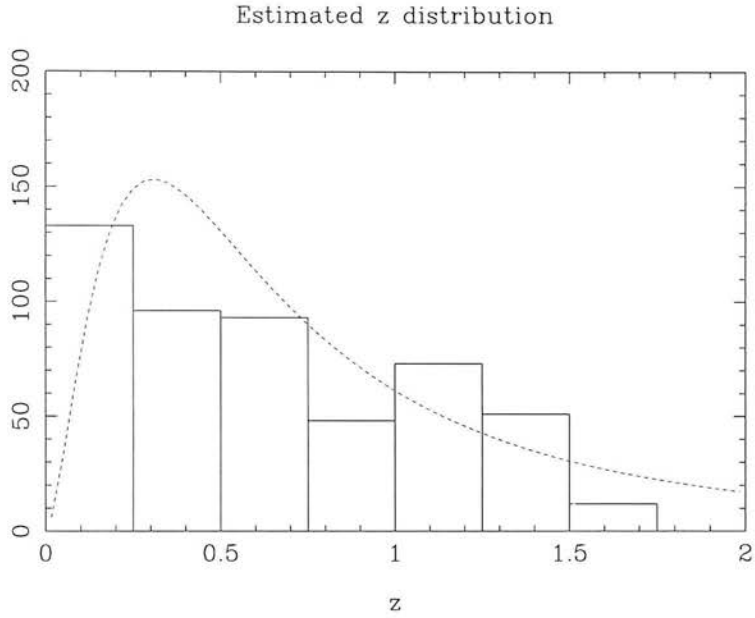

Figure 6.6: Redshift distributions for the 506 best identifications at $\gtrsim 6$ mJy as a histogram in bins of $\Delta z = 0.25$. Note the sudden drop above $z \simeq 1.5$ due to the optical completeness limit being reached. The dotted line is the expected distribution for a uniform flux-density limit of 6 mJy from Windhorst (1984).

then

$$\frac{dN}{dz} = \int_S^\infty \frac{A\phi^*}{\ln 10} \frac{dV}{dz} \frac{dS}{S(1 + P(z)/P^*)} \tag{6.14}$$

with

$$P(z)/(h^{-2}\mathrm{WHz}^{-1}\mathrm{sr}^{-1}) = 8.57 \times 10^{25}(S/\mathrm{Jy}) \left[2\left(1 - \frac{1}{\sqrt{1+z}}\right)\right]^2 (1+z)^{1+\alpha} \tag{6.15}$$

and our survey covering $A \simeq 0.0083$ sr. We will take a spectral index of $\alpha = 0.8$ to be representative.

The value of this function for $S \geq 6$ mJy is shown in figure 6.6 along with the redshift distribution estimated from the sample. The total number of sources out to $z \simeq 1.5$ expected in this model is obtained by integrating equation 6.14 with respect to z and yields $N_{\mathrm{TOT}} = 505$. This is about the total number observed but recall that only about 80% of this sample is thought to be correctly identified, therefore this model RLF predicts the incompleteness to be about 20%.

These, then, are the predictions in a *non-evolving* model, i.e. ϕ^* and P^* have no z-dependence. This is certainly too strong an assumption over a redshift range $\gtrsim 1$.

Interestingly though, this model seriously under-predicts the numbers in the lowest redshift bin $z = 0 \rightarrow 0.25$, the measured value is 133 whereas the model estimate is 87 sources in this range. This discrepancy is too large to be accounted for by the expected fraction of misclassified matchings $\sim 80\%$, unless the ranking scheme of the previous section is *biased towards optically brighter objects.* This would shift the proportion of misclassified objects towards the brighter end of the sample. It is quite easy to construct models in which this is the case - we have effectively weighted our matching candidates by $1/P_{\rm bg}(m)$ i.e. the inverse of the probability distribution of the *background* as a function of magnitude. More reliable is the likelihood ratio technique (e.g. Sutherland and Saunders 1992) where the weight would be $P_{\rm RG}(m)/P_{\rm bg}(m)$ where $P_{\rm RG}(m)$ is the probability distribution of the *actual* radio galaxy magnitudes. If $P_{\rm RG}$ is a steeply rising function of magnitude then bright objects will be *over-weighted* by our system and faint objects *under-weighted.* Such an effect may be operating here.

Figure 6.7 shows the predictions of the seven RLF models discussed in Dunlop & Peacock (1990; hereafter DP). These models were constrained by comparison to a range of different datasets based on number counts as a function of flux and frequency. The five curves in figure 6.7a show five predicted redshift distributions for the Molonglo sources based on model RLFs which were matched to the DP data using a free-form fitting technique. A significant variation is seen. Models 1 and 2 are relatively flat and do not appear seriously discrepant with our data out to the limiting redshift of ~ 1.5. Model 3 rises steeply in the range $z \sim 0.25 \rightarrow 1$ and then falls as steeply for $z \gtrsim 1$. In models 4 and 5 a similar high redshift peak occurs at $z \simeq 1.25$, though the predicted redshift distribution is broader and flatter. Notably models 1 and 3 predict ~ 100 objects in the first bin and the mismatch with the data could be accounted for here by the mismatching of $\sim 20\%$ of the sources in the catalogue. Figure 6.7b show the redshift distributions of (i) a model in which there is pure luminosity evolution of the radio sources and (ii) one in which there source density and only positive luminosity evolution. Both these fit our data quite well beyond the first bin where again there is a serious under-prediction of objects.

The susceptibility to magnitude dependent bias discussed above is still relevant to the comparison of the DP predictions and the data. Given the wide range of behaviour con-

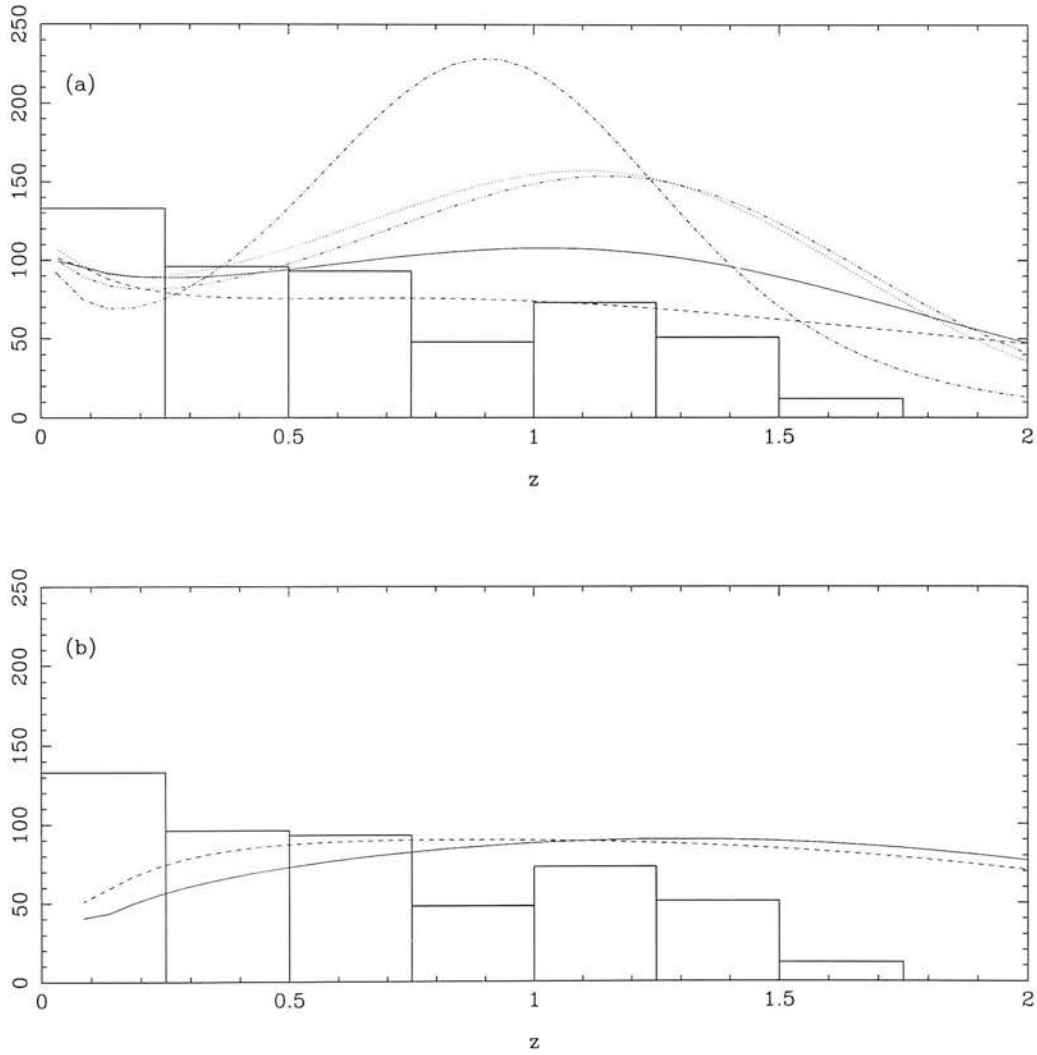

Figure 6.7: Redshift distributions predicted by model radio-luminosity functions from Dunlop & Peacock (1990) versus the estimated distribution of the Molonglo-Schmidt stack catalogue. (a) Five models derived from free-form fitting to a selection source count datasets: RLF1 – filled line, RLF2 – dashed line, RLF3 – dot-dashed line, RLF4 – dotted line, RLF5 – dash-three dots line. (b) Two models based on pure luminosity evolution (filled line) and density evolution with purely positive luminosity evolution (dashed line). The seven models show a wide range of behaviour. Apart from the first bin, $z = 0 - 0.25$, where all the models significantly under-predict the numbers, the flatter models 1, 6 and 7 offer the best match to the observations.

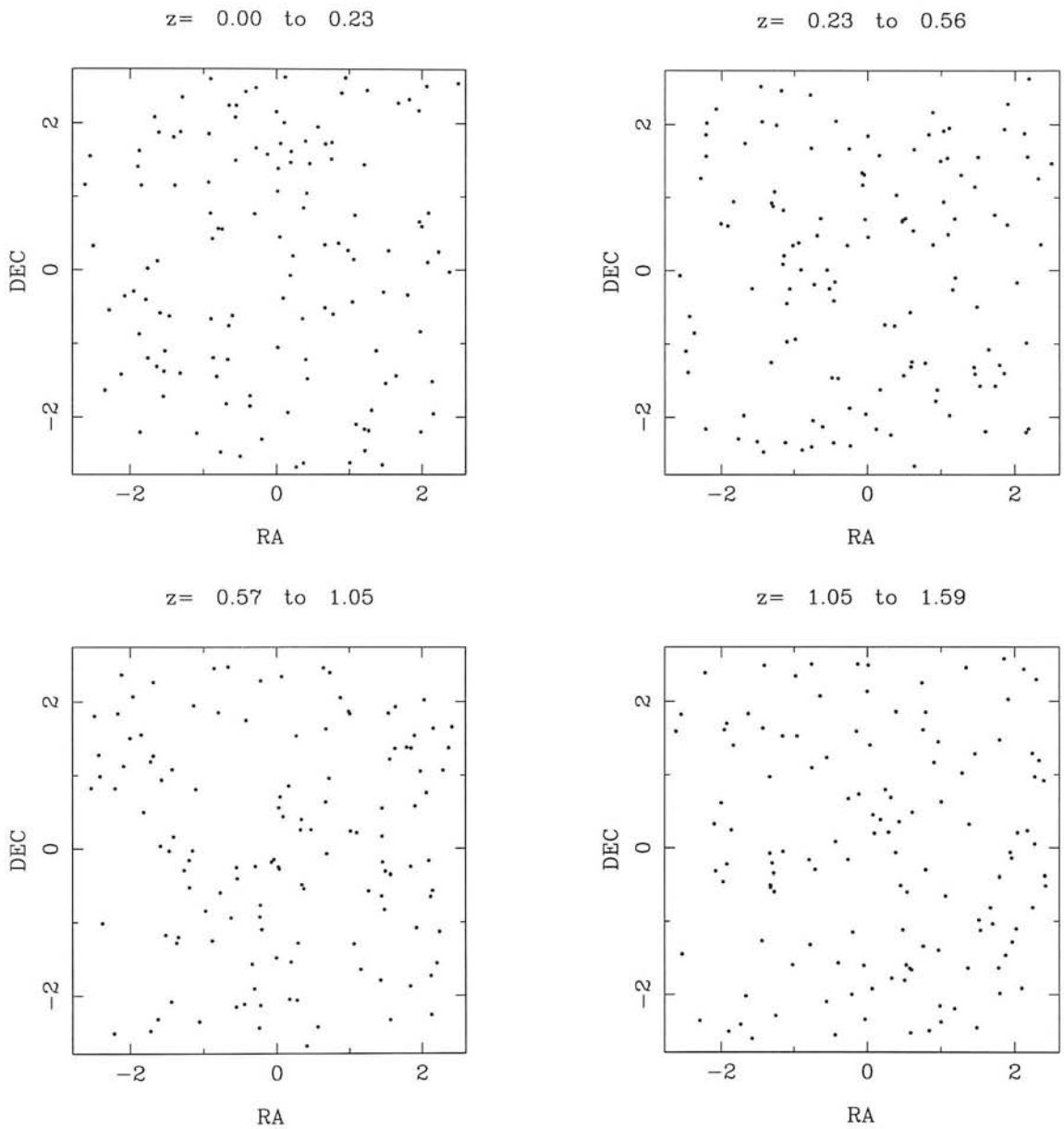

Figure 6.8: Positions (relative to the field centre) of the candidates from the radio galaxy match-up with $P^{\star} < 0.036$. The ~ 506 output galaxies are divided into 4 redshift bins.

sistent with previous datasets it is clear that any predicted $P_{\rm RG}(m)$ would be somewhat speculative. There are, however, grounds for believing the two models in figure 6.7b are closest to the true distribution of sources (Peacock, Dunlop & Windhorst, 1996). The ranking method used here, therefore, is probably the safest one. These are the closest forms to the redshift distribution of our dataset and so there should not be too severe a magnitude dependent bias in the degree of misclassification.

6.5 $w(\theta)$ & Constraints on High-z Structure

As our radial distance information for the radio galaxies is limited in precision (with redshifts estimated from magnitudes) we will be confined to measuring the *angular* clustering of galaxies in a set of broad redshift bins. The eventual outcome of this work will be in setting limits to the *three-dimensional* clustering. It is essential therefore to understand the relation between the two. This is a well established problem and is discussed by many authors (e.g. Efstathiou et al. 1991; Neuschaefer and Windhorst 1995). The bare bones of the argument are given below.

We begin with the more fundamental three-dimensional clustering of galaxies. The correlation function $\xi(r,z)$ can be represented as a power-law in the comoving scale r and $(1+z)$,

$$\xi(r,z) = \left(\frac{r}{r_0}\right)^{-\gamma} (1+z)^{-(3-\gamma+\epsilon)}. \tag{6.16}$$

The parameter ϵ allows evolution in the amplitude of galaxy clustering. $\epsilon = 0$ for clustering which is fixed in *proper* coordinates and $\epsilon = -1.2$ for clustering fixed in *comoving* coordinates. These values may be taken to bracket the range encountered in most models of galaxy formation and clustering.

The 3D clustering is related to its 2D projected analogue $w(\theta)$ by Limber's equation (Peebles 1993) which yields

$$w(\theta) = \sqrt{\pi}\frac{\Gamma\left[(\gamma-1)/2\right]}{\Gamma(\gamma/2)}\frac{G}{\theta^{\gamma-1}}r_0^{\gamma}, \tag{6.17}$$

with

$$G = \frac{\int_0^{\infty} g(z)(dN/dz)^2\,dz}{\left(\int_0^{\infty}(dN/dz)\,dz\right)^2} \tag{6.18}$$

and

$$g(z) = \left(\frac{dz}{dx}\right) x^{1-\gamma} F(x)(1+z)^{-(3+\epsilon-\gamma)}. \tag{6.19}$$

Here dN/dz is the differential galaxy redshift distribution, Γ is Euler's Gamma function and x the radial coordinate distance. $F(x)$ is a metric-dependent volume factor from Peebles (1993). It is of the form

$$F(x) = \sqrt{1 - (H_0 x/c)^2(\Omega - 1)} \tag{6.20}$$

and is unity for an Einstein-de Sitter universe.

The two-point angular correlation function gives a measure of the excess galaxy density over that expected for a random distribution on the sky. It is defined such that given a mean galaxy density on the sky of n, the point probability δP of finding a galaxy in each solid area element $\delta\Omega_1$ and $\delta\Omega_2$ separated by θ is

$$\delta P = n^2[1 + w(\theta)]\delta\Omega_1\delta\Omega_2. \tag{6.21}$$

As such it is a relatively easy statistic to obtain and has been widely used to quantify clustering in galaxy surveys without measured redshifts. Although not as useful as the 3D equivalent $\xi(r)$ (equation 1.19), measurements of $w(\theta)$ can set useful constraints on clustering models. The principal problem with its use is that the projection of sources from a broad range of redshifts onto the plane of the sky dilutes any clustering signal – larger datasets are required to detect clustering of a given real-space amplitude. Here we will attempt to use the redshift information derived in the previous section to coarsely bin the radio galaxies in radial distance. This will reduce the projection effect and hence make any existing signal easier to measure, although with a corresponding increase of noise as we have less pairs per bin. It will be left open to experiment as to whether we can recover extra information this way.

6.5.1 Measuring the Angular Clustering

The first step is to estimate how coarse the redshift bins need to be before we have enough objects to detect a clustering signal with confidence. This can be guessed at using a modified version of expression 6.8 to compare the error bar on the measurement of clustering in one angular bin $\simeq [1+w(\theta)]/\sqrt{N(\theta)}$ to the size of the expected measurement

itself which is $w(\theta)[1-f]^2$ where f is the fraction of misclassified sources – assumed to be randomly distributed on the sky. $N(\theta)$ the number of data pairs in a given separational bin of width $\Delta\theta$ from the sources and is given by

$$N(\theta) \simeq \frac{2\pi\theta\Delta\theta N_{\rm B}^2}{A} \tag{6.22}$$

with $N_{\rm B}$ the total number in the *redshift* bin and A the area over which they are spread ~ 27 deg^2. The significance, i.e. the ratio of the measurement to the error is then given by

$$\mathrm{sig} \simeq N_{\rm B} A_w \theta^{-0.8}[1-f]^2 \sqrt{\frac{2\pi\theta\Delta\theta}{A}} \simeq 0.3 N_{\rm B} A_w \sqrt{\Delta\theta} \tag{6.23}$$

where the form $w(\theta) = A_w\theta^{-0.8}$ and the right-hand expression holds for sources over $A = 27.2$ deg^2 (which are correctly matched ~80% of the time) for separations of order 1 degree. A reasonable estimate of A_w (i.e. the angular clustering at 1 degree) in the redshift ranges sampled here is $0.01 - 0.05$ (using the observed redshift distribution and expressions 6.16 to 6.20 – see also figure 6.11) and the $\Delta\theta$ used here is $0.2°$. A significance level of 1-sigma therefore requires $N_{\rm B} \sim 100$ to 1000. There is little point in the redshift bins being finer than the expected error in redshift estimation $\simeq 0.3$ at $z = 1$. The first bin of width $\Delta z = 0.3$ contain about 125 objects which is one value of $N_{\rm B}$ used for the subsequent analysis. Clearly larger values of $N_{\rm B}$ improve the signal-to-noise at the expense of redshift resolution. There are only ~ 500 objects however so the allowed increase is not great. We have analysed the data a second time using $N_{\rm B} = 250$ to see if there is any gain in sensitivity.

For a given redshift distribution we can write $w = w(\theta, r_0, \gamma, \epsilon)$ i.e. given the model parameters the machinery of equations (6.16-20) can be easily used to obtain the angular clustering predicted in that model. The inverse problem of deriving ϵ and r_0 with a knowledge of $w(\theta)$ and dN/dz is more difficult, especially where fairly noisy estimates of the clustering amplitude are expected, as here. The approach, therefore, will simply be to estimate $w(\theta)$ in coarse redshift bins and find which values of ϵ and r_0 are strongly *excluded.*

Typically $w(\theta)$ is estimated from a given sample of galaxy positions by constructing a catalogue of random galaxy positions and comparing any clustering signal from the dataset to that of the random catalogue. This involves evaluating an estimator of the form

$$w(\theta) = \frac{DD(\theta)}{RR(\theta)} - 1 \tag{6.24}$$

where $DD(\theta)$ is the number of data-data pairs and $RR(\theta)$ the number of random-random pairs for angular separations of $\theta \pm \delta\theta$. However, here we will use the estimator

$$w(\theta) = \frac{DD(\theta) - 2DR(\theta) + RR(\theta)}{RR(\theta)}. \tag{6.25}$$

with $DR(\theta)$ the cross-correlation between the data and a random catalogue. This is argued by Hamilton (1993) to be more reliable for low-amplitude signals and is shown by Landy & Szalay (1993) to have a nearly Poissonian variance (whereas the variances of simpler estimators are quite sensitive to the assumed mean density of the sample).

The data were analyzed by dividing up the data into catalogues spanning redshift ranges $z_{\rm min} \rightarrow z_{\rm max}$ such that there were $N_{\rm B}$ objects in the range and with $z_{\rm m}$ the median redshift. The clustering as a function of scale was evaluated using 6.25 with 0.2° bins for the separations. Errors in each bin were estimated using the bootstrap resampling method described by Barrow, Ghavsar & Sonada (1984). A resampled estimate for $w(\theta)$ is obtained by applying 6.25 to a resampled catalogue of $N_{\rm B}$ galaxies, randomly selected from the input catalogue of $N_{\rm B}$ galaxies with selected galaxies *not removed* from the input catalogue. That means that some galaxies are included in the resampled catalogue twice or more, whereas some galaxies do not enter at all. 200 bootstrap resampled measurements were made for each catalogue, the mean of the resampled estimates of $w(\theta)$ was taken to be the measured value of the clustering amplitude with one standard deviation either side of this value taken to be a 1σ error-bar. The clustering in the range $0 \rightarrow 1^\circ$ (5 angular bins) was then fit by minimising χ^2 with respect to the form

$$w_{\rm m}(z_{\rm m}, \theta) = A_w(z_{\rm m})\theta^{-0.8} \tag{6.26}$$

where θ here is in degrees. $A_w(z_m) \pm \sigma_w$ is therefore the measure of angular clustering at a scale of 1° at the median redshift of z_m, with error $\pm\sigma_w$. Note that negative values of A_w were not excluded from the fit and the exponent $1-\gamma$ was fixed at -0.8. The use of χ^2 in the fit deserves some explanation as the error estimates for $w(\theta)$ in each bin are *not independent*. Although minimum χ^2 gives the best fit, the error in the fitting parameter σ_w (established by the values of A_w that give $\chi^2 = \chi^2_{\rm min} + 1$) will consequently be underestimated. Fortunately it was shown by Mo, Jing and Börner (1992) that bootstrap errors are an *overestimate* of the true errors in each bin and compensate perfectly for the tendency to underestimate σ_w by χ^2 methods. Thus the σ_w estimates here are valid.

Examples of the clustering measured for each redshift range are shown in figures 6.9a and b together with least-square fits in the range $0 \rightarrow 1^\circ$ (dashed lines). Figures 6.12 and 6.13 show the best fitting values of A_w (with estimated errors) as a function of z_m for the radio galaxy catalogue with $N_B = 125$ and 250.

6.5.2 r_0 and Bias Constraints

To convert these measurements of the degree-scale clustering amplitude into constraints on r_0 and ϵ we need to relate equations 6.26 and 6.17. We have measured the clustering on a scale of 1°. This can be related to theoretical expectations via 6.17 where

$$A_w(z_m) = kGr_0^\gamma \left(\frac{\pi}{180}\right)^{1-\gamma}. \qquad (6.27)$$

Here $k = \sqrt{\pi}\,\Gamma[(\gamma-1)/2] \,/\, \Gamma(\gamma/2) = 3.679$, with γ set to 1.8. G is given by 6.18 and can be written $G = G(H_0, \Omega, dN/dz, \epsilon)$ though we will fix the first two parameters with $\Omega = 1$ and $h = 0.75$. We have estimates of the redshift distribution dN/dz for a given subset of the total catalogue (labelled by z_m). The errors derived in section 6.4.2 should be taken into account here, and are used to obtain smoothed versions of the redshift distributions for the redshift bins (shown in figure 6.10). Given these assumptions we can calculate the expected amplitude on a scale of 1° given $r_0 = 11h^{-1}$ Mpc and a chosen value of ϵ. The resulting estimates of A_w from these *predicted* values of $G(z_m, \epsilon)$ and r_0

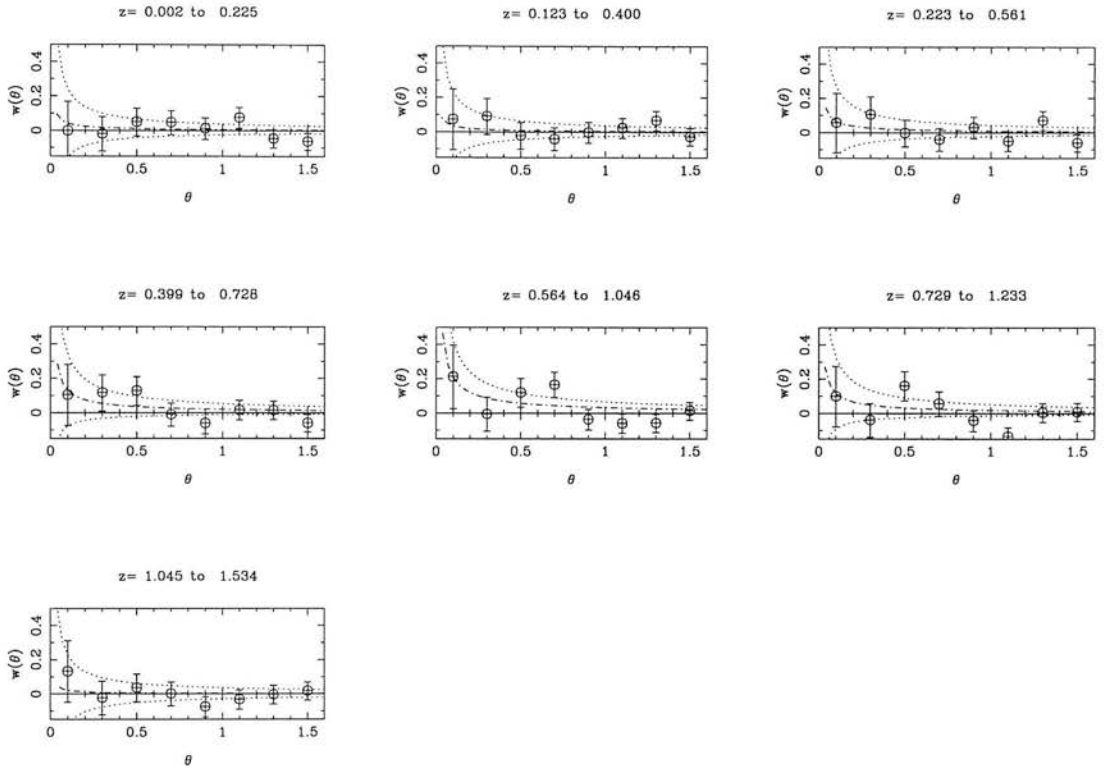

Figure 6.9: (a) The observed clustering in redshift bins of $N_{\rm B}$ radio sources. Points are shown with *Poisson* error bars which give the correct interpretation of the significance of clustering measured in an individual angular bin. For the reasons discussed in the text *bootstrap* errors are used to fit a functional form to the clustering, these are approximately $3^{1/2}$ larger. The first five bins are used to fit the form $w(\theta) = A_w \theta^{-0.8}$ (θ in degrees) which is shown as the dashed line. One sigma deviations from the best fit are shown dotted. The samples shown in successive figures are not completely independent, each successive redshift bin is $N_{\rm B}/2$ objects further into the list of sources (which are sorted according to redshift).

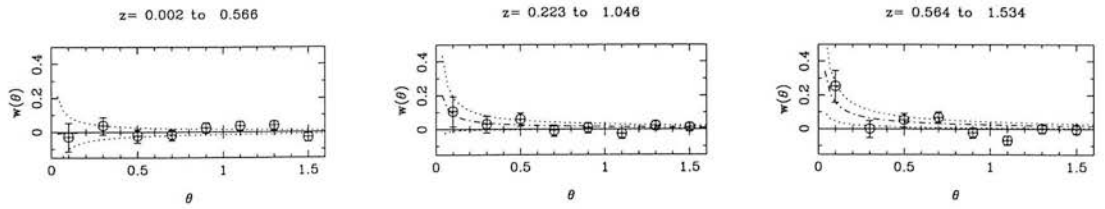

Figure 6.9: (b) As for figure 6.9a but with $N_{\rm B} = 250$ objects per redshift bin.

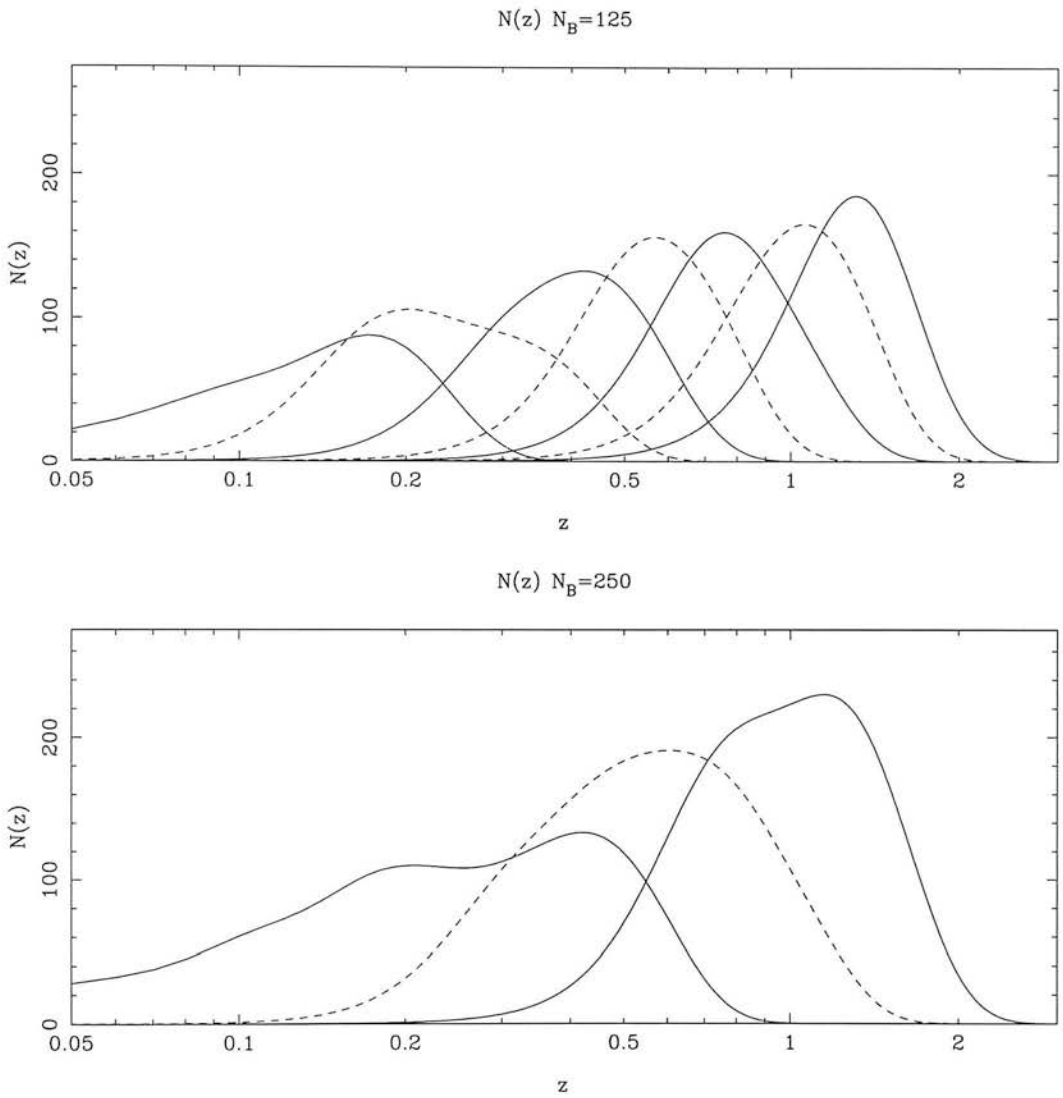

Figure 6.10: Redshift distributions for the samples used in the clustering analysis, when smoothed with the estimated error from section 6.4.2. Each successive redshift bin is $N_{\rm B}/2$ objects further into the list of sources. Alternate bins are shown as filled and dashed lines to show the resulting overlap between supposedly independent bins, when the errors are taken into account. The overlap is not too severe, especially when the bins are large ($N_{\rm B} = 250$). These distributions are used for the estimates of A_w the expected 1° clustering amplitude for $r_0 = 11h^{-1}$ Mpc shown in the next figure

are shown in figure 6.11. Writing

$$r_0^{1.8}(z_{\rm m}) \simeq \frac{A_w(z_{\rm m})}{k[1-f]^2 G\,(z_{\rm m},\epsilon)} \left[\frac{\pi}{180}\right]^{0.8} \tag{6.28}$$

and we can obtain a rather noisy estimate of the true r_0 (for each sub-catalogue with median redshift $z_{\rm m}$) using the *calculated* value of $G\,(z_{\rm m},\epsilon)$ and the *measured* value of $A_w(z_{\rm m})$. Recall f the fraction of misclassified objects was estimated to be $\simeq 0.2$ in

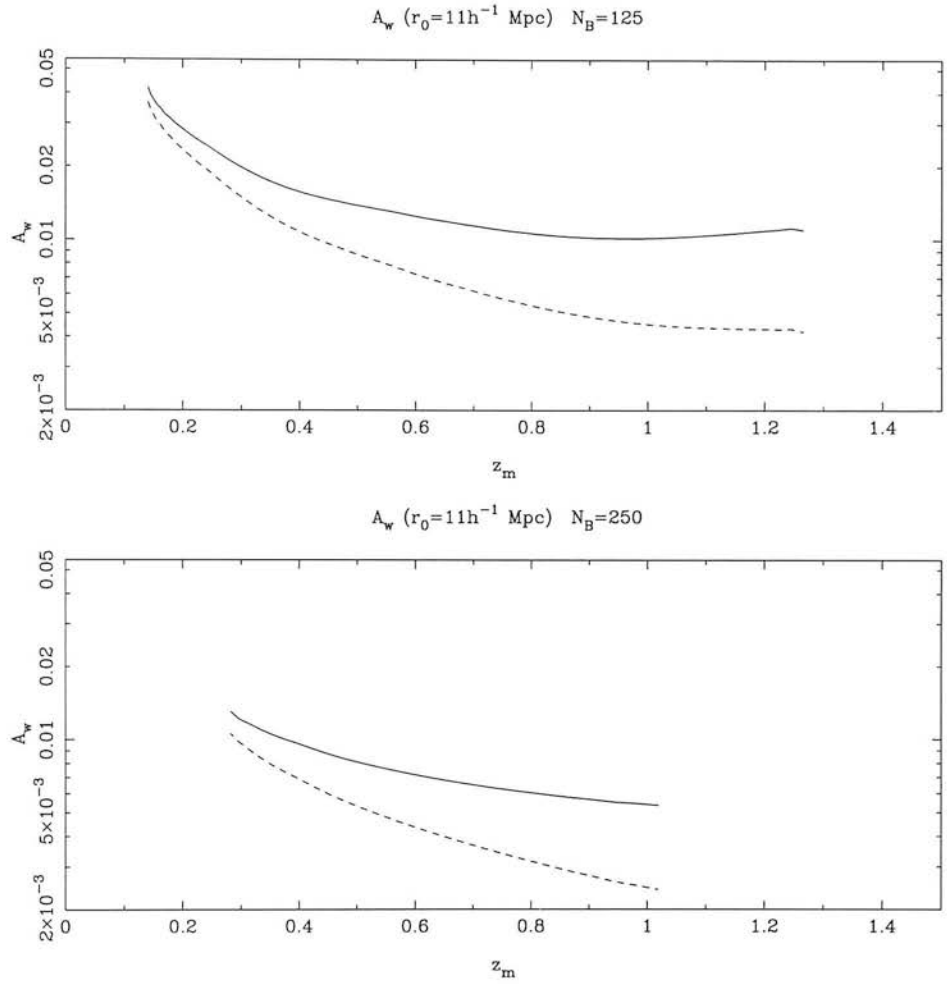

Figure 6.11: The predicted amplitude of angular correlations at 1° for the redshift distribution of figure 6.6 using a model of $\xi(r) = (r/r_0)^{-\gamma}$ and equation 6.17. The data are chosen in a redshift range $z_{\rm min} - z_{\rm max}$ such that there are $N_{\rm B} = 125$ objects in the range (top diagram) or $N_{\rm B} = 250$ (bottom diagram). $z_{\rm m}$ is the median redshift in the range. The filled line shows the prediction for $r_0 = 11h^{-1}\,{\rm Mpc}$, $\epsilon = -1.2$ the dashed line for $r_0 = 11h^{-1}\,{\rm Mpc}$, $\epsilon = 0$. The amplitude at a given $z_{\rm m}$ scales with r_0 as $(r_0/11h^{-1}\,{\rm Mpc})^{-\gamma}$. All the results here assume $\gamma = 1.8$.

section 6.4.1. This was carried out for the $N_{\rm B} = 125$ and 250 data for $\epsilon = 0$ and -1.2. The results are shown in figures 6.12 and 6.13. Note, just for clarity, if we absorbed all the redshift dependent factors into the scale length such that $\xi(r, z) = (r/r_{\rm c}[z])^{-\gamma}$ then $r_{\rm c}^{\gamma}[z] = r_0^{\gamma}[z](1+z)^{-(3-\gamma+\epsilon)}$ in terms of the notation used here.

In addition to the results from the identified Molonglo sources the figures contain an estimate of r_0 derived from the angular clustering measurement in the 4.85 GHz Green Bank survey for $S \gtrsim 25$mJy (KBK). The authors find an amplitude at 1° of $A_w \simeq 0.0055$. Although the estimated errors on this parameter were not published,

three different fitting methods were applied to the $w(\theta)$ data points and suggest an error of order ± 0.0020 in the measurement. This data point is to be reduced to an estimate of r_0 at the appropriate median redshift using 6.28. Redshift data are not available for the sample and so the integration of G was carried out using the ensemble of seven RLFs from Dunlop & Peacock 1990. With the variation in the resulting estimates of dN/dz and the suggested error in A_w, approximate 1σ confidence ranges for r_0 are

$$r_0 = \quad 10.1 - 26.6h^{-1}\,\mathrm{Mpc} \quad (\epsilon = -1.2), \tag{6.29}$$

$$r_0 = \quad 15.6 - 42.0h^{-1}\,\mathrm{Mpc} \quad (\epsilon = 0), \tag{6.30}$$

given $\gamma = 1.8$ and $\Omega_0 = 1$. In the discussion of their results, KBK compare their $w(\theta)$ measurement with the predicted values using Limber's equation and the Peacock and Nicholson value of $r_0(z = 0) \simeq 11h^{-1}\,\mathrm{Mpc}$. They conclude that their measurement exceeds the prediction by a factor of ~ 70 and discuss various arguments as to why this discrepancy is so large. It appears from the work presented here that their analysis is in error. Reference to figure 6.11 (bottom diagram) shows that amplitudes of $A_w \sim 0.005$ are not unreasonable over a large range of redshift. The interquartile redshift span of the 4.85 GHz sample, given the Dunlop & Peacock RLFs is $\simeq 0.7$ to 2 which would result in very substantial projection of sources and hence dilution of the angular clustering - over and above that shown in the figure. The error is most likely to be in their estimate of the radio luminosity function. As the corrected estimate of r_0 is not particularly anomalous it is included as a high z_{m} data point in figures 6.12 and 6.13. The Drinkwater & Schmidt (1996) upper limit of $r_0 \leq 50h^{-1}$ Mpc at $z_{\mathrm{m}} \simeq 1.1$ is shown as an arrow and seems consistent with the other data points.

What do these results tell us? Firstly the expression 6.28 is not designed to detect smooth redshift evolution of the scale parameter $r_0 = r_0(z)$. In this case r_0 would no longer be separable from G in equation 6.17 and the expression as it stood would be invalid. Rather the figures can be seen as an attempted check that we are not looking at significantly different galaxy populations at different redshifts (with different intrinsic r_0's). The errors on the measure 1° amplitude are rather too large to say anything definitive about this or the likely value of ϵ, but within 2σ, all are consistent with the low redshift Peacock & Nicholson result of $r_0 = 11h^{-1}\,\mathrm{Mpc}$. Furthermore, the highest redshift bins in each figure are in good agreement with the corrected Green Bank

4.85 GHz result and the 2.7 GHz Drinkwater & Schmidt constraint, showing that the clustering amplitudes derived in these three independent surveys are consistent with each other. If r_0 were to rise smoothly with z then we might conclude that redshift dependent biasing was in operation (see below). However the results in these figures are certainly consistent with an unbiased model.

To confront the issue of redshift dependent biasing for these radio galaxies a slightly more sophisticated approach is needed. Generally we will quantify the evolution of a biased 3D two-point correlation function via

$$\xi(r,z) = \left(\frac{r}{r_0}\right)^{-\gamma} (1+z)^{-(3-\gamma+\epsilon)} \left(\frac{b[z]}{b[0]}\right)^2 \tag{6.31}$$

and thus keep gravitational evolution of the clustering (parameterized by ϵ) distinct from the observed growth in amplitude due to bias (parameterized by $b[z]$). $b[0]$ is the bias at zero redshift. Note r_0 is set constant at the Peacock and Nicholson value of $r_0 \simeq 11h^{-1}$ Mpc from here on. Here we are implicitly assuming that biasing is not a function of scale and does not change γ significantly – both these results are approximately valid in the linear regime. Our clustering data do not have the signal to noise required to test such issues here and so will make the simplest assumption, a scale independent bias at each redshift. We will restrict the analysis to bias models of the form

$$b[z] = b[0] - \alpha + \alpha(1+z)^{\beta} \tag{6.32}$$

with α and β parameters that can be varied to describe most of the bias models encountered in the literature. This can then be included in the formalism of 6.17 to 6.20, simply by the substitution $g[z] \rightarrow g[z]b^2[z]/b^2[0]$. Carrying out the integration to give the anticipated amplitude of $[1-f]^2 w(\theta)$ at 1° then gives the model output to be compared with the measured amplitudes in figures 6.12 and 6.13. Since the signal-to-noise of the amplitude measurements is not great we will simply see which models are convincingly excluded by the data.

The first bias model considered is motivated by dynamical arguments. Nusser & Davis (1994) and Fry (1996) consider models in which galaxies which form at a characteristic redshift z_f, with a bias parameter at that epoch of b_f and subsequently move

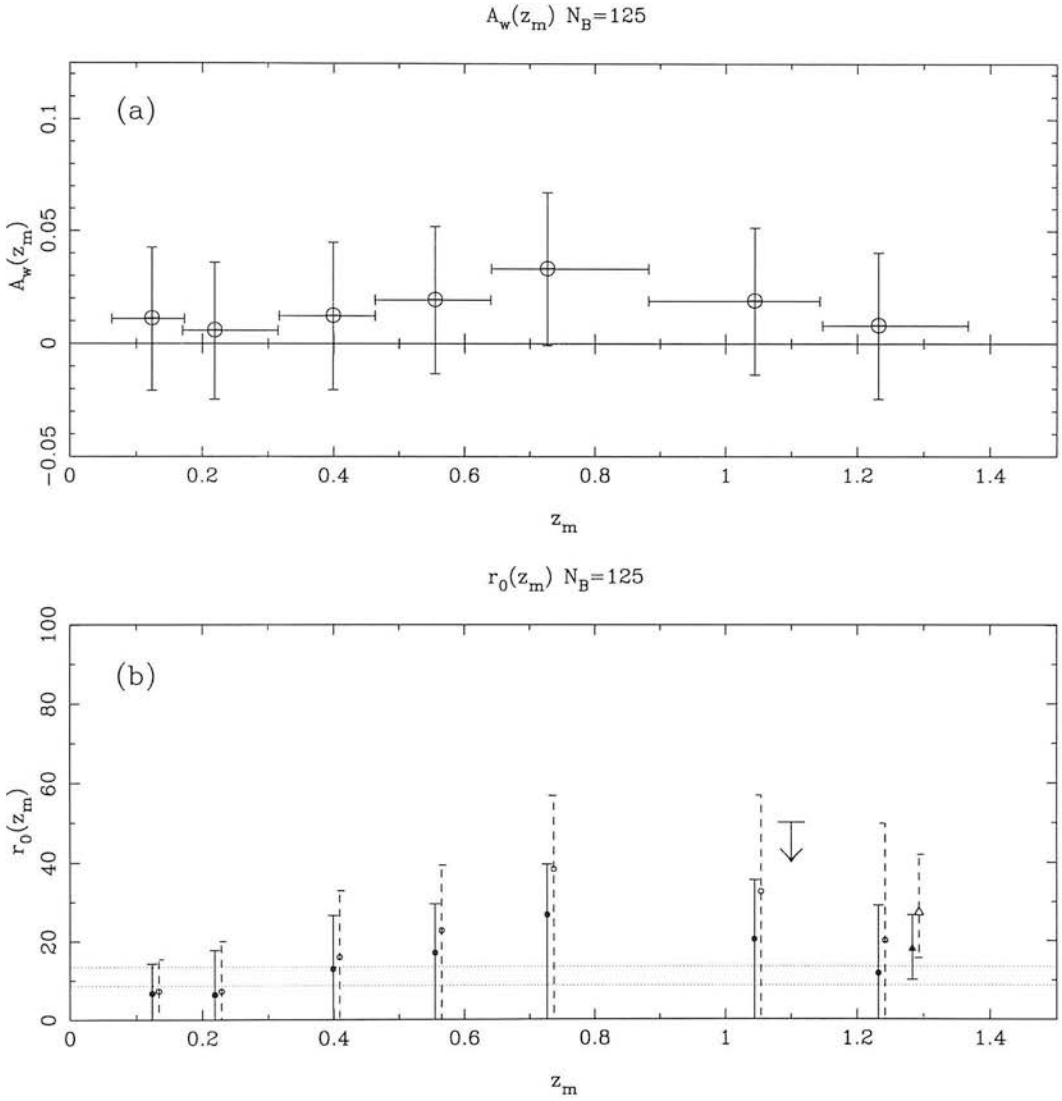

Figure 6.12: (a) The measured amplitude of correlations as the extrapolated amplitude at $\theta = 1°$. There are $N_B = 125$ objects per redshift bin with z_m the median redshift of the given sample. (b) The values of r_0 as a function of z_m using 6.28 and the values plotted in figure 6.11a. Filled circles and 1σ error bars are for $\epsilon = -1.2$, open circles and dashed 1σ error bars for $\epsilon = 0$. The horizontal bars are the interquartile ranges of the z in a given bin to give an idea of the redshift range covered. The corrected Green Bank 4.85 GHz value of r_0 is shown for $\epsilon = -1.2$ (filled triangle) and $\epsilon = 0$ (open triangle) with an estimate of the 1σ error in each case. The interquartile range for z is roughly 0.7 to 2 and is not shown. The Drinkwater & Schmidt (1996) upper limit of $r_0 \leq 50h^{-1}$ Mpc at $z_m \simeq 1.1$ is shown as a downward pointing arrow.

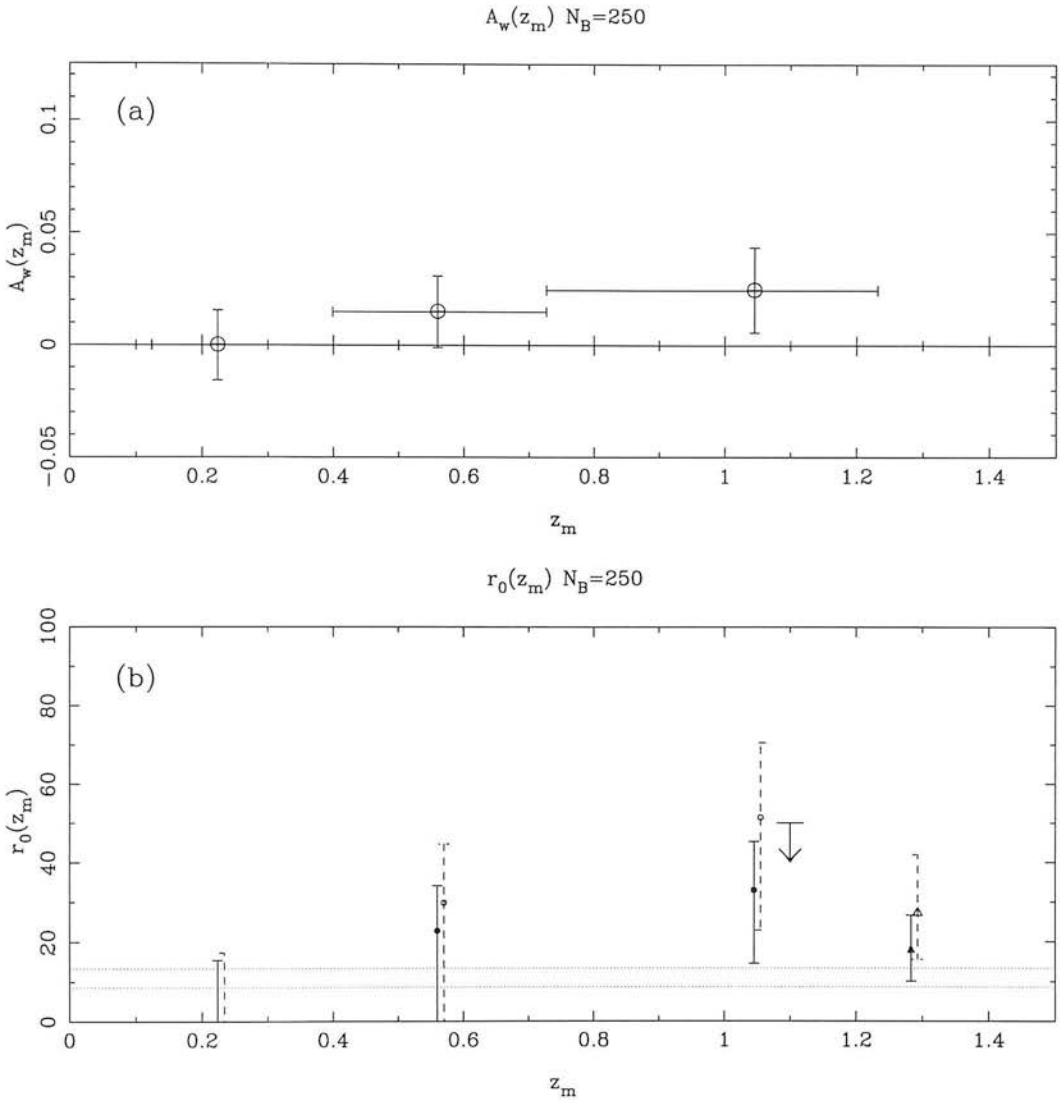

Figure 6.13: (a) As for figure 6.12 but with $N_B = 250$ objects per redshift bin. (b) As for figure 6.12 but calculating r_0 as a function of z_m using 6.28 and the values plotted in figure 6.11b.

due to gravity. The bias is defined as $b(z) = \delta_{gal}(z, z_f)/\delta_m(z)$ with $\delta_{gal}(z, z_f)$ and $\delta_m(z)$ the overdensities in galaxy numbers and the mass respectively at redshift z. Writing $\delta_{gal} = \delta_m(z) + \delta_{init}$, identifying $b_f = b(z_f) = 1 + \delta_{init}/\delta_m(z_f)$ and allowing the usual perturbation growth law for Einstein-de Sitter universes ($\delta_m \propto [1+z]^{-1}$) leads to redshift-dependent bias of the form

$$b[z] = 1 + (b_f - 1)\frac{1+z}{1+z_f} \tag{6.33}$$

for $z < z_f$ and $\Omega = 1$. This can be expressed in the form (6.32) with $\alpha = (b_f - 1)/(1+z_f)$ and $b(0) = (b_f + z_f)/(1+z_f)$. From the analysis of Peacock & Dodds (1994) we know that if IRAS galaxies trace the mass at $z = 0$ (i.e. $b_I \simeq 1$) then the local radio galaxy

bias is $b[0] = b_{\rm R} \simeq 2b_{\rm I} \simeq 2$. This is the assumption here though the effect of different values of $b[0]$ will be discussed later. Setting $b[0] = 2$ then reduces 6.33 to the form

$$b[z] = 1 + (1 + z), \tag{6.34}$$

that is, equation 6.32 with $\alpha = \beta = 1$. In their summary of bias models, Matarrese et al. (1996) dub this the *object conserving model*, since its form is determined by the equations of continuity for the matter and the individual galaxies.

The second type of biasing model arises by considering the effect large-scale components of the perturbation spectrum have on the small-scale components which determine when objects of a given mass form by gravitational collapse. In the usual model of spherically symmetric collapsing overdensities an object will form once the density in some region exceeds a critical value of $\delta_{\rm c} \simeq 1.69$ (in an Einstein-de Sitter universe). In the *peak-background split* scenario (e.g. Cole & Kaiser 1989) the large-scale density components are added to the pre-existing small-scale density field, which perturbs the threshold required for object collapse. If the large-scale component contributes an overdensity of $\delta = \eta$ then the small-scale component only needs to reach $\delta = \delta_{\rm c} - \eta$ to collapse. The resulting number density is modulated, and together with the gravitational effects of the large-scale component (producing a density contrast $\propto 1 + \eta$) yields a bias. The form of this bias can be derived using the Press-Schechter (1974) formalism. Given $\sigma^2(M, z)$, the mass-variance at redshift z of a sphere containing the galaxy mass M, we can define $\nu = \delta_{\rm c}/\sigma(M, z)$. The Press-Schechter formula gives the number density of objects in a given mass range as

$$\frac{dn}{d\ln M} \propto \nu \exp[-\nu^2/2]. \tag{6.35}$$

Perturbing the the background large-scale density components by η means $\nu \rightarrow (\delta_{\rm c} - \eta)/\sigma(M, z)$ causing a fluctuation in the predicted numbers of objects such that $n' = n(1 + \eta(\nu^2 - 1)/\delta_{\rm c})$. Writing again $\delta_{\rm gal} = \delta_{\rm m} + \delta_{\rm init}$ shows that the bias is the sum of the statistical effect $\delta_{\rm init} = (n' - n)/n$ due to the collapse of objects on small scales and the dynamical effect due to the gravity of the large-scale perturbation $\delta_{\rm m} = \eta$. The bias is

therefore

$$b[z] = 1 + \frac{\nu^2 - 1}{\delta_c} = 1 - \frac{1}{\delta_c} + \frac{\delta_c(1+z)^2}{\sigma_0^2}. \tag{6.36}$$

Fixing $b[0] \simeq 2$ and using the canonical $\delta_c = 1.69$ this can be written as

$$b[z] = 0.4 + 1.6(1+z)^2 \tag{6.37}$$

which is in the form 6.32 with $\alpha = 1.6$ and $\beta = 2$. Strictly speaking this result is for dark matter haloes. The calculation is carried out via the Press-Schechter approach which assumes that the only objects that exist at a given epoch are those that have just formed out of smaller subunits. For this reason, Matarrese et al. refer to this as the *transient model*. How applicable this model is to galaxies is not entirely clear. However it is almost certainly of relevance to clusters, with which radio galaxies are often associated and so could well be relevant over large distances, where the clustering of galaxies occupying different dark matter haloes is measured. Notably 6.36 becomes

$$b[z] = 1 + \frac{\nu_f}{\sigma(M,z)} \tag{6.38}$$

for large ν. This is the form of bias anticipated by BBKS and employed in the study of QSO clustering by Croom & Shanks (1996). In terms of 6.32 $\beta = 1$ follows from the postulate that ν is constant and defines some threshold above which galaxies can form. Thus it can be seen that the two models are effectively interchangeable depending on the assumptions made about galaxy formation.

These models are compared to the observed clustering data in figures 6.14 and 6.15. In figure 6.14 the binned clustering data for $N_B = 125$ and 250 are compared to the predictions for the evolution of A_w for models in which β =1, 2 and $\epsilon = -1.2, 0$. It is apparent from the plots that the most discrimination is achieved by the highest redshift point for which $N_B = 125$. The $N_B = 250$ data constrain the models less well despite the improved signal-to-noise for A_w, as the larger spread in redshift in each bin dilutes the effect of a rapidly evolving bias. $\beta = 1$ models show a reasonable agreement with the data where $\alpha \lesssim 2$ for $\epsilon = -1.2$ and $\alpha \lesssim 4$ for $\epsilon = 0$. Both these constraints are therefore

consistent with the bias model 6.34. $\beta = 2$ models agree when $\alpha \lesssim 1$ for $\epsilon = -1.2$ and $\alpha \lesssim 2$ for $\epsilon = 0$. Only the model with $\epsilon = 0$ is therefore consistent with expression 6.37 and even here the agreement with the highest redshift bin with $N_{\rm B} = 125$ is only at the 2σ level. The other feature of the $\beta = 1$ and 2 plots is that the unbiased model underpredicts the amplitude of the highest redshift bin for $N_{\rm B} = 250$. This is however only a 1σ offset and so the conclusion must be that *unbiased* models are also consistent with the data.

An independent check of these results can be gained by comparing the measured angular clustering of the Green Bank 4.85 GHz sources with the amplitudes predicted by the bias models. Here the redshift distribution is uncertain, though there are good reasons (Peacock, Dunlop & Windhorst 1996) to expect models 6 and 7 of Dunlop & Peacock (1990) to be applicable. Here we specifically assume model 6 which corresponds to pure luminosity evolution in the radio luminosity function. Model 7 allows luminosity *and* density evolution but is so constrained as to only affect the predicted clustering amplitude by $\sim 20\%$ for the calculations made here. The comparison of the data and models is shown in figure 6.15, where the point at $z_{\rm m} \sim 1.3$ is the Green Bank result. Also shown is A_w for *all* the 506 optically identified sources from the $S \geq 6$mJy Molonglo data at $z_{\rm m} = 0.57$. $w(\theta)$ for the whole sample is shown in figure 6.16. As expected from the trend with increasing $N_{\rm B}$ in figure 6.14, the $N_{\rm B} = 506$ Molonglo amplitude constrains the models only very weakly. In $\beta = 1$ models it allows $\alpha \lesssim 6$ for $\epsilon = -1.2$ and $\alpha \lesssim 10$ for $\epsilon = 0$. In $\beta = 2$, $\alpha \lesssim 2$ for $\epsilon = -1.2$ and $\alpha \lesssim 3$ for $\epsilon = 0$ are permitted. The Green Bank datum, however, has a much higher median redshift and substantially smaller error, and is therefore much more sensitive to evolution of the bias. Comparison with figure 6.14 shows that it provides very similar constraints to the $N_{\rm B} = 125$ data. A table of the constraints implied by the figures is given in table 6.1.

In fact, recent work on redshift distortions (summarized in Peacock 1996) suggests that $b_{\rm I}$ may be as high as ~ 2 if $\Omega_0 = 1$, in which case $b_{\rm R} = 4$. Because the tests presented here look only at the ratio $b_{\rm R}[z]/b_{\rm R}[0]$ this does not affect things too severely. The change $b_{\rm R}[0] = 2 \rightarrow 4$ weakens the constraints on α by about 30% for $\beta = 1$ and about 10% for $\beta = 2$.

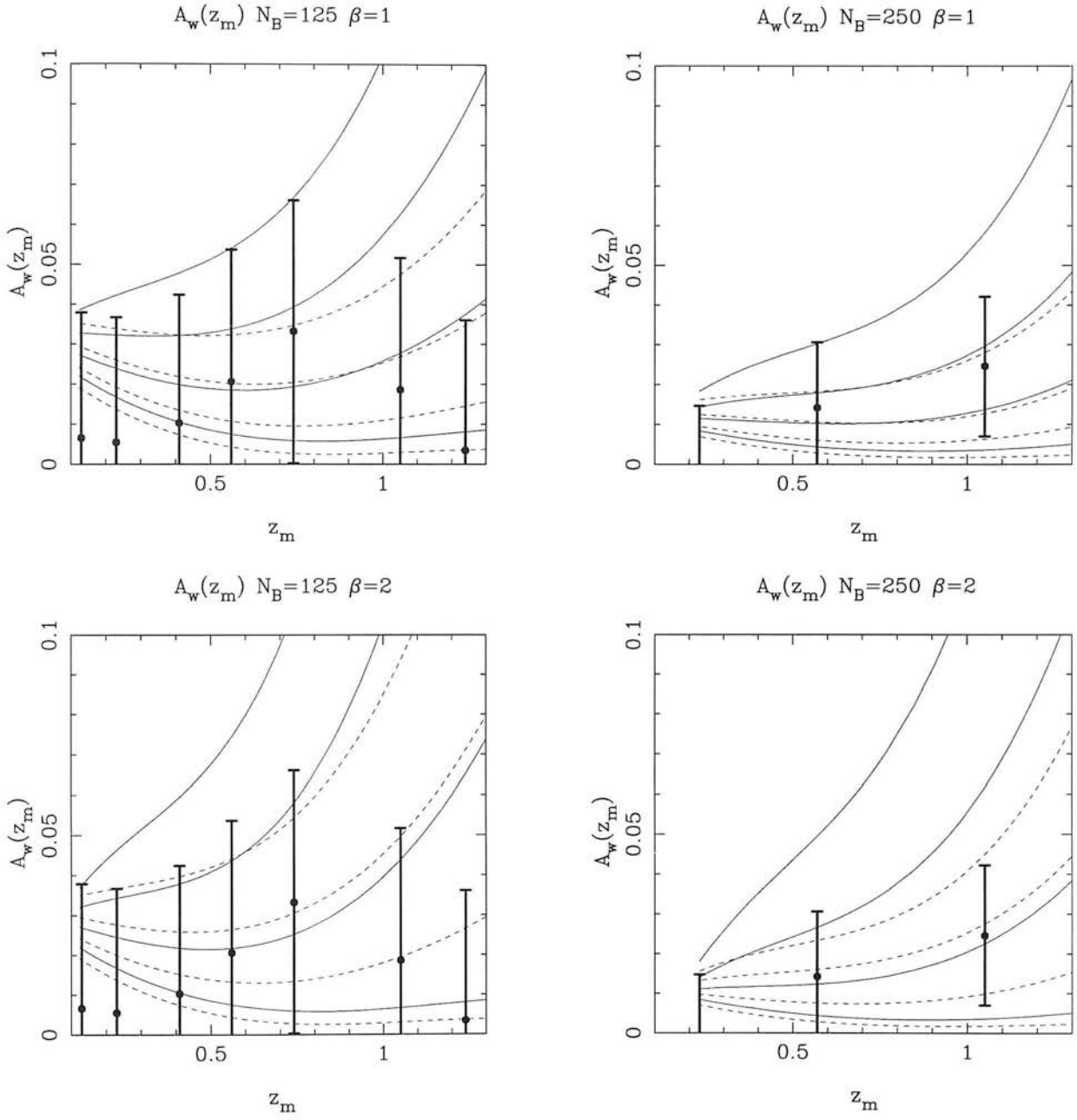

Figure 6.14: The results of the clustering analysis. $A_w(z_{\rm m})$ is the best fit amplitude of $w(\theta)$ at 1° with 1σ error bars for redshift bins of $N_{\rm B} = 125$ objects (lefthand diagrams) or $N_{\rm B} = 250$ objects (righthand diagrams). Each bin is centred on $z_{\rm m}$. Also shown are the predictions for A_w in a range of bias models of the form $b[z] = b[0] - \alpha + \alpha(1+z)^\beta$. In the top two plots, $\beta = 1$ and α takes values 0, 2, 4, 6 in ascending lines. In the bottom two plots, $\beta = 2$ and α takes values 0, 1, 2, 3 in ascending lines. In each plot, the filled lines are the predictions for an $\epsilon = -1.2$ model of clustering evolution, the dashed lines are for $\epsilon = 0$.

$\beta = 1$	$\epsilon = -1.2$	$\alpha \lesssim 2$
	$\epsilon = 0$	$\alpha \lesssim 4$
$\beta = 2$	$\epsilon = -1.2$	$\alpha \lesssim 1$
	$\epsilon = 0$	$\alpha \lesssim 2$

Table 6.1: A summary of the bias constraints (in terms of expression 6.32) set by the radio-galaxy clustering data.

The result of these comparisons is that of the theoretically motivated bias models, 6.34, 6.37 considered above, neither can be convincingly ruled out by existing high-z radio galaxy clustering data. However the constraints here are already quite close to the expected form 6.37 for the $\beta = 2$ transient model. This holds out the chance that with a moderate improvement in the data this type of bias evolution may be ruled out. Limits can already be set that rule out significantly more extreme forms of bias evolution. A complete catalogue of radio sources in UKST/SRC field 287 down to $S(843\,\mathrm{MHz}) \simeq 1\mathrm{mJy}$ would contain $\gtrsim 4$ times as many $z \lesssim 1.5$ radio-galaxies as the $S(843\,\mathrm{MHz}) \geq 6\mathrm{mJy}$ catalogue employed here. Sources within this redshift range are detectable on the J and R stacks. Given this amount of data the error bars on the clustering amplitudes presented here could be reduced by a factor ~ 2 which would subject these bias models to a much sterner test. It is inevitable that as the data on faint radio-galaxies improve the more severe the constraints on these models will become.

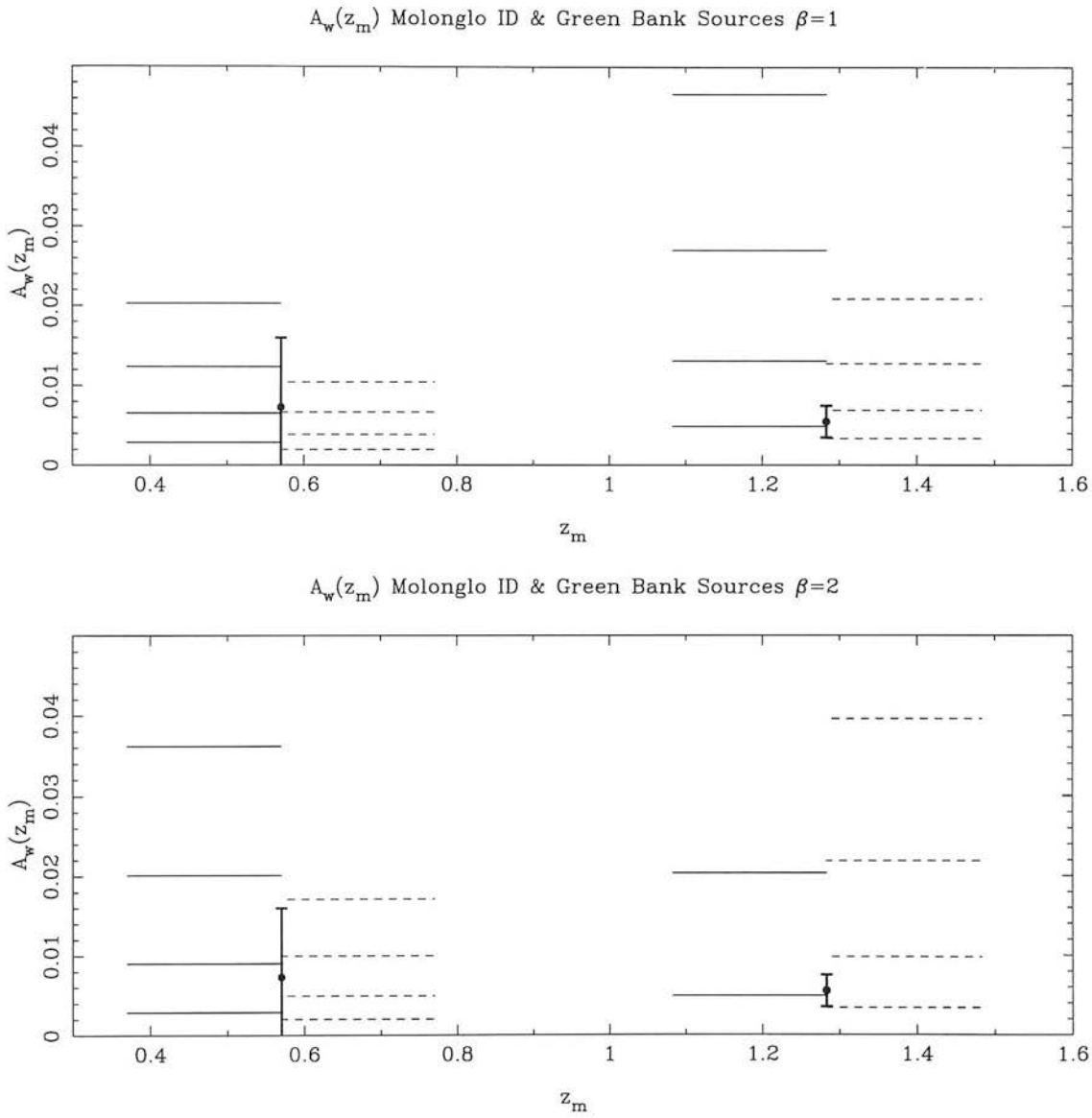

Figure 6.15: Comparison of the bias models of figure 6.14 and the results of the clustering analysis for (i) at $z_m = 0.57$ all the 506 optically matched Molonglo sources, (ii) at $z_m = 1.28$ the Green Bank sources with $S \geq 25$ mJy at 4.85 GHz. The top plot shows the predicted 1° clustering amplitude for models with $\beta = 1$ and (in ascending lines) α =0, 2, 4, 6. The bottom plot is for models with $\beta = 2$ and (in ascending lines) α =0, 1, 2, 3. In each plot, the filled lines are the predictions for an $\epsilon = -1.2$ model of clustering evolution, the dashed lines are for $\epsilon = 0$.

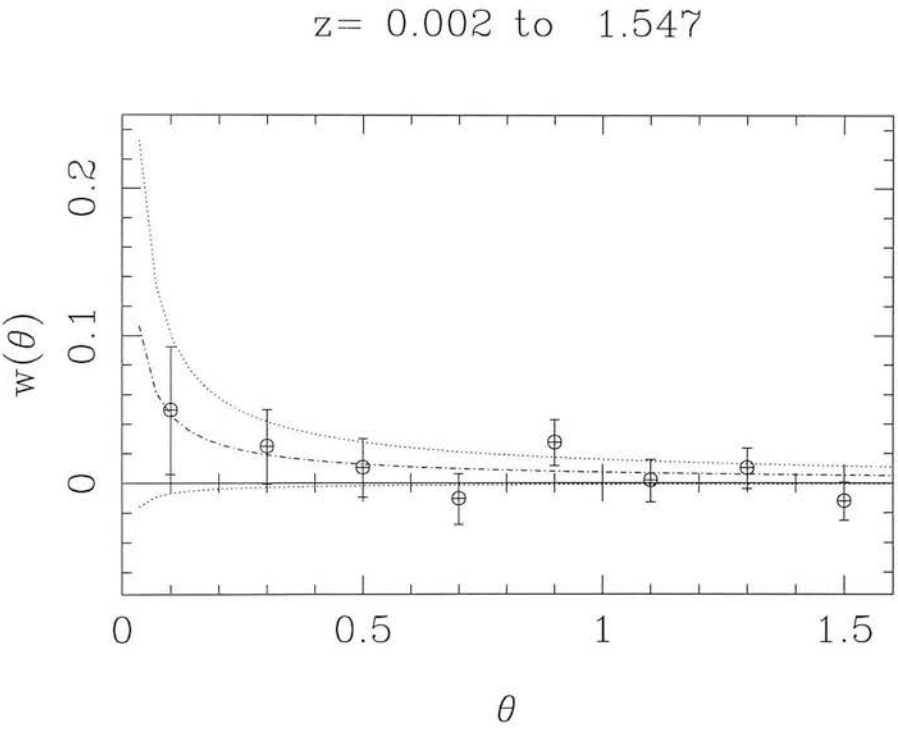

Figure 6.16: The observed clustering for all the 506 optically matched radio sources with $P^* < 0.036$. Poisson error bars are shown and the fit is performed as in figures 6.9 and 6.10. The best fit amplitude of the clustering at 1° is $A_w = 0.0073 \pm 0.0087$.

Chapter 7

Summary

This thesis has concerned itself with three aspects of large-scale structure in the Universe. In this final chapter I wish to sum up the conclusions of the work presented here, and to mention ways in which the investigations could be extended.

Chapters 2 – 4 discussed tests of a specific scenario for the origin of density perturbations in the universe, the cosmic string model. The model remains a viable alternative to inflationary explanations for cosmic structure formation. Indeed it has important advantages – the predicted horizon-scale inhomogeneity is $\delta_{\rm H} \sim [E_{\rm symm}/E_{\rm planck}]^2 \sim 10^{-5}$ (a number which has no explanation in inflationary models) and furthermore the strings may be directly detectable via their lensing effects. The work in this thesis has developed a search algorithm to look for them. It can be applied to survey data in order to pick out the tracks of lensed pairs expected when a long string lies in front of galaxies. Constraints derived from the COBE measurement fix the mass per unit length to be of order $10^{13.50}\,M_\odot\,{\rm Mpc}^{-1}$ which corresponds to pairs separated by upto $\sim 10''$.

Chapter 2 worked directly with simulations of string evolution in order to characterize the curvature and small-scale wiggliness on long strings. Understanding these effects is vital for fixing the search parameters; the less straight the string the less easy the search. Fourier analysis of the loci of strings (seen in projection on the sky) showed that the deviations from string straightness could be characterized by a scale-free power spectrum below scales of $\sim 500h^{-1}$ Mpc of the form $P_y \propto k^{-2.87}$. Inversion of this expression gave

two vital parameters, $\sigma_\theta(x)$ the rms curvature of strings over a scale x, and $\sigma_y(x)$, the thickness required of a rectangular strip of length x to encompass a typical string seen on the sky. As a flat-space string simulation was employed it was argued that these results should be a worst case (i.e. σ_θ and σ_y are too large), as universal expansion ought to damp the substructure. It would be intriguing to try this analysis on the output of matter dominated, expanding universe string simulations to see if this is the case.

The chapter concluded by discussing the density of strings to establish the volume needed for a successful search. The density of long horizon-spanning strings ρ_s during the matter dominated epoch is not well established and remains to be well pinned down by simulation. Taking an intermediate value for ρ_s an attempt was made to calculate the minimum detection redshift $z_{\min}$ that a search would need in order to stand a good chance of finding strings. Estimating this by randomly placing observers in the simulation volumes gave $z_{\min} \simeq 0.09$ for the π sterad area of the forthcoming Sloan northern sky survey, $z_{\min} \simeq 0.15$ for 100 $5^\circ \times 5^\circ$ Schmidt plates and $z_{\min} \gtrsim 1$ for the 300 deg^2 Sloan deep survey. These limits can be scaled by $(\rho_s/20l_H^{-2})^{-1/2}$ to obtain the effect of different long string densities.

The third chapter looked into the appearance of galaxies when lensed by cosmic strings. A straightforward prediction of the model is that galaxies lying behind a string are lensed into two images, identical in size, shape, magnitude and colour. Chapter 3 showed that there are numerous complications to this picture. Firstly, if the images are only separated by small angles it may be difficult to resolve the pair into two distinct images. This issue was made explicit by showing the response of an image analyzer (e.g. COSMOS) to seeing limited image data (e.g. faint Schmidt plate galaxies). Generally below a certain lensing angle ($\sim 4''$ for COSMOS data) deblending techniques fail and the two images are merged into an ellipse. Elliptical shapes are intrinsically very common in galaxy datasets thus string search techniques which trigger on ellipses are subject to significant noise. High resolution and low seeing are desirable for string survey media to limit this effect. Secondly, calculations showed that significant numbers of galaxies are only partially lensed as a result of only partly falling into the sharp-edged lensing region around a string. In this case the two images are of different magnitude and shape. In chapter 3 this effect was modelled and the characteristics of such dissimilar pairs com-

pared with the background of coincidental galaxy pairs. The conclusion was that string lensed pairs dominate over random background pairs most where the magnitude difference is small. Clearly the minimum detectable magnitude difference between images in a pair depends on the quality of the data, thus datasets with accurate galaxy magnitudes are best for string search programmes.

Chapter 3 ended with a prescription for removing spurious images from datasets prior to the operation of the string searching algorithm. With specific reference to UKST Schmidt plate data a weighting scheme for candidate lensed objects was derived. This used the predicted distribution of strings, the redshift distribution of galaxies and the redshift dependence of the lensing angle $\psi(z_s, z_g)$ to estimate the probability of a given object being due to lensing, as a function of magnitude and pair separation. Divided by the background distribution for all pairs and ellipses in the dataset, this then gives a likelihood ratio which can be used as a weighting factor for each object fed into the string detecting algorithm.

Chapter 4 introduced and tested the string searching technique. The basic function of the algorithm is to detect co-directional candidate lensing events and see if they lie in strips on the sky, at a density significantly above that expected due to chance. The extent to which differently oriented pairs and ellipses can be considered co-directional and the width of the strip required depend on the parameters σ_θ and σ_y respectively. The values established in chapter 2 were therefore built into the algorithm. The algorithm was tested on simulations of Schmidt data to which lensed galaxy pairs were added to the existing objects in accord with the expectations deduced in chapter 3, effectively hiding a string on the plate. There are two free parameters, the minimum likelihood ratio $p_{\rm lim}$ allowed for an individual lensing candidate to be considered for inclusion and the minimum number of objects $N_{\rm min}$ in a strip required for a detection to be recorded. The criterion for detection was that in searching 100 Schmidt fields a simulated string hidden on one of the fields featured in a list of the 200 densest strips. The length of list permitted was determined by the telescope time required to confirm or reject candidates by follow-up work on a larger telescope (estimated at a week's observing for 200 areas.) By varying the free parameters, optimum values were found which allowed strings to be detected to a redshift of upto $z_s = 0.07$.

Applying the optimized algorithm to 100 real Schmidt fields, a list of 200 areas was therefore established, which would contain any string at $z_s \lesssim 0.07$ in the area searched. Unfortunately this redshift limit is too low to stand a really good chance of finding string, chapter 2 showed that for this the algorithm would need to detect strings at $z_s \simeq 0.15$. Following up these 200 candidates would only set the weak string density limit $\rho_s \lesssim 90 l_H^2$, a factor ~ 3 times above that thought likely given the results of string-network simulations. Looking over greater areas with Schmidt plates does not help as this merely increases the number of fields needing follow-up work for the same limiting z_s or reduces the maximum z_s for detection if the number output strips is kept constant. Better constraints on ρ_s could be set if it could be shown that the true σ_θ and σ_y were significantly overestimated by the analysis here. Figure 4.3b shows that $z_s = 0.08$ strings can be easily detected if σ_θ is too high by ~ 3. Given COSMOS errors in position angle measurements this tighter requirement on co-directionality can only go so far. $z_s = 0.15$ detection is probably unattainable, even if strings are very much straighter than anticipated here. The investigation into searching for cosmic strings therefore concluded by estimating the improvements possible with future deep galaxy surveys focusing on the large area Sloan survey. Based on the expected improvements in depth, signal-to-noise, resolution over Schmidt data and the availability of colour as a discriminant for pairs, detection of strings out to $z_s \simeq 0.3$ is expected. At the long-string densities predicted by simulation a string would be easily detected with the Sloan data. The overall model would find it difficult to survive a failure to detect a single string by this method.

Chapter 5 moved on to consider the mismatch between Cold Dark Matter models and the observed clustering of galaxies. The quality of large-scale clustering data provided by the APM galaxy survey has permitted direct comparisons with dark matter models. Numerous authors have found that the standard model of high Ω, high H_0 CDM disagrees with observations, e.g. the Peacock & Dodds (1994) result that $\Omega h = 0.255 \pm 0.017$ for scale-invariant CDM models. The search for plausible extensions to the basic picture has established many variants such as a low Hubble constant, an open universe, Mixed Dark Matter and primordial tilt in the power spectrum. Chapter 5 investigated a model in which matter-radiation equality is delayed by the decay of a massive particle.

The mass m and lifetime τ of the particles are partially constrained by the observed large-scale power– $m^2\tau \simeq 120$ as noted by Bardeen, Bond & Efstathiou (1987). The work in this thesis has substantially limited the remaining parameter space by investigating the small-scale effects in the model. A general fitting formula for power spectra for given values of m and τ was presented. In relating the predicted small-scale power in the theory to *(i)* the abundance of high-redshift objects and *(ii)* the observed clustering on $k > 1h\,\mathrm{Mpc}^{-1}$ scales it was deduced that:-

$0.5 < m < 30$ keV

$0.2 < \tau < 500$ years.

Observations of large numbers of high-z damped Ly-α systems could rule the model out by requiring *too much* small-scale power. The reionization of the Universe in allowed variants of the model was also looked into and it was found that $z \simeq 100$ reionization was possible. This will strongly affect sub-degree CMB experiments if the decaying particle scenario is correct. Future progress with this model will therefore involve probing the clustering power spectrum and the CMB anisotropy on finer scales. For example, the properties of the Ly-α forest should depend sensitively on the small-scale power. Such an extension to the work would probably involve detailed N-Body simulations with hydrodynamic codes.

Chapter 6 was devoted to the construction of a deep catalogue of optically matched Molonglo radio galaxies ($S \geq 6$mJy at $\nu = 843$MHz) and the measurement of the clustering within it. The work was motivated partly by a wish to check clustering amplitudes suggested to be puzzlingly high in a recently published analysis of $S \geq 25$mJy, $\nu = 4.85$GHz sources (KBK). Furthermore the existence of a tight optical-magnitude vs. redshift relation for radio galaxies allows testing of models for the evolution of clustering, by looking at the clustering of sources in different redshift ranges. The first half of the chapter described the matching of radio sources to objects on 64-plate J and R-band Schmidt-plate stacks which are complete to $J = 24$ and $R = 22.5$. Rough redshift-magnitude relations were established in each band by comparison with the smaller

LBDS dataset (Peacock, Dunlop & Windhorst 1996) which has measured magnitudes and redshifts. With a significant fraction ~ 0.6 of the sources matched, the roughly established number-redshift relation was compared to partially constrained models presented in Dunlop & Peacock (1990). Models corresponding to pure-luminosity evolution and luminosity-density evolution were shown to provide a reasonable match to the Molonglo/Schmidt-stack data.

The clustering of the optically identified sources in redshift bins was then found by standard methods. The measured clustering amplitudes were compared to those predicted in models where the bias evolves with redshift. During this analysis it emerged that the KBK analysis of their clustering was incorrect, their measured clustering amplitude was reasonable and consistent with the values obtained using the Molonglo sources. The combined results were not of sufficient accuracy to disprove all but the extreme models of bias. Forms of bias evolution which arise from continuity constraints on the equations of motion for galaxies and the mass (i.e. $b[z] = b[0] - \alpha + \alpha[1+z]$) were shown to be entirely consistent with the data, as were unbiased $b[z] = b[0]$ models. Schemes in which bias in galaxy numbers arises from the differential formation and motion of dark matter haloes (predicting $b[z] = b[0] - \alpha + \alpha[1+z]^2$) were shown to be only marginally consistent with the clustering measured at the highest redshifts, ($z \simeq 1.5$).

The amplitude of clustering at higher redshifts could be obtained by matching the radio sources to deeper optical data (e.g. $z \lesssim 2.2$ for $J \simeq 25$ and $R = 23.5$). Furthermore the existing clustering measurements for $z \lesssim 1.5$ could be better pinned down by increasing the number of radio sources detected on the optical stacks. Improvement of the completeness limit to $S \geq 1$mJy over the field would yield 4 times as many objects within a redshift of 1.5 and would reduce the error-bars on the clustering amplitudes by a factor of ~ 2. Either of these relatively minor improvements to the dataset would allow much tighter constraints to be set for models of radio-galaxy clustering at high redshift.

References

Aguirre A.N., Brandenberger R.H., 1995, Brown preprint (BROWN-HET-995, astro-ph/9505031)

Albrecht A., 1990, in Gibbons G.W., Hawking S.W., Vachaspati T., eds, The Formation and Evolution of Cosmic Strings, CUP, Cambridge (A90)

Albrecht A., Turok N., 1989, Phys. Rev. D, 40, 973

Allen B., Shellard E.P.S., 1990, Phys. Rev. Lett., 64, 119

Bahcall N.A., 1995, Pub. Astr. Soc. Pacific, 107, 790

Bardeen J.M., Bond J.R., Efstathiou G., 1987, ApJ, 321, 28

Bardeen J.M., Bond J.R., Kaiser N., Szalay A.S., 1986, ApJ, 304, 15 (BBKS)

Barrow J.D., Ghavsar, S.P., Sonada D.H., 1984, MNRAS, 210, 19

Bartlett J.G., Blanchard A., Silk J., Turner M.S., 1995, Science, 267, 980

Baugh C.M., Efstathiou G., 1993, MNRAS, 265, 145

Beard S.M., MacGillivray H.T., Thanisch P.F., 1990, MNRAS, 247, 311

Bennett D.P., Stebbins A., Bouchet F.R., 1992, ApJ, 399, L5

Bennett D.P., 1990, in Gibbons G.W., Hawking S.W., Vachaspati T., eds, The Formation and Evolution of Cosmic Strings, CUP, Cambridge (Be90)

Bergbush P.A., VandenBerg D.A., 1992, ApJS, 81, 163

Bertschinger E., Watts P.N., 1988, ApJ, 328, 23

Blanchard A., Valls-Gabaud D., Mamon G.A., 1992, A&A, 264, 365

Bond J.R., Efstathiou G., 1991, Phys. Lett. B, 265, 245 (BE)

Bouchet F.R., 1990, in Gibbons G.W., Hawking S.W., Vachaspati T., eds, The Formation and Evolution of Cosmic Strings, CUP, Cambridge (Bo90)

Brandenberger R.H., 1989, in Peacock J.A., Heavens A.F., Davies A.T., eds, Proc. 36th Scottish Universities Summer School in Physics, Physics of the Early Universe, SUSSP, Edinburgh

Brandenberger R.H., 1993, in Eboli O., Ribelles V., eds, Proc. 7th Swieca Summer School in Particles and Fields, World Scientific, Singapore

Carroll S. M., Press W. M., Turner E. L., 1992, Ann. Rev. Astron. Ap., 30, 499

Cen R., Ostriker J.P., Spergel D.N., Turok N., 1991, ApJ, 383, 1

Cen R., Gnedin N.Y., Kofman L.A., Ostriker J.P., 1992, ApJ, 399, L11

Cen R., Ostriker J.P., 1992, ApJ, 399, L113

Cole S., Aragón-Salamanca A., Frenk C.S., Navarro J.F., Zepf S.E., 1994, MNRAS, 271, 781

Cole S., Kaiser N., 1989, MNRAS, 237, 1127

Cowie L.L., Hu E.M., 1987, ApJ, 318, L33

Couchman H.M.P., Carlberg R.G., 1992, ApJ, 389, 453

Couchman H.M.P., Rees M.J., 1986, MNRAS, 221, 53

Coulson D., Ferreira P., Graham P., Turok N., 1994, Nature, 368, 27

Croom S.M., Shanks T., 1996, MNRAS, 281, 893

Davis M., Lecar M., Pryor C., Witten E., 1981, ApJ, 250, 423

Dawe J.A., Metcalfe N., 1982, Proc. A.S.A., 4, 466

Dekel A., 1994, ARA&A, 32, 371

Dodelson S., Gyuk G., Turner M.S., 1994, Phys. Rev. Lett., 72, 3754

Downes A.J.B., Peacock J.A., Savage A., Carrie D.R., 1986, MNRAS, 218, 31

Drinkwater M.J., Schmidt R.W., 1996, PASA, in press

Dunlop J.S., Peacock J.A., 1993, MNRAS, 263, 936

Dunlop J.S., Peacock J.A., 1990, MNRAS, 247, 19 (DP)

Efstathiou G., 1995, MNRAS, 272, L25

Efstathiou G., 1992, MNRAS, 256, 43P

Efstathiou G., Bernstein G., Tyson J.A., Katz N., Guhathakurta P., 1991, ApJ, 380, 47

Efstathiou G., 1989, in Peacock J.A., Heavens A.F., Davies A.T., eds, Proc. 36th Scottish Universities Summer School in Physics, Physics of the Early Universe, SUSSP, Edinburgh

Efstathiou G., Rees M.J., 1988, MNRAS, 230, 5P

Feldman H.A., Kaiser N., Peacock J.A., 1994, ApJ, 426, 23

Fry J.N., 1996, ApJ, 461, L65

Gelb J., Bertschinger E., 1994, ApJ, 436, 491

Gott J.R., 1985, ApJ, 288, 422

Gunn, Knapp, 1993, ASP conf. on Sky Surveys, vol. 43, 267

Guth A.H., 1981, Phys. Rev. D, 23, 347

Haehnelt M.G., 1993, MNRAS, 265, 727

Hamilton A.J.S., 1993, ApJ, 417, 19

Hamilton A.J.S., Kumar P., Lu E., Matthews A., 1991, ApJ, 374, L1

Hara T., Mähönen P., Miyoshi S., 1993, ApJ, 414, 421

Hawkins M.R.S., 1994 in Chapman J., Cannon R., Harrison S., Hidayat B., eds, The Future Utilization of Schmidt Telescopes, ASP, San Francisco, California

Hawkins M.R.S., 1986, MNRAS, 223, 845

Hendry P.C., Lawson N.S., Lee R.A.M., McClintock P.V.E., Williams C.D.H., 1994, Nature, 368, 315

Hindmarsh M.B., Sakellariadou M., Vincent, 1996, Phys. Rev. D, in press

Hindmarsh M.B., Kibble T.W.B., 1995, Reports on Progress in Physics (Institute of Physics), 58, 477

Hindmarsh M.B., 1990, in Gibbons G.W., Hawking S.W., Vachaspati T., eds, The Formation and Evolution of Cosmic Strings, CUP, Cambridge (H90)

Hogan C.J., Narayan R., 1984, MNRAS, 211, 575

Hu E.M., 1990, ApJ, 360, L7

Hunstead R.W., 1991, Aust. J. Phys., 44, 743

Irwin M.J., 1985, MNRAS, 214, 575

Jorgensen, 1994, PASP, 106, 967

Kaiser N., 1984, ApJ, 284, L9

Kaiser N., Stebbins A., 1984, Nature, 310, 391

Kibble T.W.B., 1976, J. Phys., A9, 1387

Klypin A., Holtzmann J., Primack J., Regős E., 1993, ApJ, 416, 1

Kolb R., Turner M., 1990, The Early Universe., Addison Wesley, Redwood City, California

Koo D.C., Kron R.G., 1992 Ann. Rev. Astr. Ap., 30, 613

Kooiman B.L., Burns J.O., Klypin A.A., 1995, ApJ, 448, 500 (KBK)

Laing R.A., Riley J.M., Longair M.S., 1983, MNRAS, 204, 151

Landy S.D., Szalay A.S., 1993, ApJ, 412, 64

Lanzetta K., 1993, PASP, 105, 1063

Lanzetta K., Wolfe A.M., Turnshek D.A., Lu L., McMahon R.G., Hazard C., 1991, ApJS, 77, 1

Liddle A.R., Lyth D., 1993, Phys. Rep., 231, 1

Lilly S.J., Longair M.S., Allington-Smith J.R., 1985, MNRAS, 215, 37

Loveday J., Peterson B.A., Efstathiou G., Maddox S.J., 1992 ApJ, 390, 338

Ma C., Bertschinger E., 1994, ApJ, 434, L5

MacGillivray H.T., Stobie R.S., 1985, Vistas in Astronomy, 27, 433

Maddox S.J., Efstathiou G., Sutherland W.J., Loveday J., 1990, MNRAS, 242, 24

Mähönen P., 1996, ApJ, 459, L45

Matarrese S., Coles P., Lucchin F., Moscardini L., 1996, MNRAS, in press

Mather J.C. et al., 1994, ApJ, 420, 439

McNally S.J., Peacock J.A., 1995, MNRAS, 277, 143

Mo H.J., Miralda-Escudé J., 1994, ApJ, 430, L25

Mo H.J., Jing Y.P., Börner G., 1992, ApJ, 392, 452

Moessner R., Perivolaropoulos L., Brandenberger R., ApJ, 425, 365

Mould J., Huchra J.P., Bresolin F., Ferrarese L., Ford H.C., Freedman W.L., Graham J., Harding P., Hill R., Hoessel J.G., Hughes S.M., Illingworth G.D., Kelson D., Kennicut R.C., Madore B.F., Phelps R., Stetson P.B., Turner A., 1995, ApJ, 449, 413

Neuschaefer L.W., Windhorst R.A., 1995, ApJ, 439, 14

Nielsen H.B., Oleson P., 1973, Nucl. Phys., B61, 45

Nusser A., Davis M., 1994, MNRAS, 271, 976

Oort M.J.A., 1988, A&A, 193, 5

Padmanabhan T., 1993, Structure Formation in the Universe., Cambridge University Press, Cambridge

Paczyński B., 1986, Nature, 319, 567

Peacock J.A., Dunlop J.S., Windhorst R.A., 1996, MNRAS, (in preparation)

Peacock J.A., 1996, Lectures given at the EADN Summer School, The Structure of the Universe, Leiden (astro-ph/9601135)

Peacock J.A., 1994, in Robinson A., Terlevich R.J., eds, Proc. 33rd Herstmonceux Conference, The Nature of Compact Objects in AGN, Cambridge Univ. Press, Cambridge, p.101

Peacock J.A., Dodds S.J., 1994, MNRAS, 267, 1020 (PD)

Peacock J.A., 1992, in Martinez V., Portilla M., Sáez D., eds, New Insights into the Universe, Proc. Valencia summer school, Springer, Berlin, p1

Peacock J.A., Nicholson D., 1991, MNRAS, 253, 307 (PN)

Peebles, 1993, Principles of Physical Cosmology, Princeton University Press, Princeton

Press W.H., Schechter P., 1974, ApJ, 187, 425

Rhie S., Bennett D., 1990, Phys. Rev. Lett., 65, 1709

Riess A.G., Press W.H., Kirshner R.P., 1995, ApJ, 438, L17

Robinson J., Albrecht A., 1995, MNRAS, in press (astro-ph/9505123)

Rowan-Robinson M., 1986, The Cosmological Distance Ladder, Freeman

Saha A., Labhardt L., Schwengler H., Macchetto F.D., Panagia N., Sandage A., Tammann G.A., 1994, ApJ, 425, 14

Sakellariadou M., 1990, Phys. Rev. D, 42, 354

Sandage A., 1995, in Binggeli B., Buser R., eds, The Deep Universe, 23rd Advanced SAAS-Fee Course, Springer, Berlin

Shanks T., 1990, in Bowyer S., Leinert C., eds, The Galactic & Extragalactic Background Radiation, Dordrecht, Kluwer

Shanks, T., 1985, Vistas Astron., 28, 595

Shellard E.P.S., Allen B., 1990, in Gibbons G.W., Hawking S.W., Vachaspati T., eds, The Formation and Evolution of Cosmic Strings, CUP, Cambridge (SA90)

Shellard E.P.S., 1988, Nucl. Phys. B, 283, 624

Simpson J.J., 1985, Phys. Rev. Lett., 54, 1891

Smith A.G., Vilenkin A., 1987, Phys. Rev. D, 36, 991

Spinrad H., Djorgovski S., 1987, in Hewitt A., Burbidge G., Fang L.Z., eds, Proc. IAU Symp. 124, Observational Cosmology, Reidel, Dordrecht

Starobinsky A.A., 1985, Sov. Astr. Lett., 11, 133

Stebbins A., 1988, ApJ, 327, 584

Storrie-Lombardi L.J., McMahon R.G., Irwin M.J., Hazard C., 1995, in Meylan G., ed., Proceedings of the ESO Workshop on QSO Absorption Lines, Springer-Verlag, Berlin

Sutherland W., Saunders W., 1992, MNRAS, 259, 413

Sutherland W., 1988, MNRAS, 234, 159

Tegmark M., Silk J., Blanchard A., 1994, ApJ, 420, 484

Trimble V., 1987, Ann. Rev. Astr. Ap., 25, 423

Turok N., 1985, Phys. Rev. Lett., 55, 1801

Unewisse A.M., Hunstead R.W., Piestrzynski B., 1993, Proc. Astron. Soc. Aust., 10, 229

Vachaspati T., Vilenkin A., 1985, Phys. Rev. D, 31, 3052

Vachaspati T., Vilenkin A., 1984, Phys. Rev. D, 30, 2046

Vilenkin A., Shellard E.P.S., Cosmic Strings and other Topological Defects, CUP, Cambridge

Vilenkin A., 1986, Nature, 322, 613

Vilenkin A., 1981, Phys. Rev. D, 23, 4

Walker T.P., Steigman G., Schramm D.N., Olive K.A., Kang H.S., 1991, ApJ, 376, 51

Webster A.S., 1977, in Jauncey D.L. ed., IAU Symposium 74, Radio Astronomy and Cosmology, Dordrecht, Reidel

White M., Gelmini G., Silk J., 1994, Phys. Rev. D., in press

White M., Scott D., Silk J., 1994, ARA&A, 32, 319

White S.D.M., Efstathiou G., Frenk C.S., 1993, MNRAS, 262, 1023

White S.D.M., 1989, in Peacock J.A., Heavens A.F., Davies A.T., eds, Proc. 36th Scottish Universities Summer School in Physics, Physics of the Early Universe, SUSSP, Edinburgh

Windhorst R.A., 1984, PhD thesis, University of Leiden

Wolfe A.M., Turnshek D.A., Smith H.E., Cohen R.D., 1992, ApJ, 385, 151

Zel'dovich Ya. B., 1986, Astrophys. Sp. Phys. Rev., 5, 1

Zel'dovich Ya. B., 1972, MNRAS, 192, 663

Mon. Not. R. Astron. Soc. 277, 143–151 (1995)

The small-scale clustering power spectrum and relativistic decays

S.J. McNally[1] and J.A. Peacock[2]
[1]*Institute for Astronomy, University of Edinburgh, Blackford Hill, Edinburgh EH9 3HJ*
[2]*Royal Observatory, Blackford Hill, Edinburgh EH9 3HJ*

Accepted 1995 May 26. Received 1995 May 18; in original form 1994 December 16

ABSTRACT
We present constraints on decaying-particle models in which an enhanced relativistic density allows an $\Omega = 1$ Cold Dark Matter universe to be reconciled with acceptable values for the Hubble constant. Such models may contain extra small-scale power, which can have important consequences for enhanced object formation at high redshifts. Small-scale galaxy clustering and abundances of high-redshift damped Lyman α absorption clouds give a preferred range for the mass of any such decaying particle of 2 to 30 keV and a lifetime of 0.5 to 100 yr for models with a high Hubble constant ($h > 0.75$). A lower Hubble constant, $h \simeq 0.5$, weakens the constraint to $0.5 < m < 30$ keV, $0.2 < \tau < 500$ yr. In permitted versions of the model, reionization occurs at redshifts $\sim 10 - 200$, and this feature may be of importance in understanding degree-scale CMB anisotropies.

Key words: galaxies: clusters: general – galaxies: formation – cosmology: theory – large-scale structure of Universe.

1 INTRODUCTION

Observations of large-scale galaxy clustering have produced something of a crisis for theories of cosmological structure formation. The paradigm for the past decade has been a model where scale-invariant adiabatic primordial fluctuations cause clustering to grow in dark matter which is collisionless, and which has negligible thermal velocities; in many ways, observations have supported the basic elements of this picture. The clustering power spectrum is smooth and featureless, with no sign of the oscillatory features that would be expected if normal baryonic material were dynamically dominant (e.g. Peacock & Dodds 1994; hereafter PD). The detection of cosmic microwave background (CMB) anisotropies on a variety of angular scales favours a fluctuation spectrum which is indeed close to adiabatic and scale-invariant for wavelengths above about 100 Mpc (e.g. White, Scott & Silk 1994).

Despite these encouraging features, there has emerged a consensus that there is a problem with the shape of the fluctuation spectrum. The density of the universe should be written on the sky in the form of a break in the spectrum at around the comoving horizon scale at matter–radiation equality

$$r_{\rm H} = 16.0\,[\Omega h^2]^{-1}\ {\rm Mpc} \qquad (1)$$

(as usual, $h \equiv H_0/100\ {\rm km\,s^{-1}\,Mpc^{-1}}$). This number, and all others in the paper, assumes $T = 2.726$ K for the CMB temperature (Mather et al. 1994). Since observed wavenumbers come in units of $h\ {\rm Mpc}^{-1}$, the combination Ωh is measurable, and in practice is estimated by fitting a model of a scale-invariant spectrum modified by the Cold Dark Matter (CDM) transfer function. According to PD, an approximate 95 per cent confidence range for the apparent value of the density is

$$0.22 < \Omega h|_{\rm apparent} < 0.29 \qquad (2)$$

(allowing for effects of non-linearity and redshift-space distortions). The problem is that this number appears to be inconsistent with current estimates of h and an $\Omega = 1$ Einstein–de Sitter universe, and a variety of possible solutions have been suggested.

(1) Maybe $\Omega \simeq 0.3$. This is perhaps the most obvious solution observationally, but brings in philosophically worrying fine tunings, either if the universe is open or if vacuum energy provides the remaining fraction of the critical density.

(2) Perhaps h really is around 0.25 (Shanks 1985; Bartlett et al. 1995). This explanation has the merit of simplicity, but would fly in the face of all the experimental evidence.

(3) A primordial spectrum tilted away from scale-invariance alters the fitted apparent density. However, a large degree of tilt is required and this is difficult to reconcile with the CMB studies (Cen et al. 1992; PD).

(4) The fit assumes pure CDM. If the baryonic density parameter $\Omega_{\rm B}$ is non-zero, what is measured for $\Omega = 1$ is roughly $\Omega h \exp[-2\Omega_{\rm B}]$ (PD). If $h \simeq 0.7$, $\Omega_{\rm B} \gtrsim 0.5$ would be required; it is very hard to see how such a high value can be consistent with primordial nucleosynthesis (e.g. Walker et al. 1991).

(5) One can tinker with the dark matter content to improve things, and the Mixed Dark Matter model with roughly 20–30

per cent of the dark matter being light neutrinos has received considerable recent attention (e.g. Klypin et al. 1993).

(6) Lastly, the apparent low density can be regarded as informing us that matter–radiation equality must be later than the standard figure. This can be achieved with an enhanced density of relativistic species, probably associated with the decay of a massive particle.

With the exception of (1), all of these are measures designed to save the Einstein–de Sitter universe without abandoning the basic picture of gravitational instability. In this sense, all are tainted with something of an air of desperation. Nevertheless, because of the profound consequences of any disproof of the Einstein–de Sitter model, it is important to explore all avenues thoroughly. The least contrived escape routes seem to be those involving modifications either of the dark matter or of the relativistic content, and it is on this latter possibility that we wish to concentrate. It turns out that the characteristic prediction of such a model is of an enhanced amplitude of fluctuations on small scales, and we use this feature to place limits on the decaying particle involved in the model. In Section 2, we review the model and establish a fitting formula to describe the power spectrum that results. Section 3 assembles the relevant observational constraints in terms of small-scale clustering and the abundances of high-redshift objects.

2 CDM WITH A DECAYING PARTICLE

2.1 The basic model

Structure formation scenarios incorporating decaying particles have a long history (e.g. Davis et al. 1981; Bardeen, Bond & Efstathiou 1987). However, this model was given a strong boost by experimental work suggesting the possibility of neutrino eigenstates with $m \simeq 17$ keV (e.g. Simpson 1985). Although it is now believed that these results were spurious, the possibility of a mass of this order for e.g. the τ neutrino is far from being ruled out. Such a neutrino cannot be stable, otherwise it would close the universe many times over. An acceptable present density can be achieved if the massive neutrino decays to products that are relativistic today – either to other massless neutrinos or possibly to some exotic new species. Decays to photons are not allowed for two reasons. First, the *COBE* results on the lack of CMB spectral distortions severely limit the allowed energy injection prior to recombination (Mather et al. 1994). Secondly, the relativistic density in photons is observed, and a total relativistic density is conventionally obtained by multiplying by a factor 1.68 to allow for three species of massless neutrinos. The possibility we wish to consider here, however, is that the true relativistic density is higher. If the decays producing this enhanced background occurred at redshifts greater than conventional matter–radiation equality ($z \simeq 24\,000\,\Omega h^2$), the onset of matter domination would be delayed, and we would have an explanation of the large-scale structure problem. The other constraint on the model is that decay should happen after nucleosynthesis at $z \sim 10^9$, to ensure that the light element abundances are not affected; this leaves a wide range of possible lifetimes and hence masses for the model. We note that Dodelson, Gyuk & Turner (1994) have discussed specifically more complicated nucleosynthesis effects which occur when the decay is contemporaneous with nucleosynthesis (decay lifetime $\sim$ 10 s), but we will see below that lifetimes this short do not have such interesting consequences for the Mpc-scale fluctuation spectrum.

The analysis presented in this paper follows on from work by Bond & Efstathiou (1991; hereafter BE). They calculated density fluctuations in $\Omega = 1$ models dominated by CDM, in which 17-keV neutrinos having lifetimes between 1 and 10^4 yr decayed to relativistic products. BE derived power spectra which differ from standard CDM in two key ways.

(1) The decay increases the density of relativistic degrees of freedom ('radiation' for short) and so delays the onset of matter–radiation equality. The length scale associated with the Hubble radius at this epoch is correspondingly modified. This modification is parametrized by θ (Bardeen et al. 1987) which is the ratio of energy density in relativistic species with a decaying particle to that without. Equation (1) now reads

$$r_{\rm H} = 16.0\,[\Omega h^2]^{-1}\,\theta^{1/2}\ {\rm Mpc} \tag{3}$$

and as a result the apparent value of Ωh (the effective shape parameter for CDM transfer functions) is dependent on the mass and lifetime of the decaying particle. An appropriate choice of these parameters can reconcile the $\Omega h \simeq 0.25$ value which best fits the observed large-scale structure with the theoretically favoured $\Omega = 1$ and the observationally implied $h = 0.5 - 0.9$.

(2) If the decay time exceeds $\sim 10 m_{\rm keV}^{-2}$ yr the universe can pass through *two* periods of matter domination, the first occurring when the density of undecayed particles exceeds that of relativistic species. This is followed by a phase dominated by the relativistic decay products. The second phase of matter domination arrives when the density of the cold dark matter exceeds that of the decay products. As a result of these processes the power spectrum is characterized by two length scales. Fluctuation growth can occur in the first matter-dominated epoch – providing greater small-scale power than is generated in the standard CDM scenario, and pushing the formation of sub-cluster-size objects to higher redshift.

In this paper we extend the model of BE, allowing both the lifetime and mass of the hypothetical particle to vary. We then constrain these parameters by consideration of structure formation on large and small scales.

2.2 Power-spectrum scalings

We now sketch the dependence of θ on the mass and lifetime of the decaying particle. We adopt the units

$$m \equiv \text{mass / keV} \tag{4}$$

$$\tau \equiv \text{decay time / yr.} \tag{5}$$

We will treat the decaying particle as a heavy neutrino, in the sense that the initial number density of the particle will be set equal to that for a massless neutrino. The energy density in decaying particles therefore becomes dominant over the radiation at time $t_{\rm eq1}$ when mc^2 is of the order of the radiation energy kT. Until this point $\rho \propto T^4$ and the age of the universe is $t \sim (G\rho)^{-1/2} \propto T^{-2} \propto m^{-2}$. Once they are non-relativistic, the density of heavy neutrinos scales as $\rho \propto a^{-3}$, whereas the density of radiation in the standard massless neutrino model scales as $\rho \propto a^{-4}$. By the time of decay, the massive neutrinos therefore dominate the conventional relativistic density by a factor

$$\frac{\rho_{\rm decay}}{\rho_{\gamma+3\nu}} \simeq \frac{a_{\rm decay}}{a_{\rm eq1}} \simeq \left(\frac{\tau}{t_{\rm eq1}}\right)^{2/3} \propto m^{4/3}\tau^{2/3}. \quad (6)$$

Here $a_{\rm eq1}$ and $a_{\rm decay}$ are the scale factors at the first matter–radiation equality and at decay respectively; $\rho_{\rm decay}$ is the energy density in the relativistic decay products from the massive neutrinos; and $\rho_{\gamma+3\nu}$ is the standard energy density for radiation and three light neutrinos. This assumes an effectively instantaneous decay for the particles at time τ and a negligible mass for the two other neutrino species. We can now write

$$\theta = \frac{\rho_{\gamma+2\nu}+\rho_{\rm decay}}{\rho_{\gamma+3\nu}} \simeq \frac{1.45}{1.68}\left[1+x(m^2\tau)^{2/3}\right], \quad (7)$$

with x a dimensionless constant. By a numerical solution of the full equations describing the problem, BE obtained $x \simeq 0.15$.

We now turn to the parameter dependences of the horizon sizes at the various epochs of matter–radiation equality. The horizon scale at the the time at which the non-relativistic density of the massive neutrinos first becomes dominant is given by equation (3). Now, a massive neutrino has $\Omega h^2 = m/0.095$ in our units (e.g. Kolb & Turner 1990, but scaling to the *COBE* $T = 2.726$ K); $\theta_{\rm eq1} = 1.45/1.68$; and $\theta_{\rm eq2}$ is as given above. We therefore deduce the sizes of the comoving horizons at the two equality scales:

$$r_{\rm H}^{\rm eq1} = 1.41\, m^{-1}\ {\rm Mpc} \quad (8)$$

$$r_{\rm H}^{\rm eq2} = 14.9\, h^{-2}\left[1+x(m^2\tau)^{2/3}\right]^{1/2}\ {\rm Mpc}. \quad (9)$$

The effect of this is to yield a power spectrum with two characteristic break wavenumbers, of order the reciprocal of the appropriate $r_{\rm H}$. The result can be modelled as the sum of two CDM spectra with differing power-law break lengths and different amplitudes, i.e.

$$\Delta^2(k) = \Delta^2_{\rm LSS}(k) + \alpha^2\Delta^2_{\rm LSS}(k/\beta). \quad (10)$$

Throughout, we shall express power spectra in dimensionless form:

$$\Delta^2(k) \equiv {\rm d}\sigma^2/{\rm d}\ln k = k^3P(k)/2\pi^2. \quad (11)$$

The expression (10) says that the small-scale power spectrum looks like the CDM model which fits large-scale structure, but with a 'bump' superimposed which is a copy of the large-scale spectrum that has been shifted to smaller scales by a factor β and boosted by a factor α^2. The large-scale spectrum, $\Delta^2_{\rm LSS}$, would be just the standard BBKS CDM spectrum (Bardeen et al. 1987) with an apparent density

$$\Omega h|_{\rm apparent} = \Omega h\left(\frac{1.45}{1.68}\left[1+x(m^2\tau)^{2/3}\right]\right)^{-1/2}. \quad (12)$$

The shift β is just the ratio of the horizon sizes deduced above:

$$\beta = 10.6mh^{-2}\left[1+x(m^2\tau)^{2/3}\right]^{1/2}. \quad (13)$$

The 'boost factor' α is more subtle. Until the decay epoch, the spectrum has only the small-scale break, and there can be no growth on these scales during the second period of radiation domination between $a_{\rm decay}$ and $a_{\rm eq2}$. The spectrum on larger scales can grow, which imprints the second break. If the spectrum has a primordial power-law index n, then $\Delta^2 \propto k^{3+n}$ on large scales; the difference in power at the two breaks (k_1 & k_2, say) is then given by a translational factor $(k_1/k_2)^{3+n}$ and the growth which occurs on large scales during the second period of radiation domination (a factor $[r_{\rm H}^{\rm eq2}/r_{\rm H}^{\rm decay}]^2$ in $\delta\rho/\rho$):

$$\alpha^2 = \frac{[r_{\rm H}^{\rm eq2}/r_{\rm H}^{\rm eq1}]^{3+n}}{[r_{\rm H}^{\rm eq2}/r_{\rm H}^{\rm decay}]^4}. \quad (14)$$

In the scale-invariant $n = 1$ case (assumed hereafter), this is just $\alpha = [r_{\rm H}^{\rm decay}/r_{\rm H}^{\rm eq1}]^2$. To obtain this ratio, note that $r_{\rm H} \propto t^{1/3}$ during the relevant (matter-dominated) phase; since we start at a time $\propto m^{-2}$ and end at τ, we finally obtain

$$\alpha = y\,[m^2\tau]^{2/3}, \quad (15)$$

where y is a further dimensionless constant which must be determined by fitting an exact integration. To obtain the value of this constant, we compared the power spectrum (7) with the BE results for 17-keV neutrinos decaying at 0, 1, 10, 10^2, 10^3 and 10^4 yr. These spectra are reproduced in Fig. 1(a). It was found useful to adopt a softening parameter γ such that

$$\Delta^2(k) = \left(\,[\Delta^2_{\rm LSS}(k)]^\gamma + [\alpha^2\Delta^2_{\rm LSS}(k/\beta)]^\gamma\,\right)^{1/\gamma}. \quad (16)$$

This smooths the transition region at which the small-scale power of the second term becomes dominant over that of the first. The best fit obtained requires the prefactor for α to be $y = 1.29$, with $\gamma = 0.30$.

To sum up, we have constructed the power spectra for a universe containing $\Omega = 1$ in CDM plus a decaying massive neutrino, including both the correct large-scale shape and the size plus location of the small-scale bump. The requirement for an apparent $\Omega h = 0.25$ fixes $m^2\tau$ if the true Hubble constant is known:

$$m^2\tau \simeq (125h^2 - 7)^{3/2}, \quad (17)$$

and this also fixes the boost parameter α. The only freedom in the model is then the location of the small-scale feature, which depends only on the mass. To illustrate this procedure, Fig. 1(c) shows three models with $m^2\tau = 120$, and fixing the apparent Ωh at 0.25. There is clearly a large range of possibilities for the power at $k \gtrsim 1$, which is what makes this model of interest.

To complete the picture we must allow for the damping of power that occurs due to free streaming of the massive neutrinos whilst they are still relativistic. An analysis of this effect by Bardeen et al. (1986) shows that damping corresponds to approximately Gaussian filtering of the linear power spectrum with $R_{\rm f} = 2.6(\Omega h^2)^{-1}{\rm Mpc} = 0.247m^{-1}$ Mpc. In practice, the scales and masses of interest are such that this damping has a negligible effect. Finally, we have seen that there are a number of assumptions which lead to the restriction on α (assumed abundance of decaying particles; scale-invariant spectrum); there will be some advantages to abandoning physical preconceptions on occasion and treating α and β as completely free parameters which describe empirically any small-scale features in the power spectrum.

3 CONSTRAINTS

3.1 Normalization

We now need to place limits on the model by comparing its predictions with observations of structure in the universe. For this, we require normalization for the theoretical power spectra. This can be expressed as the linear theory rms density contrast when averaged over spheres of radius $8\,h^{-1}$ Mpc, i.e. σ_8. White, Efstathiou & Frenk (1993) use the observed abundance of rich clusters to deduce a hard allowed range of $\sigma_8 = 0.52 - 0.62$. Direct measurements of σ_8 from clustering require a

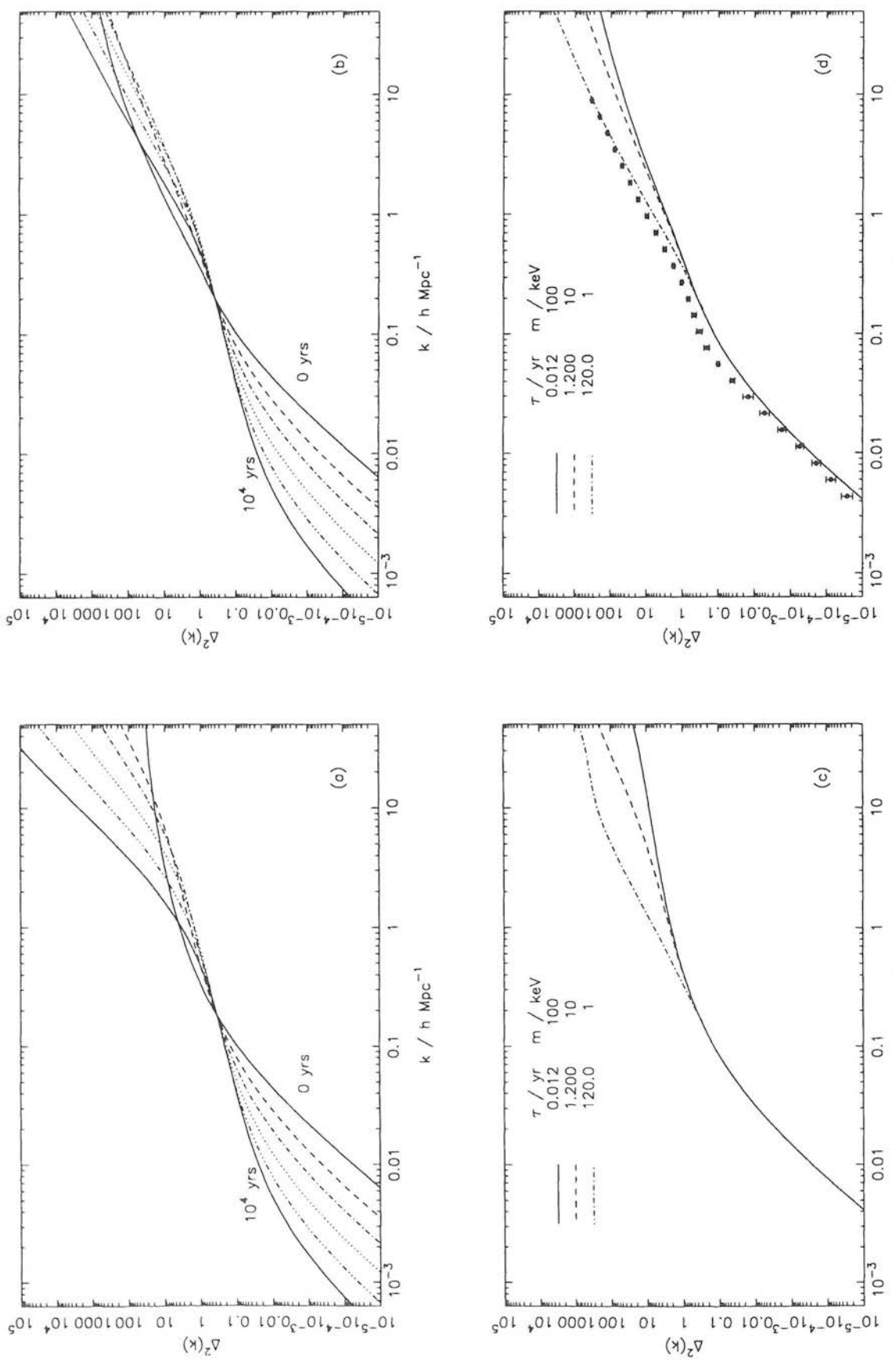

Figure 1. (a) Best fits to the Bond & Efstathiou (1991) power spectra obtained via the scalings of Section 2.2. The mass is set at 17 keV and the lifetime varied from 0 to 10^4 yr. The 0-yr curve is equivalent to standard CDM (BBKS). There is progressively more large-scale power as the lifetime is increased. $h = 0.5$ throughout. (b) The power spectra of (a) subjected to the non-linear correction of Peacock & Dodds (1994; PD). (c) Three power spectra with parameters satisfying $m^2\tau = 120$ and hence fulfilling the large-scale structure requirement (equation 2) for $\Omega h_{\rm true} = 0.5$. A range of small-scale behaviour is still possible. (d) The power spectra of (b) subjected to the non-linear correction of PD. The points with error bars are the power spectrum obtained by angular deprojection of the APM galaxy survey (Baugh & Efstathiou 1993).

knowledge of the bias parameter, and Feldman, Kaiser & Peacock (1994) give $\sigma_8 = 0.91/b - 0.18/b^{1.8}$ from the study of *IRAS* galaxies. Studies of peculiar velocities and comparison to density fields can yield estimates of b; such estimates are summarized in table 1 of Dekel (1994), and yield $1/b$ from this technique in the range 0.6 – 1.3, corresponding to $\sigma_8 = 0.47$ - 0.89. The higher values can probably be eliminated by the pairwise random motions of galaxies. This issue was studied thoroughly by Gelb & Bertschinger (1994), who concluded that $\sigma_8 > 0.7$ was untenable, and that even $\sigma_8 = 0.5$ yielded uncomfortably high velocities. We shall adopt $\sigma_8 = 0.6$, which is perhaps at the higher end of the allowed range; since we are looking to see if extra small-scale power is required, it makes sense to be conservative and adopt the highest reasonable normalization for the large-scale mass spectrum. PD give a discussion of the relation between $\Delta^2(k)$ and σ_8, and argue that σ_8 largely measures the power at $k \simeq 0.2h\,\mathrm{Mpc}^{-1}$. For BBKS scale-invariant spectra, an accurate numerical fit for the effective wavenumber is

$$k_{\mathrm{eff}}/h\,\mathrm{Mpc}^{-1} = 0.172 + 0.011[\ln(\Omega h/0.34)]^2. \qquad (18)$$

Finally, therefore, we adopt $\Delta^2(0.18\,h\,\mathrm{Mpc}^{-1}) = 0.6^2$ as our normalization.

To evolve these linear power spectra to the present day ($z = 0$) involves non-linearities which can alter the power spectrum significantly at small scales. In evolving the $\Delta^2(k) \gtrsim 1$ portion of the power spectrum we use the formulae of PD (derived from the work of Hamilton et al. 1991, which was based on N-body simulations on the relevant scales) to incorporate the effects of non-linear evolution. Whilst this correction increases the small-scale power for shallow power-law regions it actually removes power in regions with a strong k-dependence. Figs 1(b) and (d) show the non-linear correction applied to the spectra of 1(a) and (c) respectively.

3.2 High-redshift objects

One way of constraining the small-scale ($k \gtrsim 0.2\,h\,\mathrm{Mpc}^{-1}$) power is to require that it is sufficient to form the observed abundances of high-redshift objects, in particular quasars, radio galaxies and damped Lyman α systems. Radio galaxies have a well-defined mass, but this is rather large; they are also a rare population, so that current data do not set a very strong constraint on fluctuation spectra (Peacock 1994). Quasars are a more numerous population, but the ease with which observed quasar abundances can be attained is very much dependent on the (uncertain) mass assumed (e.g. Efstathiou & Rees 1988; Haehnelt 1993) and we have avoided their use here.

More stringent constraints can be derived from recent deep measurements of damped Lyα systems with H I column densities greater than $\sim 2 \times 10^{20}$ cm^{-2} (Lanzetta et al. 1991). These have been used by several authors to investigate rival dark matter models. If the fraction of baryons in the virialized dark matter haloes equals the global value Ω_{B}, then these data can be used to infer the total fraction of matter that has collapsed into bound structures at high redshifts (Ma & Bertschinger 1994; Mo & Miralda-Escudé 1994). The highest measurement at $\langle z \rangle \simeq 3.2$ implies $\Omega_{\mathrm{HI}} \simeq 0.005$, and hence a collapsed fraction of $\simeq 10$ per cent if $\Omega_{\mathrm{B}} = 0.05$. Here we apply the Walker et al. (1991) constraint to the baryon density, namely $\Omega_{\mathrm{B}}h^2 = 0.0125 \pm 0.0025$.

The assumption here will be that the damped Lyα systems are the progenitors of present day spiral galaxies. Evidence for this view has been provided by absorption in lensed quasar systems, showing the systems to be of galactic dimensions (Wolfe et al. 1992). Furthermore the baryon mass inferred in present-day galaxies is comparable to that of the damped Lyα systems at $z \simeq 3$. The photoionizing background prevents systems with circular velocities of less than about 50 km s^{-1} cooling sufficiently to form bound systems (e.g. Efstathiou 1992). We follow Mo & Miralda-Escudé (1994) and use this conservative velocity limit to estimate the minimum mass of object that the Lyα measurements detect. Virial equilibrium for a halo of mass M and radius r_{v} demands

$$v_{\mathrm{c}}^2 = \frac{GM}{r_{\mathrm{v}}}. \qquad (19)$$

For a spherically collapsed object this velocity can be converted directly into a Lagrangian comoving radius containing this mass (White et al. 1993):

$$r_0 = \frac{2^{1/2}v_{\mathrm{c}}}{H_0\Omega^{1/2}(1+z)^{1/2}(1+178\Omega^{-0.6})^{1/6}}. \qquad (20)$$

The values introduced above require $r_0 > 0.15\,h^{-1}$ Mpc.

To use the measurement to constrain our candidate power spectra we employ the well-known formalism of Press & Schechter (1974) which gives a collapsed fraction Ω_{c} above some mass scale M_{coll}, given a redshift z and a means of computing the $z = 0$ rms density contrast as a function of mass $\sigma(M, z = 0)$:

$$\Omega_{\mathrm{c}}(> M_{\mathrm{coll}}, z) = 1 - \mathrm{erf}\,[\delta_{\mathrm{c}}(1+z)/\sqrt{2}\sigma(M_{\mathrm{coll}}, z = 0)]. \qquad (21)$$

$\sigma(M)$ can be evaluated by filtering the power spectrum on the required scale. Here we use a spherical 'top hat' filter of radius R_{T} (for which $f(k) = 3(\sin y - y\cos y)/y^3$ with $y = kR_{\mathrm{T}}$) with a corresponding mass of $4\pi\rho R_{\mathrm{T}}^3/3$. Our lower mass limit corresponding to $r_0 = 0.15\,h^{-1}$ Mpc is therefore $M_{\mathrm{coll}} = 10^{9.6}h^{-1}\mathrm{M}_\odot$. δ_{c} is the critical overdensity required for collapse, which for a 'top hat' overdensity undergoing spherical collapse is 1.686. This canonical value has recently received support from N-body simulations on relevant scales by Ma & Bertschinger (1994).

Our power spectra are therefore required to produce an Ω_{c} which *exceeds* the Lyα collapsed fraction at all z, for $M > 10^{9.6}h^{-1}\mathrm{M}_\odot$. The true collapsed fraction could be higher than the observed one because some large fraction of the baryonic material in collapsed haloes could be ionized or in stars. Fig. 2 shows how various models fare in meeting this demand. The points with errors are the H I fraction in damped Lyα systems from Lanzetta (1993) and Storrie-Lombardi et al. (1995). Standard $\Omega h = 0.5$ CDM, curve (c), successfully attains a sufficient collapsed fraction at the high-redshift end. Models that agree with the APM at large scales do less well. (b) $\Omega h = 0.25$ CDM and (a) MDM with $\Omega_{\mathrm{HDM}} = 0.25$ both fall short of having enough small-scale power. The $\Omega h = 0.5$ CDM + relativistic decay model (d) for $\tau = 10$ yr and $m = 3.5$ keV has ample small-scale power thanks to the extra bump from the first epoch of matter domination.

How seriously should these constraints be taken? A pure $\Omega h = 0.25$ spectrum does not fail to fit the data by a very large amount, and it is not implausible that such a model could be rescued by tweaking the assumptions in the calculations – perhaps most readily by assuming a larger Ω_{B}. Furthermore,

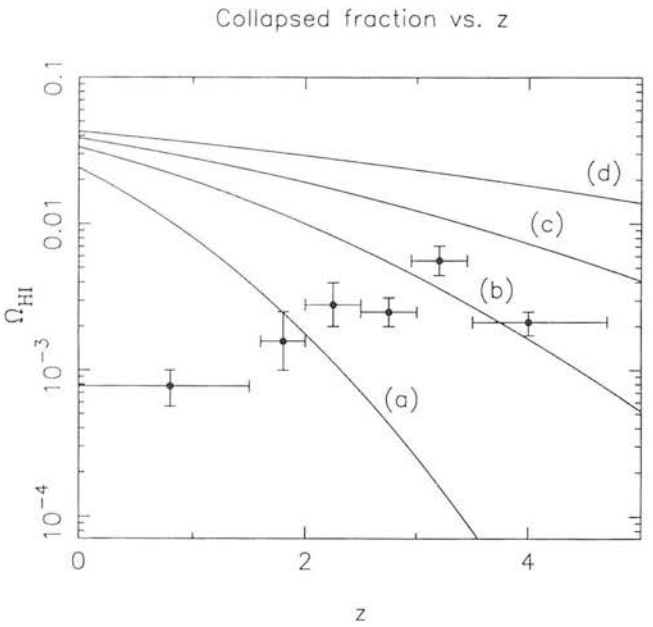

Figure 2. Collapsed baryon fractions (in terms of critical density) for four dark matter models. (a) Mixed Dark Matter with Ω_{HDM}=25 per cent, and $h = 0.5$, (b) CDM with $\Omega h = 0.25$, (c) CDM with $\Omega h = 0.5$, (d) CDM + relativistic decay model with $\Omega h = 0.5$, $\tau = 10$ yr and $m = 3.5$ keV. The points with 1σ error bars are damped Lyα system densities adopted from Lanzetta (1993) apart from the $z = 4$ point, taken from Storrie-Lombardi et al. (1995). Only models (c) and (d) have enough small-scale power to account for the collapsed fraction at $z \simeq 3.2$, though model (c) is ruled out by large-scale observations. We have assumed $\Omega_B = 0.05$ throughout, each model being normalized to $\sigma_8 = 0.6$ at $z = 0$. All these comparisons assume $h = 0.5$; since Ω_{HI} scales as h^{-1}, a higher true Hubble constant would lower the data points and make it easier for some models to satisfy the constraints.

the data themselves may not be definitive. The inferred column density of a damped Lyα system is exponentially sensitive to its velocity width, and this can easily be artificially enhanced by superposition of Lyα forest systems in the wings. Storrie-Lombardi et al. (1995) also suggest that the $\langle z \rangle = 3.2$ Lanzetta point may be slightly too high. We therefore cannot claim that the need for extra small-scale power is rigorously established. Nevertheless, because it is unlikely that all collapsed H I can escape ionization, it is valuable to explore models that allow a significant increase of the collapsed fraction at high z.

3.3 Galaxy clustering

The above constraints require only some minimum level of power; however, we are not at liberty to exceed this minimum by too large a factor. One limitation is provided by modelling the infrared Tully–Fisher relation between galaxy luminosity and circular velocity in the scenario of interest. A number of authors (e.g. Cole et al. 1994) have shown that standard $\Omega h = 0.5$, $\sigma_8 \simeq 0.7$ CDM has too much power on small scales, yielding, for a given luminosity, circular velocities which are 60 per cent larger than is observed. Without a relatively complicated modelling of galaxy formation we cannot subject our candidate spectra to the same test.

A more straightforward upper limit to the power can be provided by comparison of the candidate power spectra with the observed small-scale power spectrum, best determined by angular deprojection of the APM galaxy survey (Baugh & Efstathiou 1993, who give data down to $k \simeq 8\,h\,\mathrm{Mpc}^{-1}$). The degree of small-scale bias relating the power spectrum of mass to that of the observed light is not known with any great accuracy, but the mass-to-light ratios of clusters strongly encourage us to believe that the small-scale clustering of light must exceed that of mass, if $\Omega = 1$. Although some models have been advocated in which this would not be true (e.g. the paper by Couchman & Carlberg 1992 on $b = 1$ standard CDM), it is reasonable to regard such a situation as observationally unacceptable. We will therefore set a conservative upper limit to the allowed degree of small-scale power by demanding that the theoretical non-linear power spectrum of the mass at no point exceeds that of the light, as measured by the deprojection of the APM angular clustering. As with the Tully–Fisher relation, $\Omega h = 0.5$ CDM with our chosen normalization fails this test.

4 ALLOWED MODELS

4.1 Limits on parameters

The limits on the decaying neutrino models derived by the above methods are summarized in Figs 3 and 4.

Figs 3(a) and (b) are more 'empirical' representations of the results in that they show the values of α and β that give a permissible power spectrum in light of the Lyman α and APM constraints. 3(a) and (b) differ in the assumed value of the Hubble constant, $h = 0.5$ and 0.75 respectively. The baryon fraction depends on h and is correspondingly modified. The large-scale portion of the theoretical power is fixed at $\Omega h = 0.25$ CDM and the small-scale high-k portion alone is varied. A band of acceptable values results, which narrows as h is increased, through the change in Ω_B. As β and α are dependent on the combination $(m^2\tau)^{2/3}$, selecting a particular value of h effectively fixes the 'growth' parameter α. The dot-dashed lines on the figure indicate the growth allowed when $m^2\tau$ is such that $\Omega h = 0.5$ and $\Omega h = 0.75$ are matched on to the large-scale observations. Within the usual range discussed for h, therefore, the model is constrained to have a shift parameter $\beta \simeq 80 - 2500$ and a growth factor $\alpha \simeq 30 - 80$.

Figs 4(a) and (b) translate the results of Figs 3(a) and (b) from general form, to apply specifically to the decaying-neutrino model, identifying regions in the mass–lifetime plane ruled out by the constraints discussed above. Fig. 4(a) refers to an $\Omega h = 0.50$ model with $\Omega_B = 0.050$, Fig. 4(b) to $\Omega h = 0.75$, $\Omega_B = 0.022$. The region disallowed by the Lyα structure formation requirement at $z = 3.2$ is indicated by the darker shaded areas. In order not to exceed the small-scale APM curve, the parameters must lie somewhere in the plane away from the lighter shaded region. The dashed line from top-left to bottom-right of each plot represents $m^2\tau \simeq 120$ and 500, the values required to reconcile $\Omega h_{\mathrm{apparent}} = 0.25$ with $\Omega h_{\mathrm{true}} = 0.50$ and 0.75. We can summarize the conclusions from these figures as follows:

$$\Omega h = 0.50 \quad \Rightarrow \quad 0.5 < m < 30 \text{ keV},\ 0.2 < \tau < 500 \text{ yr} \tag{22}$$

$$\Omega h = 0.75 \quad \Rightarrow \quad 2.0 < m < 30 \text{ keV},\ 0.5 < \tau < 100 \text{ yr}. \tag{23}$$

Are these parameter values physically plausible? The dot-dashed line in Figs 4(a) and (b) shows the equation

$$m^5\tau = 3 \times 10^4 \text{ keV}^5 \text{ yr}, \tag{24}$$

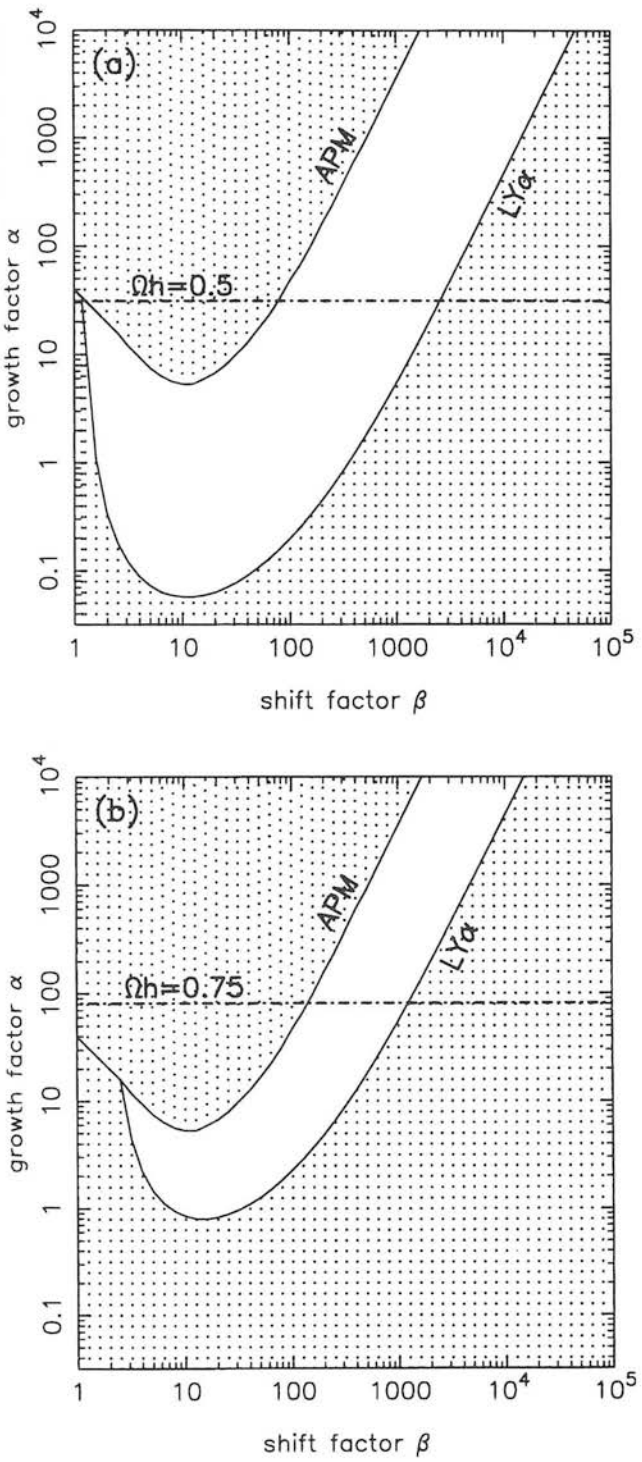

Figure 3. Constraints on the α and β parameters introduced in Section 2.2. For a given value of β, α must lie *above* the Lyα line for a sufficient collapsed fraction to form at $z = 3.2$. α must however lie *below* the APM curve to avoid exceeding the APM power spectrum for $k > 1h$ Mpc^{-1}. A band of permitted α and β values results (unshaded region). Furthermore if $m^2\tau$ is fixed to match the large-scale structure then α = const. This is shown as the dashed-dotted line in each case: (a) $\Omega_B = 0.050$, $\Omega h = 0.50$, (b) $\Omega_B = 0.022$, $\Omega h = 0.75$.

which is the form of a naive prediction for the relation between mass and lifetime for a particle that decays via the weak interaction. This takes the usual E^5 scaling of weak-interaction cross-sections and scales to the decay of the μ lepton. In neither case does this 'muon-decay' line cross the large-scale structure line in a permitted region; if the model is to be considered plausible, the decay physics involved must be more exotic.

4.2 Early reionization

The existence of significant small-scale power in decaying-particle CDM can allow structures of mass $10^5 - 10^8 h^{-1}\mathrm{M}_\odot$ to form earlier than in the standard model and so may permit early reionization of the intergalactic medium. We have performed a brief analysis based on the method of Tegmark, Silk & Blanchard (1994). They estimate a parameter f_{net}, the net efficiency of ionization processes from stars, and calculate $f_s(M)$ the collapsed fraction of the universe (which gives rise to the star formation). These they relate to an ionization fraction χ such that

$$\chi \simeq 3.8 \times 10^5 f_{\mathrm{net}} f_s. \tag{25}$$

Tegmark et al. give a range of f_{net} values they believe permissible, dubbing the top of the range 'optimistic' (in the sense of promoting early reionization), the bottom of the range 'pessimistic' and the median value 'middle-of-the-road'. Once f_{net} is set in this manner the requirement of 100 per cent reionization ($\chi > 1$) becomes a condition on f_s which can be calculated by the same Press–Schechter method as was used to analyse the Lyman α constraint. In order to get a feel for the sort of redshifts at which reionization could occur in our model we set $m^2\tau \simeq 500$, the value needed to give an apparent $\Omega h = 0.25$ in the case where $\Omega = 1$ and $h = 0.75$. We then vary the mass within the range 0.01 to 100 keV, τ being set at $500/m^2$. f_s is calculated for the resulting power spectra and used to derive the redshift at which reionization is complete.

In Fig. 5 we show the expected reionization redshifts for each of the f_{net} values suggested. The mass scale for the Press–Schechter integration (cf. equation 21) relates to the masses of the first galaxies to form, and there is a considerable range of possibilities from $10^5 h^{-1}\mathrm{M}_\odot$ (Couchman & Rees 1986) to $10^7 - 10^8 h^{-1}\mathrm{M}_\odot$ (Blanchard, Valls-Gabaud & Mamon 1992). Fortunately the power spectra are relatively flat in this range and the collapsed fraction is relatively insensitive to M_{coll}. Our results relate to the mass scale $10^7 h^{-1}\mathrm{M}_\odot$. In rough agreement with the Tegmark et al. results, typical reionization redshifts are in the range $\sim 10 - 200$ for an optimistic or middle-of-the-road f_{net}. A pessimistic f_{net} permits early reionization only around $m \sim 1$ keV. CMB photons will be significantly scattered by the reionized plasma if the optical depth between z_{ion} and $z = 0$ is $\simeq 1$. To obtain this requires $z_{\mathrm{ion}} \simeq 50$ (e.g. Padmanabhan 1993) which can occur in the relativistic decay model for $m \sim 2 - 10$ keV – within our allowed range. Such a result may well be of importance in wiping out details of the last scattering surface on angular scales around $\sim 1^\circ$ (e.g. White, Scott & Silk 1994). We note here that White, Gelmini & Silk (1994) predict a sensitive dependence of degree-scale CMB anisotropies on the parameters of the decaying particle model. They suggest that $m^2\tau$ may, in principle, be determined from the CMB, with a large 1° bump for models with large $m^2\tau$. Such a feature is excluded observationally, but we have shown that the small-scale power in this model may well cause sufficiently early reionization to complicate significantly the measurements in this range.

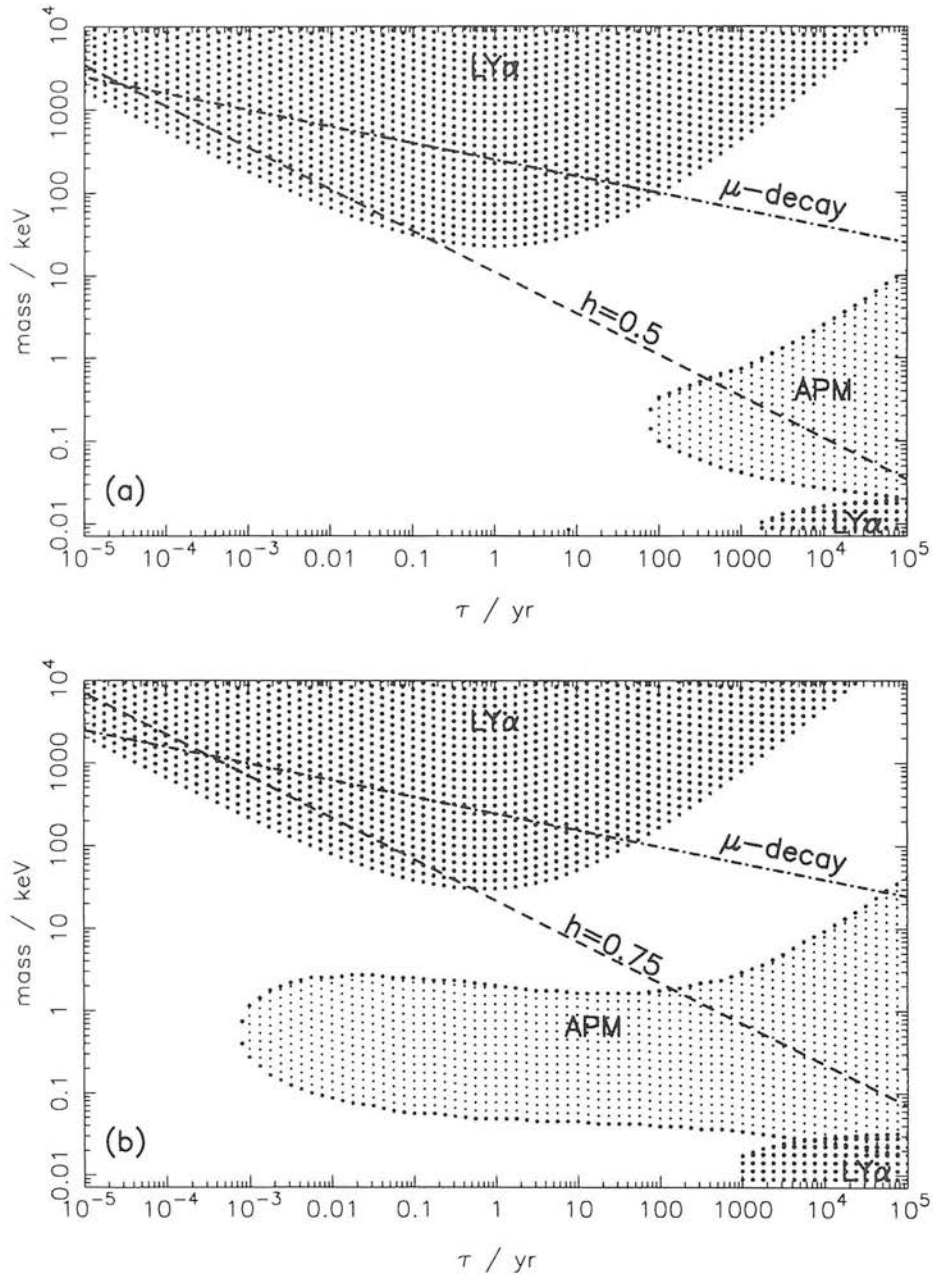

Figure 4. Constraints on mass and lifetime of hypothetical decaying neutrino. Limits are based on the damped Lyα fraction at redshift $z = 3.2$ (darker shaded region forbidden). Values that would exceed the APM power spectrum for $k > 1h$ Mpc^{-1} occupy the lighter shaded region. (a) Model constraints for $\Omega h = 0.5$, $\Omega_B = 0.050$. The dashed line shows the large-scale structure constraint for $\Omega h = 0.5$, the dot-dashed line the $m^5\tau \simeq$ const law for decaying heavy leptons. (b) Model constraints for $\Omega h = 0.75$, $\Omega_B = 0.022$. The dashed line shows the large-scale structure constraint for $\Omega h = 0.75$, the dot-dashed line the $m^5\tau \simeq$ const law for decaying heavy leptons.

5 SUMMARY

We have demonstrated that the parameters of the $\Omega = 1$ decaying-particle + CDM model can be constrained by small-scale power-spectrum requirements. Whilst we must generate sufficient power at $\sim 0.1h^{-1}$Mpc scales to affect significantly the observed number of high-z damped Lyα systems, the existence of APM clustering data on comparable scales limits how much power can be added. Successful models of this general kind are therefore quite tightly constrained. Although present data cannot be claimed to provide definitive proof for a small-scale feature in the power spectrum, interesting consequences are predicted for future data on high-redshift objects.

Within an acceptable range for h, the mass of any decaying neutrino is constrained to lie between 0.5 and 30 keV and the lifetime to lie between 0.2 and 500 yr. Structure formation can commence sufficiently early in this scenario to permit early reionization of the IGM. For a range of allowed parameters the reionization will inevitably occur sufficiently early to modify CMB fluctuations on scales of $\sim 1^\circ$ and below.

Although it thus has some attractive features, the model

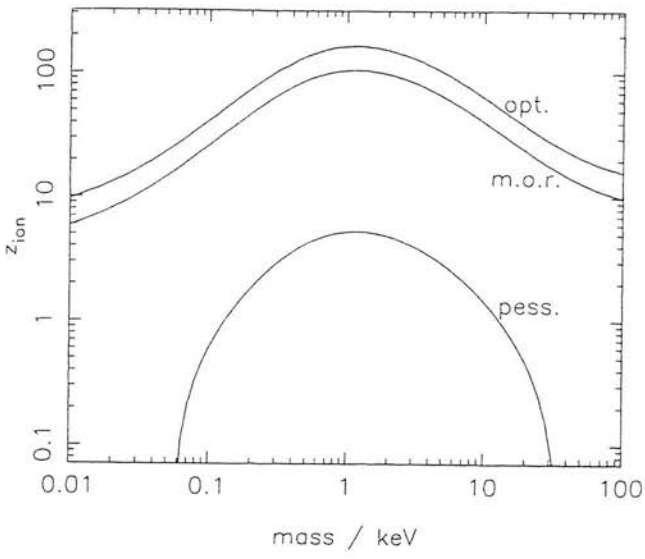

Figure 5. Reionization redshifts as a function of decaying-particle mass for the case $\Omega h = 0.75$, i.e. $m^2\tau \simeq 500$. We take the mass of the earliest galaxies to form to be $10^7 h^{-1}\mathrm{M}_\odot$ though the results are similar for the range $10^5 - 10^8 h^{-1}\mathrm{M}_\odot$. The labels 'optimistic', 'middle-of-the-road' and 'pessimistic' (abbreviated to opt., m.o.r., and pess.) refer to the efficiency of reionization by stars and are discussed in the text. Reionization occurs in the range $z \simeq 10 - 200$ for most of the parameter space investigated.

is not without its difficulties. Since we retain the Einstein–de Sitter universe, the problem of short Hubble times is not evaded, and may ultimately prove fatal. Furthermore, as with all high-density models, a convincing mechanism for biased galaxy formation needs to be supplied. However, the merit of the picture studied here is that it is reasonably well constrained and so testable directly in terms of particle physics. If the Einstein–de Sitter model is to be saved, this is arguably the least contrived way to do it.

ACKNOWLEDGMENTS

SJM acknowledges the support of a SERC/PPARC research studentship. We thank Dick Hunstead and Rocky Kolb for helpful discussions, and particularly Michael Turner for saving us from error at an early stage of this investigation.

REFERENCES

Bardeen J.M., Bond J.R., Efstathiou G., 1987, ApJ, 321, 28
Bardeen J.M., Bond J.R., Kaiser N., Szalay A.S., 1986, ApJ, 304, 15 (BBKS)
Bartlett J.G., Blanchard A., Silk J., Turner M.S., 1995, Science, 267, 980
Baugh C.M., Efstathiou G., 1993, MNRAS, 265, 145
Blanchard A., Valls-Gabaud D., Mamon G.A., 1992, A&A, 264, 365
Bond J.R., Efstathiou G., 1991, Phys. Lett. B, 265, 245 (BE)
Cen R., Gnedin N.Y., Kofman L.A., Ostriker J.P., 1992, ApJ, 399, L11
Cole S., Aragón-Salamanca A., Frenk C.S., Navarro J.F., Zepf S.E., 1994, MNRAS, 271, 781
Couchman H.M.P., Carlberg R.G., 1992, ApJ, 389, 453
Couchman H.M.P., Rees M.J., 1986, MNRAS, 221, 53
Davis M., Lecar M., Pryor C., Witten E., 1981, ApJ, 250, 423
Dekel A., 1994, ARA&A, 32, 371
Dodelson S., Gyuk G., Turner M.S., 1994, Phys. Rev. Lett., 72, 3754
Efstathiou G., 1992, MNRAS, 256, 43P
Efstathiou G., Rees M.J., 1988, MNRAS, 230, 5P
Feldman H.A., Kaiser N., Peacock J.A., 1994, ApJ, 426, 23
Gelb J., Bertschinger E., 1994, ApJ, 436, 491
Haehnelt M.G., 1993, MNRAS, 265, 727
Hamilton A.J.S., Kumar P., Lu E., Matthews A., 1991, ApJ, 374, L1
Klypin A., Holtzmann J., Primack J., Regős E., 1993, ApJ, 416, 1
Kolb R., Turner M., 1990, The Early Universe. Addison Wesley, Redwood City, California
Lanzetta K., 1993, PASP, 105, 1063
Lanzetta K., Wolfe A.M., Turnshek D.A., Lu L., McMahon R.G., Hazard C., 1991, ApJS, 77, 1
Ma C., Bertschinger E., 1994, ApJ, 434, L5
Mather J.C. et al., 1994, ApJ, 420, 439
Mo H.J., Miralda-Escudé J., 1994, ApJ, 430, L25
Padmanabhan T., 1993, Structure Formation in the Universe. Cambridge University Press, Cambridge, p.237
Peacock J.A., 1994, in Robinson A., Terlevich R.J., eds, Proc. 33rd Herstmonceux Conference, The Nature of Compact Objects in AGN. Cambridge Univ. Press, Cambridge, p.101
Peacock J.A., Dodds S.J., 1994, MNRAS, 267, 1020 (PD)
Press W.H., Schechter P., 1974, ApJ, 187, 425
Shanks T., 1985, Vistas Astron., 28, 595
Simpson J.J., 1985, Phys. Rev. Lett., 54, 1891
Storrie-Lombardi L.J., McMahon R.G., Irwin M.J., Hazard C., 1995, in Meylan G., ed., Proceedings of the ESO Workshop on QSO Absorption Lines. Springer-Verlag, Berlin, in press
Tegmark M., Silk J., Blanchard A., 1994, ApJ, 420, 484
Walker T.P., Steigman G., Schramm D.N., Olive K.A., Kang H.S., 1991, ApJ, 376, 51
White M., Gelmini G., Silk J., 1994, Phys. Rev. D, in press
White M., Scott D., Silk J., 1994, ARA&A, 32, 319
White S.D.M., Efstathiou G., Frenk C.S., 1993, MNRAS, 262, 1023
Wolfe A.M., Turnshek D.A., Smith H.E., Cohen R.D., 1992, ApJ, 385, 151

This paper has been produced using the Royal Astronomical Society/Blackwell Science LaTeX style file.